Title

Numerical Study of Hypersonic Boundary-Layer Receptivity and Stability with Freestream Hotspot Perturbations

Author

Huang, Yuet

Publication Date

2016

UNIVERSITY OF CALIFORNIA

Los Angeles

Numerical Study of Hypersonic Boundary-Layer Receptivity and Stability with Freestream Hotspot Perturbations

A dissertation submitted in partial satisfaction of the
requirements for the degree of Doctor of Philosophy
in Aerospace Engineering

by

Yuet Huang

2016

ABSTRACT OF DISSERTATION

Numerical Study of Hypersonic Boundary-Layer Receptivity and Stability with Freestream Hotspot Perturbations

by

Yuet Huang
Doctor of Philosophy in Aerospace Engineering
University of California, Los Angeles, 2016
Professor Xiaolin Zhong, Chair

This dissertation presents a numerical simulation study of linear hypersonic boundary-layer receptivity and stability over blunt compression cones with freestream hotspot perturbations. This study is conducted for freestream disturbances with broad, continuous frequency spectra over cones that have nose radii of 1, 0.5 and 0.1 mm under freestream conditions of Mach 6, 10 and 15. The simulations are carried out using the high-order shock-fitting finite-difference scheme developed by Zhong (1998), the results of which are shown to agree well with linear stability theory (LST) and experiments. The general receptivity mechanism is then studied by the simulation-LST comparisons under two parametric effects: nose bluntness and freestream Mach number. Among the new findings of the current study, the mechanisms of the receptivity process are found to be mainly caused by the fast acoustic waves that are generated behind the bow shock from the hotspot/shock interaction in the nose region. It is these fast acoustic waves that

substantially enter the boundary layer and generate mode F through the synchronization of fast acoustic waves and mode F in the upstream part of the cone. Subsequently, the synchronization of modes F and S generates mode S, or the second mode, which eventually grows into a dominant level at the downstream part of the cone. Additionally, we have obtained the receptivity coefficients of mode S along the Branch-I neutral stability curve using a method that combines LST predicted N-factors and simulated disturbance amplitudes. These receptivity coefficients agree well with those obtained from the theoretical modal decomposition method.

In addition to obtaining the general receptivity mechanism and receptivity coefficients, we have also studied the parametric effects of nose bluntness and freestream Mach number on boundary-layer receptivity and stability over cones. Specifically, our results have shown that nose bluntness reduces the boundary-layer receptivity to freestream entropy perturbations and stabilizes the perturbed boundary layer over a cone. The boundary layer is more receptive to freestream entropy perturbations at higher freestream Mach numbers, while the perturbed boundary layer is stabilized at higher freestream Mach numbers.

The current receptivity and stability study has not only shed new light on the receptivity mechanism to freestream entropy spots over blunt cones, but also advanced the understanding of nose bluntness and freestream Mach number effects on the receptivity and stability over blunt cones. Furthermore, the currently-obtained broad, continuous spectra of unstable-second-mode receptivity coefficients could potentially provide the initial amplitudes for future amplitude-based transition predicting methods.

The dissertation of Yuet Huang is approved.

Christopher R. Anderson

Ann R. Karagozian

Richard E. Wirz

Xiaolin Zhong, Committee Chair

University of California, Los Angeles

2016

TABLE OF CONTENTS

LIST OF FIGURES

LIST OF TABLES

NOMENCLATURE

a = phase speed

c_p = specific heat in a constant pressure process

c_v = specific heat in a constant volume process

$d(\ )$ or $(\ )'$ = the perturbation of a variable

$(\ )_{shk}$ = the variable immediately behind shock

$(\ )_\infty$ = the freestream variable

e = total energy per unit volume

F = frequency

F_j = inviscid flux vector in j^{th} direction

F_{vj} = viscous flux vector in j^{th} direction

H^* = local height from the wall

L^* = length scale of the boundary-layer thickness

M_∞ = freestream Mach number

P = pressure

P_∞ = freestream pressure

Pr = Prandtl number

q_j = heat flux due to thermal conduction

R = local Reynolds number

R^* = gas constant

Re_∞^* = freestream Reynolds number per unit length

s = natural coordinate along the body surface

S = entropy

S_∞ = freestream entropy

$(\ )^*$ = the dimensional variable

t = time

T = temperature

T_∞ = freestream temperature

T_o = total temperature

T_r = reference temperature

T_s = Sutherland’s temperature

T_{shk} = temperature immediately behind shock

T_{wall} = temperature at wall

u_1, u_2, u_3 = velocity components

u_∞ = freestream velocity

u_t = tangential velocity

y_n = normalized local normal distance from the wall

α = streamwise complex wave number

α_i = local growth rate

α_r = local wave number

η = coordinate in the direction normal to the wall

γ = ratio of specific heat

κ = heat conductivity coefficient

λ = second viscosity coefficient

μ = viscosity coefficient

μ_∞ = freestream viscosity coefficient

μ_r = reference viscosity coefficient

ω = circular frequency

φ = phase angle

ρ = mass density

ρ_∞ = freestream density

τ = time in computational domain

τ_{ij} = shear stress tensor

ξ = coordinate in streamwise direction

ζ = coordinate in azimuthal direction

ACKNOWLEDGEMENTS

I wish to express my sincere appreciation to my doctoral advisor and committee chair, Professor Xiaolin Zhong, for his insightful guidance and unconditional support throughout the years leading up to the completion of this dissertation. I also wish to thank Professor Christopher R. Anderson, Professor Ann R. Karagozian, and Professor Richard E. Wirz for their time, efforts and patience while serving on my committee.

Additionally, I would also like to thank my former research colleagues: Dr. Neal Parsons, Dr. Pradeep Rawat, Dr. Jia Lei, Dr. Clifton Mortensen, Dr. Akshay Prakash, Dr. Xiaowen Wang, and finally Dr. Le Duan for their patience, enthusiastic assistance, and warm encouragement when I faced difficulties at the initial and developmental stages of my research. Without their invaluable patience and assistant, I would not have been able to begin my research or produce its results in a timely manner. I also would like to thank my current colleagues, Michael Miselis, Danny Kahei Fong, Christopher Harley, Zeyu Bai, and Carleton Knisely for their invaluable exchanges of information and collaborations.

Finally, I wish to express my deep appreciation to Professor Steven P. Schneider and his group at Purdue University for providing their wind-tunnel experiments' data, results, and information.

This work was partially sponsored by the AFOSR/NASA National Center for Hypersonic Research in Laminar-Turbulent Transition and by the Air Force Office of Scientific Research, USAF, under Grant No. FA9550-07-1-0414 and Grant No. FA9550-15-1-0268, monitored by Dr. John Schmisseur and "Pon" R. Ponnappan, respectively. The views and conclusions contained herein are those of the author and should not be interpreted as necessarily representative of the official policies or endorsements, either expressed or implied, of the Air Force Office of Scientific Research or the United States Government.

VITA

2005 - 2008	B.S. in Aerospace Engineering, UCSD, San Diego, California
2008 - 2014	M.S. in Aerospace Engineering, UCLA, Los Angeles, California
2008 - 2016	Graduate Student Researcher, MAE department, UCLA, Los Angeles, California

PUBLICATIONS

1. Huang, Y. and Zhong, X., “Numerical Study of Hypersonic Boundary-Layer Receptivity with Freestream Hotspot Perturbations,” *AIAA Journal*, Vol. 52, No. 12, pp. 2652-2672, 2014.

2. Fong, K. D., Wang, X., Huang, Y., Zhong, X., McKiernan, G. R., Fisher, R. A., and Schneider, S. P., “Second Mode Suppression in Hypersonic Boundary Layer by Roughness: Design and Experiments,” *AIAA Journal*, Vol. 53, No. 10, pp. 3138-3144, 2015.

3. Miselis, M., Huang, Y., and Zhong, X., “Analysis of Receptivity Mechanisms for a Freestream Hot-Spot Perturbation on a Blunt Compression-Cone Boundary Layer,” AIAA Paper (to be published), 2016.

4. Huang, Y. and Zhong, X., "Parametric Study of Boundary-Layer Receptivity to Freestream Hot-Spot Perturbation over a Blunt Compression Cone," AIAA Paper No. 2014-0774, 2014.

5. Huang, Y. and Zhong, X., "Numerical Study of Boundary-Layer Receptivity on Blunt Compression-Cones in Mach-6 Flow with Localized Freestream Hot-Spot Perturbations," NATO AVT-Specialists’ Meeting on “Hypersonic Laminar-Turbulent Transition”, No. 20, 2012.

6. Huang, Y. and Zhong, X., "Numerical study of freestream hot-spot perturbation on boundary-layer receptivity for blunt compression-cones in Mach-6 flow," AIAA Paper No. 2011-3078, 2011.
7. Huang, Y. and Zhong, X., "Numerical study of laser-spot effects on boundary-layer receptivity for blunt compression-cones in Mach-6 freestream," AIAA Paper No. 2010-4447, 2010.

1 Introduction

1.1 Laminar-Turbulence Transition

When a vehicle travels in the atmosphere at hypersonic speeds, the perturbations from the freestream or those induced from the body of the vehicle enter the boundary layer, causing a laminar-turbulence transition of the boundary layer. Generally, the boundary-layer transition results from the nonlinear response of the boundary layer to environmental forcings [1-3]. The boundary-layer transition can significantly affect the performance and thermal protection systems of the vehicle, since the boundary-layer transition can increase both the skin friction and the surface heating rates by factors within the first order of magnitude [4-6]. Therefore, during the process of designing the aerodynamic and heat protection configurations of hypersonic aerospace vehicles, an accurate prediction of the boundary-layer laminar-turbulent transition location on the body's surface is very important. The fundamental mechanisms underlying the transition process must be understood in order to accurately predict the transition location. Despite many decades of research, the mechanisms of hypersonic laminar-turbulent transition are still not well understood.

Generally speaking there are several paths to boundary layer laminar-turbulence transition, which depend on the amplitude of the environmental disturbances. These are shown in Figure 1 [7-9]. The process of transition under weak environmental forcing disturbances is described as Path A. It can be divided into three stages: (i) boundary layer receptivity, (ii) linear eigenmode growth and interactions, and (iii) nonlinear breakdown to turbulence [4]. First, environmental disturbances enter the boundary layer and go through the receptivity process. During this receptivity process, the primary modes in the boundary layer are excited by the forcings. These primary modes will then interact with each other and form eigenmodes at the end of the receptivity process. After the receptivity process, the eigenmodes of the boundary-layer instability, which are the eigen-solutions of the homogeneous linearized stability equations [10], begin to grow exponentially. As the instability amplitude grows to a certain level, in which the nonlinearity of the stability equation becomes significant, the secondary mechanisms occur. The secondary mechanisms, which include the three-dimensional and the nonlinear interactions [11], subsequently cause the breakdown to turbulence. As the amplitude of the weak environmental forcings increases, the transition process follows Path B. Behind the receptivity process, the non-orthogonal growth arises in a stage called transient growth [7, 9]. The weak transient growth provides higher instability amplitude to the subsequent linear eigenmode growth. As the instability continues growing, the secondary mechanism occurs, which eventually leads to the breakdown to turbulence. If the environmental disturbance amplitude keeps increasing, the instability amplitude generated from the receptivity process also becomes higher. Thus, the transient growth becomes stronger, which generates stronger instability at the end of the transient growth. In Path C, the generated instability amplitude from the transient growth is high enough to skip the linear eigenmode growth, and directly leads to the secondary mechanisms. In Path D, the generated instability from transient growth has a spectrum that is as full as a turbulent spectrum, even while the boundary-layer is still laminar [7, 9]. The bypass mechanisms, which skip the secondary mechanisms and directly lead to the breakdown to turbulence, occur due to the strong transient growth [7-9]. In Path E, the very strong environmental disturbances directly lead to the breakdown of the laminar boundary layer to turbulence.

This occurs immediately after the receptivity process due to the strong initial excitation of the wave modes. There is no linear regime in this transition path [7-9]. In reality, environmental disturbances during hypersonic flight are mainly weak, therefore it is more important to study these transitions under weaker environmental disturbances, more than the stronger ones [10]. Please note that "waves", "disturbances" and "perturbations" are used interchangeably in this literature.

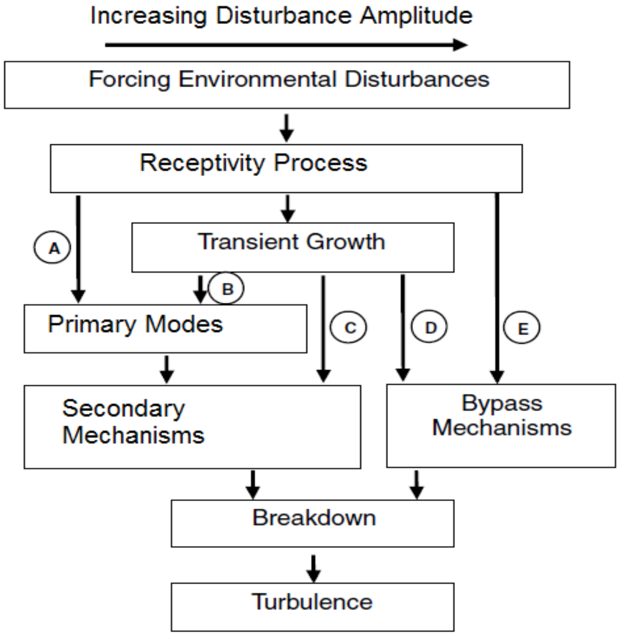

Figure 1. Paths of boundary layer transition regard to amplitude of environmental disturbances [7-9].

1.2 Predicting Methods of Transition

The boundary-layer transition process has been studied extensively in order to develop transition predicting strategies and methods. The most prevailing transition prediction method is the semi-empirical e^N method, developed by Smith and Gamberoni [12] and Ingen [13]. This method roughly predicts the transition locations based on where the e^N (the amplification ratio of the boundary-layer disturbances relative to the Branch-I neutral amplitude) reaches the empirically determined values. Since the growth of instability is exponential in the linear regime, the power index, N, namely N-factor, is used to indicate the level of amplification from the neutral amplitude. The N-factor that corresponds to transition occurrence, is determined by comparing the N-factors from the theoretical stability analyses, such as linear stability theory (LST) and parabolized stability equations (PSE), with the experimentally measured transition onset locations. Based on this strategy of obtaining the N-factors of the transition occurrence, we can see that limitations in the e^N method are evident. Firstly, owing to the fact that the transition occurs in the nonlinear regime, it is insufficient to use the growth in the linear regime to characterize the transition. Secondly, transition can take places with different amplification ratios under different disturbance environments, flow conditions and geometries of prototype. More specifically, the initial instability strength at the Branch-I neutral location prior to the instability growth must be considered when predicting where the transition occurs. Initial strength of instability at the Branch-I neutral location depends not only on the original strength of the perturbations, but also on the receptivity process after the perturbations enter the boundary layer before the Branch-I neutral location. The receptivity of the boundary layer varies based on the disturbance environment, flow condition and the geometry of the prototype. However, the e^N method does not specifically account for these disturbance environment, flow condition, and prototype geometry factors.

Previous research [14-23] determined the N-factors of the transition occurrence on circular blunt cones or a blunt body under different freestream disturbance environments with a freestream Mach number from 6 to 10, near a zero angle of attack. According to previous literature [15-23], the N-factor of transition occurrence in acoustically low noise freestream environments (e.g. quiet wind tunnels and flight environments) is typically around 8 to 11. In acoustically noisier freestream environments, such as conventional wind tunnels, the N-factor of transition occurrence is around 4 to 6. Nevertheless, an accurate correlation or physics-based method to determine the N-factor of transition occurrence for specific disturbance environments, geometry and flow conditions has never been established. To develop an accurate correlation, many simulations and experiments must be conducted under different effects, including different types and amplitudes of freestream disturbances, different prototype geometries and different flow conditions. In order to develop a physics-based prediction method of transition, which includes all factors that could affect the transition process, one must first thoroughly understand the receptivity mechanism under these different effects.

1.3 Stability of Hypersonic Boundary Layer

Based on the earlier discussion of transition paths, as illustrated in Figure 1, Path A is the transition path under weak or linear disturbance environments, such as flight environments and quiet wind tunnels. Behind the receptivity process, in which the linear environmental forcings enter the boundary layer and excite the discrete eigenmodes or the primary modes in the boundary layer, some modes interact with each other and grow exponentially, while other modes decay within the linear stability regime. The characteristics of the linear eigenmodes in the boundary layer are dependent on the stability of the boundary layer. The major instabilities in the hypersonic boundary layers with no angle of attack are the first mode instability and the second mode instability [24]. Those over the significantly curved surfaces are centrifugal or Goertler instability [25], and lastly, crossflow instabilities are the major instabilities in three-dimensional boundary layers [26].

1.3.1 Theoretical Studies

In LST, the boundary-layer stability problem is represented by the homogeneous linearized disturbance ODEs, derived from the Navier-Stokes equations with homogeneous boundary conditions. The locally parallel flow assumption is applied. The solution to the stability problem is a linear combination of normal wave modes. Mack [24] has provided an in-depth description of the linear stability theory. In the incompressible boundary layer with a favorable pressure gradient, the boundary layer has only viscous instability, namely Tollmien-Schlichting (T-S) waves. If there is an adverse pressure gradient in the boundary layer, the inviscid instability is dominant. The inflection point in the boundary-layer profile causes the inviscid instability. The most amplified frequencies for the inviscid instability waves are higher than those of the T-S waves [24].

In the compressible boundary layers in a supersonic freestream, the first mode in the boundary-layer instability is a combination of T-S waves and the inviscid instability, if a generalized inflection point (GIP) in the boundary-layer profile is present. The boundary layer of a hypersonic freestream contains a relative sonic line, which the local mean flow speed is sonic relative to the phase speed of the acoustic disturbances. The sonic line first appears at the wall of a flat plate when the boundary-layer edge Mach number is equal to 2.2. Then, the sonic line moves outward when the edge Mach number becomes greater. The acoustic disturbances is trapped in the relative supersonic region below the sonic line in the boundary layer as shown in Figure 2 [27]. In Figure 2, y_a is the normal height of the sonic line, U is the local mean flow streamwise speed, c is the phase speed of the acoustic disturbances, and a is the local speed of sound. Such trapped inviscid acoustic disturbances are the second or higher Mack modes [27]. In the boundary layer that has a relative supersonic region, the inviscid waves are always unstable regardless of the existence of GIP [24]. Mack [24] showed that the first mode at the oblique wave angle of around 60 degrees was the most unstable; the most unstable second mode was at no oblique wave angle. The most dominantly growing instability was still the two-dimensional second mode when the boundary layer edge Mach number is 4 or higher over a flat plate with a thermally insulated wall. [24, 28] Mack also determined that the wall-cooling effects stabilized the first mode and destabilized the second mode [24]. Malik [29] also showed that the two-dimensional second mode dominated the transition process over a sharp cone at lower hypersonic Mach numbers due to wall-cooling effects, which destabilized the second mode.

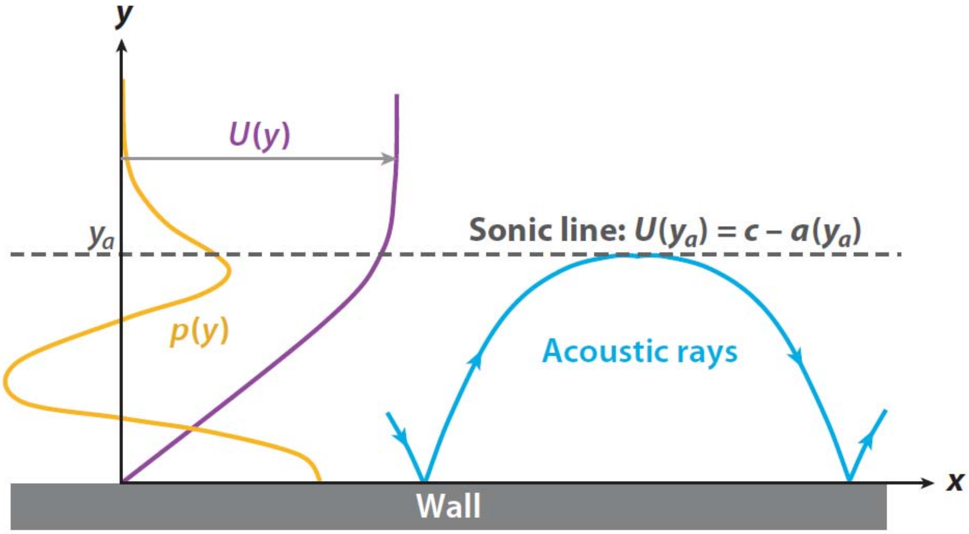

Figure 2. Schematic of the second or higher modes in the boundary layer. This figure is from Fedorov [27].

Many numerical simulation studies [3, 4, 28, 30-38], in addition to wind tunnel experimental studies [22, 23, 39-41], also found that under most of the situations of Path A in Figure 1 without significant crossflow or Goertler instabilities, the second mode was the most dominant instability, which then led to the transition. Therefore, two-dimensional second mode instability in a boundary layer is particularly important to the study of hypersonic boundary-layer transition.

There are only a few reported studies [29, 42, 43] with the adiabatic wall condition that proved the first mode is responsible for the transition. Malik [44] developed both the global and local eigenvalue methods to solve the compressible boundary-layer stability problem. He developed the multi-domain spectral collocation method to successfully resolve the outward movement of the critical layer as the Mach number outside the boundary layer increases. Malik [29] used the compressible LST to calculate the N-factors and applied the

e^N method with the transition N-factor of 10 to show that the first mode of oblique T-S waves was responsible for the transition over a sharp cone with an adiabatic wall and a freestream Mach number of up to 7.

Bountin *et al.* [42] obtained data over an adiabatic sharp cone of nose radius less than 0.1 mm from the tunnel experiment at the freestream Mach number of 5.92. Their results showed that despite the second modes' higher growth rates, the first mode is stronger and therefore responsible for the transition because of the higher initial amplitude of the first mode rather than that of the second mode.

Su *et al.* [43] conducted LST analysis for a numerical simulated steady base flow over a cone with a nose radius of 0.5 mm in the freestream of Mach 6. They compared the LST results with both the isothermal and adiabatic wall conditions. They determined that the difference in the neutral stability curves of the second mode between each wall condition was not as significant as that of the three-dimensional first mode. The critical Reynolds number for the three-dimensional first mode with adiabatic wall condition was much smaller than those of the isothermal wall condition and those of the two-dimensional second mode with both wall conditions. The unstable frequency range of the three-dimensional first mode was much wider than that of the isothermal wall and smaller than that of the two dimensional second mode. They found that the first mode growth rate with an adiabatic wall condition was higher than the one with an isothermal wall condition. The trend, however was opposite for the second mode. The maximum second mode growth rates with both wall conditions was greater than those of the first mode. Finally, they found that the streamwise N-factor curve of the first mode was higher than that of the second mode with an adiabatic wall condition, while the reverse trend was observed with the isothermal wall condition. Their results determined that the first mode might possibly be responsible for the transition process under adiabatic wall conditions.

Malik *et al.* [45] studied nose bluntness effects on stability and transition over a 7 degrees semi-vertex cone with 0.15, 0.25 and 0.7 inches of nose radii in Mach 8 freestream. The LST analysis of the steady base flow showed that the critical Reynolds number for the instability onset was increased by an order of magnitude with small nose bluntness added to a sharp cone. The LST predicted transition Reynolds numbers were also increased by the addition of small nose bluntness.

Experimental studies [46, 47] have observed transition reversal due to nose bluntness. Specifically, nose bluntness effects no longer delay the transition once the nose radius is larger than some critical values. Jia *et al.* [48] carried out LST analysis to study nose bluntness effects over three cones with different nose radii of 0.156, 0.5, and 1.5 inches in the freestream of Mach 5.5, the same as Stetson's experiment [46], where the transition reversal was originally reported. Jia *et al.* [48] found no transition reversal on the LST predicted second mode N-factors. The LST results confirmed, however that the transition was delayed by nose bluntness effects. They suggested that the transition reversal may be caused by uncontrollable noises from the conventional tunnel environment. These uncontrollable noises might have amplitude large enough to trigger the bypass mechanism, which skips the linear stability stage, thereby causing an earlier occurrence of transition. Additionally, their LST results showed that the unstable second mode was related to mode F due to wall-cooling effects. These results differ from previous stability studies [36, 49].

Herbert *et al.* [50] introduced the method of parabolic stability equations (PSE) that included nonparallel effects in compressible boundary layers. There were two types of PSE approaches: linear PSE and nonlinear PSE (NPSE) [51]. In contrast to LST, linear PSE included the effects of nonparallel boundary layer and surface curvature [51-53]. Moreover, NPSE included both these effects and nonlinear effects [51-53]. The PSE method, however did not consider disturbance environments and the effects of bow shock. Thus, PSE method cannot substitute the role of numerical simulation; PSE method, however is a more precise and extensive theoretical method for analyzing boundary-layer stability as compared to LST.

Johnson and Candler [21] developed a boundary layer stability equation solver named PSE-Chem. Their solver incorporated thermal and chemical nonequilibrium effects. The N-factors over a 5-degree cone with various nose radii of 2.5, 3.1, 3.7 and 4.8 mm in Mach 20 freestream with chemical nonequilibrium were computed. Their shock-capturing CFD solver, namely STABL, computed their steady base flow. Their N-factors showed that the effects of nose bluntness delay the transition, based on the transition onset N-factor criteria of 10.

Perez *et al.* [53] used PSE method to compute growth rates over the NASA Langley 93-10 flared cone with a nose radius of 38 microns, and over a compression cone in the Mach 6 freestream, which were the same as those computed in Wheaton *et al.* [23]. The PSE predicted growth rates in Perez *et al.* [53] were compared with the LST predicted and numerically simulated growth rates in the second mode frequency range in Huang *et al.* [54]. Generally speaking, PSE growth rates were closer than LST's predicted simulated growth rates due to the negligence of the non-parallel flow and surface curvature effects in LST. The PSE predicted growth rates agreed well with the simulated growth rates in the frequencies equal or above the second mode peak frequency, but the PSE predicted growth rates were slightly lower than the simulated ones at the frequencies below the peak frequency. They suggested that the difference between PSE predicted and simulated growth rates was due to the negligence of the distortion in the mean flow and the resulting boundary layer thickening in PSE. To capture the evolution of disturbances with increased initial disturbance amplitude and/or the broad disturbance spectrum, Perez *et al.* [53] concluded that both numerical simulation and NPSE were needed.

1.3.2 Experimental Studies

Hypersonic wind tunnel experiments focus mainly on measuring instability growth in the boundary layer, as well as the onset location or Reynolds number of boundary-layer transition over various geometries, e.g. flat plates and cones.

Mack [24] theoretically showed that the maximum spatial amplification rate of the first mode decreased significantly when the boundary layer edge Mach number was raised from 1 to 8; those of the second mode also decreased significantly when the boundary layer edge Mach number was raised from 5 to 10 over an insulated flat plate. In order to investigate parametric effects in the stability of the boundary layer and the transition location, Stetson [55] compared wind tunnel data with the flight data of cones in supersonic to hypersonic freestream with differing parameter variations. The wind tunnel data showed the following trend: the transition Reynolds number decreased with increasing freestream Mach number between Mach 1 to 3, while the minimum occurred around Mach 3 and 4. The Reynolds number consistently increased when the freestream Mach number also increased beyond Mach 3 and 4. Conversely, the flight experiments also showed the increase of transition Reynolds number in the supersonic range. He pointed out that the disturbances in the freestream of the wind tunnel were the most probable cause to the decrease of the transition Reynolds number, with an increasing freestream Mach number in the supersonic range.

Kendall [56] conducted an experimental study on the freestream Mach number effects from Mach 1.6 to 8.5 over a flat plate and a cone. It is worth noting that the freestream Mach number effects cannot be isolated from the unit Reynolds number effects, since the change of Mach number must accompany the change in unit Reynolds number in wind tunnel experiments. Moreover, the freestream noise spectra are different at differing freestream Mach numbers. Kendall found that the second mode was the dominant boundary-layer instability between the freestream Mach number from 5.6 to 8.5. The second mode appeared as rope waves over a long distance. He determined that the second mode frequency was much higher at a lower freestream Mach number. Moreover, he also suggested that the mode switching of the dominant instability between Mach 4.5 to 7.7 was related to the downshift of the second mode frequency, whereas the disturbance energy was mainly at lower frequency components in the freestream. Finally, he observed that wall-cooling effects reduced the first mode amplification rate and slightly increased that of the second mode.

Stetson *et al.* [39] conducted experimental studies on a blunt 7-degree half angle cone at Mach 8 freestream. The nose bluntness studied were 3% and 5% of the base radius. They found that nose bluntness stabilized the boundary layer. The critical location of the instabilities was found to approximately coincide with the location where the entropy layer was swallowed by the boundary layer. The sharp cone was found to have a lower critical Reynolds number, and the disturbance growth was only moderate under a long distance. The cone with the small nose bluntness, however, was found to have a higher critical

Reynolds number and the disturbance growth was more rapid. Unstable disturbances of inviscid instability in the entropy layer outside the boundary layer were also found.

Stetson [55, 57] reviewed that the increase of nose bluntness would then increase the transition Reynolds number for the cones within the “small” nose bluntness range. Within the “small” nose bluntness range, the nose radius Reynolds number was approximately less than 10^5 [46-48, 58], and the nose radius typically ranged from 1/32 inch to 1/4 inch. Contrarily, the increase of nose bluntness would decrease the transition Reynolds number, also known as the transition reversal phenomenon, for the cones within the “large” nose bluntness range where the nose radius Reynolds number was greater than 10^5.

Rufer *et al.* [59] conducted an experimental study on 7-degree half angle sharp and blunt cones. They found that sharp cone’s boundary-layer thickness was slightly thinner than that of the blunt cone at the same streamwise locations, under the same flow conditions. No instabilities were found on the sharp cone at the stagnation pressure of 91 psia with no angle of attack in the quiet flow, but instabilities were clearly seen under the same flow conditions in a noisy flow. Their measurement of the second mode frequencies under various stagnation pressures compared well with the second mode frequencies calculated by STABL code. More specifically, the difference between the experiment and the STABL calculation were equal or less than 8%.

Stetson [55] pointed out that the increase of a freestream unit Reynolds number will increase the most unstable frequency and the critical Reynolds number. As a result, the transition Reynolds number will also increase. Furthermore, he pointed out that the frequency range of disturbances in the environment was a very important factor on the transition Reynolds number. In many cases, the disturbance amplitudes at the higher frequencies were lower than the lower frequency components. Hence, if the most unstable frequency in the boundary layer was high, the transition will be delayed. The freestream acoustic disturbances in the supersonic and hypersonic wind tunnel, namely the tunnel noise, were generated by the turbulent boundary layer on the nozzle wall [55]. The frequency spectra of acoustic disturbances varied from tunnel to tunnel; therefore, the transition Reynolds numbers were also different between tunnels. Moreover, the transition Reynolds numbers measured in supersonic and hypersonic tunnels were usually lower than those in free flight.

Horvath *et al.* [60] conducted an experimental investigation on the influence of an acoustic disturbance environment in the Mach 6 wind tunnels on various parametric trends over a straight cone and a flared cone. Both cones had a 5-degree half angle. They compared the conventional Mach 6 tunnel data with the previous Mach 6 quiet tunnel data. They also computed the steady base flow of the cones by using CFD3D code, which implements the finite volume method to solve the three dimensional compressible Navier-Stokes equations. After the steady base flow was computed, they used LASTRAC code, which contains the options of LST, LPSE and NPSE, to compute the N-factors over the cones. They found that the transition onset Reynolds number under low disturbance condition of the quiet tunnel was 1.3 times greater than the one measured in the conventional tunnel, and 1.6 times greater than the one measured in the quiet tunnel under the noisy mode. The freestream conditions in these runs are comparable to each other and are measured on the flared cone. These results suggest that the noisy mode of the quiet tunnel contains a higher level of freestream acoustic disturbances, as compared to the conventional tunnel. The transition onset N-factors of the sharp flared cone in the conventional tunnel were approximately half of the N-factors of the sharp flared cone in the quiet tunnel.

Heitmann *et al.* [41, 61-65] used a laser spot as controlled perturbations to excite the second mode instability in the boundary layer over a cone and a flat plate. They [41] suggested using the laser to generate perturbations in three ways: (1) focus the laser on the model surface, both acoustic and entropy perturbations are generated locally in the boundary layer, (2) focus the laser at a point outside the boundary layer above the model surface, the expanding shock wave from the laser spot is used to perturb the boundary layer, and lastly (3) focus the laser upstream from the bow shock and the model, so the laser spot interacts with the bow shock and creates acoustic, entropy and vorticity waves behind the shock. Consequently, these waves perturbed the boundary layer. They stressed that the third method of generating perturbations can best resemble the natural transition scenario. Since the shock waves from the generation of the laser spot quickly attenuated in the freestream and passed the flow field before the entropy core of the laser spot reached the bow shock, the entropy core represented the major perturbations in this case.

Heitmann *et al.* [61, 62, 64] conducted experiments over a flat plate using the first and second approaches; they used the second approach over a cone. However, due to the complexity of the experiment on the third approach, only Schmisseur *et al.* [66, 67] conducted the freestream laser spot experiment over a cone with thorough measurements when Heitmann *et al.* [41, 62-65] published their results. Heitmann *et al.* [41] did not conduct the experiment using the third approach on a cone. In the experiments, they measured the boundary-layer disturbances downstream of the models and calculated the frequency spectra and growth rates of the disturbances. They demonstrated that the laser spot contained perturbations within the unstable frequency range of the second mode. During their experiments on both a flat plate and cone, the laser spot also successfully triggered the second mode instability. They also showed that the instability properties, such as the unstable frequency range and growth rates of the second mode triggered by the controlled perturbations, were the same as those triggered by natural disturbance environments.

Wheaton *et al.* [23] conducted an experimental study on a compression cone with a 1 mm nose radius in Boeing/AFOSR Mach-6 Quiet Tunnel (BAM6QT). They measured the second mode instability and second harmonics under both the quiet and noisy modes. The experimental second mode peak frequency under quiet mode with a stagnation pressure of $140\ \text{psia}$ was around $290\ \text{kHz}$. Noticeably, the peak frequency did not shift significantly, since the boundary-layer thickness was constant throughout the entire compression region of the cone. They used STABL solver to compute the steady base flow over a compression cone with a 1 mm nose radius in Mach 6 freestream with a stagnation pressure of $140\ \text{psia}$. Then, they used both LST and PSE-Chem solvers to calculate the N-factors over the compression cone. Their LST and PSE results indicated a maximum N-factor of 16 at the aft end $\left(x^* \approx 0.45\ \text{m}\right)$ of the compression cone. The predicted frequency range of the unstable second mode from the theoretical methods agreed well with the frequency range in the quiet mode measurement. Under the quiet mode, no transition was observed from the measured frequency spectra, even at the location where the N-factor was 13. From their noisy mode measured spectra, however, the transition appeared at $x^* = 0.3\ \text{m}$ where the N-factor was 7. Due to the concave geometry of the compression cone, Goertler instability also existed in the boundary layer. Li *et al.* [68], however, used PSE to show that the N-factor of the Goertler instability ($N = 4.6$ at $x^* = 0.4\ \text{m}$) was more than three times smaller than the N-factors of the second mode ($N = 15$ at $x^* = 0.4\ \text{m}$) over the compression cone. Thus, the second mode was the dominant instability in the linear stability regime over the compression cone.

1.3.3 Numerical Studies

In recent decades, due to rapid developments in computing power, numerical simulations of full unsteady Navier-Stokes equations over wide spatial domains of the hypersonic flow became a very powerful tool in studying boundary-layer transition. Many researchers in the field of hypersonic boundary-layer transition use numerical simulations and they have allowed researchers to discover more details about, and even new mechanisms in different stages of the boundary-layer transition. These were previously difficult to measure during wind-tunnel experiments and predict when using theoretical approaches.

Heitmann *et al.* [69] used DLR TAU code, which implements the finite-volume method, to perform a numerical simulation of the boundary layer perturbed by a laser spot that was initially imposed above the boundary layer and behind the bow shock of a sharp straight cone in a Mach 5.85 freestream. The boundary layer was perturbed by the spherical acoustic waves of the laser spot, but was not perturbed by the entropy core. The simulated time-histories at different sampling locations reasonably agreed with the experimental results in Heitmann *et al.* [61]. The simulated growth rates and the unstable second mode frequency range agreed reasonably well with LST.

Heitmann *et al.* [41] used DLR TAU code to simulate the laser spot perturbed flow over a sharp cone with Mach 5.9 freestream. The laser spot was initially placed upstream from the bow shock on the stagnation line. They found that the freestream laser spot contained the unstable frequency range of the second mode, and the laser spot successfully excited the second mode over the cone. They also observed the weakly unstable first mode on the cone. It is worth noting out that their focus was on the subsequent instability growth rather than the receptivity process before the growth.

Zhong [58] conducted a numerical study on boundary-layer stability with nose bluntness effects over an 8-degree half angle blunt cone in Mach 5.5 freestream by using high-ordered finite difference schemes with unsteady shock-fitting grids. Three nose radii of 0.0156 inch, 0.5 inch, and 1.5 inch were studied. These radii were mainly in the range of "large" nose bluntness [46, 58]. Such a study was intended to investigate the transition reversal due to nose bluntness observed in Stetson's wind tunnel experiment [46], so the flow conditions and the geometry of the cone were the same as the experiment. Zhong showed that the surface-coordinate-based local Reynolds number along the boundary-layer edge significantly decreased with the increase of nose bluntness and entropy layer effects. With the assumption that the variation of the transition Reynolds numbers was insignificant, the significant decrease of local Reynolds number was the main reason for the downstream shift of the transition location with the increase of nose bluntness within the "small" nose bluntness range. However, the transition reversal was not found in the simulation. Zhong also studied the surface blow/suction perturbed boundary layer over a cone with a 1.5 inch nose radius. He investigated the development of the disturbances both outside and inside the boundary layer throughout the cone. The unsteady simulation showed the second mode growth in the boundary layer; furthermore, the maximum growth rate agreed well with the LST prediction made by Lei *et al.* [70].

Kara *et al.* [71] conducted a numerical investigation of boundary-layer receptivity and stability over a 5-degree half angle cone in Mach 6 freestream by using fifth ordered WENO scheme. The boundary layer was perturbed by planar freestream slow acoustic waves with a single frequency at no incidence angle. The cone had three nose radii of 0.001 inch (nose Reynolds number of 650), 0.05 inch (nose Reynolds number of 32500) and 0.10 inch (nose Reynolds number of 65000). They carried out both an unsteady simulation and a PSE analysis. Their results indicated that nose bluntness carried strong stabilizing effects on boundary-layer stability. More specifically, the transition Reynolds number increased along with an increase in the nose Reynolds number. The bluntest cone (with a nose Reynolds number of 65000) had a transition Reynolds number that was 1.8 times greater than that of the sharp cone with no nose bluntness. They explained that this stabilizing effect is due to the longer distance of the entropy layer behind the blunt nose region over a blunter cone. By comparing two cases of the same nose Reynolds number but with different nose radii, they concluded that the nose Reynolds number was a key factor in deciding the stability and receptivity properties of the boundary layer, rather than the nose radius itself. Hence, nose-bluntness effects were directly related to the unit Reynolds number effects. The most amplified dimensionless frequency decreased with an increase in nose bluntness. They calculated the receptivity coefficient from PSE and concluded that the receptivity coefficient was lower under a higher nose Reynolds number. It is worth noting that their receptivity coefficient was defined as the ratio between the amplitude of the wall-pressure disturbances at the neutral point, and the freestream amplitude of the acoustic disturbances. Moreover, the receptivity coefficient at the most amplified frequency of the second mode was not required to be the maximum receptivity coefficient at the neutral point. Therefore, a comparison of the maximum receptivity coefficients would be more definitive to conclude the trend in receptivity.

Sivasubramanian *et al.* [38] conducted a numerical simulation of three-dimensional transient flow over a 7-degree half angle cone with a nose radius of 0.05 mm in Mach 6 freestream by using high ordered finite difference code. The flow was perturbed by a pulse of flow through a hole (blow and suction) on the cone surface upstream. This pulse of flow subsequently induced a wave packet in the boundary layer, which contained a wide range of frequency components. Their flow conditions were based on those of the BAM6QT tunnel at Purdue University. They studied the three-dimensional wave-packet evolution in the transition process and determined that the two-dimensional second mode was the dominant boundary-layer instability in the linear development of the wave packet. Moreover, the weaker oblique first mode waves, which appeared on the lateral sides of the wave packet, were also observed.

Laible *et al.* [72] numerically studied the effects of cone flaring in transition by simulating a straight cone and a flared cone of with a nose radius of 0.00254 mm in Mach 6 freestream. The flaring radius was 2.364 m and the initial half angle was 5 degrees. Both cones were the same length. Their flow conditions were based on the BAM6QT tunnel at Purdue University. The flow was perturbed by the blow and suction slot at the cone surface upstream. They found that the frequency of the most amplified waves remained constant throughout the flaring region of the cone, in contrast to the straight cone in which the frequency decreased downstream. This is due to the constant boundary-layer thickness over the flaring region, which differs from the streamwise growing boundary-layer thickness over the straight cone. The growth rates on the flared cone were also found to be greater than those on the straight cone. Additionally, the maximum N-factor at the end of the flared cone was found to be significantly greater than that of the straight cone.

Along with receptivity studies, many other numerical studies on boundary-layer stability are presented. These numerical studies in receptivity will be reviewed in Section 1.4.2.

1.4 Receptivity of Hypersonic Boundary Layer to Freestream Perturbations

Transition occurs at a location where the local boundary-layer instabilities have grown to certain amplitudes; the nonlinear breakdown to turbulence can then take place. Stability analysis provides an instability amplification ratio from the initial amplitude at the neutral point. In order to accurately predict the transition location, the initial amplitude of instability at the neutral point must be determined in addition to the stability analysis. Because disturbances have to go through the receptivity process before reaching the initial neutral point of instability growth, the receptivity mechanism must be studied in order to obtain the initial amplitude at the neutral point, with known information of the external perturbations. In other words, the purpose of studying receptivity is to find the relationship between external perturbations and instabilities in a boundary layer.

As discussed in Section 1.2 of the transition prediction method, the receptivity of the boundary layer varies based on the disturbance environment, flow condition, and the geometry of the prototype. A parametric study of the receptivity mechanism is thus necessary in order to establish an accurate transition prediction method.

Strictly speaking, boundary-layer receptivity is the receptive property of a boundary layer to external perturbations. Boundary-layer receptivity process is the process of exciting instability waves after the entrance of external perturbations into a boundary layer. As discussed in Section 1.1 of laminar-turbulence transition, the receptivity process is the preliminary stage in a transition process. In contrast to the stability problem, a receptivity problem has a forcing-driven boundary layer. Thus, depending on the actual form of forcings, the boundary-layer receptivity process involves either homogeneous disturbance equations with nonhomogeneous boundary conditions or nonhomogeneous equations with homogeneous boundary conditions. However, that equations and boundary conditions can both be nonhomogeneous. This is no longer an eigenvalue problem, thus no eigensolution. [1]

For a blunt body in a hypersonic freestream, there is a bow shock detached from the blunt nose. According to Crocco's Theorem, the gradient of entropy—which is related to entropy layer—is created due to the generation of vorticity by the curvature of the bow shock in the nose region. The schematics of the entropy layer and boundary layer over a blunt cone behind the bow shock are shown in Figure 3. The entropy layer merges into or is swallowed by the boundary layer after a short distance downstream from the nose region. The entropy layer has significant effects on boundary-layer receptivity and stability. Kara *et al.* [71, 73] showed that the span distance of the entropy layer leads to an increase in transition Reynolds number. Additionally, Zhong [58] showed that the entropy layer caused a reduction in the local Reynolds number along the boundary-layer edge, and thus a downstream shift of the transition location.

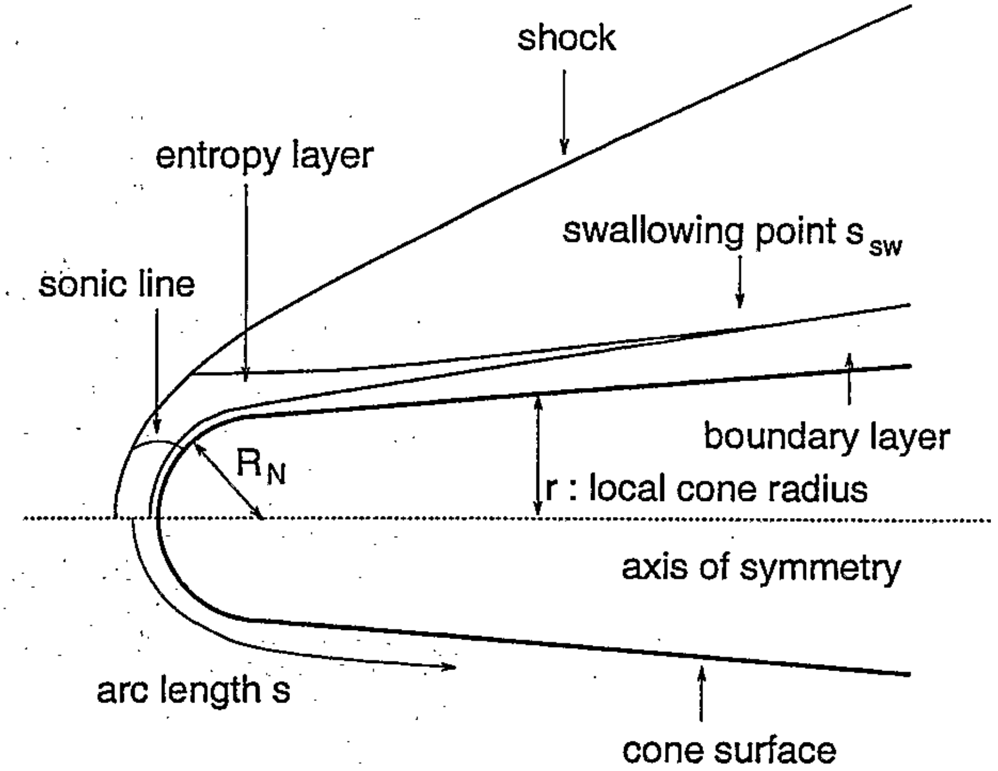

Figure 3. Schematics of entropy layer merging into boundary layer behind the nose region over a blunt cone. This figure is from Rosenboom *et al.* [74]

Kovasznay [75] revealed three modes of disturbances in compressible flows: acoustic mode, entropy mode (in the form of entropy spots), and vorticity mode. If these disturbances are weak, the modes are independent of each other. McKenzie *et al.* [76] pointed out that the weak freestream disturbances of any mode impinging the shock from the upstream side, the acoustic, entropy and vorticity disturbances would always be generated behind the shock with the different exiting wave angles and amplitudes from the interaction between the freestream disturbances and the shock; furthermore, there is no reflection of acoustic disturbances due to the nature of the supersonic flow. On the other hand, when the weak acoustic disturbances impinge the shock from the downstream side, there are no disturbances generated on the upstream side of the shock, but there are reflected disturbances on all three modes with different exiting wave angles and amplitudes. Moreover, owing to the fact that the interaction mechanisms of various incident disturbance modes with shock are distinct to each other, the exiting wave angles and amplitudes of the generated disturbances from each incident mode also differ from one another. Hence, boundary-layer receptivity to each freestream disturbance mode could potentially be different.

The schematics of the supersonic or hypersonic perturbed flow over a blunt body are shown in Figure 4. The freestream disturbances of any mode interact with the bow shock and generate fast acoustic waves, slow acoustic waves (if the flow behind the shock is supersonic), entropy waves, and vorticity waves behind the shock. Unlike entropy waves and vorticity waves, which both travel with the flow, fast acoustic waves travel faster than the flow, while slow acoustic waves travel slower than the flow. These acoustic, entropy, and vorticity waves eventually interact with the boundary layer and excite the instabilities in this layer via the receptivity process. Moreover, when acoustic waves are inside or near the nose region, they can hit and reflect off the wall, thereby impinging the shock and generating a new set of the fast acoustic waves, slow acoustic waves, entropy waves and vorticity waves behind the bow shock. This reflection cycle can occur many times inside and near the nose region, thus further complicating the boundary-layer receptivity process. Furthermore, when interacting with these disturbances, the shock shape can also distort and oscillate.

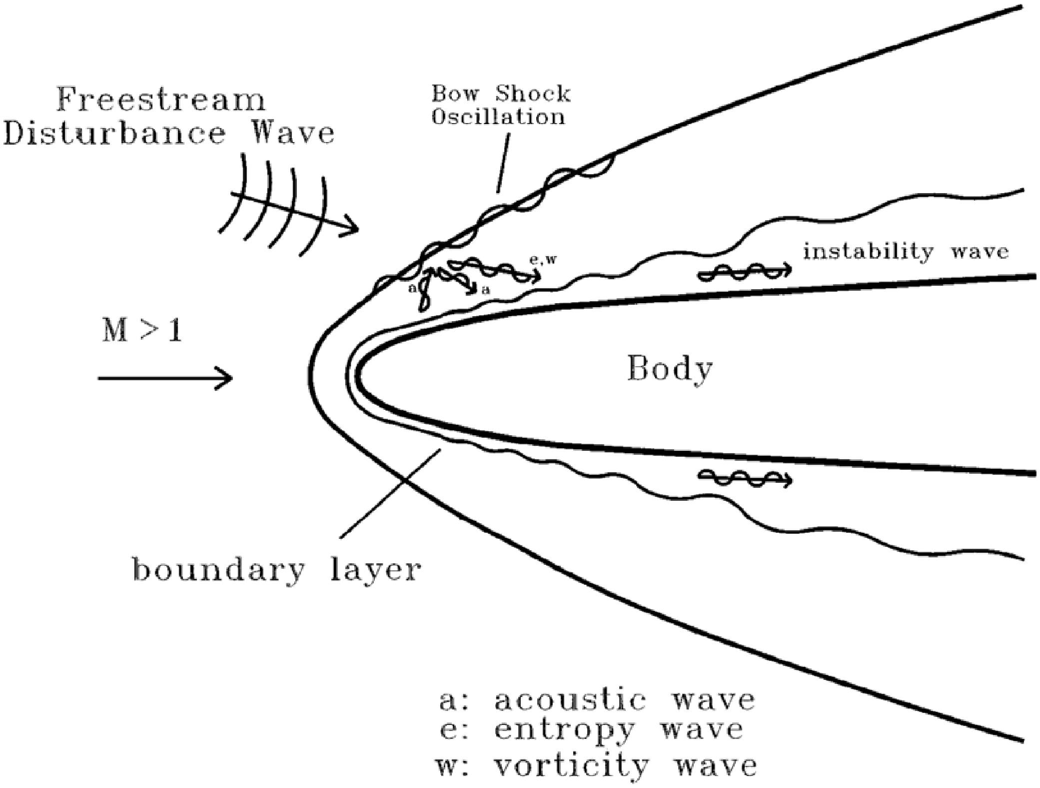

Figure 4. Schematic of boundary-layer receptivity to freestream perturbations in super/hypersonic flow. This figure is from Zhong [77].

1.4.1 Theoretical Studies

The terminology of boundary-layer normal mode families has changed throughout the development of receptivity study. Ma *et al.* [49] performed LST analysis on a sharp-edge flat plate in Mach 4.5 freestream. We use the LST results from that case to demonstrate the old terminology of boundary-layer disturbances in the receptivity process. Linearized stability equations have a solution of a linear combination of normal modes. The spectra of eigenvalues of the normal modes are shown in Figure 5. There are three continuous spectra: the one on the left, along $\alpha_i = 0$, is the continuous spectrum of fast acoustic waves.

The standing one on the middle is the continuous spectrum of entropy and vorticity waves, and finally the horizontal one on the right represents the continuous spectrum of slow acoustic waves. There are also discrete modes, Mode I and the Mack mode, currently shown as the second Mack mode in the figure. Mode I originates and travels from the continuous fast acoustic waves spectrum to a higher α_r, while the dimensionless circular frequency, ω, increases (the increase in either/both frequency and/or local Reynolds number). The plot's arrow represents the locus of traveling.

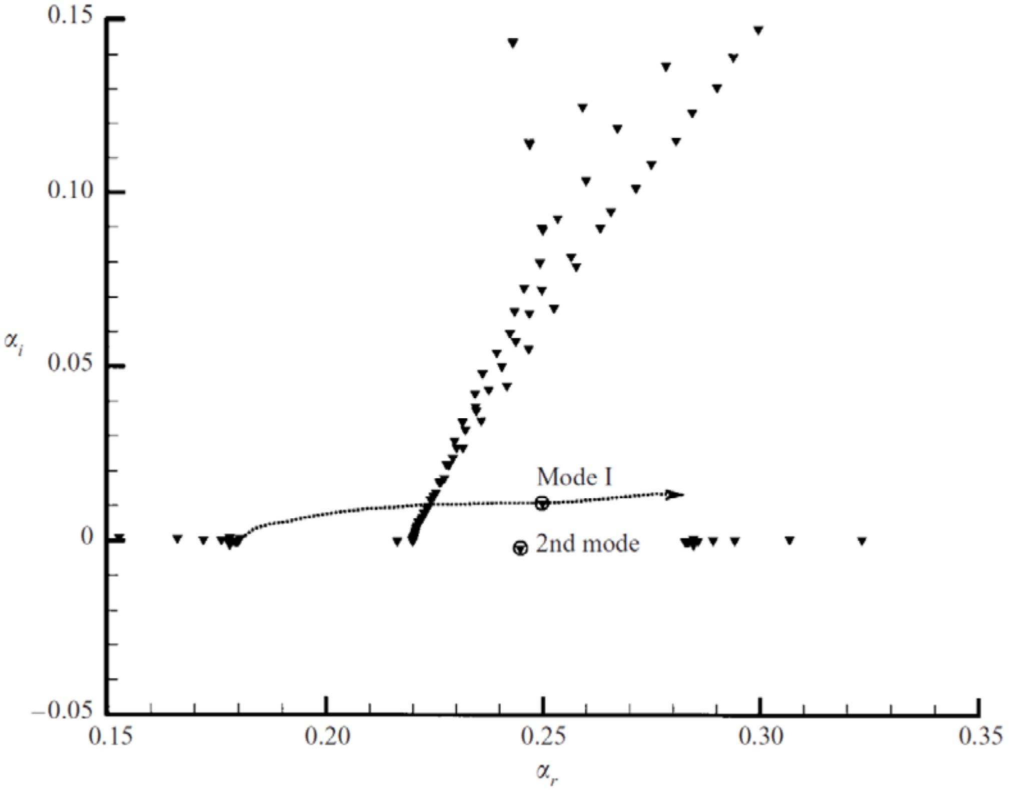

Figure 5. Eigenvalue spectra at $F = 2.2 \times 10^{-4}$ and $R = 1000$ over a flat plate in Mach 4.5 freestream. This figure is from Ma *et al.* [49].

In Figure 6, the dimensionless phase speeds are plotted along with dimensionless circular frequency, a similarity variable that includes the local Reynolds number and frequency. The plot clearly shows the names of the discrete modes, as defined by Ma *et al.* The upper horizontal dash line is the phase speed of the fast acoustic waves with a speed of $1+1/M_\infty$. The middle dash line represents entropy and vorticity waves which convect with the flow. Lastly, the lowest dash line represents slow acoustic waves at a speed of $1-1/M_\infty$. Mode I, II, III, IV, etc. are induced by the synchronization between mode I, II, III, IV, etc. and the fast acoustic waves. The first mode is induced by the synchronization between the first mode and the slow acoustic waves. The higher Mack modes are excited by the synchronization of the discrete modes. For instance, the synchronization of the first mode and mode I excites the second Mack mode.

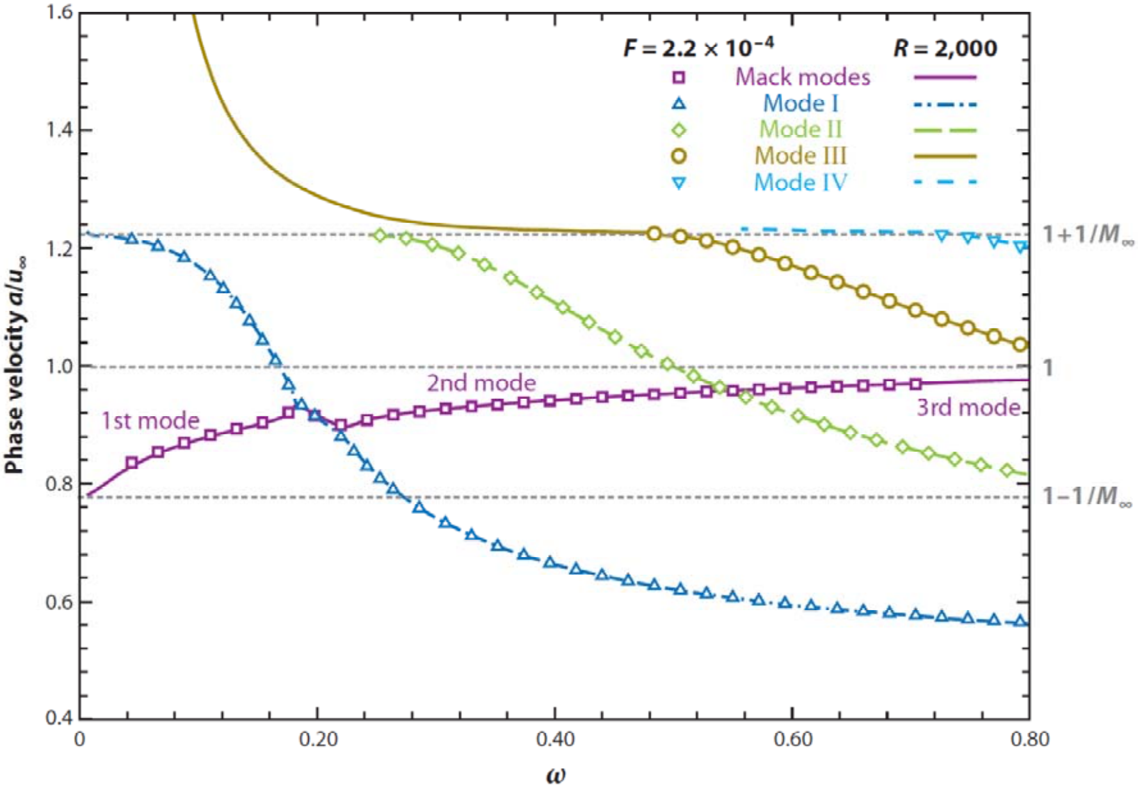

Figure 6. Dimensionless phase speed plot from LST over a flat plate in Mach 4.5 freestream. This figure is from Zhong *et al.* [3, 49].

Fedorov *et al.* [78] suggested new terminology for boundary-layer normal modes based on their receptivity features. "Mode I" was renamed "fast mode" or mode F due to its synchronization with fast acoustic waves upstream. The mode that synchronizes with slow acoustic waves upstream near the leading edge was renamed "slow mode" or mode S. Both modes are shown in Figure 7 (a). The former "mode II", "mode III", "mode IV", etc. are named mode $F^{(2)}$, $F^{(3)}$, $F^{(4)}$, etc., respectively. There are three synchronization regions illustrated by the rectangular boxes and circles in Figure 7 (a). Region 1 shows the synchronization between acoustic waves and the discrete modes, Region 2 is the synchronization between mode F and the entropy/vorticity waves, and Region 3 represents the synchronization between discrete normal modes. Depending on the flow parameters, there can be several unstable maxima in the growth rates along ω. The unstable maximum before the synchronization of the discrete modes is the first mode, and the first unstable maximum behind the synchronization of the discrete modes is the second mode. An example of growth rates is shown in Figure 7 (b). Noticeably, the negative growth rate, α_i, is plotted along the local Reynolds number. In this example, the minimum α_i between $R = 500$ to 2500 is the first mode, and the minimum α_i between $R = 3700$ to 4600 is the second mode. Both the first and second modes are related to mode S.

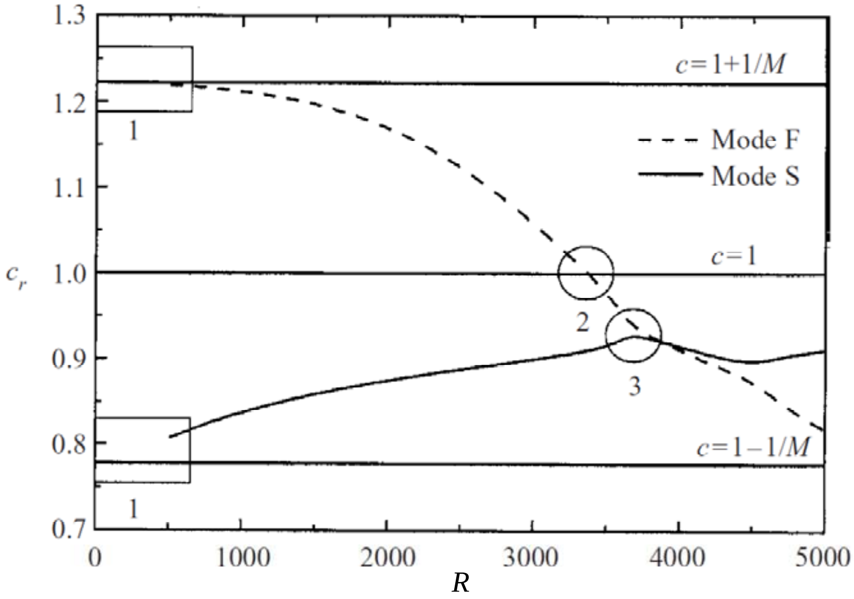

(a)

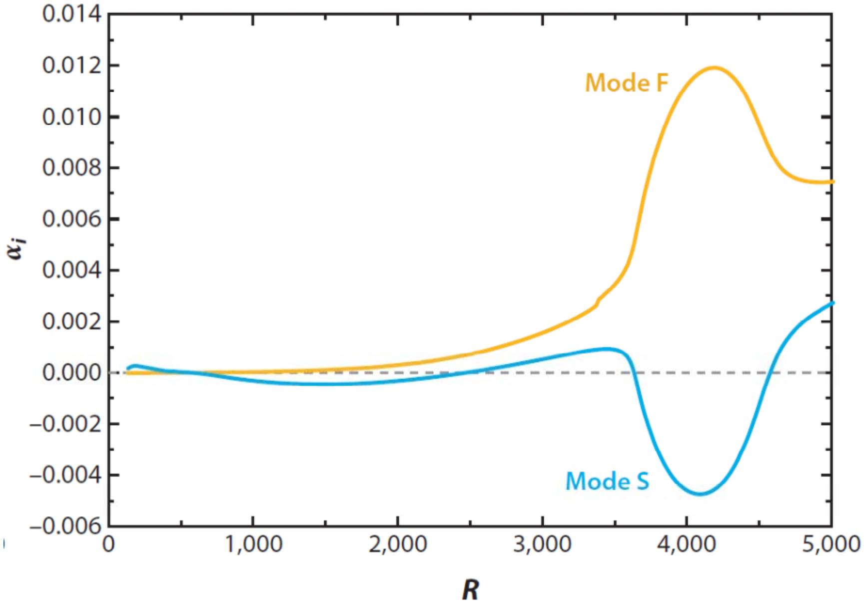

(b)

Figure 7. Dimensionless (a) phase speed and (b) negative growth rate plot over a flat plate in Mach 4.5 freestream at $F = 5\times10^{-5}$. Both plots from Fedorov [27, 79].

Fedorov *et al.* [78, 80] developed a theoretical model to explain the intermodal exchange mechanism in the synchronization of discrete modes. They showed that there are two branch points in the upstream and downstream vicinity of the synchronization point of mode F and mode S, where the frequency and the real part of the phase speed are equal for both modes on the real axis of the spatial coordinates or Reynolds number. A branch point is where the frequency, phase speed and growth rate are equal for modes F and S. The locations of the branch points vary with differing flow parameters. The branch point, however, does not exist in most practical flows with a real x axis (or Reynolds numbers) only, except for a very specific disturbance frequency with a very cold wall. Instead, the branch point appears along the complex Reynolds number with a non-zero imaginary part. According to their theoretical model, whether mode S or mode F becomes unstable during synchronization is determined by which complex Reynolds number plane (positive or negative complex plane) the branch points are individually located around the synchronization point. Fedorov *et al.* [78, 80] determined that the vicinity of the branch points to the synchronization point, due to nonparallel effects, caused the strong interactions between mode S and mode F.

Fedorov [79] theoretically modeled and studied receptivity to weak freestream acoustic disturbances over a flat plate with a sharp leading-edge from Mach 4.5 to 5.92. In order to vary the locations of the branch points in the complex plane, an adiabatic wall and very cold wall were considered. The results showed that the direct excitation of the unstable mode S by the receptivity to the freestream slow acoustic mode at the leading edge generated a peak amplitude of around 50 times greater than that of the unstable mode S excited from the synchronization of mode S and mode F over the adiabatic wall. This observation supports the following conclusion from Su *et al.* [43]: the first mode is responsible for the transition process with adiabatic wall conditions. The cold wall case showed the opposite trend as compared to the adiabatic wall case: mode S, which was excited by the synchronization of mode S and mode F, was stronger than those excited directly by the receptivity to the freestream slow acoustic waves at the leading edge. Fedorov [79] explained: having the higher relative strength of the intermodal exchange mechanism during discrete modes synchronization is a result from having the upstream branch point being very close to the real axis over a cooled wall. This explanation can also be used to explain the destabilizing effects of the second mode under wall-cooling effects. The results from the theoretical model agreed well with the results from the Mach 6 flat plate experiment by Maslov *et al.* [81]. The theoretically modeled results, however, only agreed qualitatively with the simulation of flow over a flat plate at Mach 4.5 in Ma *et al.* [82]. This was due to the model's limitations in predicting the receptivity coefficients of high frequency disturbances.

To study boundary-layer receptivity to freestream fast acoustic waves over a flat plate with leading-edge bluntness at Mach 5.92, Egorov *et al.* [83] developed a theoretical model that incorporated a numerically-simulated steady-base entropy layer. They concluded that small bluntness can cause a significant decrease in the receptivity coefficient over a flat plate.

Fedorov [27] reviewed receptivity paths to external weak disturbances over a flat plate with a sharp leading edge at Mach 4.5, as shown in Figure 8. Path A1 is the receptivity path to fast acoustic waves. The stable mode F in the boundary layer is excited by the synchronization between fast acoustic waves and mode F near the leading edge. The mode S related second mode is excited via the intermodal exchange mechanism between mode F and mode S at the synchronization point. The mode S related second mode experiences exponential growth until a level in which the nonlinear breakdown to turbulence is triggered. Path A2 represents the receptivity path to entropy/vorticity waves. The synchronization between entropy/vorticity waves and the mode F excites the stable mode F in Region 2, as shown in Figure 7 (a). Mode S is excited via the intermodal exchange mechanism between modes F and S at the synchronization point. The mode S related second mode experiences exponential growth until a level in which the nonlinear breakdown to turbulence is triggered. It is worth noting that although both Path A1 and A2 can excite mode S via the synchronization between mode S and mode F, the receptivity coefficients of mode S for both paths are different. In Path A3, the unstable mode S is directly excited by the synchronization of slow acoustic waves with mode S near the leading edge. Both the mode S related first mode and second modes are excited. Mode S grows exponentially in the linear regime, thus triggering the nonlinear breakdown to transition.

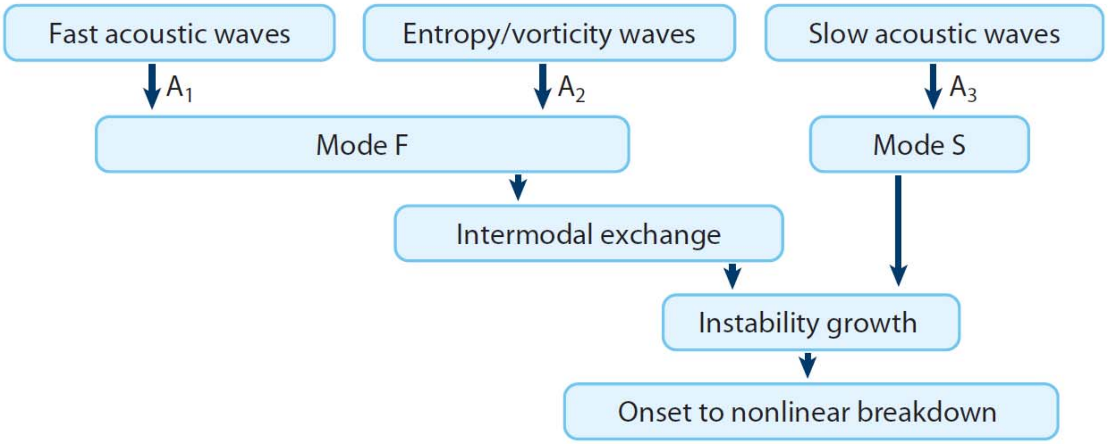

Figure 8. Path A with details of receptivity mechanism over a flat plate at Mach 4.5. This figure is from Fedorov [27].

Although these theoretical receptivity models can provide very in-depth analyses of the receptivity mechanism, which are otherwise difficult for numerical simulations and experiments to reveal, the limitations of the theoretical models are due to their assumptions of the simplified flow features over simple prototype geometry. These are the theoretical approaches' main obstacles. It would be more beneficial to develop approaches that combine both theoretical analyses and numerical simulations or experiments. Tumin [84, 85] developed a theoretical method to decompose numerically simulated linear disturbances in the flow field into discrete modes and the modes of the continuous spectra. This method is a very useful in studying the receptivity and stability of the compressible boundary layer. Tumin *et al.* [86] successfully used the method to decompose a numerically simulated unsteady flow field over a sharp wedge at a half angle of 5.3 degrees in Mach 8 freestream. The two-dimensional periodic-in-time blow and suction were introduced upstream at the surface of the wedge. The amplitudes of mode S and mode F at various locations along the wedge were decomposed based on simulated disturbances, thus revealing the development of discrete modes in the flow field over the sharp wedge.

1.4.2 Numerical Studies

Ma *et al.* [4, 35] performed numerical simulation studies on a sharp-edged flat plate with periodic freestream planar single-frequency sinusoidal fast acoustic, slow acoustic, entropy and vorticity waves, and an acoustic wave beam at Mach 4.5. They found the following receptivity path of freestream acoustic waves: the stable mode I was first excited by the resonant interaction between fast acoustic waves and mode I near the leading edge. Then, mode I synchronized with the second mode and converted to the unstable second mode. The induced disturbances, however, had very strong multi-mode modulations around the synchronization point. There were also strong modulations at the region where the unstable second mode was supposed to be dominant. Fast acoustic waves also excited mode II shortly behind the appearance of the unstable second mode. The boundary-layer disturbances were dominated by mode II after its excitation. The receptivity paths of the freestream entropy and vorticity waves were essentially similar to those of the freestream fast acoustic waves. Mode I was excited by the fast acoustic waves generated from the interaction between freestream entropy or vorticity waves and the oblique shock near the leading edge. The simulated results showed that the disturbances, which had relatively strong mode I, experienced very strong multi-mode modulations between the leading edge and the synchronization point. The disturbances also have modulations at the locations around the synchronization point. The receptivity path of freestream slow acoustic waves differed from the other three types of freestream waves. More specifically, the first and second Mack modes were excited directly by the resonance interaction between the first mode and the slow acoustic waves near the leading edge. The receptivity paths over a flat plate found by Ma *et al.* [4, 35] essentially conformed with those reviewed in Fedorov [27]. Also studied were the effects of incident wave angles, frequencies, and wall temperature conditions. They found that the receptivity of the second mode was not as sensitive to the change in incidence angle as compared to that of mode I. During a change in frequency, the receptivity of the second mode was more sensitive than that of mode I. In regard to wall temperature conditions, the receptivity of the second mode over the isothermal wall was found to be weaker than the receptivity of second mode over the adiabatic wall. Furthermore, the second mode growth rates over the isothermal wall were found to be smaller than those over the adiabatic wall. Noticeably, their receptivity analyses were based on response coefficients that were not separated from the other normal modes.

Zhong *et al.* [36] performed a numerical study over a blunt cone with planar periodic fast acoustic waves in a Mach 7.99 freestream. In their study, the induced boundary-layer disturbances contained a relatively strong mode I at the locations shortly behind the nose region. This relatively strong mode in the disturbances became the fast acoustic waves in the middle region of the cone. The modulations were strong at the locations between the nose region and the synchronization point. The disturbances became dominated by the second mode after the synchronization between mode I and the second mode. The following is noteworthy: although both the mechanisms of receptivity to freestream fast acoustic waves over a blunt cone and a flat plate were governed by the resonant interaction between fast acoustic waves and mode I near or inside the nose region, and the resonant interaction between mode I and the unstable second mode at the synchronization point, the receptivity path over a blunt cone was not quite the same as the receptivity path over a flat plate in Ma *et al.* [35]. The comparison implied that the receptivity mechanism over different geometries could be different. Zhong *et al.* [36] also found that the synchronization location was downstream from the Branch-I neutral location of the second mode; although the second mode was unstable before the synchronization location, no growing second mode dominated disturbances were found.

Zhong [87] conducted an unsteady numerical study on receptivity with nose bluntness effects on a 7-degree half angle straight cone in Mach 8 axisymmetric freestream. The boundary layer was perturbed by the periodic planar freestream fast acoustic waves of 15 discrete frequencies. The numerical study was conducted in order to investigate the transition reversal phenomenon due to nose bluntness, as observed in Stetson's stability experiment [39]. The flow conditions and cone geometry used in Zhong's numerical study [87] were therefore the same as those used in Stetson's experiment, and the nose radii used were mainly in the "large" bluntness range [46, 58]. Zhong [87] compared his unsteady results with LST and found that the receptivity mechanism between all three radii was essentially the same. More specifically, the receptivity consisted of the resonant interactions between mode I and the forcing fast acoustic waves near the nose region, as well as the resonant interaction between the induced stable mode I disturbances and the second mode downstream. Zhong found that the initial second mode excitation location always moved downstream under the increase of nose bluntness. Thus, no transition reversal was found.

Balakumar *et al.* [88] conducted a numerical study of receptivity over straight and flared cones with both periodic freestream planar fast and slow acoustic waves at Mach 6. The freestream condition was based on the BAM6QT tunnel at Purdue University. Three types of cones were studied: a 7-degree straight sharper cone, a blunter compression cone that was used by Wheaton *et al.* [23], and a sharper flared cone that was tested in the NASA Langley Mach-6 tunnel. In their analyses over the compression cone, LST predicted that the most amplified frequency would be about 279 kHz; they used the sampling frequency of 292.5 kHz to compare the simulation to the theoretically predicted results. They found no unstable first mode over the compression cone, although there was an unstable first mode found over the other cones. The receptivity path of the simulated boundary-layer disturbances excited by the freestream fast acoustic waves was very similar to the path obtained by Zhong *et al.* [36]. However, the receptivity path of the simulated boundary-layer disturbances excited by the freestream slow acoustic waves over the compression cone was very different from those over the other two sharper cones studied, and different from those over flat plates with freestream slow acoustic waves [4, 27]. The simulated boundary-layer disturbances with freestream slow acoustic waves over the compression cone had relatively strong entropy/vorticity waves after being excited by the slow acoustic waves near the nose region. The reason for having such a different path was unknown. Eventually, behind the synchronization point of mode S and mode F, the mode S related unstable second mode became dominant for both the receptivity paths of the freestream fast and slow acoustic waves. The receptivity path of the simulated boundary-layer disturbances induced by the freestream slow acoustic waves over the other two sharper cones was that the mode S related first and second Mack modes were excited directly by the resonance interaction between mode S and the slow acoustic waves near the nose region. This receptivity path was similar but not quite the same as the path over a flat plate in Ma *et al.* [4]. Again, the difference in the receptivity mechanisms over different prototype geometries was implied from the receptivity path comparison. Balakumar *et al.* [88] also found that due to the nose-bluntness effects, the receptivity coefficient with freestream acoustic waves at the neutral point over a sharper cone was several orders of magnitude higher than that over a blunter compression cone. Balakumar *et al.* [88] also suggested that even though the growth rates of the second modes were higher under the adverse pressure gradient effects over the compression cone, the transition could still be delayed due to nose bluntness effects. The most amplified frequency was found to be higher over the compression cone as compared to the straight cone. It is worth noting that they defined their receptivity coefficient as the ratio between the amplitude of the wall-pressure disturbances at the neutral point, and the freestream amplitude of the acoustic disturbances.

Balakumar *et al.* [31] numerically studied the receptivity of freestream vortical disturbances over a 7-degree straight sharper cone in the BAM6QT tunnel condition. The simulated boundary-layer disturbances had relatively strong vortical waves upstream from the synchronization point of mode S and mode F; the mode S related second mode dominated behind the synchronization point of mode S and mode F. However, the exact receptivity path was not clearly determined because of the strong modulations throughout the entire cone. The receptivity coefficient with freestream vortical disturbances was found to be three times less than the coefficient with freestream slow acoustic waves.

Egorov *et al.* [32, 89-91] conducted numerical receptivity studies over a flat plate with a sharp leading edge in Mach 6 freestream. The flow was perturbed by linear freestream continuous planar acoustic, entropy, and vorticity waves of a single frequency with various incident inclination angles. The numerical results using freestream slow acoustic waves agreed relatively well with the theoretically modeled receptivity results in Fedorov [79]. The results using freestream fast acoustic waves, however, were poorly agreed, due to the fact that the theoretical model did not include a shock wave near the leading edge and the singular point appeared in the theoretical model at the synchronization point of mode F and vorticity/entropy waves. The receptivity paths of the freestream fast and slow acoustic waves at various incident inclination angles agree with Path A1 and A3 in Figure 8, respectively. Moreover, the grown disturbance amplitude downstream, induced by the freestream slow acoustic waves, was found to be 10 times higher than the amplitude induced by freestream fast acoustic waves. Since the boundary-layer disturbances were driven mainly by the generated acoustic waves from the interactions of the freestream entropy or vorticity waves and the oblique shock near the leading edge, the receptivity paths with freestream entropy and vorticity waves are similar to either Path A1 or A3, depending on the incident inclination angle. However, the heavy modulations between entropy/vorticity waves and acoustic waves in the boundary layer may occur before the synchronization of mode S and mode F.

Egorov *et al.* [32, 33, 92] also studied a porous coated wall and a wavy wall. Their results showed that the amplitude of the second mode can be suppressed by carefully designed porous and wavy surfaces, based on the second mode wavelength.

Fedorov *et al.* [93, 94] performed a numerical simulation of temporally sinusoidal linear temperature spots over a flat plate in a Mach 6 flow. They computed a case with temperature spots initially imposed at a short distance above the boundary layer in the flow field behind the oblique shock. In another case, temperature spots were initially imposed in front of the shock at a short distance above the level of the plate. In the first case, the temperature spots interacted weakly with the boundary layer and excited mode F downstream at the synchronization point of entropy/vorticity waves and mode F. Then, the mode S related second mode was excited by the synchronization between mode S and mode

F via the intermodal exchange mechanism, as discussed by Fedorov *et al.* [80]. The latter case involved shock/spot interaction. The results indicated that shock/spot interaction generated fast acoustic waves, slow acoustic waves, and entropy waves, but only the acoustic waves eventually interacted with the boundary layer. After these acoustic waves penetrated the boundary layer, slow acoustic waves excited mode S via the synchronization of slow acoustic waves and mode S in the boundary layer near the leading edge of the plate. Behind the synchronization point of mode F and mode S, the second mode was excited. The instability amplitudes of the latter case were an order of magnitude higher than those in the first case.

1.4.3 Experimental Studies

Unlike stability experiments, experimental receptivity studies involving supersonic and hypersonic boundary layers have been quite sparse. This was due to the technical difficulties in measuring the very weak boundary-layer disturbances during the receptivity process, in generating the well-controlled-and-defined freestream perturbations, and in minimizing the tunnel noise.

Maslov *et al.* [81] conducted an experimental study of boundary-layer receptivity to the controlled freestream two-dimensional and three-dimensional acoustic waves with various incident inclination angles over a sharp leading-edge flat plate at Mach 5.92. By comparing their measurement of the boundary-layer responses to previous measurements at different freestream Mach numbers, they concluded that a higher freestream Mach number can lead to an increase of receptivity coefficients with external acoustic disturbances over a flat plate.

In addition to the receptivity study with controlled freestream acoustic disturbances, those with controlled freestream entropy disturbances were also conducted. Schmisseur *et al.* [67, 95] conducted a preliminary study of the receptivity of a freestream laser-generated hotspot, or so called laser spot, over an elliptical cone in a Mach 4 flow. Figure 9 [67, 95] shows the schematics of the laser spot and cone setup in the experimental studies. The laser spot was initially generated at a location upstream from the cone on the centerline. Then, the laser spot convected with the hypersonic freestream toward the cone nose, interacted with and passed through the bow shock, eventually traveled further downstream around the cone. Noticeably, Schmisseur *et al.* [67, 95] used a laser spot with a temperature perturbation amplitude that was too high for the receptivity process to fall into linear regime. The perturbed flow response above the cone was measured, but no detailed receptivity mechanisms were revealed in their work.

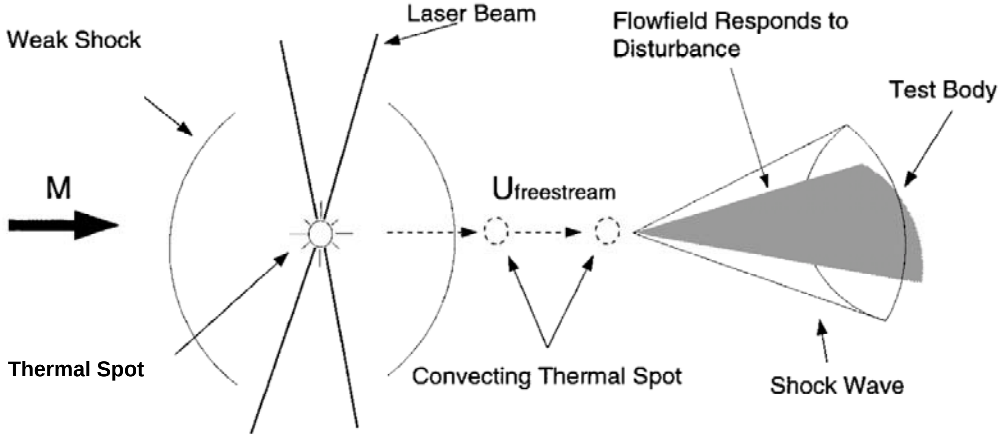

Figure 9. Schematic of the experimental laser spot and cone scenario. A modified figure from Schmisseur *et al.* [67]

Salyer *et al.* [96, 97] characterized the laser spot and used it in a boundary-layer receptivity experiment for a hemisphere-cylinder model in Mach 4 freestream. The laser spot consisted of a Gaussian distributed (in temperature or density perturbations) thermal spot or hotspot, surrounded by a rapidly dissipating weak shock. The hotspot had a radius of around 3 mm, and the maximum magnitude of the density perturbations at the spot center was more than 0.5 times of the freestream value, which was quite large for receptivity in linear regime. Salyer *et al.* [96, 97] completed benchmark tests for generating laser spots in their wind tunnel and measured the responses of the perturbed boundary layers, but they did not present a detailed analysis of the receptivity mechanisms.

Chou *et al.* [22, 98, 99] successfully measured the second mode dominant instability over a compression cone, as designed by Wheaton *et al.* [23], with two nose radii of 1 mm and 0.16 mm in BAM6QT. The controlled laser spot in Chou *et al.* [22, 98, 99] was generated as the freestream entropy perturbations in order to interact with the bow shock, thus triggering the receptivity process and the subsequent transition stages. The freestream hotspot had a Gaussian profile with a radius of 4 mm. The measured maximum magnitude of the stagnation pressure perturbations at the spot center in the freestream was more than 0.4 times of the freestream value, which was very large for receptivity in linear regime. Thus, there was a high degree of nonlinearity in the growth observed farther downstream on the cones. It is worth noting that a hotspot is a natural wave packet that carries a broad continuous frequency spectrum. Bandwidth and amplitudes in the wave packet are dependent on the profile of the hotspot. The hotspot in Chou *et al.* [22, 98, 99] carried the broad continuous frequency spectrum, which included the second mode and higher harmonics frequency ranges. Therefore, these boundary-layer instabilities were effectively triggered downstream. The instabilities downstream were measured and found to be stronger on the sharper cone. From the approximation based on their instability measurements, Chou *et al.* found that the initial amplitude of the instability growth on the sharper compression cone was 2.5 orders of magnitude larger than the blunter compression cone. In addition, they found that their measured wave packet time-history profiles in the boundary layer were similar to the simulated ones in Huang *et al.* [100]. Moreover, the experimental spectra were very similar to the simulated spectra in Huang *et al.* [100], once the freestream unit Reynolds numbers were matched for the compression cone case with a 1 mm nose radius.

1.5 Current Research Status and Unresolved Topics

After reviewing previous publications on supersonic and hypersonic boundary-layer receptivity and stability problems, it is apparent that boundary-layer receptivity and stability with planar freestream acoustic waves of a single or a few discrete frequencies has been studied extensively. Such studies were conducted using flat plates and cones under various parametric effects, including the effects of incident angle, nose bluntness, freestream unit Reynolds number, freestream Mach number, etc. Moreover, receptivity and stability with freestream entropy and vorticity perturbations over simple flat plates with sharp leading edges—which have no entropy layer effects—have also been studied, though not extensively. In relation to blunt cones, receptivity and stability with freestream vorticity waves other than freestream acoustic waves have rarely been studied. All studies show that receptivity mechanisms and stability are different based on differing freestream perturbations and model geometries. Thus, without detailed analyses, conclusions cannot be extrapolated from one kind of freestream perturbation and model geometry to the others.

Receptivity and stability to freestream entropy perturbations over cones, which are much more complicated flow fields that include the effects of entropy layer and bow shock, are still at the initial stage where only the measurements of the subsequently grown instabilities and transition have been obtained. Still undiscovered are the detailed mechanisms of the initial boundary-layer receptivity process and instability growth in the linear regime with freestream entropy perturbations over cones. A complete and detailed investigation of receptivity and stability mechanisms over a cone is therefore necessary at this current research stage. Additionally, in order to understand the variations of receptivity and stability mechanisms under different parametric effects, further systematic parametric studies on receptivity and stability mechanisms are needed.

Only a few discrete frequency components of freestream perturbations were introduced in the aforementioned theoretical and numerical studies. The introduction of freestream perturbations that contain a wide band of continuous frequency spectrum can reveal a more complete picture of receptivity and stability, thereby making the parametric studies more conclusive. The introduction of such form of freestream perturbations is therefore desired at this point.

Furthermore, since separating normal modes from boundary-layer disturbances is a very difficult process, most of the receptivity coefficients obtained in the previous numerical and experimental studies were not of a single boundary-layer normal mode. In order to develop a physical-based transition predicting method, however, it is necessary to obtain receptivity coefficients of a second mode related normal mode at Branch-I neutral point. Therefore, the implementation of the aforementioned theoretical modal decomposition method or any alternative method is desired at this point.

1.6 Objectives

In response to the above unresolved topics, a complete and detailed study of hypersonic boundary-layer receptivity and stability with freestream entropy perturbations of a wide continuous frequency spectrum over a blunt cone—which includes the effects of entropy layer and bow shock—is needed. Thus, the main objectives of this work are as follows:

1) To systematically study the characteristics of boundary-layer disturbances—which are carried into the boundary layer over a blunt cone by freestream entropy perturbations—throughout the receptivity process and instability growth over a wide frequency spectrum in the linear regime.
2) To investigate linear boundary-layer receptivity and stability mechanisms with freestream entropy perturbations.
3) To obtain receptivity coefficients in order to provide the initial conditions of boundary-layer instabilities in the linear regime with freestream entropy spot.
4) To systematically study the variations of receptivity and stability mechanisms with freestream entropy perturbations under different parametric effects.

1.7 Plan of Approach

The current numerical study of receptivity and stability is divided into two parts: (i) receptivity and stability analyses of the standard case, and (ii) parametric studies on receptivity and stability. Among many types of parametric effects, this current study addresses nose bluntness effects and freestream Mach number effects, which are crucial for designing hypersonic vehicles and are commonly encountered during flight. The standard case is the benchmark case, from which all subsequent cases with differing parameters extend. In order to see the trends of receptivity and stability, the cases' results with different parameters are therefore compared with the standard case.

In this study, one standard case and four parametric cases are investigated. Each case is represented by a simple case name; case names and key parameters are summarized in the following table:

Table 1. Summary of Case Parameters

Case Name	Nose Radius	Freestream Mach Number
1	0.001 m	6
A1	0.0005 m	6
A2	0.0001 m	6
B1	0.001 m	10
B2	0.001 m	15

The parametric cases are categorized into two areas: nose bluntness effects and freestream Mach number effects. Cases A1 and A2 are used to study nose bluntness effects and Cases B1 and B2 are used to study the freestream Mach number effects. Case 1 is the standard case. More details on flow parameters are revealed in Section 4.1.

The numerical simulations and investigations of the standard case and each parametric case consist of seven steps: (i) the simulation of a steady base flow, (ii) the investigation of steady base flow profiles and entropy layer effects in the steady base flow, (iii) LST analysis based on this steady base flow, (iv) the unsteady flow simulation with imposed freestream hotspot perturbations, (v) the investigation of the evolution of boundary-layer disturbances throughout the receptivity process, as well as the instability growth over a wide frequency spectrum, (vi) the calculation of receptivity coefficients, and lastly, (vii) the investigation of the receptivity mechanism and second mode development by comparing the simulated results with LST analysis.

Finally, all the results in each parametric case are compared with the other case under the same parametric effects; these results are also compared to the standard case. Thus, these case comparisons reveal trends of the receptivity and stability mechanisms under both parametric effects.

The Mach 6 compression cone receptivity experiments conducted at Purdue University [99, 101] initially motivated this current numerical study. Thus, the cone model is the compression cone designed by Wheaton *et al.* [23] (see Figure 10), a blunt cone with a circular-flared geometry along its body. The flow conditions used in Cases 0, A1, and A2 are identical to the Mach 6 tunnel conditions in Wheaton *et al.* [23]. The compression cone's geometry causes higher amplification rates, N-factors and earlier transition when compared to a corresponding straight cone, due to the adverse pressure gradient that occurs along the flared geometry of the cone. [23, 28, 72]. In the Mach 6 freestream, this geometry also creates an approximately constant boundary-layer thickness along the cone body in a streamwise direction. As a result, the second mode frequencies do not alter much along the cone. [23]

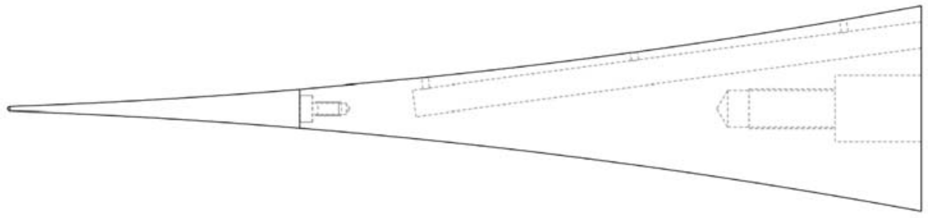

Figure 10. Schematic diagram of compression cone. This figure is from Wheaton *et al.* [23]

The current study uses a hotspot or entropy spot as the freestream perturbations. A hotspot is a natural wave packet that carries a broad continuous frequency spectrum. In flight environment, a hotspot can have an arbitrary shape and profile. The hotspot used in this work has a Gaussian distribution of temperature and density perturbations in the radial direction, with a maximum magnitude of perturbations at its center [96, 97]. More hotspot details will be discussed in Section 2.4.

2 Governing Equations and Numerical Methods

2.1 Governing Equations

The current simulation of axisymmetric hypersonic perfect-gas flow around a compression cone is two-dimensional, i.e. it does not depend on the circumferential coordinate. The code that is written to perform the simulation, however, is capable of computing a three-dimensional flow. Thus, the governing equations in the code are three-dimensional Navier-Stokes equations in conservative-law form and in Cartesian coordinates:

$$\frac{\partial U^*}{\partial t^*}+\frac{\partial F_j^*}{\partial x_j^*}+\frac{\partial F_{vj}^*}{\partial x_j^*}=0, \qquad (j=1,2,3) \tag{1}$$

The tensor notation, $\left(x_1^*, x_2^*, x_3^*\right)$ represents the Cartesian coordinates, $\left(x^*, y^*, z^*\right)$.

Vector U^* contains five conservative flow variables:

$$U^*=\begin{bmatrix}\rho^* & \rho^* u_1^* & \rho^* u_2^* & \rho^* u_3^* & e^*\end{bmatrix}^T \tag{2}$$

The inviscid flux vector, F_j^*, and the viscous flux vector, F_{vj}^*, are defined as:

$$F_j^*=\begin{bmatrix}\rho^* u_j^* \\ \rho^* u_1^* u_j^*+p^*\delta_{1j} \\ \rho^* u_2^* u_j^*+p^*\delta_{2j} \\ \rho^* u_3^* u_j^*+p^*\delta_{3j} \\ (e^*+p^*)u_j^*\end{bmatrix} \tag{3}$$

$$F_{vj}^* = \begin{bmatrix} 0 \\ -\tau_{1j}^* \\ -\tau_{2j}^* \\ -\tau_{3j}^* \\ -\tau_{jk}^* u_k^* - q_j^* \end{bmatrix}, \qquad (k = 1, 2, 3) \tag{4}$$

The equation of state and transport equations are

$$p^* = \rho^* R^* T^* \tag{5}$$

$$e^* = \rho^* \left(c_v^* T^* + \frac{1}{2} u_k^* u_k^* \right) \frac{dy}{dx} \tag{6}$$

$$\tau_{ij}^* = \mu^* \left(\frac{\partial u_i^*}{\partial x_j^*} + \frac{\partial u_j^*}{\partial x_i^*} \right) - \lambda^* \frac{\partial u_k^*}{\partial x_k^*} \delta_{ij}, \qquad \lambda^* = \frac{2}{3} \mu^* \tag{7}$$

$$q_j^* = -\kappa^* \frac{\partial T^*}{\partial x_j^*} \tag{8}$$

where c_v^* is constant with a given γ, and κ^* can be determined with a constant Prandtl number. The viscosity coefficient is defined by Sutherland's law:

$$\mu^* = \mu_r^* \left(\frac{T^*}{T_r^*} \right)^{\frac{3}{2}} \left(\frac{T_r^* + T_s^*}{T^* + T_s^*} \right) \tag{9}$$

2.2 Coordinates Transformation

In this current study, a body-fitted curvilinear shock-fitting grid around the compression cone is used to discretize the flow field over the blunt compression cone. The computational domain of the shock-fitting grid is bound between the shock and the wall. In order to implement the numerical methods without the dependence of the non-uniform grid, the

Navier-Stokes equations in Cartesian coordinates (x, y, z, t) are transformed into the body-fitted curvilinear computational domain coordinates (ξ, η, ζ, τ) as expressed in Eq. (10). Figure 11 demonstrates a partial view of computational domain, where the upper boundary is the shock, the lower boundary is the wall, ξ is the coordinate in streamwise direction, η is the coordinate in the direction normal to the wall, and ζ is the coordinate in the azimuthal direction. The grid surfaces, in which $\xi = \text{constant}$ and $\zeta = \text{constant}$, are perpendicular to the wall surface. The coordinate transformation relations between the Cartesian coordinates and the body-fitted curvilinear computational domain coordinates are:

$$\begin{cases} \xi = \xi(x, y, z) \\ \eta = \eta(x, y, z, t) \\ \zeta = \zeta(x, y, z) \\ \tau = t \end{cases} \Leftrightarrow \begin{cases} x = x(\xi, \eta, \zeta, \tau) \\ y = y(\xi, \eta, \zeta, \tau) \\ z = z(\xi, \eta, \zeta, \tau) \\ t = \tau \end{cases} \tag{10}$$

Since the shock is not steady during the computation, each grid point on the shock-fitting grid is also unsteady. Therefore, all Cartesian coordinates on each grid point are time dependent. In the computational domain coordinates, however, only the normal direction coordinate, η , is time dependent. The coordinate in streamwise direction, ξ , and the coordinate in the azimuthal direction, ζ , are not time dependent because they are fixed to the solid wall. Time in computational domain, τ , is identical to physical time, t .

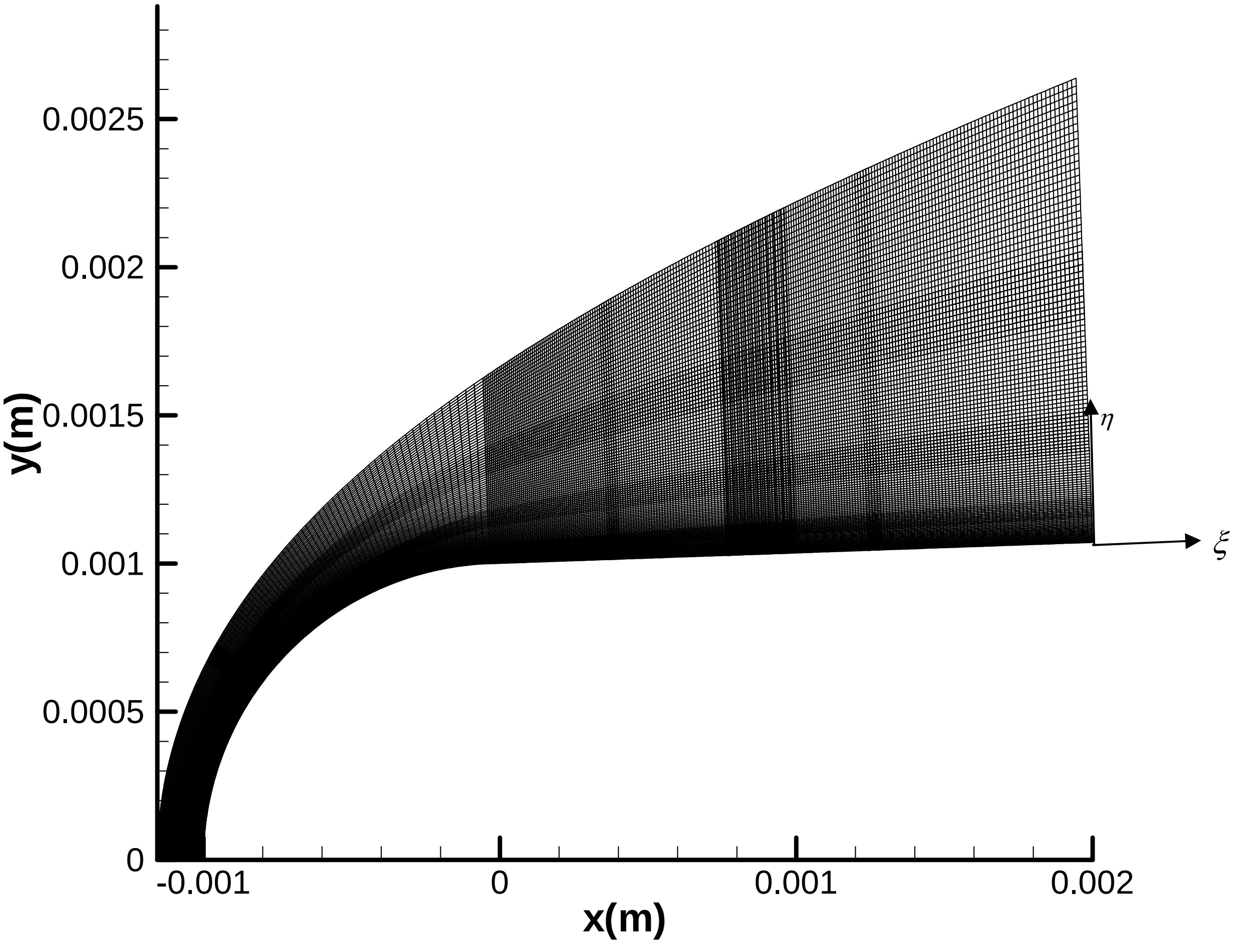

Figure 11. Partial view of grid configuration in zone 1, 2 and 3 near the nose region in Case 1.

The partial derivatives are transformed between the physical and computational domain coordinates according to the chain rule. The expressions in terms of the transformation matrices, A and B, are:

$$\begin{bmatrix} \frac{\partial}{\partial x} \\ \frac{\partial}{\partial y} \\ \frac{\partial}{\partial z} \\ \frac{\partial}{\partial t} \end{bmatrix} = \underbrace{\begin{bmatrix} \xi_x & \eta_x & \varsigma_x & 0 \\ \xi_y & \eta_y & \varsigma_y & 0 \\ \xi_z & \eta_z & \varsigma_z & 0 \\ \xi_t & \eta_t & \varsigma_t & 1 \end{bmatrix}}_{A} \begin{bmatrix} \frac{\partial}{\partial \xi} \\ \frac{\partial}{\partial \eta} \\ \frac{\partial}{\partial \varsigma} \\ \frac{\partial}{\partial \tau} \end{bmatrix} \Leftrightarrow \begin{bmatrix} \frac{\partial}{\partial \xi} \\ \frac{\partial}{\partial \eta} \\ \frac{\partial}{\partial \varsigma} \\ \frac{\partial}{\partial \tau} \end{bmatrix} = \underbrace{\begin{bmatrix} x_\xi & y_\xi & z_\xi & 0 \\ x_\eta & y_\eta & z_\eta & 0 \\ x_\varsigma & y_\varsigma & z_\varsigma & 0 \\ x_\tau & y_\tau & z_\tau & 1 \end{bmatrix}}_{B} \begin{bmatrix} \frac{\partial}{\partial x} \\ \frac{\partial}{\partial y} \\ \frac{\partial}{\partial z} \\ \frac{\partial}{\partial t} \end{bmatrix} \qquad (11)$$

Noticeably, A is the inverse of B. Furthermore, ξ_t and ς_t are zeros excluding η_t, because the grid surfaces where $\xi = \text{constant}$ and $\varsigma = \text{constant}$ do not move while the shock boundary is moving.

By applying the transformation relation to three-dimensional Navier-Stokes equations in conservative-law form and Cartesian coordinates in Eq. (1) along with some derivative manipulations, the final governing equations in conservative-law form in body-fitted curvilinear computational domain coordinates become:

$$\frac{1}{J}\frac{\partial U}{\partial \tau} + \frac{\partial \hat{E}}{\partial \xi} + \frac{\partial \hat{F}}{\partial \eta} + \frac{\partial \hat{G}}{\partial \zeta} + \frac{\partial \hat{E}_v}{\partial \xi} + \frac{\partial \hat{F}_v}{\partial \eta} + \frac{\partial \hat{G}_v}{\partial \zeta} + U\frac{\partial (1/J)}{\partial \tau} = 0 \qquad (12)$$

where

$$\begin{aligned} \hat{E} &= \frac{F_1\xi_x + F_2\xi_y + F_3\xi_z}{J} \\ \hat{F} &= \frac{F_1\eta_x + F_2\eta_y + F_3\eta_z + U\eta_t}{J} \\ \hat{G} &= \frac{F_1\zeta_x + F_2\zeta_y + F_3\zeta_z}{J} \\ \hat{E}_v &= \frac{F_{v1}\xi_x + F_{v2}\xi_y + F_{v3}\xi_z}{J} \\ \hat{F}_v &= \frac{F_{v1}\eta_x + F_{v2}\eta_y + F_{v3}\eta_z}{J} \\ \hat{G}_v &= \frac{F_{v1}\zeta_x + F_{v2}\zeta_y + F_{v3}\zeta_z}{J} \end{aligned} \qquad (13)$$

and J is the Jacobian of the coordinate transformation that is defined as:

$$\frac{1}{J} = \det\left(B\right) = x_{\xi}\left(y_{\eta}z_{\varsigma} - y_{\varsigma}z_{\eta}\right) - x_{\eta}\left(y_{\xi}z_{\varsigma} - y_{\varsigma}z_{\xi}\right) + x_{\varsigma}\left(y_{\xi}z_{\eta} - y_{\eta}z_{\xi}\right) \qquad (14)$$

The grid transformation metrics, $\xi_x, \xi_y, \xi_z, \eta_x, \eta_y, \eta_z, \eta_t, \zeta_x, \zeta_y, \zeta_z$, are related to their inverse metrics (the entries of the transformation matrix B) in the following expressions:

$$\begin{cases} \xi_x = J\left(y_{\eta}z_{\varsigma} - y_{\varsigma}z_{\eta}\right) \\ \xi_y = J\left(x_{\varsigma}z_{\eta} - x_{\eta}z_{\varsigma}\right) \\ \xi_z = J\left(x_{\eta}y_{\varsigma} - x_{\varsigma}y_{\eta}\right) \end{cases} \begin{cases} \eta_x = J\left(y_{\varsigma}z_{\xi} - y_{\xi}z_{\varsigma}\right) \\ \eta_y = J\left(z_{\varsigma}x_{\xi} - z_{\xi}x_{\varsigma}\right) \\ \eta_z = J\left(x_{\varsigma}y_{\xi} - x_{\xi}y_{\varsigma}\right) \end{cases} \begin{cases} \varsigma_x = J\left(y_{\xi}z_{\eta} - y_{\eta}z_{\xi}\right) \\ \varsigma_y = J\left(z_{\xi}x_{\eta} - z_{\eta}x_{\xi}\right), \\ \varsigma_z = J\left(x_{\xi}y_{\eta} - x_{\eta}y_{\xi}\right) \end{cases} \qquad (15)$$

$$\eta_t = -J\left[x_{\tau}\left(\frac{\eta_x}{J}\right) + y_{\tau}\left(\frac{\eta_y}{J}\right) + z_{\tau}\left(\frac{\eta_z}{J}\right)\right]$$

The inverse grid transformation metrics and the Jacobian of the coordinate transformation are determined at each time step with information of body geometry, the grid point distributions along the grid lines, the concurrent local shock height (wall-normal) between the wall and the shock boundary, $H\left(\xi,\zeta,\tau\right)$, and its first-order time derivative, $H_{\tau}\left(\xi,\zeta,\tau\right)$. The terms, $\hat{E},\hat{F},\hat{G}$, are the transformed inviscid fluxes, while the viscous fluxes $\hat{E}_v,\hat{F}_v,\hat{G}_v$ contain first-order spatial derivatives of temperature and velocity. In the code, all Cartesian coordinates are implemented in terms of local shock height, the height ratio of each grid point to the local shock height, and the local wall coordinates. Therefore, the grid transformation metrics are also computed from the partial derivatives of these terms.

In Figure 11, the computational domain has four boundaries. The boundary at the shock is computed using Rankine-Hugoniot relations. The surface of the solid wall is assumed to be no-slip and isothermal. The pressure at the wall is computed from the flow field by using a high-order polynomial extrapolation based on the interior points. The boundary at the stagnation line is a singularity in the current computational domain, thus it is extrapolated by a high-order polynomial based on the adjacent points. The exit boundary is also computed by a high-order polynomial extrapolation based on the interior points upstream owing to characteristic nature of the supersonic flow at the exit. The details of the shock-fitting formulations are explained in Section 2.3.

2.3 High-Order Shock-Fitting Method

In this linear boundary-layer receptivity and stability study, the magnitude of freestream perturbations is very low, $O\left(10^{-4}\right)$ of the freestream flow parameter, and the boundary-layer disturbances throughout the receptivity and stability stage can be even weaker than those of the freestream. However, the shock-capturing methods typically have fuzzy shock locations and a lower order of accuracy when resolving the shock. These shock-capturing methods can create a numerical inaccuracy that is large enough to contaminate the simulation of the subsequent weak disturbances generated from the shock/hotspot interactions [102]. In this study, therefore, a method that accurately resolves the shock/hotspot interaction is critical.

A high-order shock-fitting method can accurately resolve the location and velocity of the bow-shock; it can also maintain a uniformly high order of accuracy at the shock by setting the shock front as one of the boundaries of the computation domain [77]. To compute both steady and unsteady hypersonic viscous flow over a blunt cone, this study implements the high-order shock-fitting method, which was previously developed in Zhong [77].

Zhong [77] presented a high-order shock-fitting method to simulate the hypersonic flow field bounded by the shock and the wall of a blunt body. The numerical experiments for the shock-fitting method computed the steady flow over a two-dimensional cylinder and the unsteady periodic flow over a parabolic leading edge at zero angle of attack with two-dimensional and oblique three-dimensional freestream acoustic waves. The results of the flow over the cylinder were validated when compared to those of the shock-fitting spectral method and the experiment; LST and the linear shock theory were used to validate the results of the flow over the parabolic leading edge.

The shock-fitting method is based on the shock jump condition across the shock and characteristic compatibility relation from behind the shock. The method assumes a sharp discontinuity location at the shock, and the viscous effects on the shock are insignificant when the bow shock is detached far away from the wall. The shock boundary is the outer-most η grid line above the wall, namely:

$$\eta(x, y, z, t) = \eta_{\max} = \text{constant} \tag{16}$$

In terms of grid transformation metrics, the local normal vector of the shock front is:

$$\vec{n} = n_x \hat{i} + n_y \hat{j} + n_z \hat{k} = \frac{\eta_x \hat{i} + \eta_y \hat{j} + \eta_z \hat{k}}{|\nabla \eta|} \tag{17}$$

where:

$$|\nabla \eta| = \sqrt{\eta_x^{\,2} + \eta_y^{\,2} + \eta_z^{\,2}} \tag{18}$$

From Eq. (15), the shock velocity and the flow velocity in the local normal direction are given by the following equations, in terms of grid transformation metrics:

$$-\frac{\eta_t}{|\nabla \eta|} = \frac{x_\tau \eta_x + y_\tau \eta_y + z_\tau \eta_z}{|\nabla \eta|} = \frac{\partial x_j}{\partial t} \cdot \vec{n} = v_n \tag{19}$$

$$u_n = \vec{u} \cdot \vec{n} = \frac{u_1 \eta_x + u_2 \eta_y + u_3 \eta_z}{|\nabla \eta|} \tag{20}$$

Since the shock-fitting method treats the shock front as one of the boundaries, the shock location, velocity, and flow variables at the shock boundary must be resolved in order to compute the flow field behind the shock. Rankine-Hugoniot shock relation ensures the conservation of the inviscid flux vector along η grid line across the shock in the computational space:

$$\hat{F}_{shk} = \hat{F}_{\infty} \tag{21}$$

From Eq. (13), the Rankine-Hugoniot shock relation in Eq. (21) is rearranged to become:

$$\left(\vec{F}_{shk} - \vec{F}_{\infty}\right)\cdot \vec{a} + \left(U_{shk} - U_{\infty}\right) b = 0 \tag{22}$$

where

$$\vec{a} = \left(\frac{\eta_x}{J}\right)_{shk} \hat{i} + \left(\frac{\eta_y}{J}\right)_{shk} \hat{j} + \left(\frac{\eta_z}{J}\right)_{shk} \hat{k} \tag{23}$$

$$b = \left(\frac{\eta_t}{J}\right)_{shk} \tag{24}$$

From Rankine-Hugoniot shock relation in Eq. (21), the flow variables immediately behind the shock can be determined by the jump conditions across the shock:

$$p_{shk} = p_{\infty}\left[1 + \frac{2\gamma}{\gamma+1}\left(M_{n\infty}^2 - 1\right)\right] \tag{25}$$

$$\rho_{shk} = \rho_{\infty}\left[\frac{(\gamma+1)M_{n\infty}^2}{(\gamma-1)M_{n\infty}^2 + 2}\right] \tag{26}$$

$$u_{n,shk} = v_n + \frac{\rho_{\infty}}{\rho_{shk}}(u_{n\infty} - v_n) \tag{27}$$

$$\vec{u}_{shk} = \vec{u}_{\infty} + (u_{n,shk} - u_{n\infty})\vec{n} \tag{28}$$

$$\vec{u}_{t,shk} = \vec{u}_{\infty} - u_{n\infty}\vec{n} \tag{29}$$

where the subscripts "t" and "n" represent the components that are tangential and normal to the shock front, respectively.

In addition to Rankine-Hugoniot relations, the compatibility relation of the shock from behind is also utilized in the shock-fitting method. The Jacobian matrix of the η-

directional inviscid flux vector in the quasi-linear conservative-law form of the Navier-Stokes equations in Eq. (12) is:

$$\hat{B} = \frac{\partial \hat{F}}{\partial U} \tag{30}$$

The Jacobian matrix $\hat{B}$ has five total eigenvalues for the three-dimensional case; the eigenvalue corresponding to the characteristic field approaching the shock from behind is:

$$\lambda_5 = \frac{|\nabla \eta|}{J}\left(u_n - v_n + c\right)_{shk} \tag{31}$$

where the left eigenvector corresponding to λ_5 behind the shock is:

$$\vec{l}_5 = \begin{bmatrix} \frac{\gamma-1}{2}\left(u_1^{\,2} + u_2^{\,2} + u_3^{\,2}\right) - cu_n \\ -(\gamma-1)u_1 + cn_x \\ -(\gamma-1)u_2 + cn_y \\ -(\gamma-1)u_3 + cn_z \\ \gamma - 1 \end{bmatrix}_{shk} \tag{32}$$

The left eigenvector, the eigenvalues and the Jacobian matrix behind the shock satisfy the following relation:

$$\vec{l}_5 \cdot \hat{B}_{shk} = \frac{|\nabla \eta|}{J}\left(u_n - v_n + c\right)_{shk} \vec{l}_5 \tag{33}$$

The compatibility relation immediately behind the shock is thus obtained by rearranging and multiplying the conservative-law form of the Navier-Stokes equations in Eq. (12) by the left eigenvector, $\vec{l}_5$:

$$\vec{l}_5 \cdot \left(\frac{\partial U}{\partial \tau}\right) = \vec{l}_5 \cdot \left(-\frac{\partial \hat{E}}{\partial \xi} - \frac{\partial \hat{F}}{\partial \eta} - \frac{\partial \hat{G}}{\partial \zeta} - \frac{\partial \hat{E}_v}{\partial \xi} - \frac{\partial \hat{F}_v}{\partial \eta} - \frac{\partial \hat{G}_v}{\partial \zeta} - U\frac{\partial (1/J)}{\partial \tau}\right) J \tag{34}$$

In unsteady flow simulation, the shock-fitting grid is a moving grid in time, due to unsteady shock motion. Based on the first-order time derivative of the Rankine-Hugoniot relations in Eq. (22)—with the multiplication of the left eigenvector, and the characteristic compatibility relations immediately behind the shock in Eq. (33)—the equation to obtain shock velocity is expressed in the following form [77]:

$$\frac{\partial b}{\partial \tau}=\frac{-1}{\left[\vec{I}_5\cdot(U_{shk}-U_{\infty})\right]}\left[\frac{|\nabla \eta|}{J}\left(u_n-v_n+c\right)_{shk}\vec{I}_5\cdot\left(\frac{\partial U}{\partial \tau}\right)_{shk}+\vec{I}_5\cdot\left(F_{shk}-F_{\infty}\right)\cdot\frac{\partial \vec{a}}{\partial \tau}-\left(\vec{I}_5\cdot\hat{B}_{\infty}\right)\frac{\partial U_{\infty}}{\partial \tau}\right] \quad (35)$$

Alternatively, the time derivatives in Eq. (35) of the grid transformation metrics can be expressed as functions of $H \text{ and } H_\tau$:

$$\frac{\partial \vec{a}}{\partial \tau}=\frac{\partial}{\partial \tau}\left(\frac{\eta_x}{J}\right)_{shk}\hat{i}+\frac{\partial}{\partial \tau}\left(\frac{\eta_y}{J}\right)_{shk}\hat{j}+\frac{\partial}{\partial \tau}\left(\frac{\eta_z}{J}\right)_{shk}\hat{k}=\vec{g}\left(\xi,\zeta,H,H_\tau\right) \quad (36)$$

$$\frac{\partial b}{\partial \tau}=\frac{\partial}{\partial \tau}\left(\frac{\eta_\tau}{J}\right)_{shk}=d_1\left(\xi,\zeta,H,H_\tau\right)+d_2\left(\xi,\zeta,H,H_\tau\right)\frac{\partial H_\tau}{\partial \tau} \quad (37)$$

Finally, shock motion can be solved by the following time-derivative functions of the local shock height:

$$\begin{cases}\dfrac{\partial H_\tau}{\partial \tau}=f\left(\xi,\zeta,U_{shk},\vec{I}_5\cdot\left(\dfrac{\partial U}{\partial \tau}\right)_{shk},U_{\infty},\dfrac{\partial U_{\infty}}{\partial \tau},H,H_\tau\right)\\ \dfrac{\partial H}{\partial \tau}=H_\tau\end{cases} \quad (38)$$

The subscript "shk" indicates the value behind the shock, while subscript "∞" indicates the freestream value. Term c is the speed of sound, u_n is the velocity component of the flow in the shock normal direction, and $\vec{I}_5\cdot\left(\frac{\partial U}{\partial \tau}\right)_{shk}$ is obtained by Eq. (34). The flow variables immediately behind the shock can be obtained by the jump conditions in Eqs. (25) through (29).

The shock velocity and shock position are unknown at each time step in the simulation. These unknowns can be solved by integrating the time derivatives of the local shock height in Eq. (38), as determined from the instantaneous freestream conditions and the local solutions behind the bow shock. The spatial derivatives of the inviscid fluxes in the ξ and η directions in computational space are discretized by using a fifth-order finite-difference upwind scheme with local Lax-Friedrichs flux-splitting formulation. A sixth-order central finite-difference scheme is used for discretizing the spatial derivatives of the viscous fluxes in ξ and η directions in computational space. The flow in the azimuthal direction is assumed to be periodic in this study, since the two-dimensional effects in the axisymmetric flow are focused. The Fourier collocation method is used for the spatial derivatives of both the inviscid and viscous fluxes in the periodic azimuthal direction, while the Runge-Kutta method is used for time-marching. More details on finite difference schemes and other numerical method implementations of the current numerical simulation can be found in Zhong's paper [77].

2.4 Model for Freestream Entropy-Spot Perturbations

In a flight environment, entropy spot or hotspot can have an arbitrary shape and profile. In this study, we choose a simplified form of a hotspot: a spherical hotspot with a Gaussian temperature and density profile. The freestream laser spot that was generated at Purdue University was similar to the hotspot in this study. More specifically, the previous freestream benchmark tests of the laser spot at Purdue University shows that it had an approximately Gaussian temperature or density profile with a weak shock surrounding it. [67, 95-97] Since the weak shock dissipated very rapidly while the entropy core remained mostly constant in the freestream, calibrating the initial distance between the laser spot and the bow shock could minimize the influence of the weak shock. Therefore, the simulation results of the current study can be compared with the experimental results.

In the current study, the freestream hotspot is modeled by Gaussian entropy perturbations. More specifically, the temperature profile in the freestream is

$$T^*\left(x^*, y^*, z^*, t^*\right) = \Delta T^*_{\max} \exp\left(-\frac{R_c^{*2}}{2\sigma^2}\right) + T^*_\infty \tag{39}$$

where σ is a Gaussian shaping factor, $\Delta T^*_{\max}$ is the maximum freestream temperature perturbation amplitude, and R_c^* is the radial distance from the center of the entropy spot to any point $\left(x^*, y^*, z^*\right)$ in space:

$$R_c^* = \sqrt{\left(x^* - x^*_{spot}\right)^2 + \left(y^* - y^*_{spot}\right)^2 + \left(z^* - z^*_{spot}\right)^2} \tag{40}$$

In Eq. (40), $(x^*_{spot}, y^*_{spot}, z^*_{spot})$ is the instantaneous coordinate of the entropy spot's center:

$$\begin{cases} x^*_{spot} = x^*_0 + u^*_\infty t^* \\ y^*_{spot} = y^*_0 = 0 \\ z^*_{spot} = z^*_0 = 0 \end{cases} \tag{41}$$

where u^*_∞ is the freestream velocity. In Eq. (41), $\left(x^*_0, y^*_0, z^*_0\right)$ is the initial coordinate of the center of entropy spot at $t^* = 0$. Here y^*_{spot} and z^*_{spot} are zero because we consider an axisymmetric flow in this study, and the hotspot in the freestream is located on the x axis, or the centerline of the cone.

Based on the ideal gas law, the perturbed freestream density is

$$\rho^*(x^*, y^*, z^*, t^*) = \frac{p^*_\infty}{R^* T^*} \tag{42}$$

where P^*_∞ is a constant as there are no acoustic perturbations in the freestream.

2.5 Spectral Analysis of Boundary-Layer Instability

In a simulation, the hotspot induced wave packet contains a wide range of frequencies. In order to study the characteristics of each frequency component, a temporal Fourier spectral analysis is conducted on the time histories of perturbations at various sampling locations.

In terms of the discrete spectral components, an arbitrary flow variable time function, $h(t)$, is represented as:

$$h(t_k) \equiv h_k \approx \sum_{n=0}^{N-1} H(F_n) e^{-2\pi i F_n t_k} \tag{43}$$

where $H\left(F_n\right)$ is the spectral value at the nth discretized frequency, F_n, while N is the total number of Fourier collocation points that are used to discretize the time function, $h\left(t\right)$. The discretized time function is h_k, defined as the value of $h\left(t\right)$ at $t = t_k$.

In this work, $h\left(t\right)$ is the time-history of local boundary-layer perturbations, while $H\left(F_n\right)$ is the spectral value of the boundary-layer perturbations in the frequency domain. $H\left(F_n\right)$ is a complex value; $\left|H\left(F_n\right)\right|$ is the local perturbation amplitude.

After obtaining the frequency spectra of the boundary-layer perturbations from the unsteady simulation, the local spatial growth rates, local wave numbers, and the wall-normal boundary-layer mode shapes are then compared with LST for the receptivity study. Local growth rates are determined by [24]:

$$-\alpha_i = \frac{1}{\left|H\left(F_n\right)\right|}\frac{d\left|H\left(F_n\right)\right|}{ds} \tag{44}$$

Local wave numbers are determined by [24]:

$$\alpha_r = \frac{d\varphi_n}{ds} \tag{45}$$

where φ_n is the phase angle of $H\left(F_n\right)$ at the nth discretized frequency. The wall-normal mode shape is the spatial distribution of the local perturbation amplitude, $\left|H\left(F_n\right)\right|$, along the normal to the cone surface.

3 Boundary-Layer Receptivity and Stability in the Standard Case

3.1 Freestream Flow Conditions and Compression Cone Geometries

In the standard case, Case 1, the freestream conditions are based on those of the Mach 6 Quiet Tunnel (BAM6QT) at Purdue University [23]. The cone placed in freestream has zero angle of attack； the flow around the cone is axisymmetric. The wall of the cone is smooth, rigid, and isothermal. Further details of the freestream conditions are summarized in Table 2.

Table 2. Freestream conditions of Case 1.

M_∞	6.0
ρ_∞^*	$0.0403\ \mathrm{kg/m^3}$
T_∞^*	52.8 K
T_o^*	433.0 K
T_{wall}^*	300.0 K
γ	1.4
Pr	0.72
R^*	$287.04\ \mathrm{N \cdot m / kg \cdot K}$ (air)
μ_r^*	$1.7894 \times 10^{-5}\ \mathrm{kg / m \cdot s}$ (sea level)
T_r^*	288 K (sea level)
T_s^*	110.3 K
Re_∞^*	$1.026 \times 10^7\ \mathrm{m}^{-1}$

The geometry of the blunt compression cone is the same as that used in the experimental studies by Wheaton *et al.* [23] It consists of two parts: a spherical nose section followed by a flared section. The spherical nose of the cone is blunt with a small radius of $1\,\mathrm{mm}$. The starting point of the flared surface is tangent to the spherical nose surface with an initial angle of 2 degrees. The flared geometry is a circular arc that has a radius of $3.0\,\mathrm{m}$. The total length of the cone, measured from the tip of the spherical nose to the base of the cone along the centerline, is $0.45\,\mathrm{m}$. Figure 10 illustrates the schematics of the blunt compression cone.

3.2 Simulation Results and Analyses

Due to the limited computer power of computing a huge amount of grid points at once, the simulation is divided into 21 zones. Zone 1 is the computation domain in the stagnation region over the hemispherical cone nose. Zone 2 through zone 21 is the computation domain in the compression region over the cone. For zones 1 through 12, the total grid resolution is 2280×120; for zones 13 through 21, the total grid resolution is 2160×240. The periodic azimuthal direction has 4 points to resolve the axisymmetric flow in the spectral method. Figure 11 shows a partial view of the computational grid around the cone. The reflection—which is created during the exiting of disturbances at the downstream boundary of each zone—is minimal due to overlap regions. During the computation, the profiles of the disturbances at different frequencies near the exit of each zone are monitored to ensure enough overlap points in the streamwise direction for the inlet of the next zone to skip the reflection-affected area. The computation of each zone lasts until the disturbances fully exit the zone. At the end of the computation, the overall relative amplitude of the perturbations in each zone is $O(10^{-9})$. The maximum time-step size of recording the unsteady inlet boundary conditions is $1.12\times10^{-7}\,\mathrm{s}$, which is sufficient to resolve the second mode instability at the high end of the studied frequency range. It is worth noting that the current zonal method used in our simulations is fundamentally the same as the flow with periodic disturbances previously published [4, 36, 77].

The grid convergence study of steady base flow was achieved with two grids in Section IV of Lei *et al.* [103]. The freestream Mach number used in their grid convergence study was 5.5 and their freestream unit Reynolds number was $1.9\times10^{7}\,\mathrm{m}^{-1}$, higher than the current case. The cone used in their study was a straight blunt cone with a nose radius of $4\ \mathrm{mm}$; a half angle of the cone was 8 degrees. A case with a higher freestream unit Reynolds number required a higher computational resolution. Therefore, the resolution independence study shows that both sets of 120 and 240 grid points in wall-normal direction were sufficient for their simulation, thus also sufficient for this work. The grid convergence study of the current steady base flow is presented in Section 3.2.1. Additionally, Section 3.2.4 presents the grid convergence study of the current unsteady flow.

3.2.1 Steady Base Flow Solutions

To conduct the study in this work, the first step is computing the steady base flow over the compression cone. Before carrying out the physical analysis of the steady base flow, a grid convergence study is performed to validate the current grid resolution. The cone case's simulation results are mainly sensitive to the resolution in the wall-normal direction. Hence, the grid convergence study is carried out between a wall-normal resolution and its double. The steady base wall-normal profiles of density, pressure, and temperature at the end of the cone, $s = 0.4\ \mathrm{m}$, of both resolutions are shown in Figure 12, Figure 14, and Figure 16. Both profiles of each flow variable agree very well. The differences can be better illustrated by calculating the relative error between the two sets of data from both grid resolutions. The relative errors between the profiles of both grid resolutions are presented in Figure 13, Figure 15, and Figure 17. The differences mainly appear around the Mach wave, which is near the shock boundary, and the edge of the boundary layer, where the change of gradient is large. The relative errors of density and temperature are $O(10^{-3})$ and the relative error of pressure is $O(10^{-4})$. Since the grid convergence study shows that the current resolution in wall-normal direction are sufficient to resolve the profiles of the flow variables, the resulting steady base flow is used to conduct the unsteady simulation in the latter part of this work.

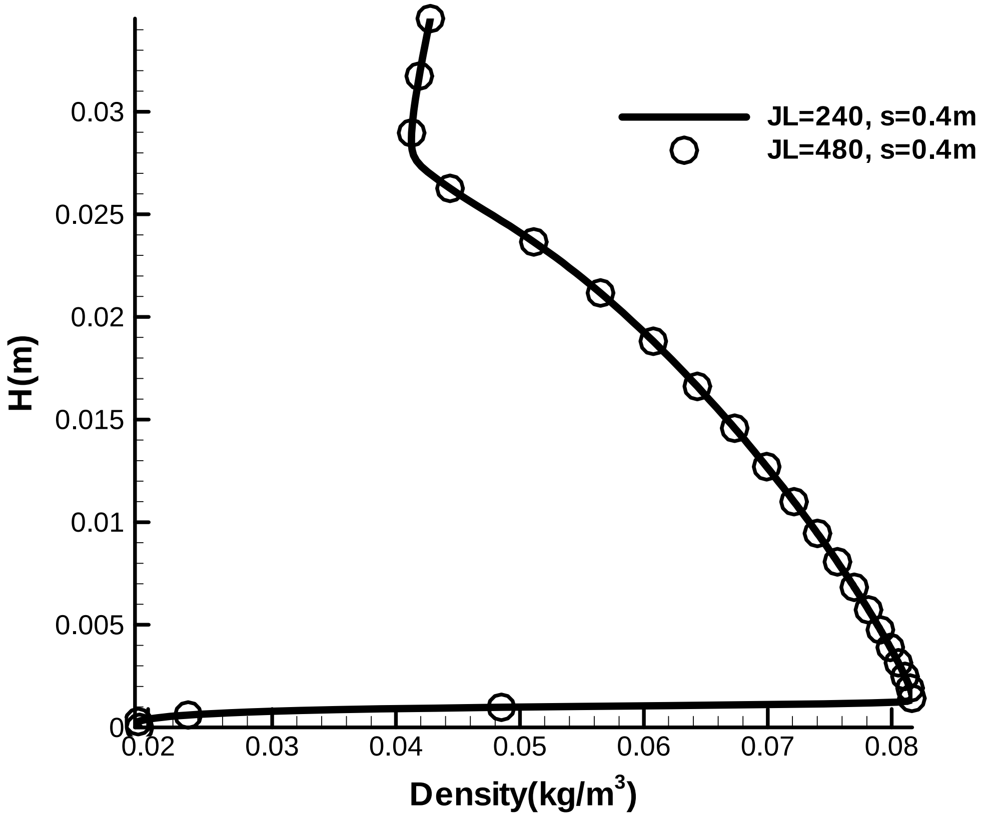

Figure 12. Comparison of the steady base density profiles between the j-direction resolution of 240 grids and 480 grids.

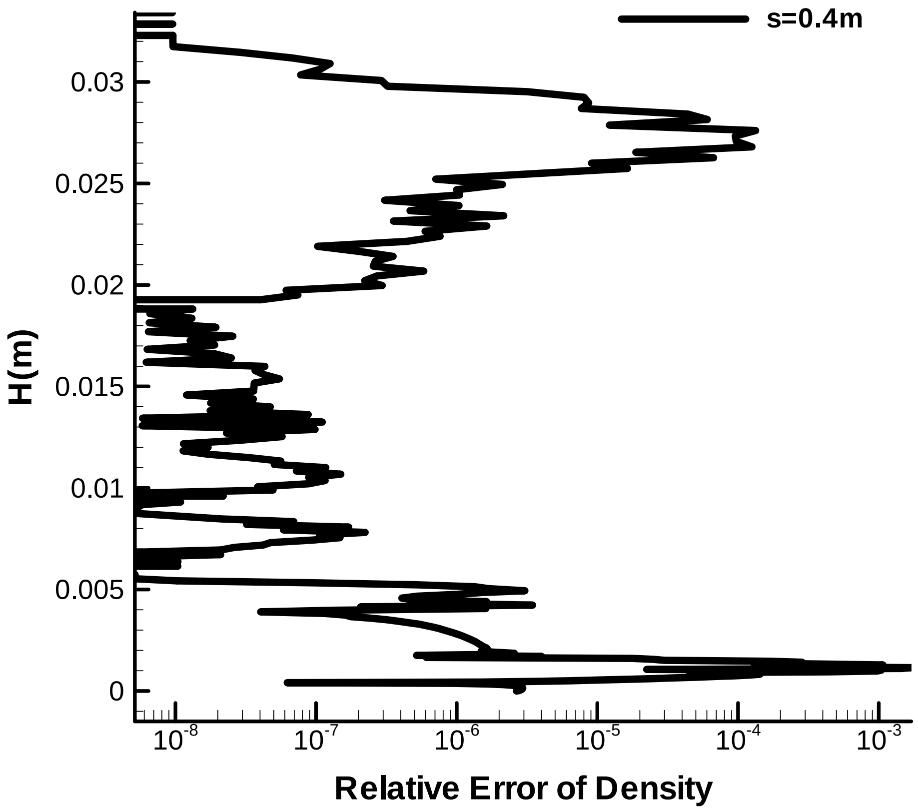

Figure 13. Relative error between the density profiles of 240 grids and 480 grids in j direction.

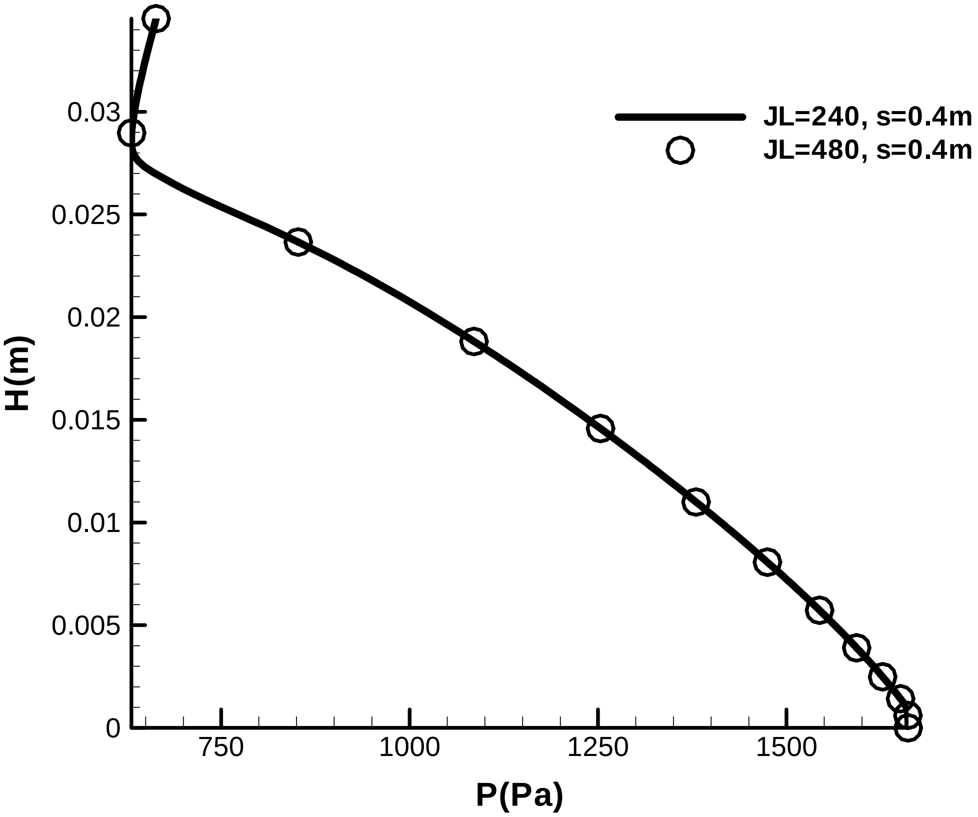

Figure 14. Comparison of the steady base pressure profiles between the j-direction resolution of 240 grids and 480 grids.

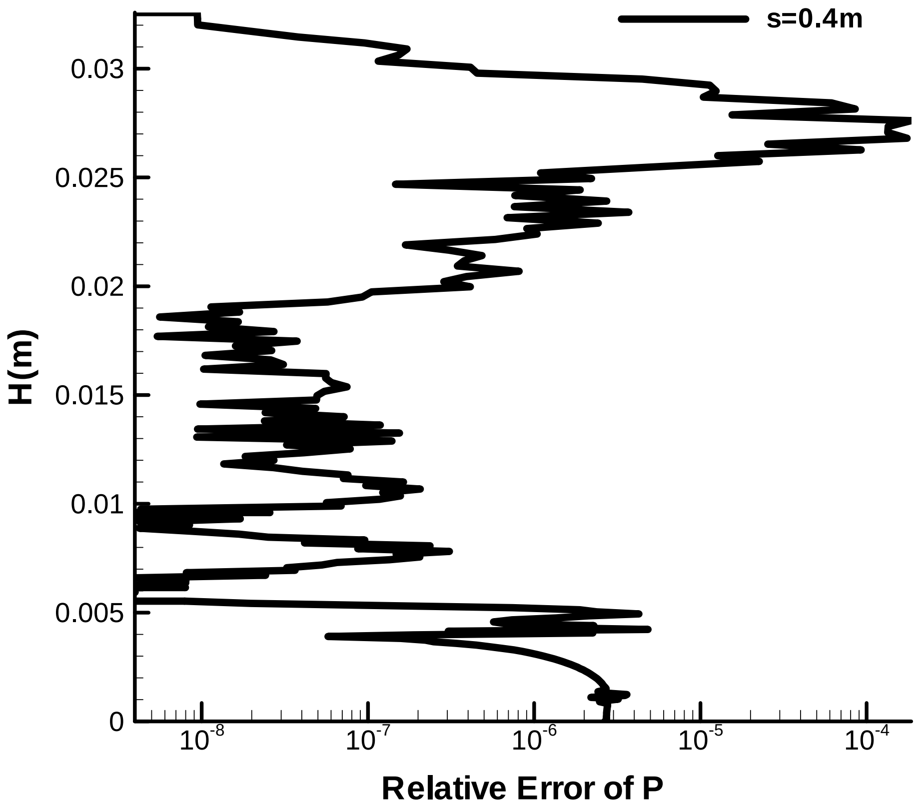

Figure 15. Relative error between the pressure profiles of 240 grids and 480 grids in j direction.

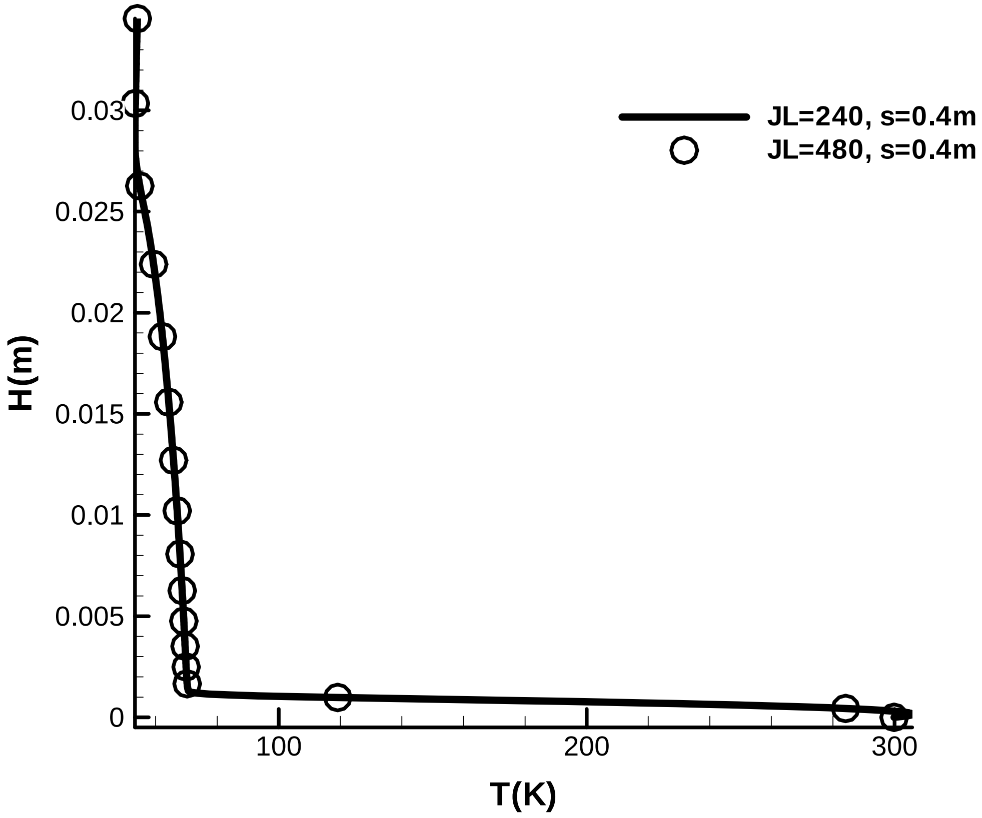

Figure 16. Comparison of the steady base temperature profiles between the j-direction resolution of 240 grids and 480 grids.

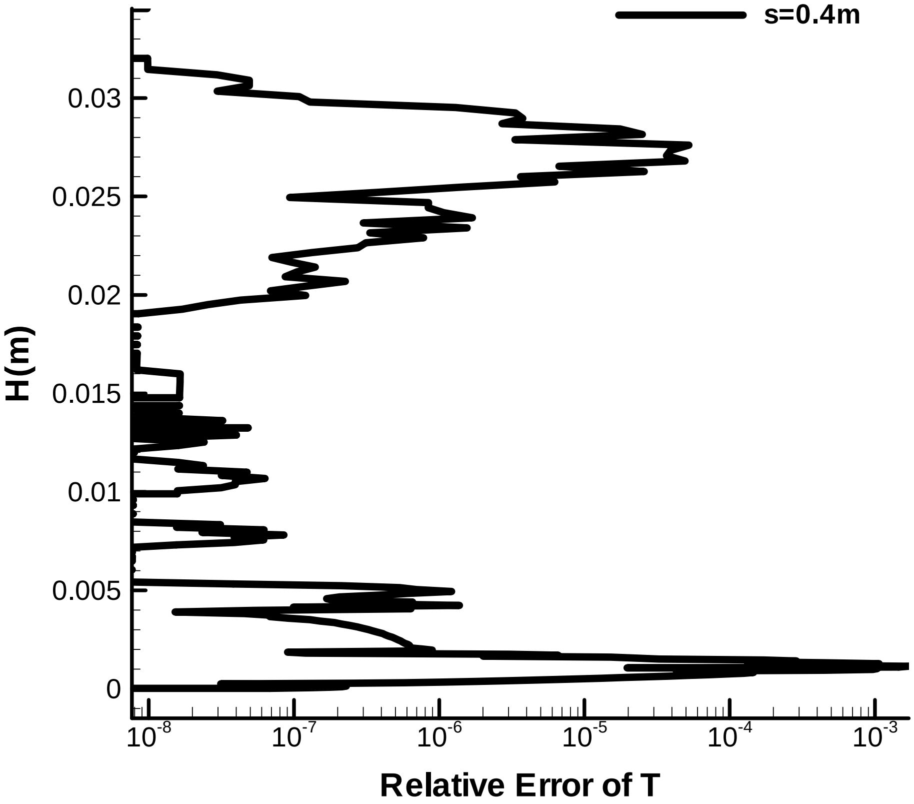

Figure 17. Relative error between the temperature profiles of 240 grids and 480 grids in j direction.

The Mach number contours in Figure 18 and the Mach number profiles at various locations in Figure 19 show that the Mach number near the wall increases drastically over a short distance behind the nose region. Then, it gradually decreases downstream along the cone where the adverse pressure gradient occurs on the concave flaring surface of the cone. Eventually, a region of relatively low Mach number appears above the wall near the bottom of the cone. The thickness of the Mach boundary layer is consistently about 0.001 m in Figure 19 (b) through (d). The constant boundary-layer thickness prevents the shift of the unstable frequency, as discussed in Section 3.2.4. There is a dent near the top of the profile in Figure 19 (d), this is due to the Mach waves developed under the compression effects of the concave cone surface. At farther downstream locations beyond the current computation domain, these Mach waves could eventually form a shock outside the boundary layer. Such Mach waves are also seen in the steady base flow over a flared cone in Mach 6 freestream by Zhong [28].

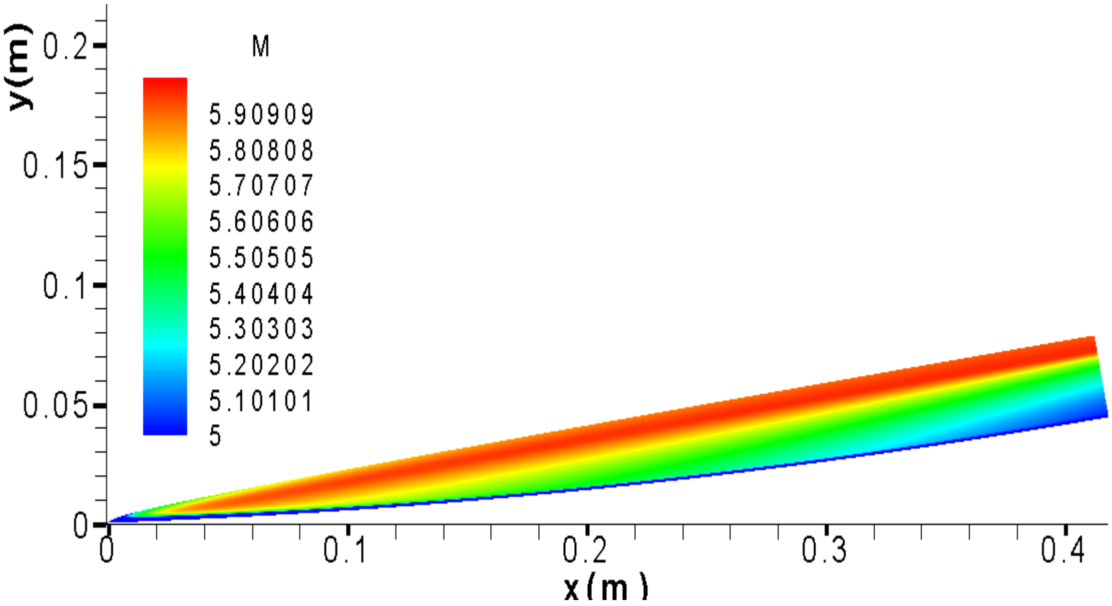

Figure 18. Mach number contours of the steady base flow.

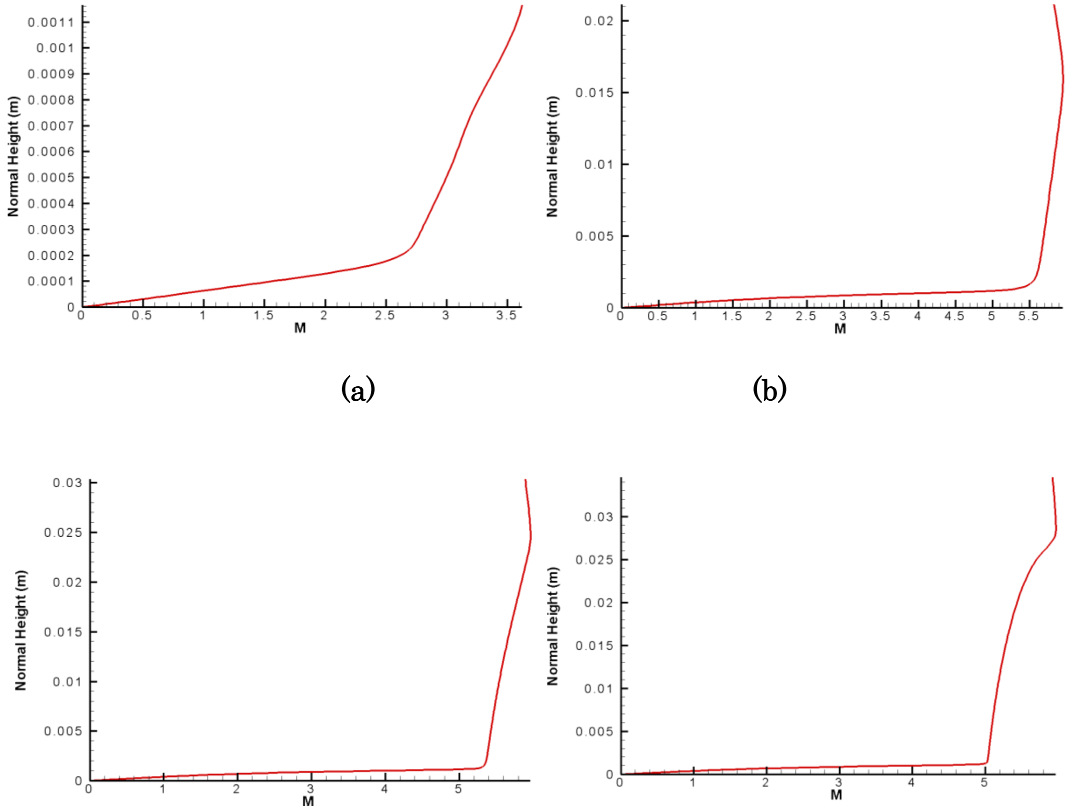

(a) (b)

(c) (d)

Figure 19. Mach number profiles of steady base flow at four locations along the cone surface: (a) $x^* = 0.001\,\mathrm{m}$, (b) $x^* = 0.138\,\mathrm{m}$, (c) $x^* = 0.258\,\mathrm{m}$, and (d) $x^* = 0.418\,\mathrm{m}$.

Wheaton *et al.* [23] computed their steady base flow using STABL. Their flow conditions and cone geometry were the same as those used in the current study; the same physical phenomena observed in Figure 18 were also seen in their steady base flow. In order to compare this current steady base flow with Wheaton *et al.* [23], the current shock-shape is overlaid onto that of Wheaton *et al.* [23] in Figure 20. In this figure, both shock-shapes agree reasonably well with each other. This observation shows that the performed computation, using the current shock-fitting code, is consistent with other methods.

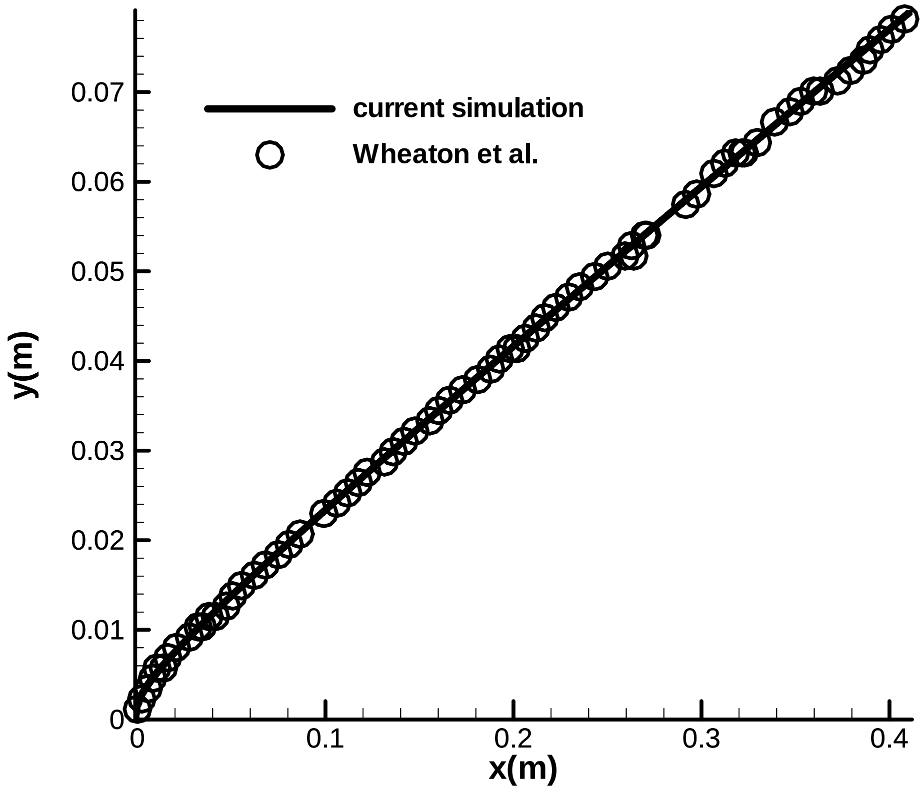

Figure 20. Comparison of shock fronts of steady base flow between our current simulation and the one of Wheaton *et al.* [23]

In the nose region, the curvature of bow shock creates vorticity in the flow field behind the shock. Per Crocco's Theorem, the gradient of entropy, (which relates to the entropy layer), is also created due to the generation of vorticity by the shock curvature. In this current study, we characterize the entropy layer effects by using a parameter named generalized velocity gradient, $\rho\left(du_t/dy_n\right)$; the peak of such a parameter within a compressible boundary layer is defined as a generalized inflection point. Lees and Lin [104] showed that the existence of generalized inflection point was a necessary and sufficient condition for the existence of inviscid instability in a compressible boundary layer. Figure 21 and Figure 22 demonstrate the evolution of the generalized inflection point that involves the interaction of the entropy and boundary layers. The dimensionless wall-normal height, y_n, is normalized by the local thickness of boundary layer in both figures in order to maintain self-similarity. The abbreviated mathematical notation, ρDU, represents the generalized velocity gradient. Lastly, both the local Reynolds numbers and the corresponding x-coordinates are shown in the legend for various locations.

In Figure 21, the wall-normal profiles of ρDU at various locations upstream near the nose region are shown. The viscous effects from the wall occur throughout the entire upstream flow field near the nose region. The earliest location of R=127 is immediately behind the nose region. At this location, a peak initially enters the flow field from shock. In the subsequent locations of R=154 to 207, the peak moves towards the wall; meanwhile, its amplitude attenuates. These observations imply that the entropy layer generated by the shock moves toward the wall while moving downstream. During this movement, the entropy layer is gradually swallowed by the boundary layer.

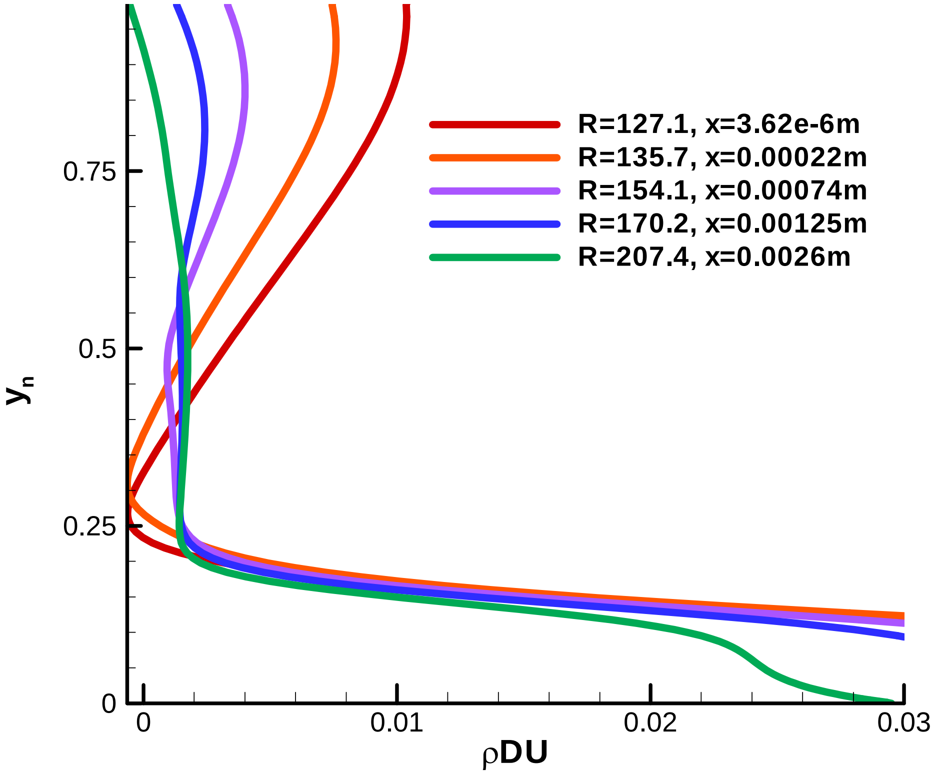

Figure 21. Wall-normal profiles of the generalized velocity gradient at various locations upstream near by the nose region.

The wall-normal profiles of generalized velocity gradient at further downstream locations are demonstrated in Figure 22. At the location of R=272.9, the peak is completely swallowed by the boundary layer. A turning point appears around the local boundary-layer normalized height of 0.2, which is near the wall. At the location of R=471, a peak of generalized velocity gradient, the generalized inflection point, first appears below the turning point at the local boundary-layer normalized height of 0.2. According to Mack [24], and Lees and Lin [104], the inviscid neutral waves exist at that generalized inflection point where the discontinuity of Reynolds stress appears. This is the sufficient condition for the existence of inviscid instability in the boundary layer. Mack [24], and Lees and Lin [104] also pointed out that the phase velocity of the neutral inviscid wave is the same as the mean velocity at the generalized inflection point. From the subsequent locations from R=471 to 1506, the generalized inflection point moves toward the edge of the boundary-layer. As mentioned in Mack [24], this results from increasing the Mach number of the flow above the boundary layer at those subsequent locations, thereby causing the increase of mean velocity at the generalized inflection point. Thus, the phase velocity of the neutral inviscid wave also increases. The outward movement of the generalized inflection point leads to a more unstable boundary layer. In Figure 22, the generalized inflection point stays at an almost constant self-similar wall-normal height of 0.75, which nears the edge of the boundary layer, at the locations downstream from R=1506.

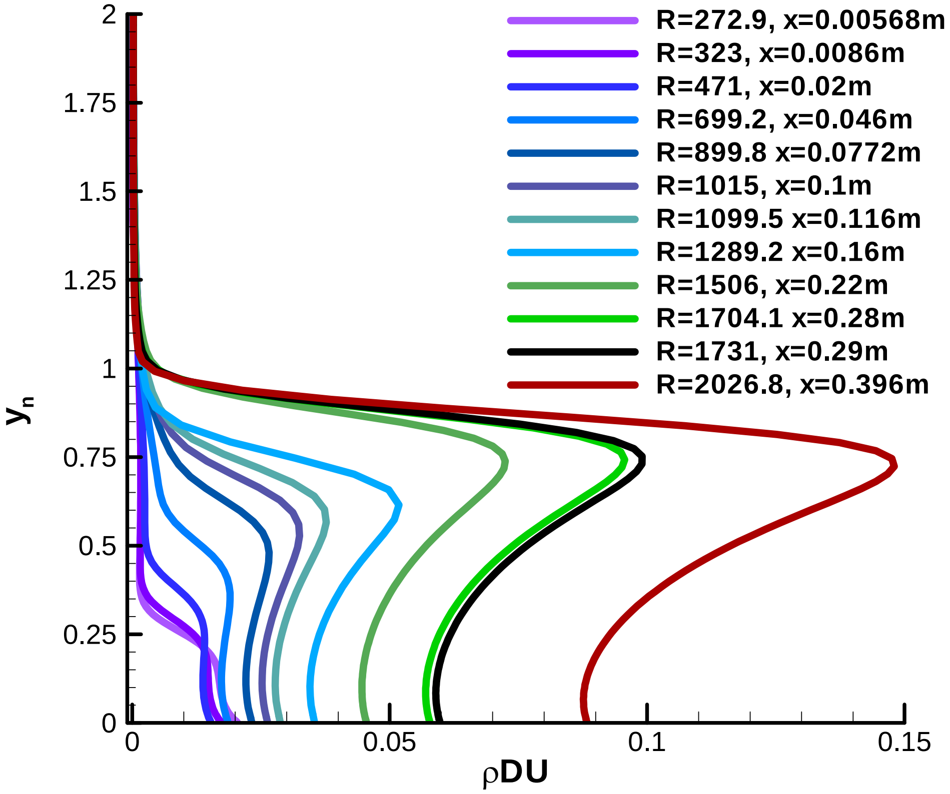

Figure 22. Wall-normal profiles of generalized velocity gradient at various downstream locations.

3.2.2 Linear Stability Theory

In order to extract the theoretical interpretations of boundary-layer receptivity and stability from the numerically simulated boundary-layer disturbances, linear stability theory (LST) analyses are conducted based on the steady base flows in the current study. Additionally, the results from the LST analysis can also be used to validate the simulated results. The derivations of LST are shown in Mack [24] and Malik [44]. A summary of LST is provided in this section. In LST analysis, we solve the normal modes of the linearized stability equations that are derived from compressible viscous Navier-Stokes equations for a calorically perfect Newtonian gas in Cartesian coordinates:

$$\rho\left[\frac{\partial\vec{u}}{\partial t}+\left(\vec{u}\cdot\nabla\right)\vec{u}\right]=-\nabla p+\nabla\cdot\left[\lambda\left(\nabla\cdot\vec{u}\right)\bar{I}+\mu\left(\nabla\vec{u}+\nabla\vec{u}^{T}\right)\right] \tag{46}$$

$$\frac{\partial\rho}{\partial t}=\nabla\cdot\left(\rho\vec{u}\right)=0 \tag{47}$$

$$\rho c_{p}\left[\frac{\partial T}{\partial t}+\left(\vec{u}\cdot\nabla\right)T\right]=-\nabla\cdot\left(\kappa\nabla T\right)+\frac{\partial p}{\partial t}+\vec{u}\cdot\nabla p+\Phi \tag{48}$$

where the pressure and the viscous dissipation function are expressed in:

$$p=\rho R^{*}T \tag{49}$$

$$\Phi=\lambda\left(\nabla\cdot\vec{u}\right)^{2}+\frac{\mu}{2}\left[\nabla\vec{u}+\nabla\vec{u}^{T}\right]^{2} \tag{50}$$

where the viscous coefficients are determined by Sutherland's law. Noticeably, the Cartesian coordinates in the above Navier-Stokes equations are local, in which the x coordinates are streamwisely parallel to the wall. The y coordinates are normal to the wall and the z coordinates are in the azimuthal direction along the wall.

The stability equations are based on expressing the flow variables as: the sum of the steady base flow variables plus perturbations, as follows:

$$q = \bar{q} + \tilde{q} \Leftrightarrow \begin{cases} u_1 = \bar{U} + \tilde{u} \\ u_2 = \bar{V} + \tilde{v} \\ u_3 = \bar{W} + \tilde{w} \\ p = \bar{P} + \tilde{p} \\ T = \bar{T} + \tilde{T} \\ \rho = \bar{\rho} + \tilde{\rho} \\ \mu = \bar{\mu} + \tilde{\mu} \\ \lambda = \bar{\lambda} + \tilde{\lambda} \\ \kappa = \bar{\kappa} + \tilde{\kappa} \end{cases} \tag{51}$$

where the steady base flow variables are computed in the numerical simulation in the current study.

In the derivation of LST, the steady base boundary layer growth is insignificant if the streamwise domain length of the analyzed flow field is very short. In the current LST analyses, the normal modes are solved based on the steady base flow profile of one sampling streamwise location at a time. Hence, the assumptions of locally parallel flow, in which the streamwise variation of the steady base flow variables within one sampling location are assumed to be insignificant when compared to the wall-normal variation, are made. Also, the vertical velocity component of the steady base flow is insignificant under the locally parallel flow assumptions.

When substituting the summation form of the steady base value and perturbation into the Navier-Stokes equations, and if the perturbations in the flow are very small in magnitude, the higher-order perturbation terms can be dropped. Consequently, the equations are linearized. By subtracting the steady base flow solutions from the Navier-Stokes equations, and applying the locally parallel flow assumptions, the final linearized stability equations eventually become [44]:

$$
\begin{aligned}
\Big(\frac{\partial \tilde{u}}{\partial t} + U\frac{\partial \tilde{u}}{\partial x} + \tilde{v}\frac{dU}{dy} + W\frac{\partial \tilde{u}}{\partial z}\Big)/T = -\frac{\partial \tilde{p}}{\partial x} + \frac{\mu}{R}\Bigg[& l_2\frac{\partial^2 \tilde{u}}{\partial x^2} + l_1\left(\frac{\partial^2 \tilde{v}}{\partial x \partial y} + \frac{\partial^2 \tilde{w}}{\partial x \partial z}\right) \\
& + \frac{\partial^2 \tilde{u}}{\partial y^2} + \frac{\partial^2 \tilde{u}}{\partial z^2} + \frac{1}{\mu}\frac{d\mu}{dT}\frac{dT}{dy}\left(\frac{\partial \tilde{u}}{\partial y} + \frac{\partial \tilde{v}}{\partial x}\right) \\
& + \frac{1}{\mu}\frac{d\mu}{dT}\left(\frac{\partial^2 U}{\partial y^2}\tilde{T} + \frac{dU}{dy}\frac{\partial \tilde{T}}{\partial y}\right) + \frac{1}{\mu}\frac{d^2\mu}{dT^2}\frac{dT}{dy}\frac{dU}{dy}\tilde{T}\Bigg]
\end{aligned}
\tag{52}
$$

$$
\begin{aligned}
\Big(\frac{\partial \tilde{v}}{\partial t} + U\frac{\partial \tilde{v}}{\partial x} + W\frac{\partial \tilde{v}}{\partial z}\Big)/T = -\frac{\partial \tilde{p}}{\partial y} + \frac{\mu}{R}\Bigg[& \frac{\partial^2 \tilde{v}}{\partial x^2} + l_1\left(\frac{\partial^2 \tilde{u}}{\partial x \partial y} + \frac{\partial^2 \tilde{w}}{\partial x \partial z}\right) \\
& + l_2\frac{\partial^2 \tilde{v}}{\partial y^2} + \frac{\partial^2 \tilde{v}}{\partial z^2} + \frac{1}{\mu}\frac{d\mu}{dT}\left(\frac{\partial \tilde{T}}{\partial x}\frac{\partial U}{\partial y} + \frac{\partial \tilde{T}}{\partial z}\frac{\partial W}{\partial y}\right) \\
& + \frac{1}{\mu}\frac{d\mu}{dT}\frac{dT}{dy}\left\{ l_0\left(\frac{\partial \tilde{u}}{\partial x} + \frac{\partial \tilde{w}}{\partial z}\right) + l_2\frac{\partial \tilde{v}}{\partial y}\right\}\Bigg]
\end{aligned}
\tag{53}
$$

$$
\begin{aligned}
\Big(\frac{\partial \tilde{w}}{\partial t} + U\frac{\partial \tilde{w}}{\partial x} + \tilde{v}\frac{dW}{dy} + W\frac{\partial \tilde{w}}{\partial z}\Big)/T = -\frac{\partial \tilde{p}}{\partial z} + \frac{\mu}{R}\Bigg[& \frac{\partial^2 \tilde{w}}{\partial x^2} + l_1\left(\frac{\partial^2 \tilde{u}}{\partial x \partial z} + \frac{\partial^2 \tilde{v}}{\partial y \partial z}\right) \\
& + \frac{\partial^2 \tilde{w}}{\partial y^2} + l_2\frac{\partial^2 \tilde{w}}{\partial z^2} + \frac{1}{\mu}\frac{d\mu}{dT}\frac{dT}{dy}\left(\frac{\partial \tilde{v}}{\partial z} + \frac{\partial \tilde{u}}{\partial y}\right) \\
& + \frac{1}{\mu}\frac{d\mu}{dT}\left(\frac{\partial^2 W}{\partial y^2}\tilde{T} + \frac{dW}{dy}\frac{\partial \tilde{T}}{\partial y}\right) + \frac{1}{\mu}\frac{d^2\mu}{dT^2}\frac{dT}{dy}\frac{dW}{dy}\tilde{T}\Bigg]
\end{aligned}
\tag{54}
$$

$$
\begin{aligned}
& \frac{\gamma M^2}{T}\frac{\partial \tilde{p}}{\partial t} - \frac{1}{T^2}\frac{\partial \tilde{T}}{\partial t} + \frac{1}{T}\frac{\partial \tilde{u}}{\partial x} + U\left(\frac{\gamma M^2}{T}\frac{\partial \tilde{p}}{\partial x} - \frac{1}{T^2}\frac{\partial \tilde{T}}{\partial x}\right) \\
& \qquad + \frac{1}{T}\frac{\partial \tilde{u}}{\partial y} - \frac{1}{T^2}\frac{\partial \tilde{T}}{\partial y}\tilde{v} + \frac{1}{T}\frac{\partial \tilde{w}}{\partial z} + W\left(\frac{\gamma M^2}{T}\frac{\partial \tilde{p}}{\partial z} - \frac{1}{T^2}\frac{\partial \tilde{T}}{\partial z}\right) = 0
\end{aligned}
\tag{55}
$$

$$\begin{aligned}\left(\frac{\partial \tilde{T}}{\partial t}+U\frac{\partial \tilde{T}}{\partial x}+\tilde{v}\frac{\partial \tilde{T}}{\partial y}+W\frac{\partial \tilde{T}}{\partial z}\right)/T &= (\gamma-1)M^2\left[\frac{\partial \tilde{p}}{\partial t}+U\frac{\partial \tilde{p}}{\partial x}+W\frac{\partial \tilde{p}}{\partial z}\right]\\ &+\frac{\mu}{R\sigma}\left[\frac{\partial^2 \tilde{T}}{\partial x^2}+\frac{\partial^2 \tilde{T}}{\partial y^2}+\frac{\partial^2 \tilde{T}}{\partial z^2}+\frac{2}{k}\frac{dk}{dT}\frac{dT}{dy}\frac{\partial \tilde{T}}{\partial y}\ldots\right.\\ &\left.\ldots+\left(\frac{1}{k}\frac{dk}{dt}\frac{d^2T}{dy^2}+\frac{1}{k}\frac{d^2k}{dT}\left(\frac{dT}{dy}\right)^2\right)\tilde{T}\right]\\ &+(\gamma-1)M^2\frac{\mu}{R}\left[2\frac{dU}{dy}\left(\frac{\partial \tilde{u}}{\partial y}+\frac{\partial \tilde{v}}{\partial x}\right)\ldots\right.\\ &\left.\ldots+2\frac{dW}{dy}\left(\frac{\partial \tilde{w}}{\partial y}+\frac{\partial \tilde{v}}{\partial z}\right)+\frac{1}{\mu}\frac{d\mu}{dT}\left(\left(\frac{dU}{dy}\right)^2+\left(\frac{dW}{dy}\right)^2\right)\right]\end{aligned} \qquad (56)$$

Where $l_j = j-\lambda/\mu$, and the bar sign above the steady base flow variables are dropped for convenience.

The x, y and z coordinates in the linear stability equations are renamed s, y_n and z_a in the current study, in an effort to prevent confusion with the Cartesian coordinates used in the governing equations of the numerical simulation. Finally, the normal modes of the linearized stability equations have the form:

$$\tilde{q}=\hat{q}(y_n)e^{i(-\omega t+\alpha s+\beta z_a)} \qquad (57)$$

where $\tilde{q}$ is the dimensionless disturbances of an arbitrary flow variable normalized by its corresponding freestream quantity. $\hat{q}$ is the eigenfunction of the normal mode. In spatial stability theory, the circular frequency ω is a real number. However, the streamwise wave number, also the eigenvalue, α, has a real part α_r and an imaginary part α_i. More specifically, α_r is the spatial real wave number, and $-\alpha_i$ is the spatial growth rate of each specific normal mode. In the current study of the axisymmetric flow around cones, two-dimensional disturbances are considered. Therefore, the azimuthal wave number, β, is zero in the current study.

By substituting the normal mode expression back into the linearized stability equations, the system of equations is turned into a matrix form of an eigenvalue problem:

$$\left(AD^2 + BD + C\right)\vec{\phi} = 0 \tag{58}$$

where the eigenvector is

$$\vec{\phi} = \left[\hat{u}, \hat{v}, \hat{p}, \hat{T}, \hat{w}\right]^T \tag{59}$$

and the derivative $D \equiv d/dy$. The matrices A, B and C contain the eigenvalue α. The details of these matrices are revealed in Malik [44]. Malik [44] derived the multi-domain spectral collocation method to solve for the eigenvalues and corresponding eigenfunctions of linearized stability equations. The current LST code implements this method. The boundary conditions for Eq. (58) are:

$$\begin{cases} y = 0: & \phi_{1,2,4,5} = 0 \\ y \to \infty: & \phi_{1,2,4,5} \to 0 \end{cases} \tag{60}$$

where the velocity and temperature perturbations vanish at the isothermal wall and outside the boundary layer.

In the LST analyses, special dimensionless quantities are used in order to generalize the results obtained under various flow parameters. The relations between these dimensional quantities and dimensionless quantities are shown as follows. The local Reynolds number based on the length scale of the boundary-layer thickness is:

$$R = \frac{\rho_\infty^* u_\infty^* L^*}{\mu_\infty^*} \tag{61}$$

where the length scale of the boundary-layer thickness is:

$$L^* = \sqrt{\frac{\mu_\infty^* s^*}{\rho_\infty^* u_\infty^*}} \tag{62}$$

Thus, the relations between the freestream unit Reynolds number and R is:

$$R = \sqrt{s^* \left(\mathrm{Re}_\infty^*\right)} \tag{63}$$

The disturbance frequency is characterized by the dimensionless frequency:

$$F = \frac{\omega^* \mu_\infty^*}{\rho_\infty^* u_\infty^{*\,2}} \tag{64}$$

The dimensionless circular frequency and the dimensionless complex wave number are defined as:

$$\omega = \frac{\omega^* L^*}{u_\infty^*} \tag{65}$$

$$\alpha = \alpha^* L^* \tag{66}$$

The relation between dimensionless circular frequency and dimensionless frequency becomes:

$$\omega = RF \tag{67}$$

The dimensionless phase speed of the disturbances in the streamwise direction is related to the wave number by:

$$a = \frac{\omega}{\alpha_r} \tag{68}$$

The dimensionless phase speed is normalized by the freestream velocity.

For unstable waves, the growth of amplitudes can be measured by an N-factor. An N-factor is the exponential power index of the amplification rate A/A_0, which is the ratio of an amplified disturbance amplitude to its initial unamplified disturbance amplitude, namely:

$$e^N = \frac{A}{A_0} = \exp\int_{s_0^*}^{s^*} \frac{1}{A}\frac{dA}{ds} ds^* \tag{69}$$

Hence, an N-factor is the integration of the spatial growth rate from the neutrally stable location s_0^* to an arbitrary location s^*:

$$N = \int_{s_0^*}^{s^*} -\alpha_i^* ds^* \tag{70}$$

From Eq. (70), an N-factor represents the accumulative relative change from the neutrally stable location to an arbitrary location downstream. In the e^N method for transition prediction, the location of laminar-turbulent transition is empirically related to a critical value of the N-factor. In a low-noise wind tunnel, the typical critical N-factor for sharp cones is 8 to 11 [23]. Thus, transition is expected to occur at any downstream location where the N-factors are larger than or equal to that of the critical range.

For the flow over the compression cone, LST analysis is performed and the current results are compared with those by Wheaton *et al.* [23] for validation of both the steady base flow and the LST code. They performed LST and PSE analyses on their steady base flow over the same cone [23]. Five frequencies were used in their LST analysis: 257.498 kHz, 271.797 kHz, 278.996 kHz, 292.494 kHz, and 297.494 kHz. Nearly the same set of five frequencies is used in the current LST calculations. Comparisons of our LST results on the N-factors and growth rates of the second mode with Wheaton *et al.* [23]'s LST N-factors and PSE growth rates are shown in Figure 23 and Figure 24, respectively. The current LST calculation shows that the N-factor reaches 13 and the growth rate reaches 58 m^{-1} at $x^* = 0.42\,\text{m}$. Thus, from the earliest neutral location in the plot, $x^* = 0.113\text{ m}$, to the end of the computation domain, $x^* = 0.42\text{ m}$, the overall gradient of N-factor is $42.3\,\text{m}^{-1}$. Both figures show that the results agree well with the highest four frequencies, while the differences are larger for the lowest frequency. Additionally, both instability onset locations agree well. The magnitudes of the current N-factors and growth rates appear lower than those of Wheaton *et al.* [23]. This could possibly be due to a difference in the numerical method that is used to compute the steady base flow. Furthermore, the LST and PSE codes used by Wheaton *et al.* [23] are different than those used in this study; the streamwise curvature effect is not considered in the current LST model. Since detailed LST and PSE models are not provided in their paper, the authors are unable to investigate further.

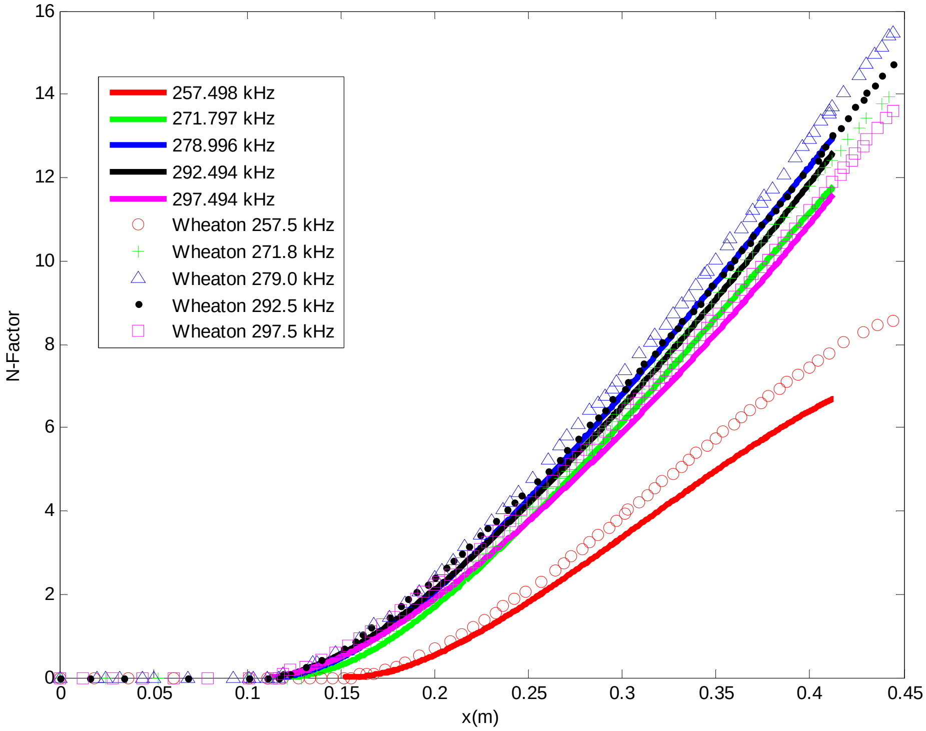

Figure 23. Comparison of the second mode N-factors from the current LST analysis with those of Wheaton *et al.* [23]

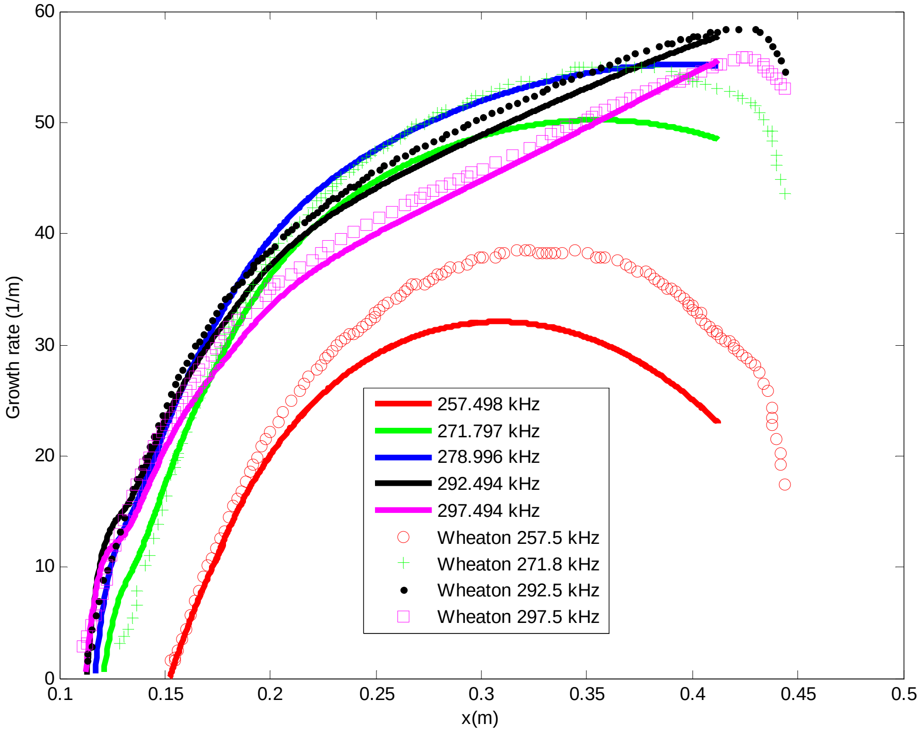

Figure 24. Comparison of the second mode growth rates from the current LST analysis with those of Wheaton *et al.* [23]

A neutral stability curve is used to demonstrate the stability topography in a flow field. A neutral stability curve is generated by collecting the Branch-I neutral locations of many sampling frequency components. To be more specific, since the neutral locations are different between frequencies, one needs to run spatial LST for each sampling frequency, then record the first neutral location encountered in each run. A large amount of sampling frequency is necessary to enhance the smoothness of the neutral stability curve, thus ensuring the accuracy of interpolation between the adjacent sampling frequencies in future use.

The neutral stability curve of the standard case is shown in Figure 25, in order to demonstrate the general linear stability properties of this flow. The critical location is $s^* = 0.109\text{ m}$ at a frequency of 298 kHz. The second mode instability, which is the dominant instability in the current boundary-layer waves, only appears at the locations of $s^* > 0.109\text{ m}$. The wave components of lower frequencies ($F^* < 298\text{ kHz}$) become unstable much earlier than those of higher frequencies ($F^* > 298\text{ kHz}$). This observation implies that second mode instability tends to occur at lower frequencies. In other words, the higher frequency components are more stable. The median of the second mode frequency range at $s^* = 0.154\text{ m}$ is 287 kHz. Thus, the median frequency shifting rate from the critical point to $s^* = 0.156\text{ m}$ is -244 kHz/m.

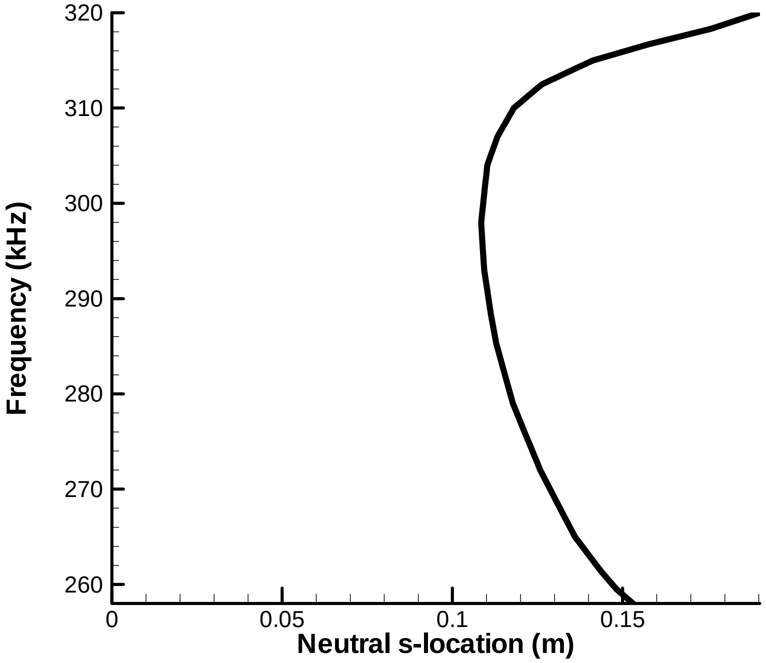

Figure 25. Dimensional neutral stability curve of the second mode.

The dimensional variables, such as the frequency and the location in Figure 25, can reveal more practical aspects, when comparing the current results with experimental results. However, when studying the theoretical aspects of the boundary-layer receptivity and stability, expressing the quantities in self-similarity is beneficial in order to extract relevant information between cases of various parameters. The dimensional flow quantities are normalized by the freestream variables according to the formulations discussed in the earlier part of this section. To be more specific, the dimensional frequency is normalized by freestream density, velocity, and viscosity. The streamwise coordinate can be expressed in terms of a local Reynolds number that is based on the boundary-layer thickness length scale.

Figure 26 shows the neutral stability curve in self-similar variables. Because of the square root over the s^* in Eq. (63), the shape differs from the one in dimensional variables; however, it does reveal the similar trend as the dimensional one. The critical Reynolds number is 1060 and the corresponding dimensionless frequency is 2.08×10^{-4}. The median of the second mode frequency range at $R=1260$ is 2.01×10^{-4}. Thus, the dimensionless median frequency shifting rate from the critical point to $R=1260$ is -3.5×10^{-8}. When the local Reynolds number is less than 1060, no second mode instability exists. The wave components of lower frequencies ($F<2.08\times10^{-4}$) become unstable much earlier than those of higher frequencies ($F>2.08\times10^{-4}$). Such observation, again, implies that the instability tends to occur at lower frequencies. In the other words, the higher frequency components are more stable.

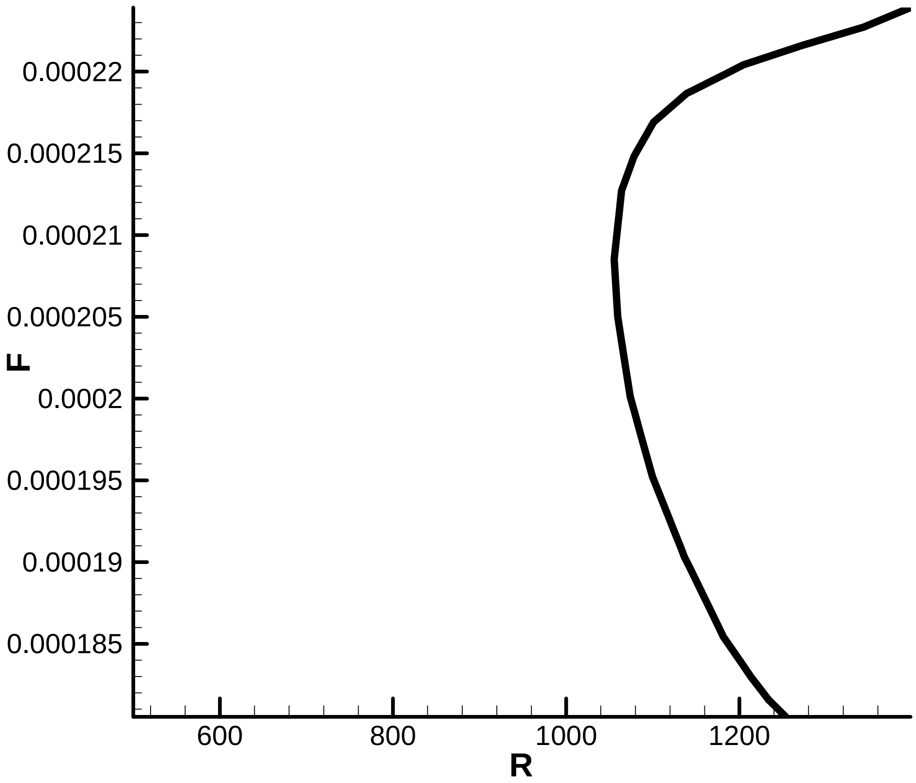

Figure 26. Dimensionless neutral stability curve of the second mode.

In LST, each dimensionless circular frequency, ω, corresponds to a unique eigenvalue for each normal mode in a perfectly self-similar flow field. Figure 27 shows the corresponding dimensionless circular frequencies for the eigenvalues at the neutral location. In a perfectly self-similar flow field, the dimensionless circular frequency that corresponds to the unique Branch-I neutral eigenvalue of mode S, is a constant value, regardless of the frequency and local Reynolds number. However, in the flow field around a blunt cone, self-similarity cannot be maintained due to the geometry of the blunt nose. As a result, the dimensionless circular frequencies at the neutral locations are not constant for all frequency components in Figure 27. However, the variation of dimensionless circular frequencies at the neutral locations is small, ranging from 0.215 to 0.31. This reveals the proximity of self-similarity in the flow field around the neutral locations. The mean of the dimensionless circular frequency at the neutral locations is 0.263.

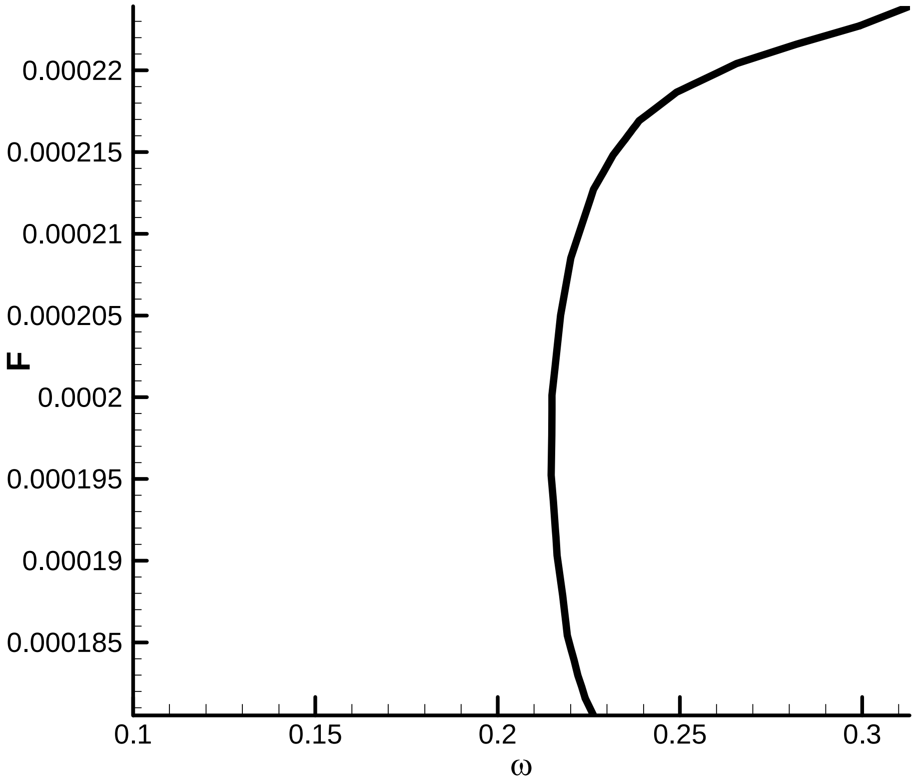

Figure 27. Dimensionless circular frequencies along the neutral stability curve.

Previously discussed were the linear stability properties of the second mode. The overall spatial behaviors of normal modes in the boundary layer, however, have not yet been revealed. Hence, an investigation of mode F and mode S is presented next.

The LST-predicted spatial dimensionless phase speeds of the mode F and mode S along the dimensionless circular frequency over the cone at the sampling frequency of 293 kHz (the most amplified sampling frequency in the second mode frequency range, which is shown later in Section 3.2.5) are calculated from α_r by Eqs. (63), (67) and (68). The plot of the dimensionless phase speeds is shown in Figure 28. The three horizontal lines represent the dimensionless phase speeds of fast acoustic, slow acoustic, and entropy/vorticity waves. These were determined using freestream flow conditions in front of the bow shock. As a result, they only serve as qualitative references to show the existence of three wave modes. The actual phase speeds depend on local non-constant flow conditions.

The upstream fast acoustic waves' synchronized mode F has a phase speed that decreases from a phase speed of 1.09 upstream, to a phase speed of 0.88 downstream. There is a break in the phase speeds of mode F from $\omega = 0.18$ to 0.205. This is due to the synchronization between mode F and the entropy/vorticity waves. More specifically, the eigenvalue of the discrete mode F merges into the entropy/vorticity spectrum and reappears while moving downstream. As a result, the trace of the eigenvalue of mode F is interrupted by the entropy/vorticity spectrum. Since the actual phase speed of entropy/vorticity waves depends on local flow conditions, the break appears below the freestream phase speed of entropy/vorticity waves.

The upstream slow acoustic waves' synchronized mode S has a phase speed that changes from a phase speed of the slow acoustic waves upstream, to a phase speed of around 0.89 downstream. The mode S synchronizes with the mode F at $\omega = 0.26$. Behind the synchronization point, the flaring of the cone causes the proximity between the phase speeds of mode F and mode S.

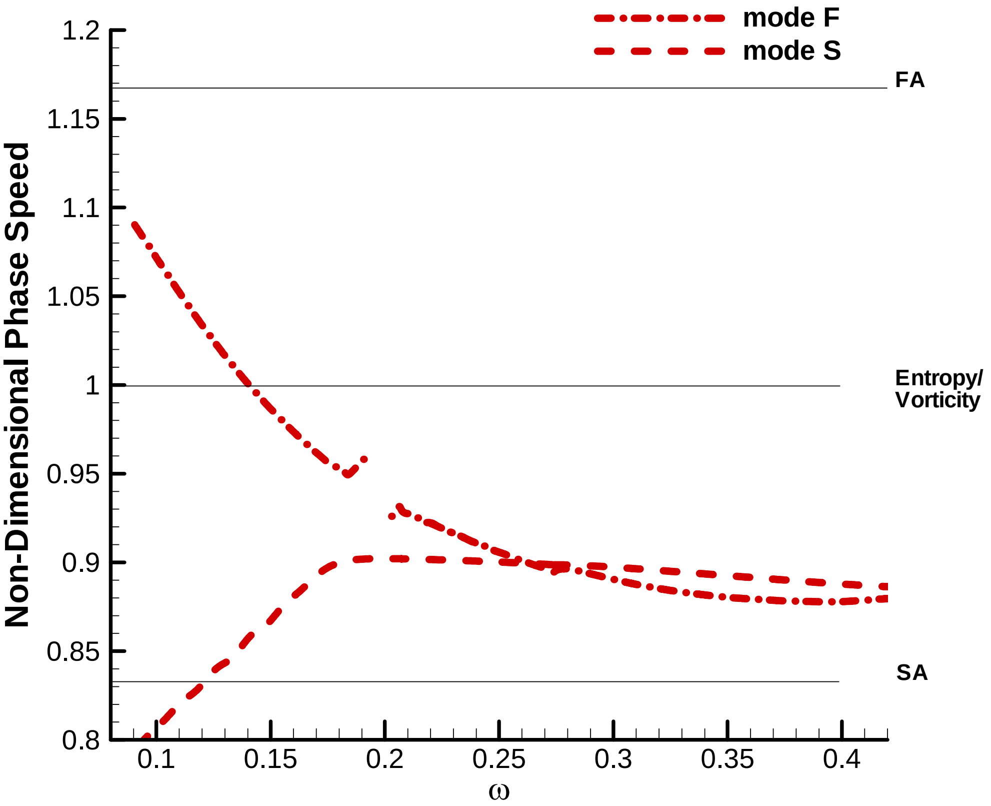

Figure 28. Streamwise phase speeds of mode F and mode S at the frequency of 293 kHz along the dimensionless circular frequency.

In addition to the streamwise phase speeds, the streamwise dimensional growth rates are also calculated from α_i by Eqs. (62) and (66). The streamwise dimensional growth rates along the dimensionless circular frequency at 293 kHz are shown in Figure 29. Mode S is stable before the Branch-I neutral point at $\omega = 0.215$ and only becomes unstable behind this dimensionless circular frequency. Mode F is stable everywhere throughout the cone. These observations indicate that the unstable second mode is related to mode S. Moreover, the unstable second mode begins shortly upstream from the synchronization of mode F and mode S at $\omega = 0.26$. Within the break due to the synchronization of mode F and the entropy/vorticity waves, the growth rate of mode F has a drop, or rather a jump in α_i, which indicates stabilizing effects on mode F due to the synchronization between mode F and entropy/vorticity waves. This jump in α_i is also found in Fedorov *et al.* [78, 80].

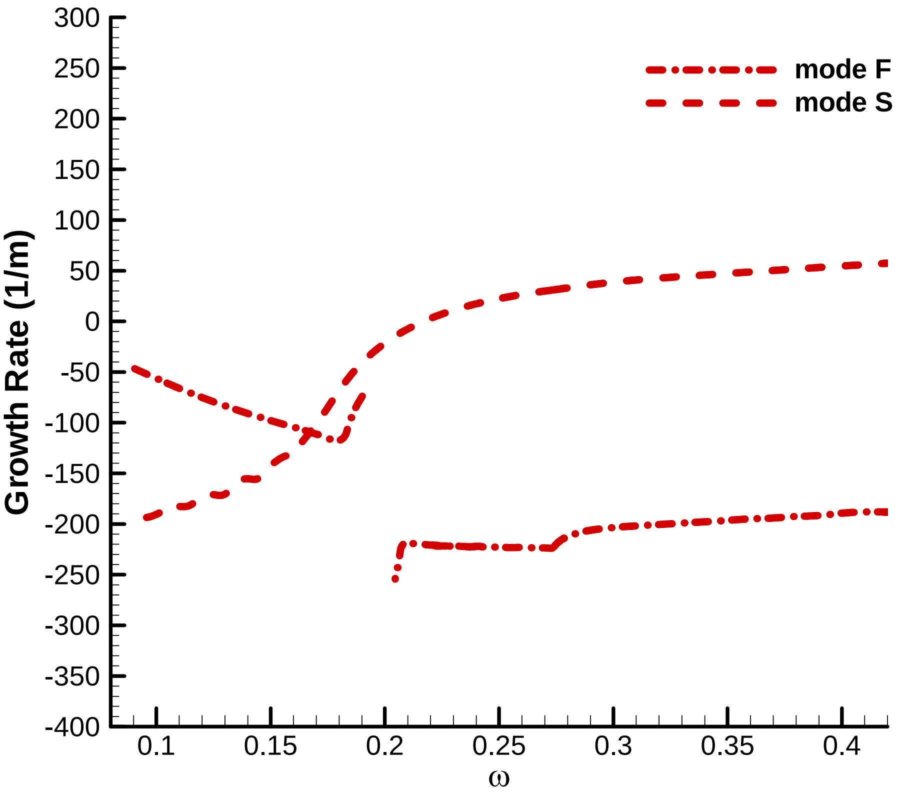

Figure 29. Streamwise growth rates of mode F and mode S at the frequency of 293 kHz along the dimensionless circular frequency.

3.2.3 Structures of Unsteady Hotspot Perturbed Flow

In this study we consider the axisymmetric flow field with an axisymmetric freestream hotspot that is initially aligned with the centerline of the cone. The freestream hotspot has a radius of approximately $0.003\ \mathrm{m}$. The radial Gaussian temperature profile of the hotspot in the freestream is shown in Figure 30. At the center of the hotspot, the temperature is maximal; the radial coordinate is zero. The hotspot is initially placed at a location not far upstream from the bow shock, along the cone's centerline. The hotspot core radius is controlled by a dimensionless Gaussian factor, σ. In the current study, the dimensionless Gaussian factor is 0.001. The shape parameters of the freestream hotspot perturbations are based on the laser spot experiments of Salyer *et al.* [96, 97].

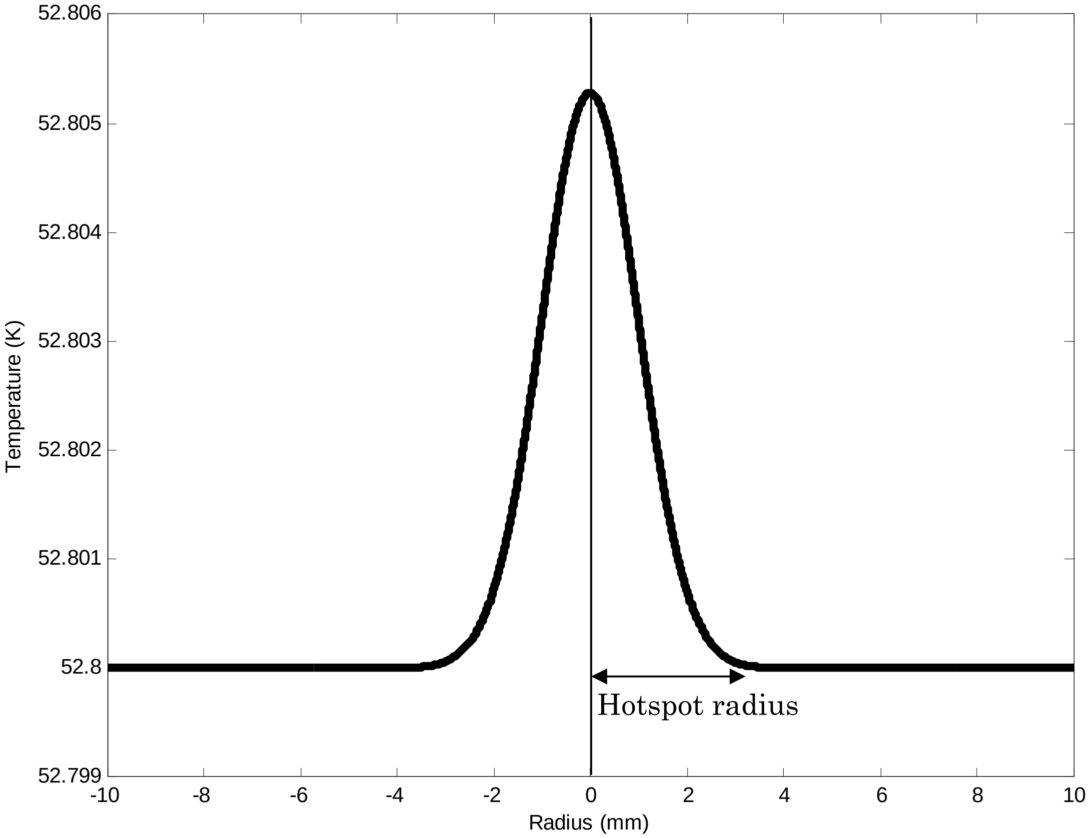

Figure 30. Gaussian distribution of perturbed temperature in radial direction.

The receptivity process in the current study is in the linear regime, thus the hotspot with a very weak amplitude is imposed in the freestream. Previously, Ma *et al.* [4] and Zhong *et al.* [36] chose their freestream relative perturbation amplitudes as $O\left(10^{-4}\right)$ in order to keep the development of boundary-layer disturbances within the linear regime. Therefore, the freestream maximum relative amplitude of temperature perturbations at the center of the hotspot, ε, is chosen to be:

$$\varepsilon = \frac{\Delta T_{\max}}{T_\infty} = 10^{-4} \tag{71}$$

Having obtained a steady base flow solution, the unsteady numerical simulation is performed by imposing hotspot perturbations into the freestream in front of the bow-shock. The Gaussian formulations given by Eqs. (39) through (42) are used to analytically model a three-dimensional hotspot that convects with the freestream. Moreover, the freestream hotspot is imposed onto the computational domain as an unsteady shock boundary condition.

The flow variable perturbations shown in Figure 31 through Figure 36 are normalized by the corresponding freestream flow variables, i.e. P'^{*}/P_{∞}^{*} and S'^{*}/S_{∞}^{*}. The structures of hotspot-induced perturbations in the nose region over the cone are demonstrated in Figure 31 and Figure 32. This is the region where the hotspot first enters the shock layer. The magnitude of pressure perturbations in Figure 31 reaches a local maximum at the stagnation point, while the entropy perturbations in Figure 32 have a maximum absolute magnitude at the stagnation line next to the bow-shock. Additionally, the small length scale of entropy waves next to the wall near the stagnation point is a consequence of the entropy waves moving at the local flow velocity without reflection at the wall. In contrast to entropy waves, acoustic waves propagate and are reflected at the wall towards the bow shock. As a result, Figure 31 shows the pressure perturbations that do not have the small length scale wave next to the wall near the stagnation point. The hotspot enters the shock layer from the freestream and its induced perturbations travel downstream with the flow. Eventually they pass through the furthest right exit boundary of the nose region and move into the next computation zone.

As the hotspot induced perturbations travel further into the middle region of the cone, the size of hotspot induced perturbations is much wider and longer as compared to the hotspot induced perturbations in the upstream region. The structures of hotspot induced perturbations in the middle region over the cone are demonstrated in Figure 33 and Figure 34. Since the size of a single computation zone is not large enough to demonstrate the entire hotspot induced perturbations in a single snapshot, several snapshots are used to demonstrate the parts of the perturbations that pass by a zone. The main body of the pressure perturbations has two parts: the front part and the rear part. The front part contains fast acoustic waves that travel first in the hotspot main body. The rear part, containing slow acoustic waves, travels behind the front part in the main body. The entropy perturbations are also shown in two parts: the main body and the first tail (another tail, namely the second tail, appears behind the first tail in the downstream region). The first tail travels behind the main body and is oscillatory.

While the hotspot induced perturbations arrive in the downstream region of the cone, unstable waves appear in the tail and travel slower than the main body of the hotspot. The flow structures of hotspot induced perturbations in the downstream region over the cone are demonstrated in Figure 35 and Figure 36. The pressure perturbations are shown in three sections in Figure 35. In this region, an oscillatory tail appears behind the main body of pressure perturbations. The main body, which consists of a front and rear part, becomes subdominant in wave amplitudes while the perturbations in the tail exceed those of the main body in this region.

Entropy perturbations are shown in Figure 36. The first tail in entropy perturbations is oscillatory. The entropy perturbations in the main body of the hotspot are weaker than those in the middle region. The second tail, which is stronger than the first, appears behind the first tail. The waves in the second tail have the highest amplitude among the entire wave packet. Moreover, the second tail of the entropy perturbations are “rope” structured waves located at the edge of the boundary layer. The wavelength of these rope waves is approximately twice of the boundary-layer thickness. These are typical features of second mode dominated waves. [39]

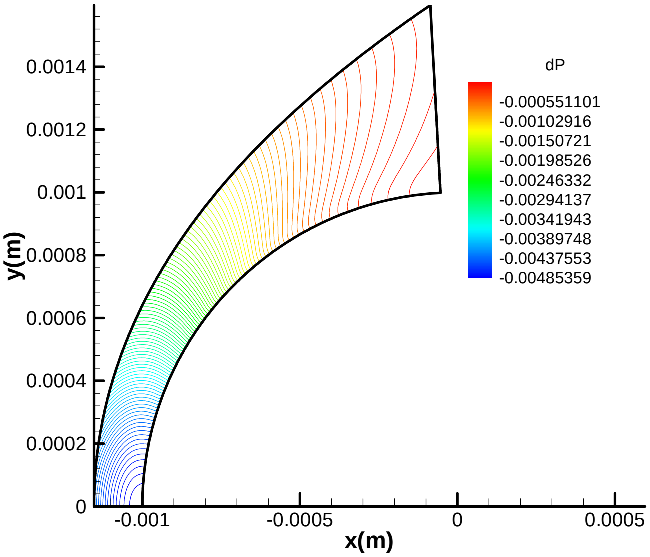

Figure 31. Contours of hotspot pressure perturbations behind the shock in nose region over the compression cone.

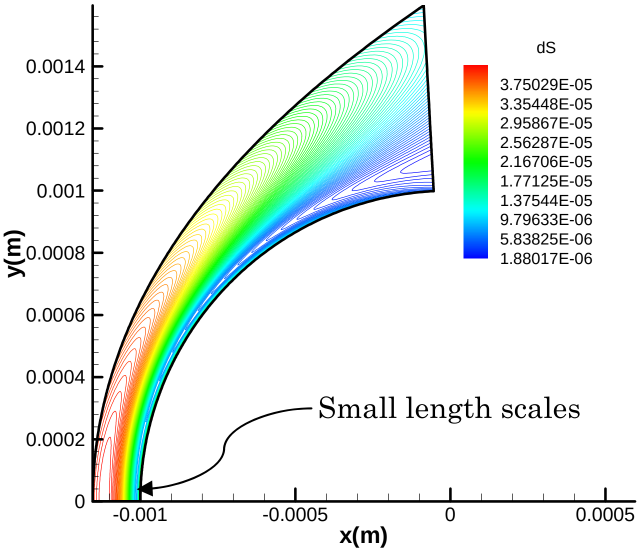

Figure 32. Contours of hotspot entropy perturbations behind the shock in nose region over the compression cone.

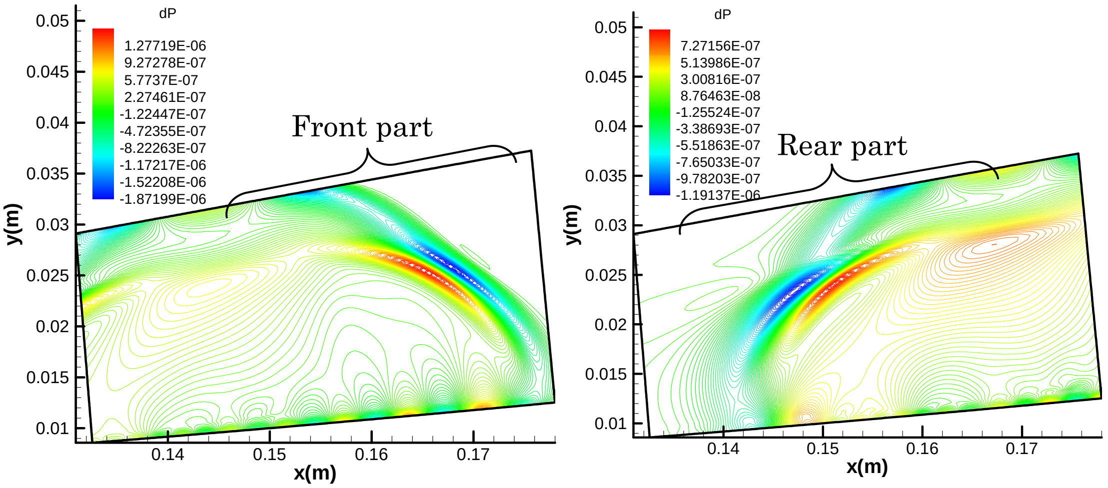

(a) (b)

Figure 33. Contours of hotspot pressure perturbations in middle region over the compression cone: (a) the front part, and (b) the rear part.

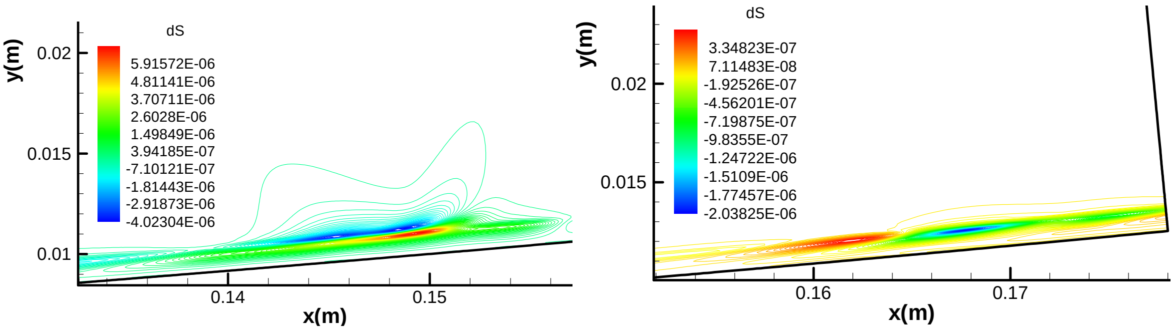

(a) (b)

Figure 34. Contours of hotspot entropy perturbations in middle region over the compression cone: (a) the main body, and (b) the first tail.

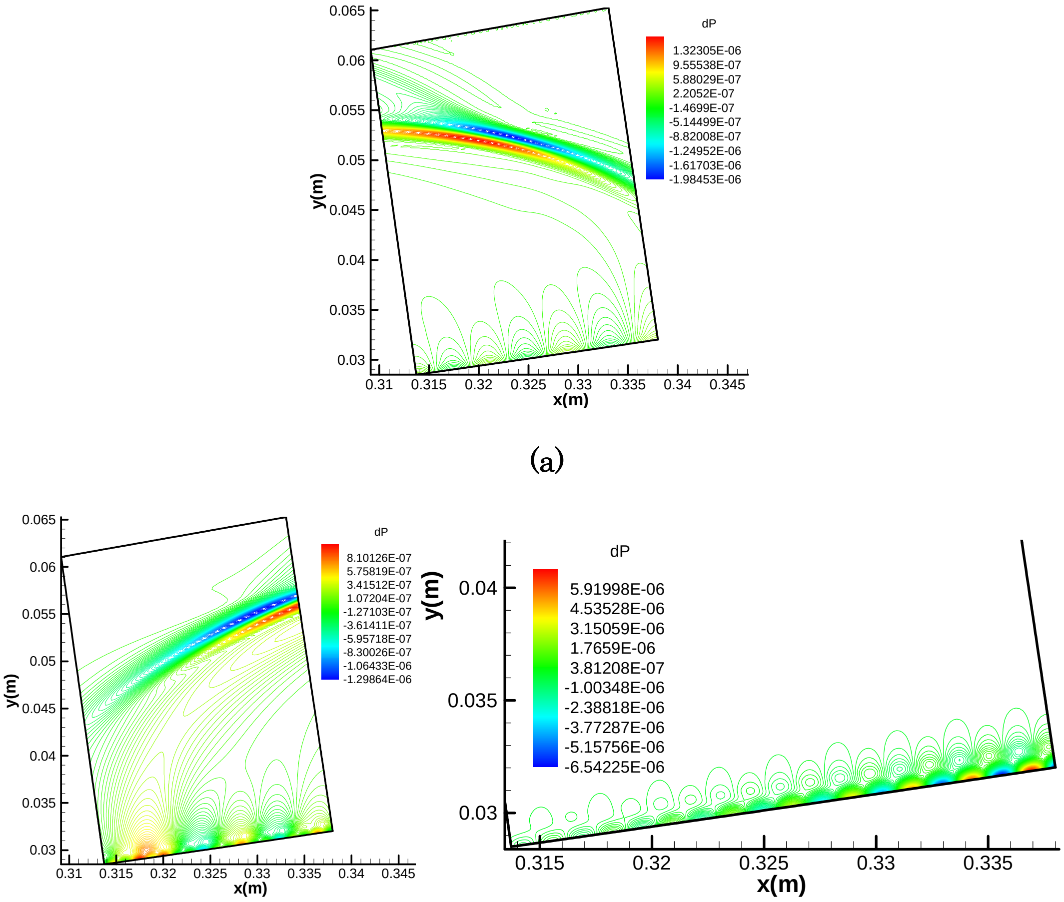

(a)

(b)

(c)

Figure 35. Contours of hotspot pressure perturbations in downstream region over the compression cone: (a) the front part, (b) the rear part, and (c) the tail.

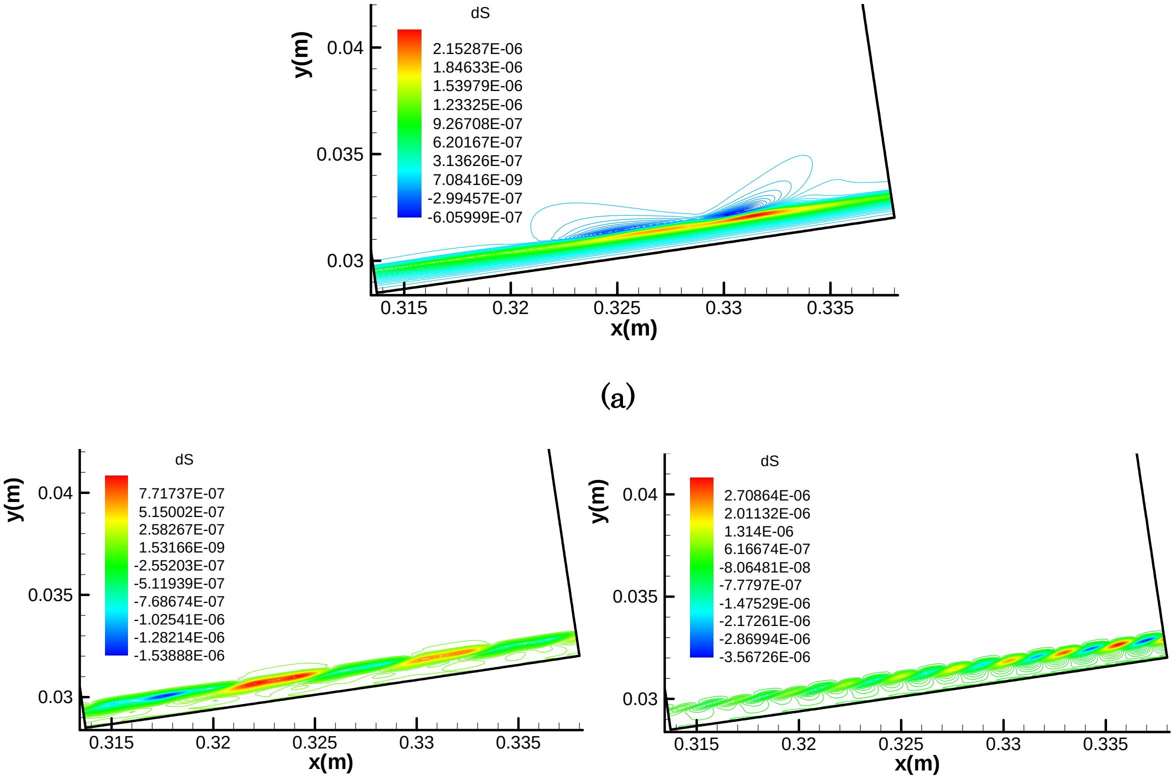

(a)

(b) (c)

Figure 36. Contours of hotspot entropy perturbations in downstream region over the compression cone: (a) the main body, (b) the first tail, and (c) the second tail.

3.2.4 Analysis of Boundary-Layer Disturbances and Computation of Receptivity Coefficients

The numerical solution for the time history of wall-pressure perturbations is recorded at various spatial locations along the cone surface. Figure 37 and Figure 38 show the time-history traces of wall-pressure perturbations, where the pressure perturbations are normalized with respect to freestream pressure.

Figure 37 shows wall-pressure perturbations traveling through the upstream part of the cone. In this upstream part of the cone, the perturbation time-history profiles start with a relatively monotonic shape. They gradually decay while traveling downstream and split into a multi-peak shape. In the range from $x^* = 0.0337$ m to 0.0925 m, the profile has a frequency of around 160 kHz, which falls within the frequency range of the possible stable mode F (120 kHz to 240 kHz) in Figure 42. The perturbations are indeed likely to be stable mode F predominant. However, there are initial transients and other wave modes that also exist in the perturbations.

Figure 38 shows wall-pressure perturbations in the downstream part of the cone. In this region, multi-peak shaped perturbations begin to split into two parts in time: one that is more oscillatory, followed by another with a smoother profile. These waves are associated with the main body (both front part and rear parts) of the pressure perturbations in Figure 33 and Figure 35. The more oscillatory part has a frequency of about 160 kHz. The waves are indeed likely to be stable mode F predominant. As the hotspot induced perturbations travel further downstream, the perturbation amplitudes decay. Starting at $x^* = 0.25$ m, or 56% of the total cone length, a new perturbation waveform appears. In the subsequent locations, the amplitudes of this new waveform grow rapidly. The amplitudes of this new waveform soon surpass those of the original decaying ones and become the dominant instability in the boundary layer. This new waveform is most likely related to the second mode. At the same locations of the wave growth, a less dominant growing waveform also appears before the most dominant waveform. These two new wave structures can clearly be seen in the profile at $x^* = 0.333$ m in Figure 38. More specifically, the most dominant one is centered around $t^* = 0.54$ ms, while the less dominant one is located around $t^* = 0.49$ ms. The frequency of the most dominant growing waves is found to be around 291 kHz, while that of the less dominant growing waves is 285 kHz. Both waves fall in the frequency range of the second mode. The furthest computed location in the current numerical simulation is $x^* = 0.394\ \mathrm{m}$. The maximum relative magnitude of the second mode dominated pressure waves to the local steady base flow pressure reaches $O\left(10^{-5}\right)$ at this surface location [54].

For the purpose of quantifying the growth of the overall amplitude of the wave packet, the earlier introduced concept of spatial growth rate is also useful in this time-history analysis. The average growth rate of the overall wave packet is introduced by modifying Eq. (44). Specifically, the $\left|H\left(F_n\right)\right|$ in the equation is replaced with the maximum pressure wave packet amplitudes, $\left|p^*_{\max}{}'/p^*_\infty\right|$, and the s-coordinates is replaced with the x-coordinates. The derivative is approximated by dividing the difference between the initial and the final maximum wave packet amplitude, by the difference in the initial and the final x-coordinate. The final equation is thus modified to be:

$$\text{average growth rate} = \frac{1}{\left|p^*_{\max}{}'/p^*_\infty\right|_0} \frac{\left|p^*_{\max}{}'/p^*_\infty\right|_1 - \left|p^*_{\max}{}'/p^*_\infty\right|_0}{\Delta x^*} \qquad (72)$$

The subscripts “0” and “1” next to the amplitudes represent the initial location and the final location, respectively. By obtaining the maximum amplitudes at two selected locations, for instance, $x^* = 0.0135\ \mathrm{m}$ to $0.21\ \mathrm{m}$, one can obtain the calculated average growth rate of the overall stable wave packet from $x^* = 0.0135\ \mathrm{m}$ to $0.21\ \mathrm{m}$ as $-4.83\ \mathrm{m}^{-1}$. Similarly, the average growth rate of the overall second mode dominant wave packet from $x^* = 0.313\ \mathrm{m}$ to $0.333\ \mathrm{m}$ is $106\ \mathrm{m}^{-1}$. This average growth rate provides a quantified parameter that can measure the growth or decay in the above type of overall wave packet evolution study. This average growth rate is particularly useful in the comparisons between cases in the parametric study presented in the latter part of this work.

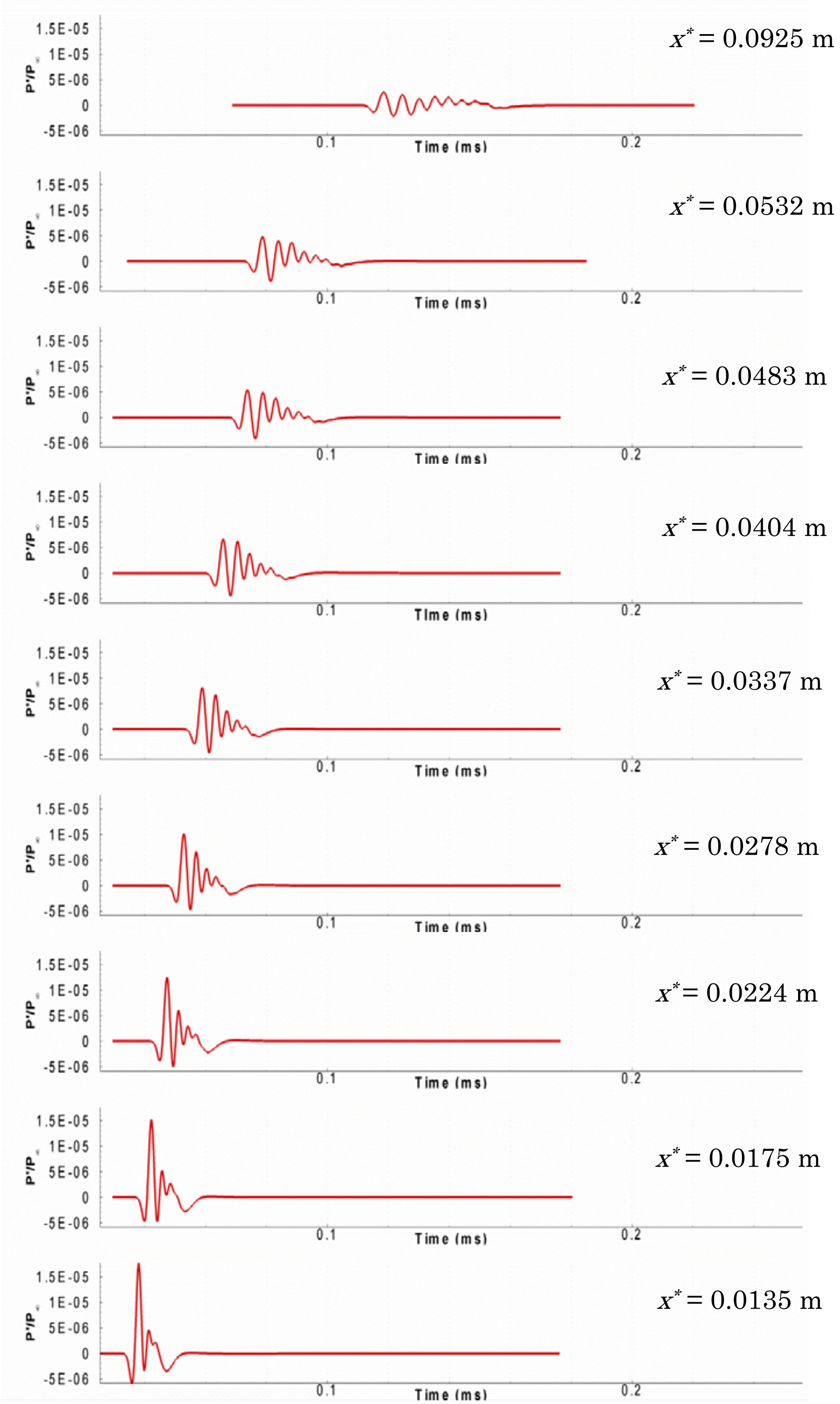

Figure 37. Time-history traces of wall-pressure perturbations at various streamwise locations in upstream part of the cone.

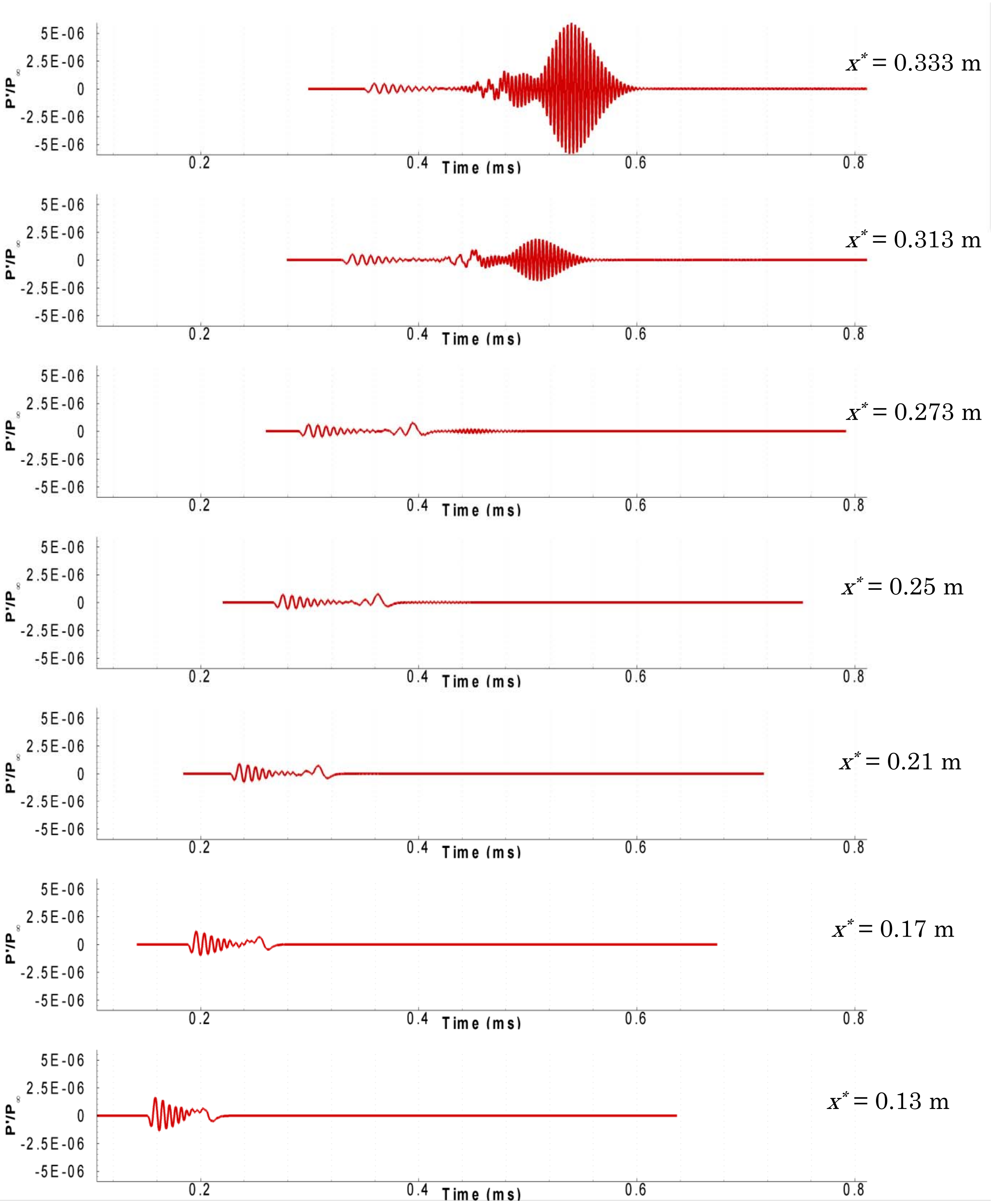

Figure 38. Time-history traces of wall-pressure perturbations at various streamwise locations in downstream part of the cone.

In order to investigate the mechanism of boundary-layer instability induced by the hotspot, Fourier transformation based on the time history of wall-pressure perturbations is carried out at various surface locations. The details are shown in Section 2.5. The simulated perturbations are single impulse, which are temporally "transient", i.e. they do not continue to repeat in time at a given location. The transient perturbed flow at a location eventually returns back to its steady base flow after the passage of the perturbations. When conducting the Fourier transformation, the time history of a single impulse is windowed with no more perturbations existing on either side. More specifically, the Fourier transformed amplitudes in the current study are independent of the width of the time-window, as long as the relative amplitudes of the pressure perturbations at both end are $O(10^{-9})$. In this way, a periodicity of the signal is assumed in the time domain. The maximum recording time-step size of the time-histories is 1.12×10^{-7} s, which is sufficient to resolve the second mode instability at the high end of the studied frequency range. When post-processing the data from the simulation using the current windowed-Fourier transformation, our Fourier-transformed results are confirmed to be independent from the time-step size used. We have validated the current windowed-Fourier transformation by comparing two cases of an unsteady hypersonic flow over a flat plate with a pulse and a single frequency wave, respectively. Using the traditional Fourier transformation for periodic waves, we addressed the case of a single frequency wave. The results show that the transformed amplitudes of both cases agree well, therefore, the current windowed-Fourier transformation of a finite width pulse can adequately represent a wide spectrum of frequency.

Having a sufficient spatial resolution can minimize numerical error, which will eventually be amplified downstream and significantly affect the accuracy of the simulated results. To ensure the sufficiency of the spatial resolution, a grid convergence study is conducted by comparing the current results with results from a finer grid. For a wall-bounded flow, the boundary layer contains large gradients of flow variables and should be well resolved in order to attain accurate results. Therefore, a grid refinement study is performed only in the wall-normal direction. The essential part of this study concerns the results of an unsteady flow simulation with transient perturbations. Hence, in the grid convergence study, the frequency spectra of the pressure perturbations at the wall and the growth rates at a downstream location of $s^* = 0.4\ \mathrm{m}$ with two sets of grids are compared; the current grid has 240 points and the finer grid has 480 points in the wall-normal direction. The comparison of frequency spectra of the pressure perturbations at the wall is shown in Figure 39 (a). Within the frequency range of the second mode between 260 kHz to 310 kHz, both spectrum compare very well. The relative error of the normalized amplitude within the frequency range of the second mode is $O(10^{-3})$. The comparison of the growth rates within the frequency range of the second mode between two sets of grid is shown in Figure 39 (b). The comparison is very good around the maxima at 282 kHz. Apart from 282 kHz, the growth rates have more error. The relative error of growth rates within the frequency range of the second mode is $O(10^{-2})$. These growth rates are more sensitive to small error. Hence, the relative error of growth rates appears to be more significant than that of the normalized amplitudes of the pressure perturbations at the wall. Both comparisons imply the high convergence of the current grid.

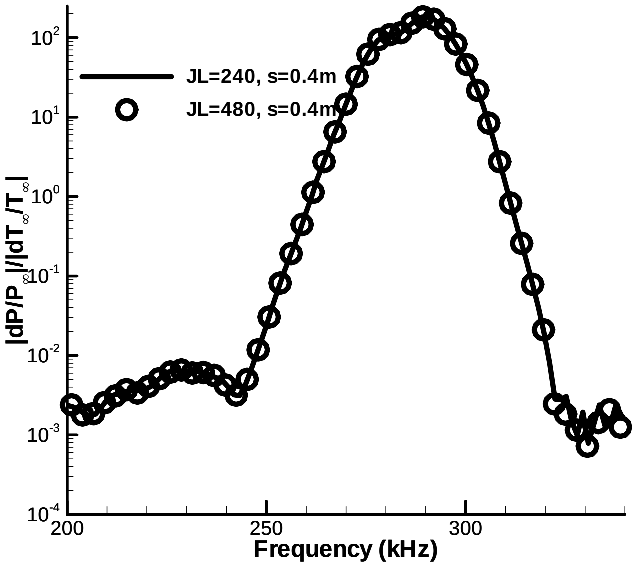

(a)

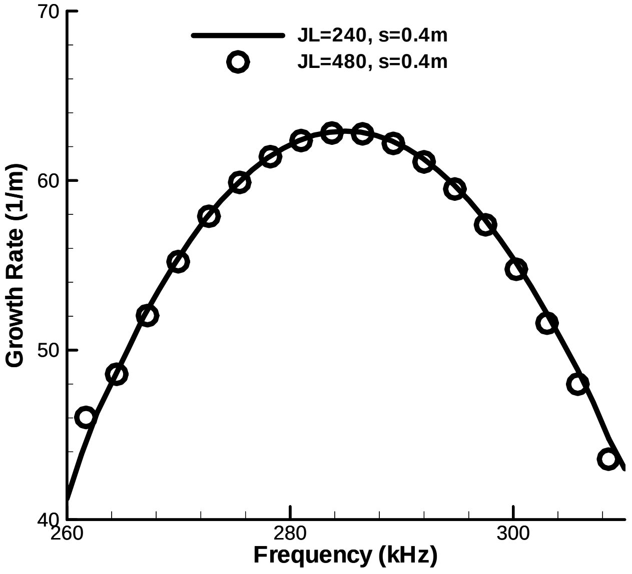

(b)

Figure 39. Comparisons of frequency spectrum of (a) the normalized amplitude, and (b) growth rate of pressure perturbations at the wall between the j-direction resolutions of 240 grids and 480 grids.

The freestream hotspot perturbations used in the current study have a Gaussian temperature profile in time. The frequency spectrum of the freestream hotspot is shown in Figure 40; this spectrum also has a Gaussian distribution. The freestream temperature perturbations have higher amplitudes when the frequency is lower, while the amplitudes decrease with increasing frequency.

It is worth noting that the small magnitudes in Figure 40 are the Fourier transformation (in the unit of 1/Hz) of the initial disturbances in the freestream. In order to obtain a relative wave amplitude in a given frequency range, we need to integrate the magnitudes in that figure along the frequency, which is in the order of 100 kHz. As a result, the relative wave amplitudes in the time domain, within the interested frequency range of up to 420 kHz, are about 10^{-5} to 10^{-6}. We use double precision in the current computations with machine epsilon of approximately 10^{-16}. Both the disturbances in the freestream and behind the shock have small Fourier-transformed amplitudes with frequencies below 420 kHz, but they are not yet close enough to the machine epsilon for a double precision system.

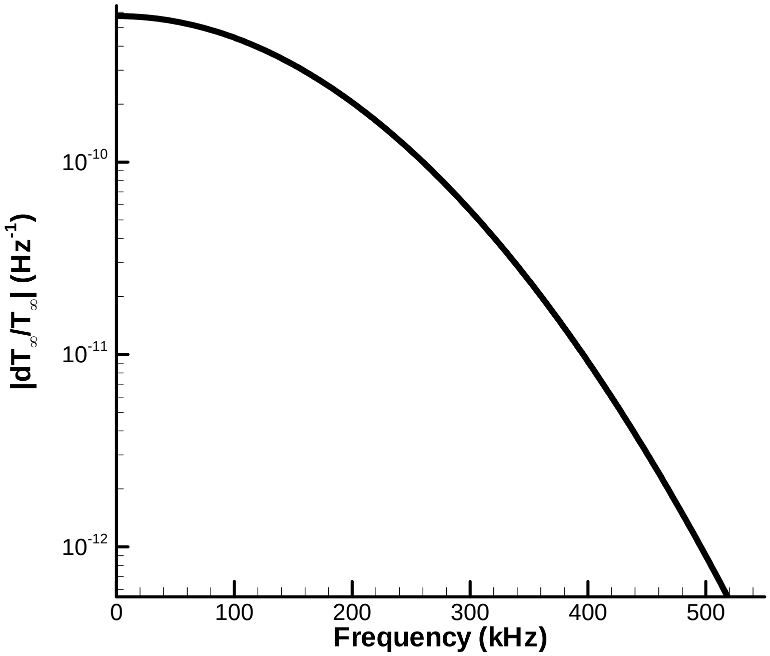

Figure 40. Frequency spectrum of freestream hotspot temperature perturbations.

Figure 40 shows that the amplitudes of the freestream forcing disturbances are not uniform at different frequencies. Hence, in order to include such frequency effects in the analyses of boundary-layer receptivity and instability growth, it is necessary to normalize the amplitudes of the wall-pressure-perturbations with those of the freestream hotspot. As the wall disturbances are pressure disturbances, and the freestream hotspot is temperature perturbations, the normalization is defined as:

$$\text{normalized amplitude} = \frac{\left| dP(f)/P_\infty \right|}{\left| dT_\infty(f)/T_\infty \right|} \tag{73}$$

where the dimensionless amplitude of the boundary-layer pressure disturbances is normalized by that of the freestream temperature perturbations of the same frequency.

This normalized amplitude is a more accurate description of the receptivity strength and instability growth.

The normalized amplitude frequency spectra of the behind-shock acoustic waves and entropy waves in the nose region are shown in Figure 41 (a) and (b). In order to compare the relative strength in the local flow field between the pressure and entropy perturbations, the local perturbation amplitude is divided by the local steady base value immediately behind the shock. Both pressure and entropy waves are the result of the combined interactions of the shock with freestream hotspot perturbations, and the reflected acoustic waves behind the shock. Each line represents the spectrum at a shock location that has a specific angle between the stagnation line in front of the cone nose, and the line that connects the shock location and the origin. Under the current flow conditions, the maximum generated acoustic and entropy waves behind the shock appear on the stagnation line where the angle is 0. These generated waves decay mainly at downstream shock locations in the nose region. The normalized amplitudes of the acoustic wave spectra or pressure perturbations have local maxima at a frequency from 180 to 160 kHz at angles from 0 to 40 degrees. The resonance of the acoustic waves that bounces between the shock and the wall in the nose region cause these maxima. Moreover, the downshift of the resonance frequency downstream is due to the increasing downstream shock-layer thickness in the nose region. The amplitudes of entropy waves mainly increase with an increasing frequency. In Figure 41 (a), the maximum normalized amplitude for the pressure disturbances just behind the shock is 1.08 at the stagnation line, or 0 degrees with a frequency of 180 kHz. Such maximum relative strength of pressure perturbations immediately behind the shock is slightly higher than the relative strength of freestream perturbations. This is due to the resonance interaction around the stagnation line. The overall amplitudes fall in a range from 0.26 to 1.08. The mean value of amplitude in this range is 0.67.

In Figure 41 (b), the maximum strength of the entropy perturbations is 0.116 at 0 degrees with a frequency of 520 kHz. The overall amplitudes fall in a range from 0.01 to 0.116. The mean value of amplitudes in this range is 0.063. By comparing the amplitudes of both perturbations, one can observe that the normalized amplitudes of acoustic waves or pressure perturbations are around an order of magnitude higher than the entropy perturbations. This observation indicates that after the hotspot/shock interaction in the nose region, the perturbations are mainly acoustic waves.

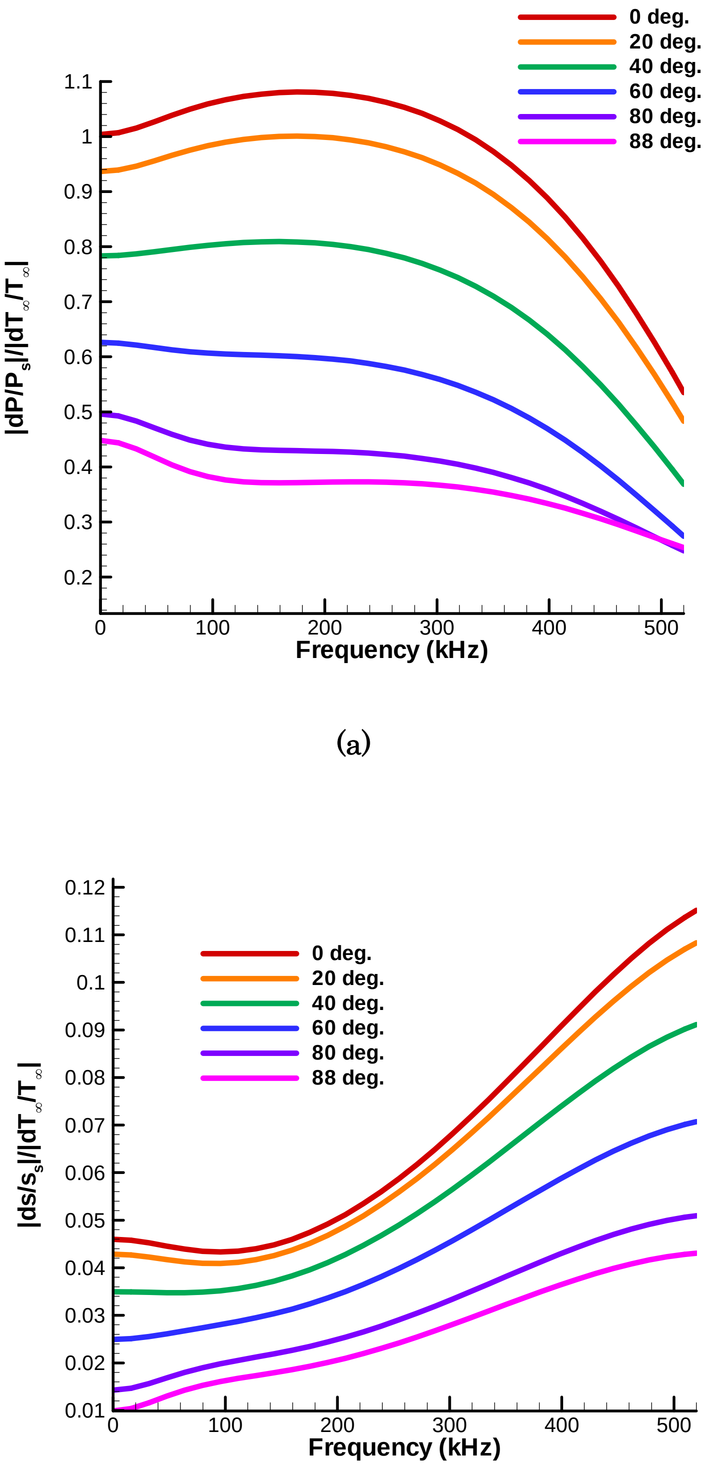

(a)

(b)

Figure 41. Frequency spectrum of normalized amplitudes of (a) pressure perturbations and (b) entropy perturbations immediately behind the shock in the nose region.

Figure 42 shows the normalized frequency spectra in the flared region of the cone. In this figure there is a large peak of spatial growth of amplitudes with a frequency ranging from about 240 kHz to 320 kHz. The mean frequency of this range is 280 kHz, and the width of this range is 80 kHz. This growing peak is the instability dominated by the second mode. The second mode dominated peak grows from the initial maximum normalized amplitude of 5×10^{-3} at $x^* = 0.17\text{ m}$ to 181 at $x^* = 0.394\text{ m}$. Thus, the Eq. (72) defined average growth rate of the second mode dominated growing peak from $x^* = 0.17\text{ m}$ to 0.394 m is $1.616\times10^5\text{ m}^{-1}$. Since the growth of the boundary layer instability modes in linear flow regime is exponential, only having the average growth rate is insufficient to describe the strength of the growing or decaying process. Therefore, we introduce the average logarithm gradient, which uses the average spatial gradient of logarithms of the initial and final amplitudes. Using this average logarithm gradient, one can quantify the strength of the exponential growth and conveniently compare it to the growth of the boundary-layer instabilities between different parametric cases. In the current study, we choose a logarithm based on 10. Hence, the average spatial gradient of the 10-based logarithm of the maximum amplitudes of the second mode dominated growing peak from $x^* = 0.17\text{ m}$ to 0.394 m is 20.4 m^{-1}. The frequency corresponding to the maximum amplitude is about 290 kHz and the frequency shift is insignificant. There is no significant shift expected because the boundary-layer thickness does not change significantly along the cone's compression region. This observation is also discussed in Section 3.2.1. The frequency of the peak from the experiment, which was reported by Wheaton *et al.* [23] under similar flow conditions, is 290 kHz.

In Figure 42, the bump—which is within a frequency range from 120 kHz to 240 kHz—decays spatially from $x^* = 0.13\ \mathrm{m}$ to $0.21\ \mathrm{m}$. The mean frequency of the range is 180 kHz. The boundary layer disturbances within this spatial range have a relatively strong stable mode F that is discussed in the next section of receptivity mechanisms. The maximum normalized amplitude the bump decay from is 0.0942 with a frequency of 168 kHz at $x^* = 0.13\ \mathrm{m}$ to 0.0418 with a frequency of 142 kHz at $x^* = 0.2495\ \mathrm{m}$. Thus, the average growth rate of the bump from $x^* = 0.13\ \mathrm{m}$ to $0.2495\ \mathrm{m}$ is $-4.65\ \mathrm{m}^{-1}$. The average spatial gradient of the 10-based logarithm of the maximum amplitudes is $-2.95\ \mathrm{m}^{-1}$. The oscillations in the spectra are caused by multi-mode wave modulations, which are complex physical processes with a coexistence of many wave modes. Noticeably, no such oscillation appears over peaks that are dominated by Mack modes.

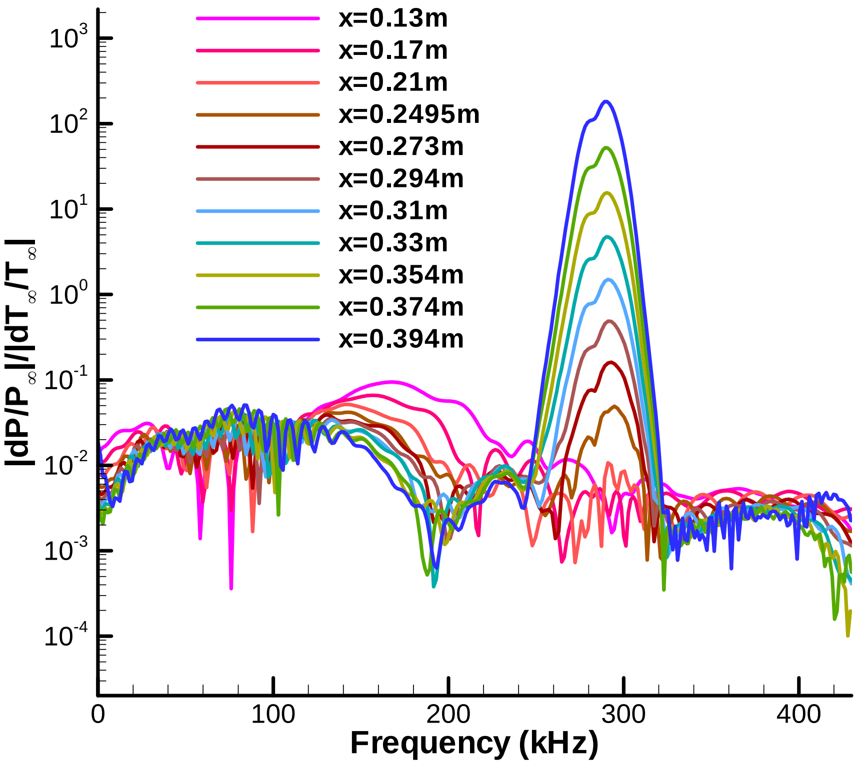

Figure 42. Frequency spectra of the normalized wall-pressure perturbations at various streamwise locations.

Since the boundary-layer disturbances in the current study fall in the linear regime, the normalized amplitudes are independent of the shape function of freestream forcing waves. The dimensionless amplitudes of the local disturbances at the wall can be obtained linearly by multiplying the dimensionless freestream forcing amplitude of a different shape function and the normalized amplitude at each frequency according to Eq. (73).

In recent years, Professor Steven P. Schneider's group at Purdue University has completed several compression cone experiments in their quiet Mach-6 wind tunnel (BAM6QT). Wheaton *et al.* [23] have presented their frequency spectrum of wall-pressure perturbations over a blunt compression cone that is identical to the one used in the current study. Chou [22, 98] completed a laser-spot experiment and presented a spectrum of wall-pressure perturbations over the same cone used in this study. Likewise, the experimental researchers McKiernan *et al.* in [105] conducted an experiment that studied surface roughness effects over the same cone as that used in the this study. They presented the frequency spectra of wall-pressure perturbations for both blunt compression cones with and without surface roughness.

In the experiment conducted by Wheaton *et al.* [23], the flow conditions were very close to those in the current study. However, the source of freestream perturbations was due to the noise of the turbulence over the wall of the wind tunnel. The amplitude of the tunnel noise perturbations was far larger than the linear freestream perturbations that are used in the current study. Therefore, the development of the boundary-layer perturbations does not fall within the linear regime and the magnitudes of the pressure perturbations at the wall are not comparable to those in the current study. However, the frequency range of the dominant growth can still be compared. Figure 43 compares the spectra of our simulated pressure perturbations at the wall with the experimental and LST-predicted spectra at $x^* = 0.4$ m in Wheaton *et al.* [23] The colored solid lines represent our simulated results, while symbols represent their experimental and LST analysis results. For the purpose of clear demonstration, the maximum magnitude of the growing peak in our simulated results is manually adjusted to match that of the experiment in Wheaton *et al.* [23]. The frequency of our dominantly growing peak is 290 kHz, and the dominantly growing frequency ranges from about 240 kHz to 320 kHz. These features are very similar to the experimental and LST-predicted features in Wheaton *et al.* [23]. Furthermore, the peak of second harmonic waves appears around 580 kHz at the locations of $x^* = 0.378$ m and 0.4 m in our simulated results, which is very close to Wheaton *et al.* [23]'s experimental peak as well.

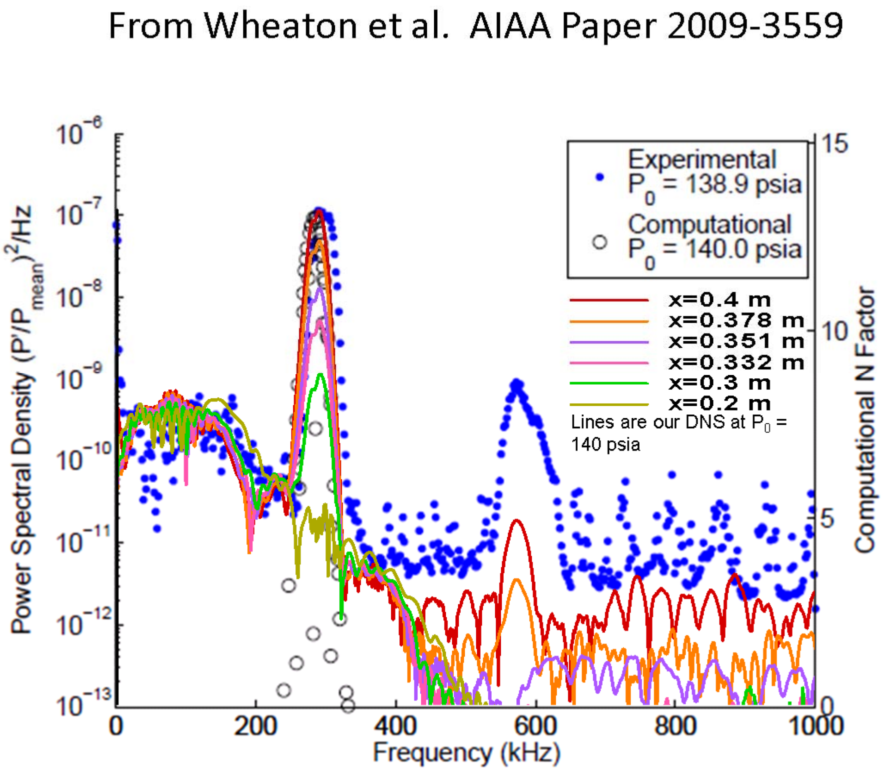

(c) x = 0.4 m, quiet flow

Figure 43. Comparison of the wall-pressure perturbation frequency spectra from the current simulation and Wheaton *et al.* [23]

Chou [22, 98] used a laser spot as the amplitude-wise well-controlled and repeatable freestream perturbations. The profile of the laser spot is similar to the one studied by Schmisseur *et al.* [66, 67] and Salyer *et al.* [96, 97]: essentially an entropy sphere with a nearly-Gaussian distribution. The maximum amplitude at the center of the experimental laser spot is several orders of magnitude higher than the hotspot in the current simulation.

The radius of the experimental laser spot is around $4\ \text{mm}$, which is close to the current simulation's hotspot radius. The blunt compression cone used in their experiment is identical to the cone used in the current simulation. However, the freestream flow conditions in their experiment differ from those used in the current simulation. For instance, the experimental stagnation pressure is $740.3\ \text{kPa}$, the current simulation's stagnation pressure is $965\ \text{kPa}$. Figure 44 compares the spectra of simulated wall-pressure perturbations to the experimental spectra in Chou [98]. In this figure, colored symbols represent our results and solid colored lines represent Chou [98]'s results. Since our definition of dimensional amplitude differs from that used in Chou [98], only relative amplitudes can be compared. More specifically, the simulated maximum amplitude of the dominantly growing peak at $x^* = 0.4\ \text{m}$ is scaled to be the same as the experimental one. Thus, the relative amplitude growth at the earlier locations can be compared. In Figure 44, after scaling, the relative amplitudes of the growing second-mode dominant peak at $x^* = 0.378\ \text{m}$ and $0.351\ \text{m}$ agree well with the experiment. Both second-mode dominant peaks are also very similar in shape. For instance, both peaks have a dent at the left side of the crest and the widths of the growing peaks are similar. The simulated second-mode dominant unstable frequency range and the simulated second harmonic unstable frequency ranges, however, are both higher than those from the experiment. This difference is likely due to a difference in freestream conditions.

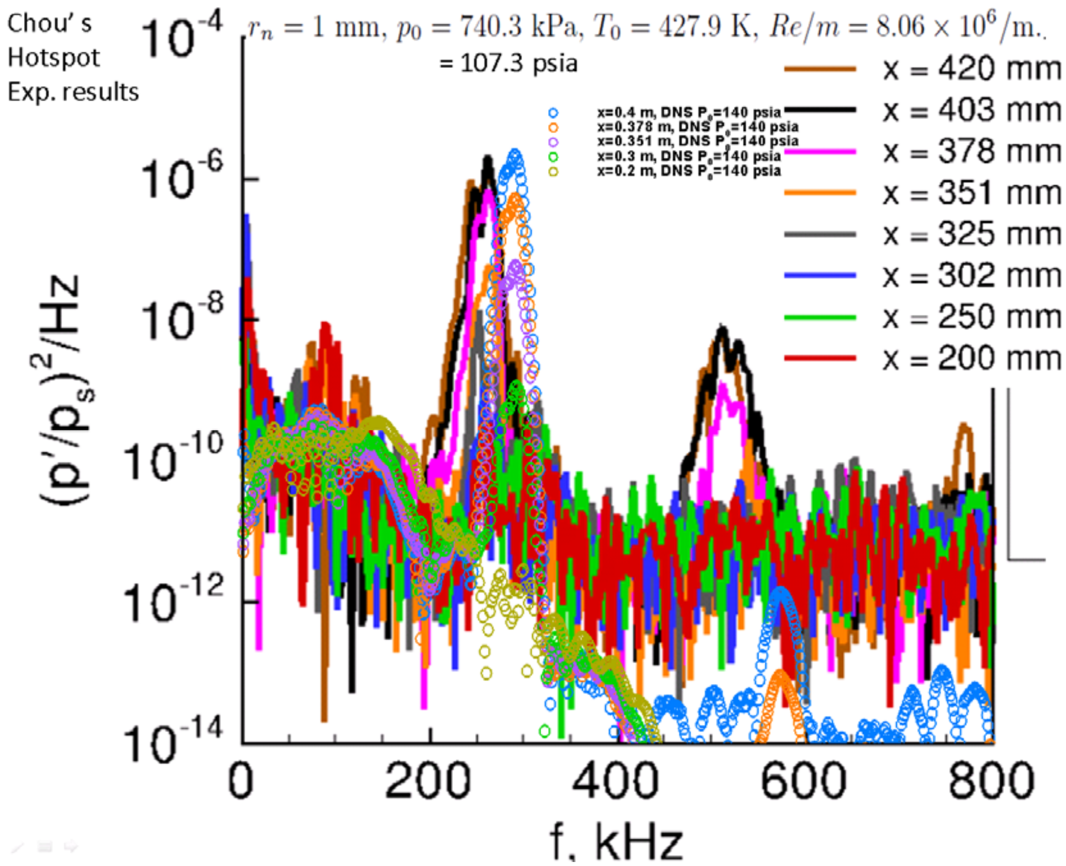

Figure 44. Comparison between the spectra of the current simulated wall-pressure perturbations and the experimental ones in Chou [98].

In the experiment study conducted by McKiernan *et al.* in [105], the same compression cone without roughness was studied. The source of freestream perturbation was turbulent noise at the wall of the wind tunnel. The amplitude of the perturbations was far higher than those used in the current simulation. Therefore, their evolution of boundary-layer disturbances may not fall in the linear regime. The unit Reynolds number used in the experiment was $1.01 \times 10^7 \,\mathrm{m}^{-1}$ and their stagnation pressure was 150 psia. Conversely, the unit Reynolds number used in this current simulation is $1.026 \times 10^7 \,\mathrm{m}^{-1}$ with a stagnation pressure of 140 psia . Thus, the flow conditions in McKiernan *et al.* [105]'s experiment are not exactly the same, but close to those used in the current simulation.

A comparison of spectra between the current unsteady hotspot simulation and the experiment performed by McKiernan *et al.* in [105] is shown in Figure 45. There are two locations, $x^* = 0.332\ \mathrm{m}$ and $0.4\ \mathrm{m}$, available for comparison. The solid colored lines represent the spectra from the experiment, and the colored symbols represent the simulated spectra. The experiment's most amplified frequency (278 kHz) is lower than the simulated one (290 kHz) and the experimental second mode unstable frequency ranges from 252 kHz to 320 kHz. The simulated one ranges from 246 kHz to 325 kHz. These differences in frequency are likely due to a difference in flow conditions.

The definition of Fourier transformed dimensional amplitude used in the experimental study performed by McKiernan *et al.* in [105] differs from the one used in this current simulation. Hence, Figure 45 only compares relative amplitudes. More specifically, the amplitude of the simulated spectrum is scaled to be the same as the experimental one at $x^* = 0.4\ \mathrm{m}$; the simulated amplitude at the earlier location is also based on this scaling. After scaling, the simulated relative amplitude in the unstable second mode frequency range at $x^* = 0.332\ \mathrm{m}$ is lower than the experiment's, although not vastly. The amplitude difference could be due to a difference in flow conditions and other environmental conditions in the experiment.

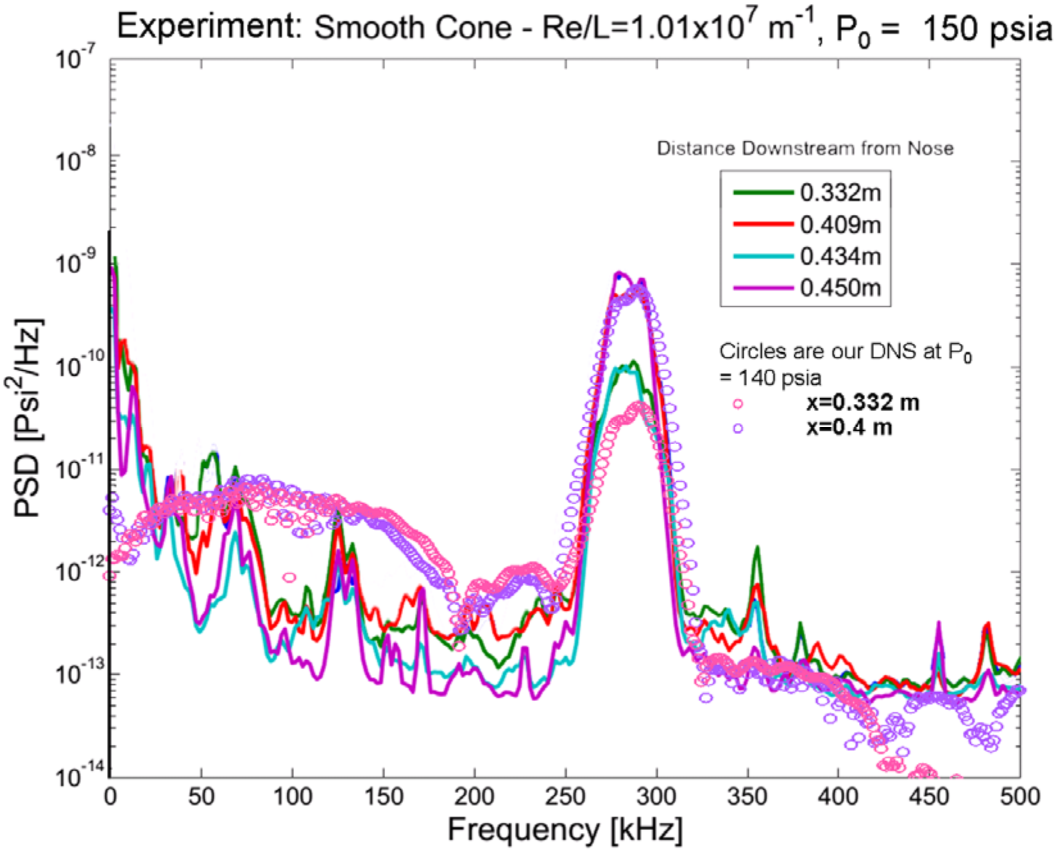

Figure 45. Comparison between the spectra of the current simulated wall-pressure perturbations and the experimental ones by McKiernan *et al.* [105]

Disturbances in the boundary layer contain discrete spectrum wave modes, including mode F and mode S, and continuous spectrum wave modes such as fast acoustic, slow acoustic, and entropy/vorticity waves. The amplitudes in the previous frequency spectra are the total sum of all discrete and continuous wave modes. In a receptivity study, the receptivity strength of each mode is one of the main features investigated. More specifically, to characterize the strength of receptivity prior to the growth of boundary-layer disturbances, there exists a receptivity coefficient defined as: the ratio of the wave amplitude of a specific mode and frequency at the Branch-I neutral location, located immediately behind the receptivity process, to the perturbation amplitude of the specific frequency in freestream. In fact, the normalized amplitude defined in Eq. (73) at the Branch-I neutral location is the receptivity coefficient.

In order to determine the receptivity coefficient of each mode, a method to separate all modes from a wave package of boundary-layer disturbances is needed. Tumin [84, 85] developed a method which implements theoretical bi-orthogonal decomposition to calculate the amplitude of each mode in a wave packet. In our research group, however, the implementation of this theoretical method was still under development at the time our simulations were completed. However, a method that utilizes the simulated wave amplitudes and the LST predicted N-factor was developed to approximate the amplitude of the unstable mode at the Branch-I neutral location. Based on Eq. (69), one can rewrite the equation as:

$$A_0 = \frac{A}{e^N} \tag{74}$$

where A_0 is the initial amplitude of the unstable mode at Branch-I neutral location, A is the amplitude of the unstable mode wave at a location in the linear growth regime, and N is the N-factor at the location. Practically, A can be approximated by selecting the simulated overall boundary-layer disturbance amplitude at the location where the unstable mode wave is very dominant. The dominance of unstable mode means the amplitude of the unstable mode grows to a very large value as compared to other modes in boundary-layer disturbances. Typically, the most unstable-mode dominant location is very downstream before reaching the Branch-II neutral location. In this case, since the Branch-II neutral location is located outside of computation domain, the location at the end of the farthest computation zone is chosen. Moreover, only frequency components within the dominant growth frequency range can be selected. N-factor can be determined using LST analysis as discussed in Section 3.2.2. In terms of normalized amplitude and receptivity coefficients, Eq. (74) can be rewritten as:

$$\left.\frac{\left|dP(f)/P_\infty\right|}{\left|dT_\infty(f)/T_\infty\right|}\right|_{0,S} \approx \frac{\left|dP(f)/P_\infty\right|}{\left|dT_\infty(f)/T_\infty\right|}\Big/ e^N \tag{75}$$

where subscripts $0,S$ represent the Branch-I neutral location and the dominant unstable mode, which in this case is mode S (this finding is explained in the next section). The term on the left side of Eq. (75) is the receptivity coefficient. In this equation, the receptivity coefficient is approximated by the term on the right side: the simulated normalized amplitude of the boundary-layer disturbances at the unstable-mode dominant location, and the LST determined N-factor at that location.

Figure 46 shows the frequency spectra of simulated overall boundary-layer disturbances as well as the receptivity coefficient of the unstable mode S at the Branch-I neutral location. Such frequency spectra are shown within the frequency range of the dominant growth. The amplitudes of the simulated boundary-layer disturbances that contains all wave modes are recorded at the LST predicted Branch-I neutral locations, which are shown as the neutral stability curve in Figure 25. The solid line in Figure 46 represents such overall boundary-layer disturbances. At the locations of Branch-I neutral stability, no dominant mode appears yet. In other words, the amplitudes of each mode are comparable. Therefore, the modulation between each mode waves occurs, resulting in the oscillatory amplitude curve for the overall boundary-layer disturbances. The receptivity coefficient of mode S is shown in the dash line. It is approximated by Eq. (75) for many sampling frequencies. The curve is far smoother than the curve of the overall boundary-layer disturbances because the receptivity coefficient only represents a single mode. The minor oscillation on the curve is due to the difference between the LST-predicted pure mode S solution and the simulated overall wave solution at the selected downstream location near the end of the computation zone. The peak of mode S's receptivity coefficient is between 286 kHz to 320 kHz; the maximum range of receptivity coefficient (~ 0.0022) appears between 297 kHz to 310 kHz. Thus, the initial peak frequency of mode S at the Branch-I neutral location is higher than that of the final mode S dominant peak downstream, which is 290 kHz. Such shift in frequency range is due to the fact that the boundary-layer thickness at the Branch-I neutral locations ($s^* = 0.11\ \mathrm{m}$ to $0.12\ \mathrm{m}$) for the initial maximum mode S frequency range (297 kHz to 310 kHz) is less than the one further downstream in the dominant growth region. The amplitudes of mode S at the Branch-I neutral locations are well contained in the overall disturbances amplitudes. The overall boundary-layer disturbances have amplitudes from 0.002 to 0.013, with a mean value of 0.0075. It is worth noting that the overall boundary-layer disturbances have an amplitude of 0.009 at 292.5 kHz, which is very close to the receptivity coefficient of 9.3×10^{-3} at 292.5 kHz with freestream fast acoustic waves in Balakumar *et al.* [88]. The amplitudes or receptivity coefficients of mode S are from 0.0003 to 0.0022, while the mean value is 0.00125. The ratio of the mean amplitude of mode S to that of the overall boundary-layer disturbances is 17%. The frequency that has the maximum amplitude ratio (79%) of mode S to the overall disturbances at the Branch-I neutral locations is 304 kHz.

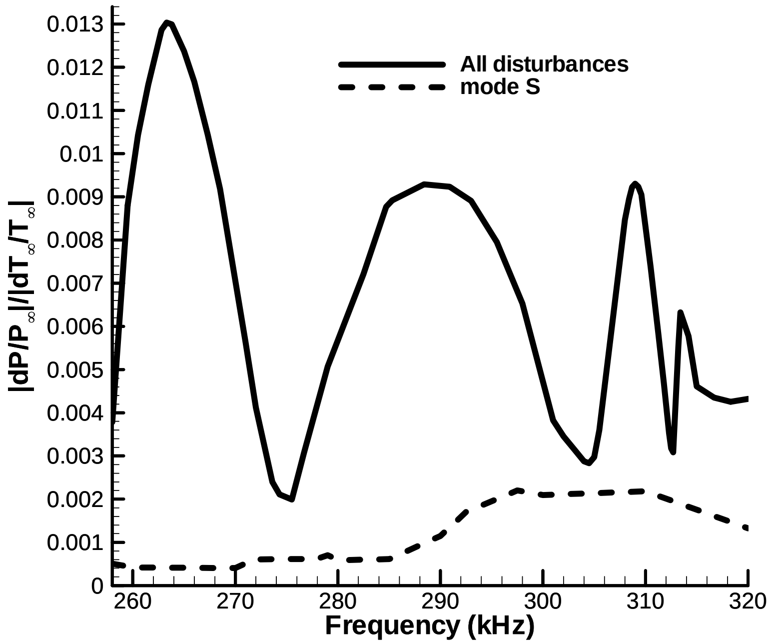

Figure 46. Frequency spectra of the simulated overall boundary-layer disturbances and the approximated receptivity coefficient of the unstable mode S at the Branch-I neutral location.

Very recently my research group at UCLA, under the guidance of Professor Xiaolin Zhong, developed a code which implements the theoretical bi-orthogonal decomposition method [106]. This decomposition method was developed by Tumin [84, 85]. Based on the time histories of unsteady disturbances in the linear flow regime, which are obtained from the numerical simulation, the decomposition method can separate the amplitudes of each normal mode of the discrete and continuous spectra from the wave packet in the flow field.

Miselis *et al.* [106] has been conducting the discrete normal mode decomposition on the unsteady flow field in Case 1. Both amplitudes of the mode S and mode F are obtained at various locations from the middle region to downstream region over the compression cone. The normalized amplitudes, or so-called receptivity coefficients of mode S and mode F over a wide continuous frequency range, are shown in Figure 47. Noticeably, the solid lines represent discrete modes and the symbols represent the overall boundary-layer disturbances or wave packet, which is the sum of all normal modes. The amplitudes are presented in logarithmic scale. The scales on the horizontal and vertical axes are the same in all three plots.

In Figure 47 (a), the amplitudes of mode S and the overall wave packet are shown. Within the second mode frequency range, from about 240 kHz to 320 kHz, the growing normalized amplitudes of mode S from $x^* = 0.25\ \mathrm{m}$ to $0.394\ \mathrm{m}$ are very close to those of the overall wave packet. In Figure 47 (b), the normalized amplitudes of mode F from $x^* = 0.25\ \mathrm{m}$ to $0.394\ \mathrm{m}$ are one to two orders of magnitude lower than those of mode S. The sum of mode S and mode F amplitudes from $x^* = 0.25\ \mathrm{m}$ to $0.394\ \mathrm{m}$ in Figure 47 (c) agree very well with the overall wave packet. These comparisons confirm this section's earlier conclusion of receptivity mechanism: the mode S-related second mode grows and becomes dominant in the boundary-layer disturbances behind the synchronization point.

Contrary to the LST prediction that mode F at the second mode frequency is stable everywhere above the cone, the amplitudes of mode F within the second mode frequency range in Figure 47 (b) grow downstream. Such growth of the mode F downstream is due to the proximity of mode S and mode F phase speeds behind the synchronization point, which are seen in the phase speed plot in Figure 52. Such proximity of the mode S and mode F behind the synchronization point creates such weak synchronization effects that a small part of the energy from the dominant growth of the mode S-related second mode is transferred to mode F through the proximity of the phase speeds. To confirm this explanation, future theoretical studies are required.

Within the frequency range from 120 kHz to 240 kHz in Figure 47 (a), mode S normalized amplitudes are mainly either neutral or decaying and around an order of magnitude lower than those of the wave packet. However, in Figure 47 (b), mode F normalized amplitudes are decaying and agreeing very well with those of the wave packet. Similarly, the sum of mode F and mode S amplitudes within the frequency range from 120 kHz to 240 kHz in Figure 47 (c) agrees very well with the wave packet amplitudes. These observations imply that mode F is dominant at the frequencies lower than the second mode frequency range.

In Figure 47, at the frequencies higher than the second mode frequency range before reaching $x^* = 0.394\text{ m}$, neither mode F nor mode S are dominant in the boundary-layer disturbances. However, the amplitudes of the mode F are relatively higher than mode S. Further downstream, the mode F becomes dominant in the boundary-layer disturbances at $x^* = 0.394\text{ m}$. This observation indicates the presence of the outstanding mode $F^{(2)}$ in the boundary-layer disturbances at the higher frequencies beginning with $x^* = 0.394\text{ m}$.

The approximated receptivity coefficients of mode S along the LST predicted second-mode neutral curve are discussed in Section 3.2.4 and shown in Figure 46. The maximum approximated receptivity coefficient of mode S along the LST predicted neutral curve within the second mode frequency range is about 0.0022 at 297 kHz. In Figure 47, the initial growth location of boundary-layer disturbances is $x^* = 0.17\text{ m}$, and the corresponding initial normalized peak amplitude of mode S within the second mode frequency range is about 2×10^{-3} at 295 kHz. Since the maximum approximated receptivity coefficients and the corresponding frequency agree well with those obtained by the bi-orthogonal decomposition method, the receptivity coefficient approximation method, (as introduced in Section 3.2.4), is valid. Additionally, the receptivity coefficients of mode F at

$x^* = 0.17$ m within the second mode frequency range are roughly an order of magnitude lower than mode S. Therefore, mode S is stronger than mode F at the initial growing location of the boundary-layer disturbances.

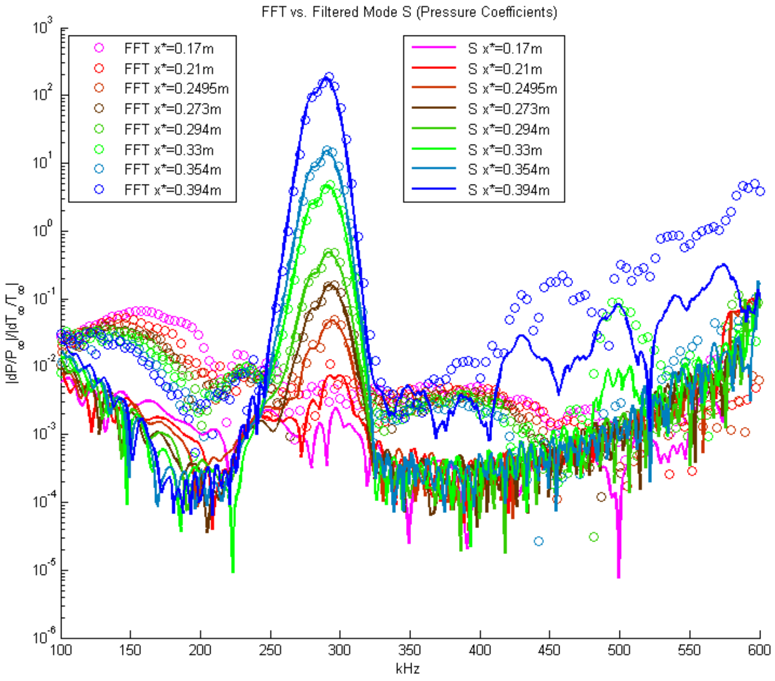
FFT vs. Filtered Mode S (Pressure Coefficients)
FFT x*=0.17m
FFT x*=0.21m
FFT x*=0.2495m
FFT x*=0.273m
FFT x*=0.294m
FFT x*=0.33m
FFT x*=0.354m
FFT x*=0.394m
S x*=0.17m
S x*=0.21m
S x*=0.2495m
S x*=0.273m
S x*=0.294m
S x*=0.33m
S x*=0.354m
S x*=0.394m
$|dP/P_\infty|/|dT_\infty/T_\infty|$
10^{3}
10^{2}
10^{1}
10^{0}
10^{-1}
10^{-2}
10^{-3}
10^{-4}
10^{-5}
10^{-6}
100
150
200
250
300
350
400
450
500
550
600
kHz

(a)

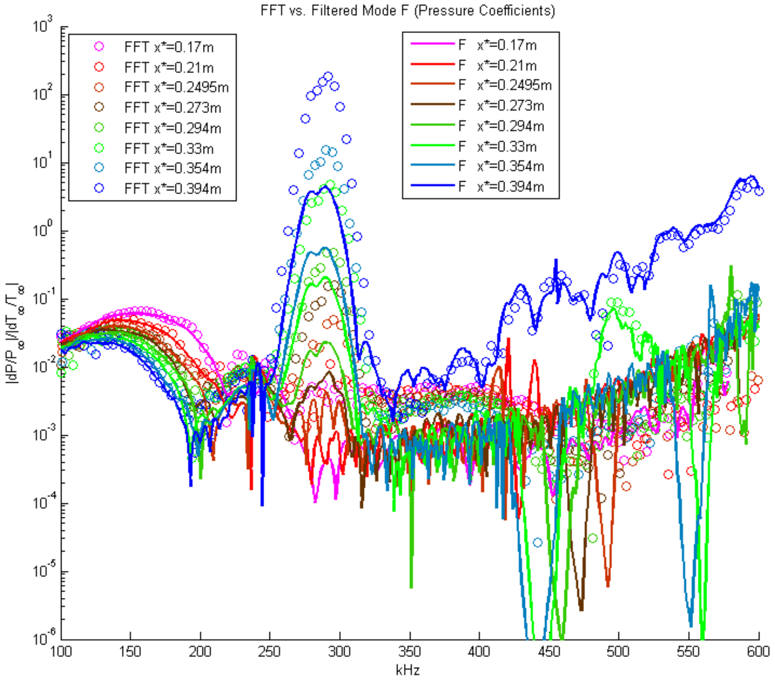
FFT vs. Filtered Mode F (Pressure Coefficients)
FFT x*=0.17m
FFT x*=0.21m
FFT x*=0.2495m
FFT x*=0.273m
FFT x*=0.294m
FFT x*=0.33m
FFT x*=0.354m
FFT x*=0.394m
F x*=0.17m
F x*=0.21m
F x*=0.2495m
F x*=0.273m
F x*=0.294m
F x*=0.33m
F x*=0.354m
F x*=0.394m
$|dP/P_\infty|/|dT_\infty/T_\infty|$
10^{3}
10^{2}
10^{1}
10^{0}
10^{-1}
10^{-2}
10^{-3}
10^{-4}
10^{-5}
10^{-6}
100
150
200
250
300
350
400
450
500
550
600
kHz

(b)

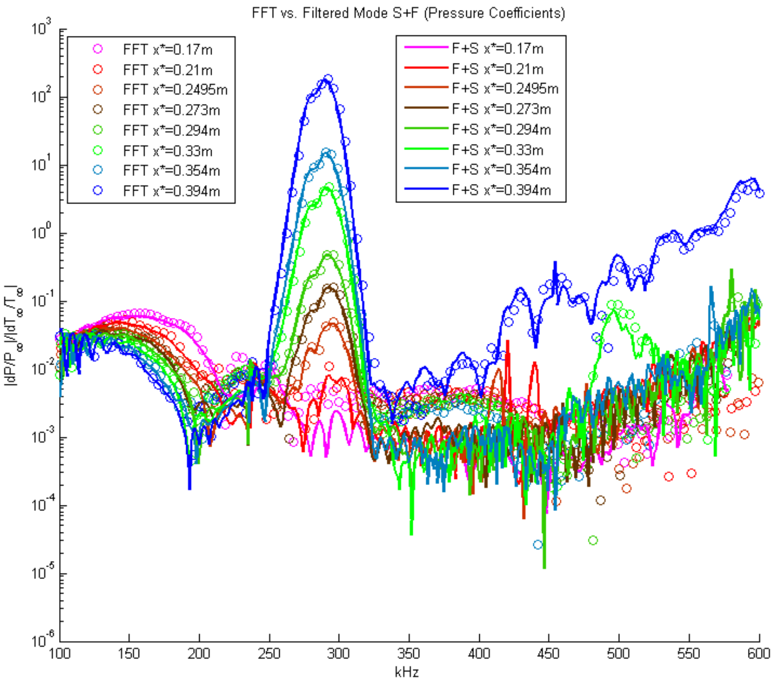

(c)

Figure 47. The receptivity coefficient comparisons of (a) the mode S, (b) the mode F, and (c) the sum of mode F and mode S with the overall wave packet.

The normalized amplitude is used to quantify the strength of boundary-layer disturbance growth relative to freestream perturbations during the receptivity process and linear growth. The waves, which are transformed into the frequency domain, become complex values. Therefore, each wave component has a phase angle. Since the phase angle of each freestream perturbation component is different, the relative phase angles of boundary-layer disturbances to that of the freestream used to describe the phase shift. The frequency spectrum of relative phase angles of the overall boundary-layer disturbances at the end of the cone is shown in Figure 48. The phase shift consistently increases as the frequency increases. The bumps are most likely caused by the multi-mode wave modulations. Finally, by obtaining relative phase angles, in addition to the normalized amplitudes, one can reconstruct the actual waveform of the wall-pressure disturbances within the linear receptivity regime from the freestream entropy perturbations with different shape-functions [107]. The phase angles of mode S, however, cannot be determined from the approximation method. The future implementation of the theoretical modal decomposition method is required to obtain the phase angles of mode S.

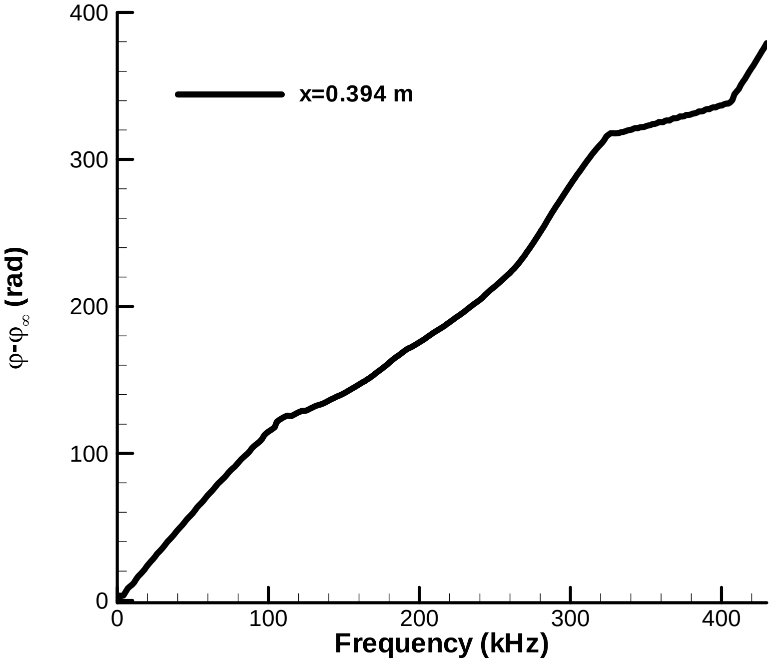

Figure 48. The frequency spectrum of phase angle difference between the induced wall-pressure disturbances and the freestream temperature disturbances.

3.2.5 Mechanism of Boundary-Layer Receptivity

After the frequency spectra are found, an investigation of the spatial modal evolution of the perturbations prior to the second mode dominance is conducted. It is a crucial step to understand the receptivity mechanism. Figure 49 shows the spatial development of wall-pressure-perturbation amplitudes from the upstream region to the downstream region. In the plot, the five simulated second mode sampling frequencies are very close to the five frequencies used in the LST study. These five frequencies start with high initial amplitudes where the hotspot just passes through the shock and the boundary-layer disturbances are excited in the upstream region. Then, the perturbations decay while moving downstream. When they reach $s^* \approx 0.19\ \mathrm{m}$, the perturbations begin to grow exponentially downstream. The oscillatory features of curves are the result of the modulation of multiple wave modes when there is no single dominant instability mode. This multi-mode modulation phenomenon is expected in the synchronization zone. These oscillatory features are commonly seen in many numerical studies [4, 28, 31, 35, 36, 94], but are not the spurious result of Fourier decomposition.

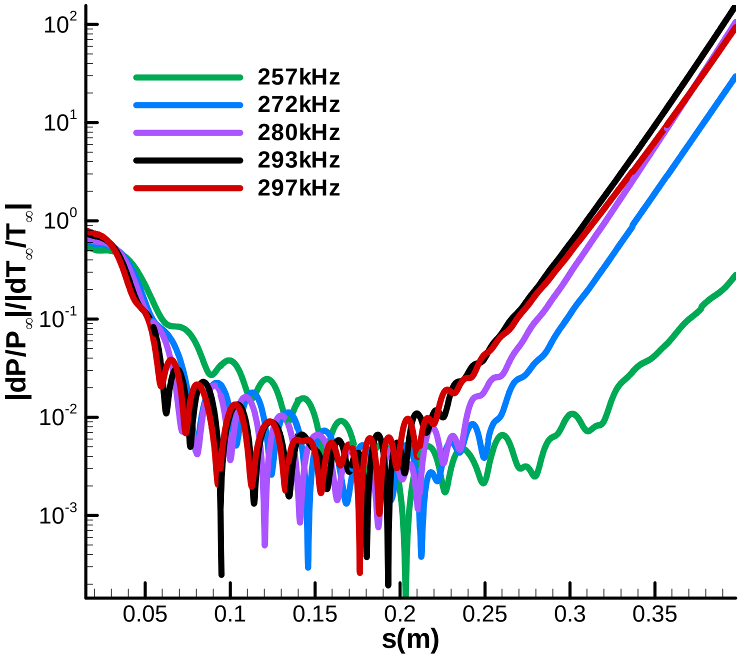

Figure 49. The spatial development of numerically simulated wall-pressure perturbations for five sampling frequencies in the second mode frequency range.

The following comparisons between the current simulated results and those from LST aim to quantitatively validate the current simulation. The validation is performed in the downstream region because it is more difficult to resolve the flow details there. The simulated growth rate is calculated using Eq. (44). The comparison between the numerically simulated spatial growth rates, and those found from LST over the second mode frequency range at four surface locations, is shown in Figure 50. At a fixed location, LST and the current numerical simulation predict nearly the same peak frequency for the second mode dominated growth. However, the numerically simulated maximum growth rate is slightly higher than the one predicted by LST. Table 3 shows the comparison of peak frequencies and growth rates between the simulation results and LST. The relative differences in growth rates consistently decrease when the second mode becomes more dominant in the simulated disturbances downstream. The relative differences of the peak frequencies at all four locations are below 1%, which indicate a very good agreement between the frequencies of the maximum simulated growth rates and LST. The reason for the differences in the growth rates is because there are modulations that result from the physical interaction between multiple modes, which cannot be decomposed by Fourier decomposition. Moreover, the non-parallel and surface curvature effects are not accounted for in the current LST model.

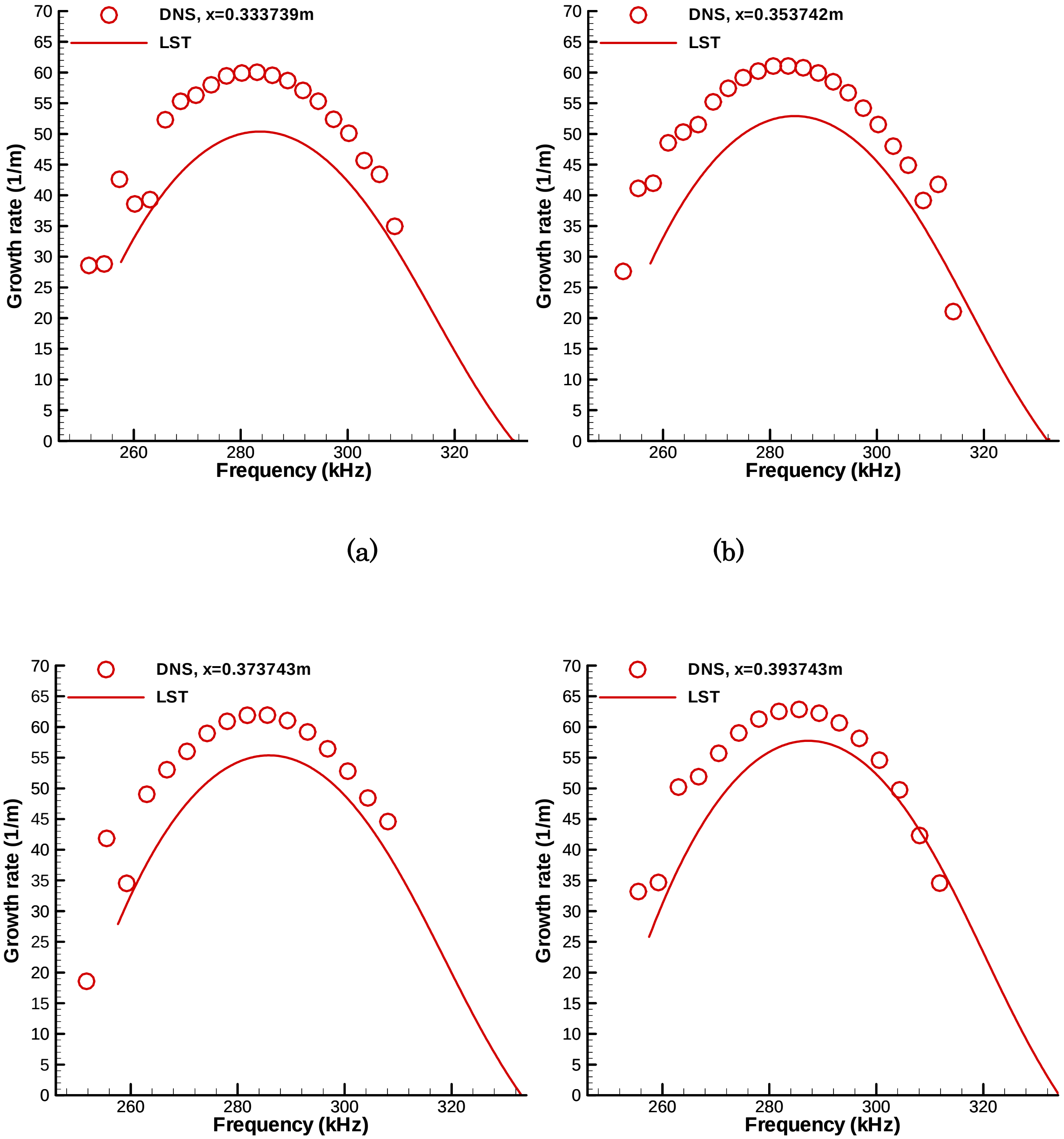

(a) (b)

(c) (d)

Figure 50. Comparison of the growth rates between numerical simulation and LST as a function of frequency in the unstable second mode region: (a) $x^* = 0.333739$ m (b) $x^* = 0.353742$ m, (c) $x^* = 0.373743$ m, and (d) $x^* = 0.393743$ m.

Table 3. Comparison of growth rate spectra between the current simulation results and LST.

x location (m)	Relative difference of Maximum growth rates	LST peak frequency (kHz)	Simulated peak frequency (kHz)
0.33	16%	284	282
0.35	13%	284.5	283.5
0.37	11%	286	284
0.39	8%	287.5	286

The simulated dimensional wave number is calculated from Eq. (45). Figure 51 compares the frequency spectra of wave numbers at the same four surface locations. The maximum relative differences between two sets of wave numbers are: 7.5% at $x^* = 0.33$ m , 5.2% at $x^* = 0.35$ m , 2.3% at $x^* = 0.37$ m , and below 1% at $x^* = 0.39$ m . The simulated wave numbers agree with those of LST very well at the downstream location of $x^* = 0.39$ m .

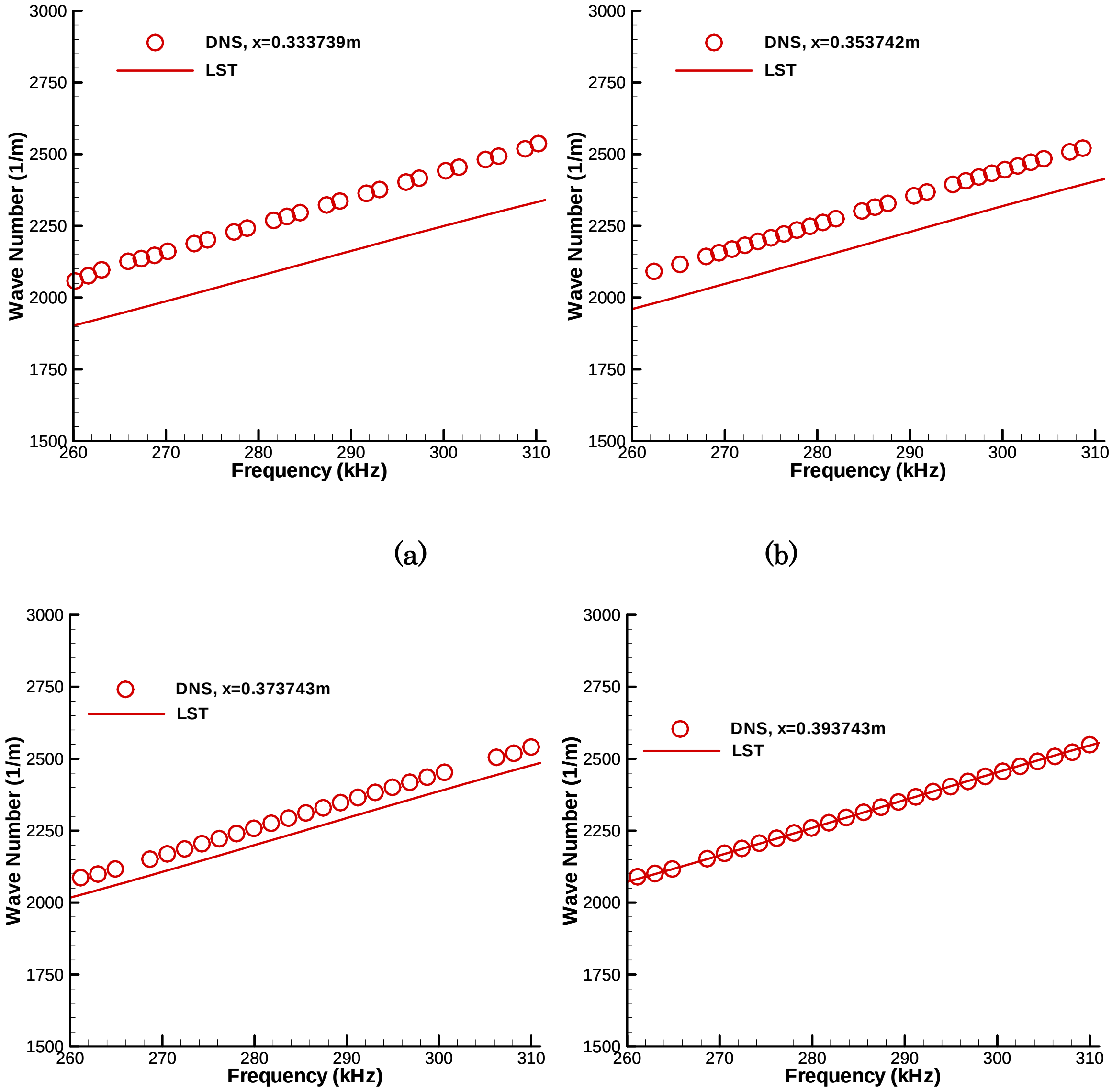

(a) (b)

(c) (d)

Figure 51. Comparison of the wave numbers between numerical simulation and LST as a function of frequency in the unstable second mode region: (a) $x^* = 0.333739$ m (b) $x^* = 0.353742$ m, (c) $x^* = 0.373743$ m, and (d) $x^* = 0.393743$ m.

Figure 57 (f) shows an excellent agreement between the mode shapes of the current simulation and LST, with the most amplified second mode sampling frequency of 293 kHz behind the synchronization point. Based on these agreements, it is concluded that the numerical simulation has successfully captured the linear second mode development of boundary-layer perturbations.

The simulation results do not clearly indicate the modal evolution throughout the receptivity process. Therefore, we have to compare the simulation results to the theoretical results in order to identify the dominant wave modes in the boundary layer with a fixed frequency. The frequency analyzed is the most amplified one (293 kHz) in the second mode range. The simulated dimensionless phase speed is computed using Eqs. (45), (66), and (68). The comparison between the simulated phase speed and the phase speed obtained from LST is shown in Figure 52. The three horizontal lines are the dimensionless phase speeds of fast acoustic, slow acoustic, and entropy/vorticity waves determined using freestream flow conditions in front of the bow shock. As a result, they only serve as qualitative references to show the existence of the three wave modes. The actual phase speeds depend on local non-constant flow conditions. Figure 52 shows the following trend: the phase speed of the simulated disturbances decreases from the phase speed of the fast acoustic wave in the nose region. The simulated phase speed closely matches the LST-predicted mode F with very slight oscillations until $s^* = 0.04\text{ m}$. The comparison shows that the disturbances are likely to be initially excited in the boundary layer by the fast acoustic waves near the nose. The comparison also shows that mode F is relatively strong in the boundary-layer disturbances before $s^* = 0.04\text{ m}$. The oscillations begin after the phase speed of the waves reaches that of entropy/vorticity waves, then rises up to the phase speed of fast acoustic waves between $0.04\text{ m} < s^* < 0.2\text{ m}$. The modulation between different wave modes causes the strong oscillations in that region. More specifically, there are several disturbance modes exist in the simulated boundary-layer disturbances, while LST assumes clean boundary-layer waves with pure mode F and mode S. As a result, the modulations of the simulated results reflect the co-existence of other modes. Moreover, all the modes are relatively strong in the modulation region. The same phenomenon was also discussed by Ma and Zhong [4, 35, 36].

In Figure 52, the phase speed in the modulation region is close to the fast acoustic waves. It indicates that the boundary-layer disturbances contain a significant proportion of fast acoustic waves in that region relative to the other modes. As the waves propagate further downstream, the phase speed decreases and becomes almost the same as mode S behind the synchronization point of mode S and mode F at $s^* = 0.16 \text{ m}$. This observation indicates that the dominance of mode S in the boundary-layer disturbances begins after the synchronization between mode S and mode F.

In Fedorov *et al.* [80, 108], a branch point is where both the real and imaginary parts of the phase speed are equal for mode F and mode S. The second mode instability is excited downstream from the branch point. The branch point, however, does not exist in most practical flows with a real x-axis (or Reynolds numbers) only, except for a very specific disturbance frequency with a very cold wall. Instead, the branch point appears along the complex Reynolds number with a non-zero imaginary part. In the case of practical flow, mode F and mode S have resonance interaction when the real part of the wave number and frequency are the same near the branch point, despite the difference in growth rates. Therefore, we define the synchronization point, which is also the resonant point, between mode F and mode S as the point where the real parts of the phase speed are equal for mode

F and mode S. Ma and Zhong [4, 35, 36] have shown that this synchronization point plays an important role in the receptivity process.

In Figure 52 to Figure 56, there is a break in the phase speeds, wave numbers, and growth rates of mode F around $s^* = 0.09\ \mathrm{m}$. This is due to the eigenvalue of the discrete mode F merging into the entropy/vorticity spectrum and reappearing while moving downstream before reaching the synchronization point of modes F and S. As a result, the eigenvalue of mode F is interrupted by the entropy/vorticity spectrum. Since the actual phase speed of entropy/vorticity waves depends on local flow conditions, the break appears below the freestream phase speed of entropy/vorticity waves in Figure 52. This break is typical for hypersonic flow over a cone. This break also appears in the LST predicted phase speeds in Figure 11 in Zhong and Ma for a Mach 8 flow over a cone [36]. As demonstrated in Figure 10 of Zhong and Ma [36], this is a result of mode F crossing the continuous spectrum.

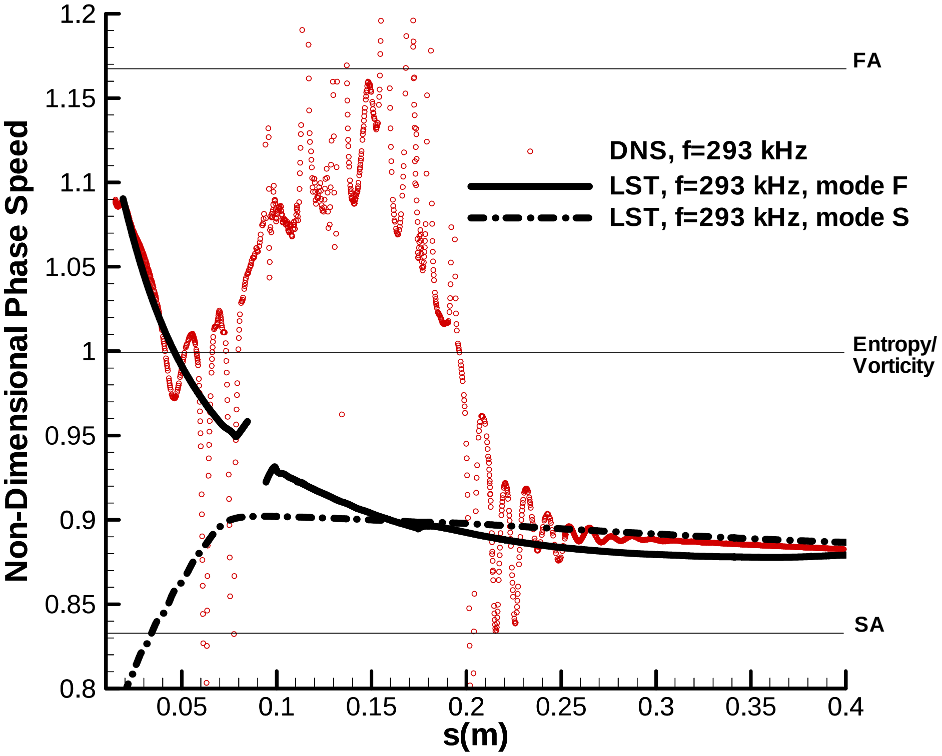

Figure 52. Comparison of the streamwise phase speeds of the simulated wall-pressure disturbances with those of mode F and mode S by LST at the frequency of 293 kHz.

The previous plot of dimensionless phase speed is expressed in terms of dimensional streamwise coordinates along the surface of the compression cone. It provides intuitive ideas and practical information by referring to the spatial location along the cone. It is especially convenient during comparisons with the experiment results or providing guidance to experimental study or vehicle design processes. In parametric studies, it is more convenient to express results in terms of dimensionless parameters, such as self-similarity parameters, because self-similarity parameters allow comparison of common characteristics between different cases regardless of the dimensional differences. The horizontal axis in Figure 53 has a dimensionless circular frequency, ω , instead of a dimensional streamwise location along the cone surface, s^*. According to Eq. (67), the dimensionless circular frequency contains both the factors of local Reynolds number and frequency.

In Figure 53, the synchronization point of mode F and mode S is at $\omega = 0.26$. From $\omega = 0.09$ to 0.14, the simulated phase speed decreases to that of entropy/vorticity waves, and the simulated phase speed is in the proximity of mode F. This observation implies that the boundary-layer disturbances have relatively strong mode F and it is most likely initially excited by the fast acoustic waves in the earlier region near the nose. The earlier results of show there are mainly acoustic waves carried into the shock layer in the nose region that also confirm this implication. The oscillation in the simulated phase speed is due to the modulation of different wave modes in the boundary layer, when various wave modes are have comparable amplitudes as explained previously. From $\omega = 0.16$ to 0.185, the simulated phase speed oscillates between slow acoustic waves and entropy/vorticity waves. This observation indicates that the slow acoustic waves, mode S, mode F, and entropy/vorticity waves are relatively strong between $\omega = 0.16$ and 0.185. From $\omega = 0.185$ to 0.26, the simulated boundary-layer disturbances approach the synchronization point. Then, the simulated phase speed jumps up and oscillates around the phase speed of fast acoustic waves. This observation indicates that the fast acoustic waves are relatively strong around the synchronization point. Immediately behind the synchronization point, the simulated phase speed drops down and converges to that of mode S. Simultaneously, the oscillation gradually disappears behind the synchronization point, and the simulated phase speed curve eventually becomes smooth downstream. These observations indicate the domination of mode S in the boundary-layer disturbances after the synchronization between mode F and mode S.

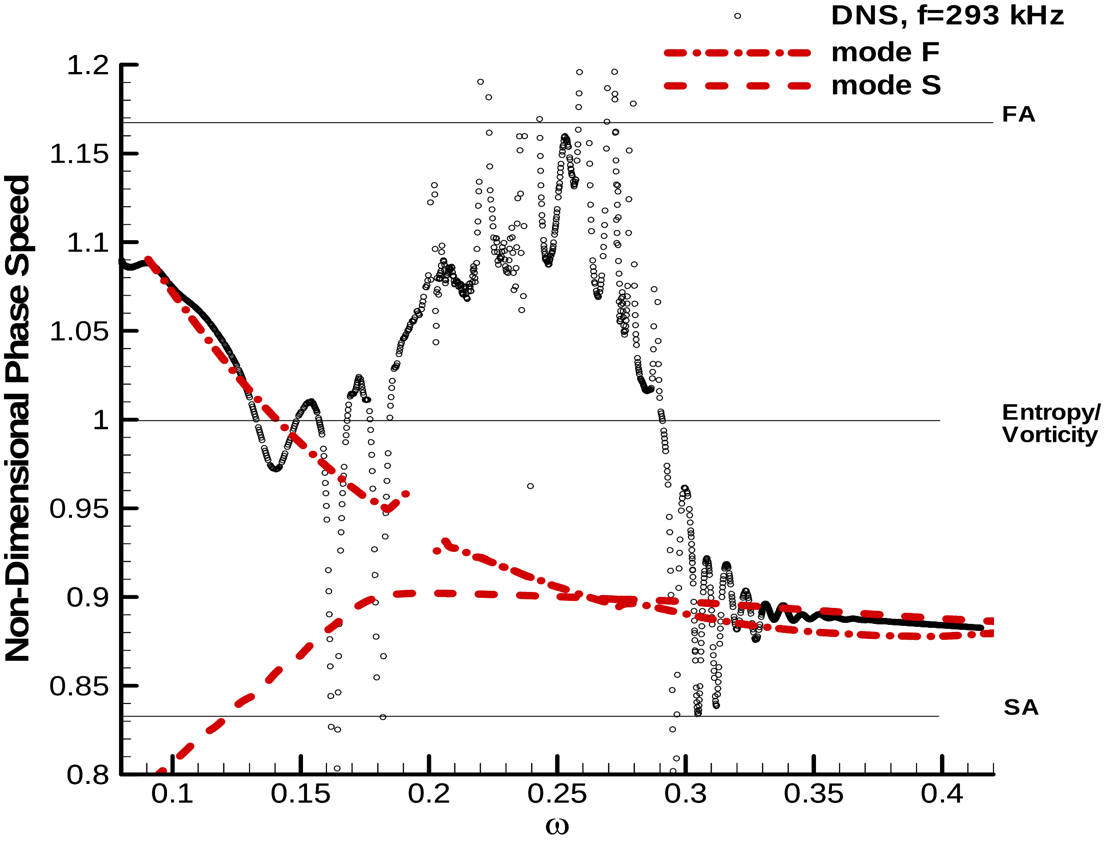

Figure 53. Comparison of the streamwise phase speeds of the simulated wall pressure disturbances with those of mode F and mode S by LST at the frequency of 293 kHz along the dimensionless circular frequency.

The simulated dimensionless wave number is calculated by Eqs. (45) and (66). The wave number comparison between numerical simulation and LST is shown in Figure 54. The plot confirms the observations made at the phase speed comparison: the induced waves contain relatively strong mode F before the disturbances reach $s^* = 0.04$ m and modulation between all the waves occurs between $0.04\ \mathrm{m} < s^* < 0.2\ \mathrm{m}$. The wave numbers of mode F and mode S cross each other around $s^* = 0.16\ \mathrm{m}$, hence the synchronization point is located there. Though the wave numbers of mode F and mode S seem to be very close as shown in Figure 54, they are in fact different in the region behind the synchronization point. The differences can be more clearly seen in the non-dimensional phase speed comparison in Figure 52. Therefore, there is only a synchronization point, not a synchronization line or a long region.

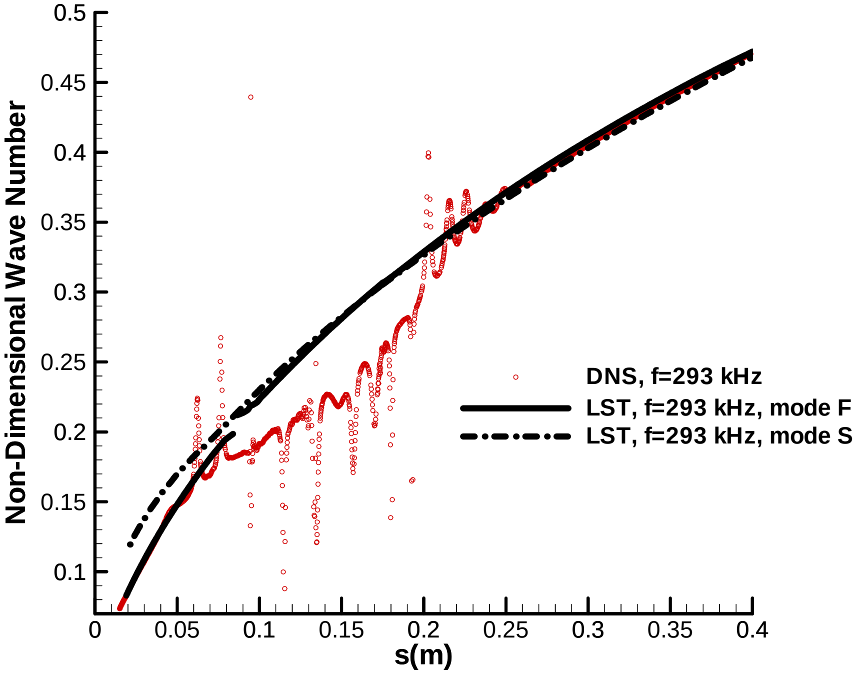

Figure 54. Comparison of the streamwise wave numbers of the simulated wall-pressure disturbances with those of mode F and mode S by LST at the frequency of 293 kHz.

The stability of the boundary-layer disturbances at different locations is determined by their growth rates. The simulated growth rate is calculated by Eq. (44). The comparison between the simulated growth rate and the one obtained from LST is shown in Figure 55. There are oscillations in the simulated growth rate as a result of multi-mode wave modulations. The simulated growth rate eventually converges to the unstable growth rate of mode S behind $s^* \approx 0.19$ m. Both growth rates of the simulation and mode S compare very well downstream. The plot also shows that mode F is stable everywhere while mode S is stable before $s^* = 0.11$ m and it becomes unstable behind this location. These observations indicate that the unstable second mode is related to mode S and the induced disturbances become second mode dominated behind the synchronization point ($s^* = 0.16$ m), the similar conclusion made in the preceding discussion of the phase speed plot in Figure 52. In addition, even though the unstable region of mode S begins earlier than the synchronization point, the disturbances of 293 kHz in Figure 49 grow only behind $s^* \approx 0.19$ m. From this observation, we further conclude that the synchronization of mode F and mode S leads to the dominance in the boundary-layer disturbances by the growing second mode. Ma and Zhong [4, 35, 36] have also shown that even the modulation region exists, the resonance interactions of mode F and mode S at the synchronization point still lead to the second mode dominance in the boundary-layer disturbances.

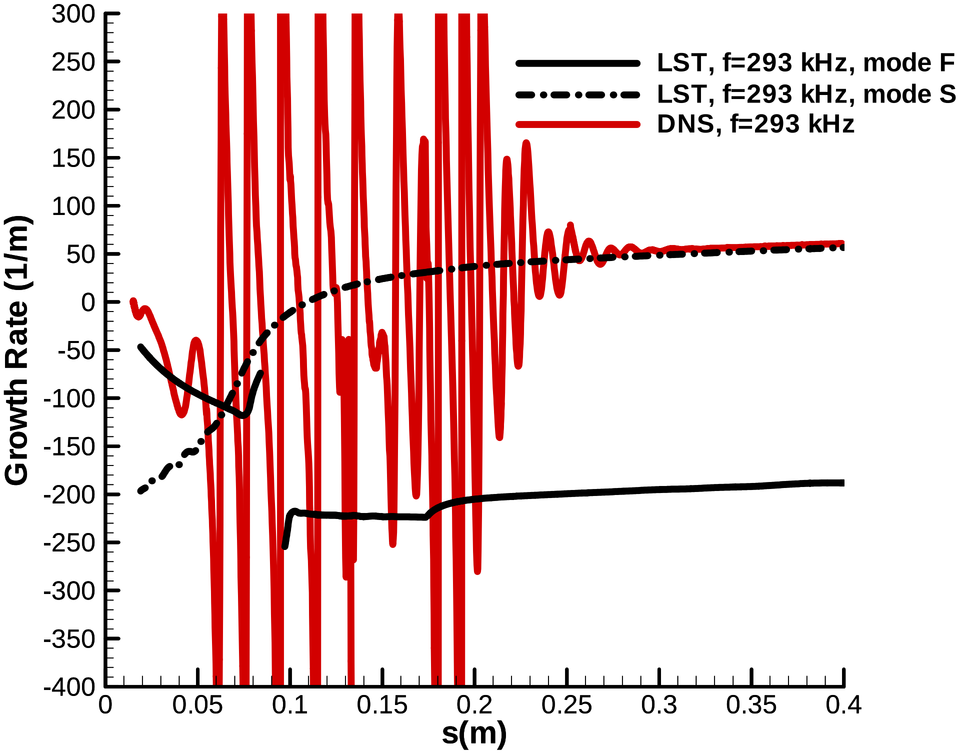

Figure 55. Comparison of the growth rates of the simulated wall-pressure disturbances with those of mode F and mode S by LST at the frequency of 293 kHz.

Figure 56 shows the comparison between the simulated growth rate and the one obtained from LST in self-similar variable, which allows the comparison of common characteristics between different parametric cases regardless of the dimensional differences. The horizontal axis in Figure 56 has the dimensionless circular frequency, ω, instead of the dimensional streamwise location along the cone surface, s^*. According to Eq. (67), the dimensionless circular frequency contains both the factors of local Reynolds number and frequency.

In Figure 56, there are oscillations in the simulated growth rate as a result of multi-mode wave modulations. The simulated growth rate eventually converges to the unstable growth rate of mode S behind $\omega \approx 0.29$. Both growth rates of the simulation and mode S compare very well downstream. The plot also shows that mode F is stable everywhere, while mode S is stable before $\omega = 0.215$ and it becomes unstable behind this dimensionless circular frequency. These observations indicate that the unstable second mode is related to mode S and the induced disturbances become second mode-dominated behind the synchronization point ($\omega = 0.26$), which is the similar conclusion made in the preceding discussion of the phase speed plot in Figure 53. As previously confirmed in the dimensional receptivity mechanism analyses, even though the unstable region of mode S begins earlier than the synchronization point, the boundary-layer disturbances of 293 kHz only grow behind the synchronization point. From this observation, we further conclude that the synchronization of mode F and mode S leads to the dominance of boundary-layer disturbances by the growing second mode. This conclusion is the same as the conclusion in the earlier dimensional receptivity mechanism analyses.

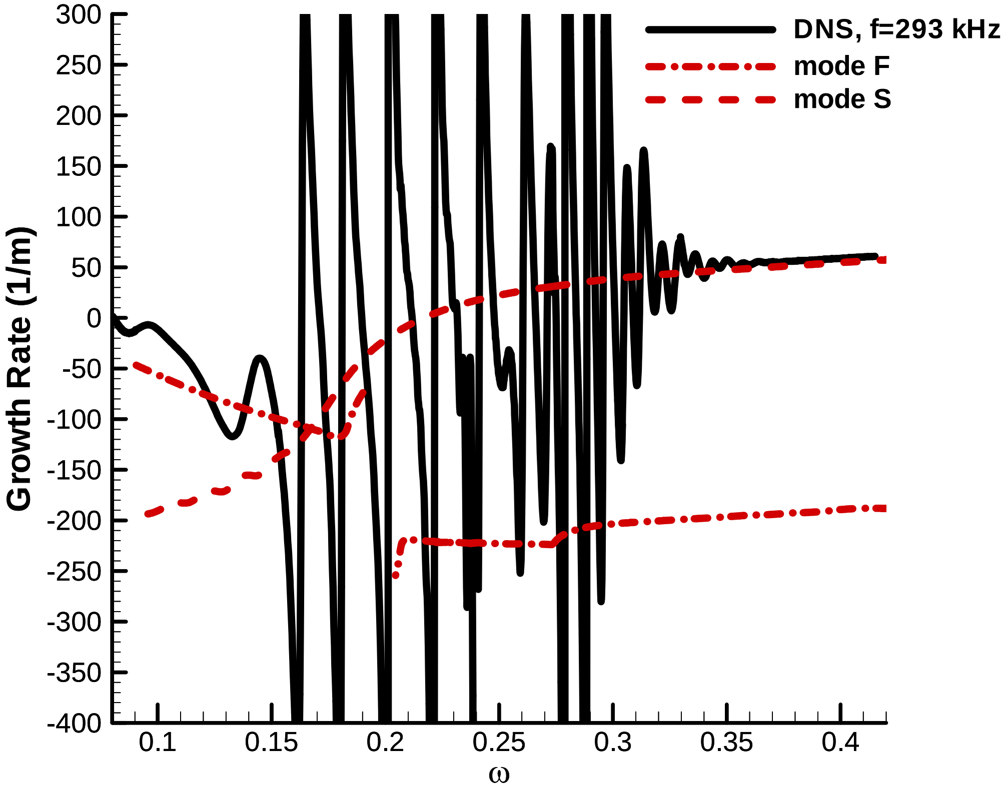

Figure 56. Comparison of the streamwise growth rates of the simulated wall pressure disturbances with those of mode F and mode S by LST at the frequency of 293 kHz along the dimensionless circular frequency.

In order to confirm the previous identification of modal evolution in the induced boundary-layer disturbances, we compare the boundary-layer mode shapes between simulation and LST at different locations. These are shown in Figure 57 (a) through (f). At $s^* = 0.03\ \text{m}$ where the modulations begin to appear upstream, the simulated mode shape is almost the same as that of mode F. This comparison shows that in the upstream region of multi-mode wave modulation with boundary-layer disturbances that have a relatively strong mode F. While moving further downstream to $s^* = 0.0687$ m and $s^* = 0.1083$ m , which are near the locations of both ends of the break in the phase speed of mode F, the simulated mode shape begins to deviate from mode F; at this point it does not approach mode S. These observations show neither mode F nor mode S can stand out amongst all wave components in the induced disturbances when the eigenvalue of mode F is in the vicinity of the entropy/vorticity spectrum. The differences outside the boundary layer between the simulated mode shape and the LST reflect the existence of freestream transient forcing outside the boundary layer in the simulated results, while the LST is free from freestream forcings. When the boundary-layer disturbances reach the vicinity of synchronization point at $s^* = 0.1612$ m , the simulated mode shape begins to approach mode S. When the disturbances move further downstream from the synchronization point to $s^* = 0.246$ m and $s^* = 0.314$ m , the comparisons show that the simulated mode shape converges to mode S. Especially at $s^* = 0.314$ m , the simulated mode shape agrees very well to mode S. The comparisons at the last two locations behind the synchronization point show that mode S has stronger and more rapid domination in boundary-layer disturbances after they pass through the synchronization point. These observations of mode shapes confirm the receptivity path obtained in the phase speed, wave number, and growth rate comparisons.

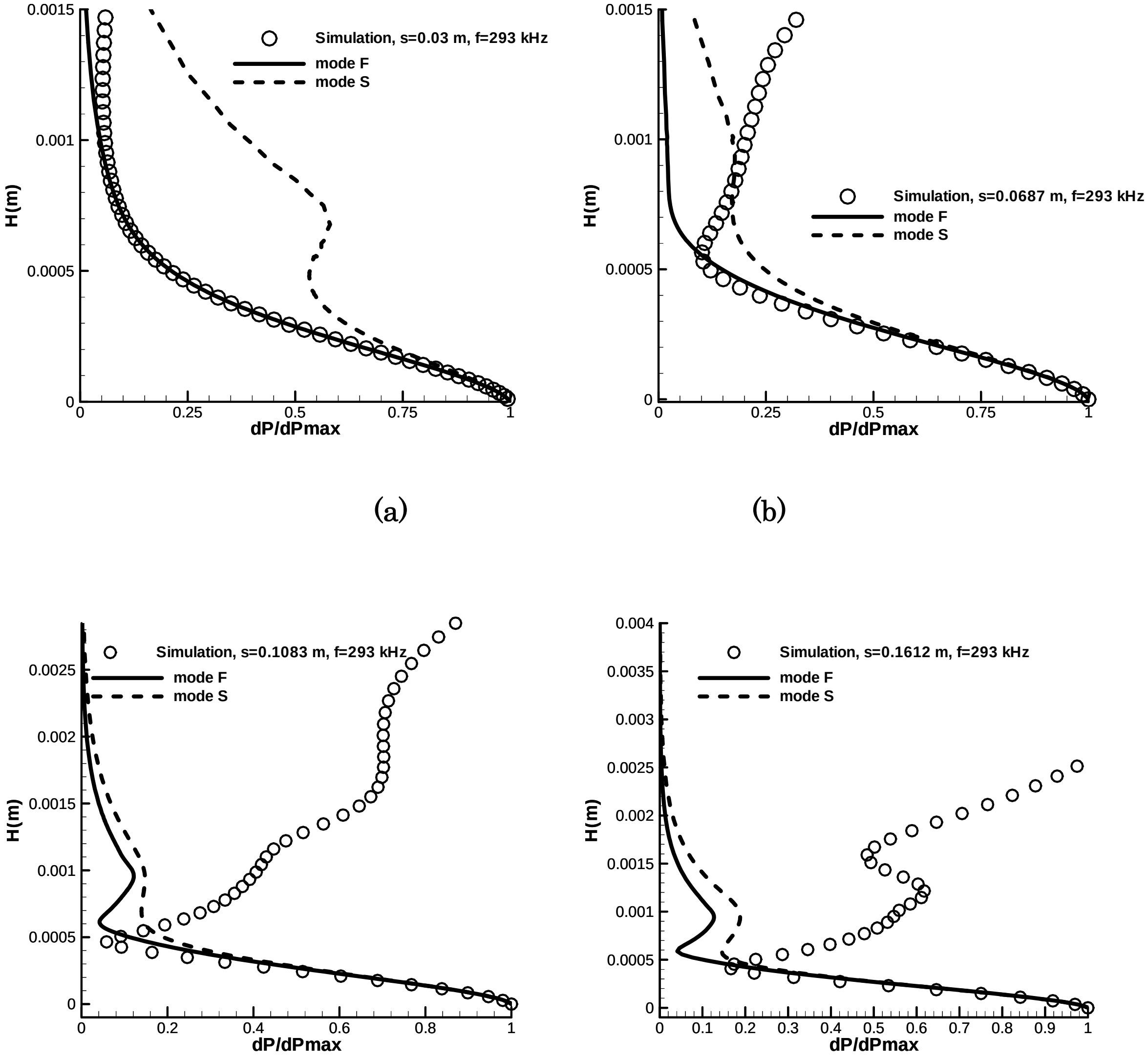
Simulation, s=0.03 m, f=293 kHz
mode F
mode S
H(m)
dP/dPmax
0.0015
0.001
0.0005
0
0
0.25
0.5
0.75
1
Simulation, s=0.0687 m, f=293 kHz
mode F
mode S
H(m)
dP/dPmax
0.0015
0.001
0.0005
0
0
0.25
0.5
0.75
1
Simulation, s=0.1083 m, f=293 kHz
mode F
mode S
H(m)
dP/dPmax
0.0025
0.002
0.0015
0.001
0.0005
0
0
0.2
0.4
0.6
0.8
1
Simulation, s=0.1612 m, f=293 kHz
mode F
mode S
H(m)
dP/dPmax
0.004
0.0035
0.003
0.0025
0.002
0.0015
0.001
0.0005
0
0
0.1
0.2
0.3
0.4
0.5
0.6
0.7
0.8
0.9
1

(a) (b)

(c) (d)

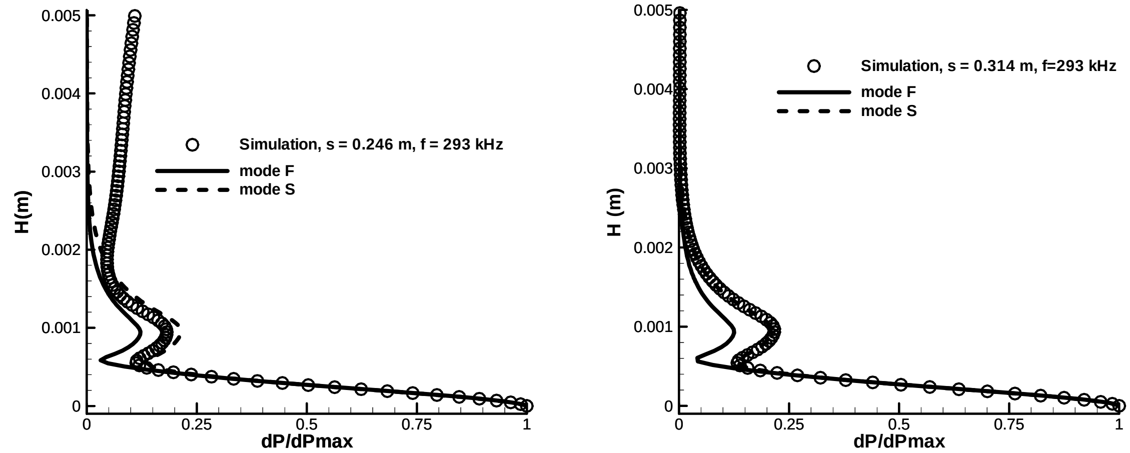

(e) (f)

Figure 57. Comparisons of wall-normal mode shapes of pressure perturbations between the simulation and LST at the frequency of 293 kHz at various locations.

The receptivity mechanism analyzed in this section agrees with the receptivity to freestream acoustic waves over a blunt cone, as reported in Zhong *et al.* [36], and the receptivity to freestream entropy waves over a flat plate in Ma *et al.* [4] However, this essentially differs from the receptivity over a flat plate reported by Fedorov *et al.* [94], where the case of freestream temperature spots, mode S is excited after the slow acoustic waves penetrate the boundary layer; this slow acoustic waves are generated by the spot-shock interaction.

4 Parametric Effects of Nose Bluntness and Freestream Mach Number

4.1 Freestream Conditions and Compression Cone Geometries of Parametric Cases

In the previous section the mechanisms of boundary-layer receptivity and stability in the standard case were discussed. In the next stage, the generalization of the linear receptivity and stability mechanisms with freestream entropy perturbations over blunt cones is established by studying receptivity and stability mechanisms with various parametric effects. Among these, the parametric effects of nose bluntness and freestream Mach number are chosen in the current study. When designing the aerodynamic configuration of a hypersonic vehicle, these effects are crucial.

In order to investigate the effects of nose bluntness and freestream Mach number, there are a total of five cases (Case 1, A1, A2, B1, B2), which are summarized earlier in Table 1. In the nose bluntness effect study, we set up two cases with different nose-radii, namely Cases A1 and A2. These are extended from the standard case, namely Case 1. Focusing only on nose bluntness effects, the freestream conditions used in Cases A1 and A2 are identical to Case 1, which are based on Mach-6 Quiet Tunnel at Purdue University (BAM6QT) [23]. The cone has a zero angle of attack to the freestream; the flow around the cone is axisymmetric. The wall of the cone is smooth, rigid, and isothermal. The full freestream conditions are shown earlier in Table 2.

The geometries of the blunt compression cone in Cases A1 and A2 are similar to the one that is used in Case 1. The schematics of the blunt compression cones are illustrated in Figure 10. The cone has a spherical nose section followed by a flared section. The starting point of the flared surface is tangent to the spherical nose surface with an initial angle of 2 degrees, while the flared geometry is a circular arc with a radius of $3.0\ \mathrm{m}$.

The nose radii of Cases A1 and A2 are different from Case 1. Case A1 has a nose radius of $0.5\ \mathrm{mm}$, and Case A2 has a nose radius of $0.1\ \mathrm{mm}$. The total length of the cone can be varied based on the development of boundary-layer disturbances over the cone in each case.

In the freestream Mach number effect study, we also set up two cases with different freestream Mach numbers, namely Cases B1 and B2, extended from the standard case, namely Case 1. Since the cone geometry effects are not focused in Cases B1 and B2, the cones we used to study in Cases B1 and B2 are the same as the cone in Case 1.

In order to focus only on the freestream Mach number effect without changing the other aspects in the flow field behind the shock, we increase the freestream Mach number in each case yet retain the freestream unit Reynolds number and the ratio of the total temperature in the flow to wall temperature from Case 1. More specifically, Table 4 lists the full flow conditions of Case B1:

Table 4. Freestream conditions of Case B1.

M_∞	10.0
ρ_∞^*	$0.01175\ \mathrm{kg/m^3}$
T_∞^*	20.6 K
T_o^*	432.6 K
T_{wall}^*	299.7 K
γ	1.4
Pr	0.72
R^*	$287.04\ \mathrm{N \cdot m / kg \cdot K}$ (air)
μ_r^*	$1.7894 \times 10^{-5} \mathrm{kg/m \cdot s}$ (sea level)
T_r^*	288 K (sea level)
T_s^*	110.3 K
Re_∞^*	$1.026 \times 10^7\ \mathrm{m}^{-1}$

Furthermore, the full flow conditions of Case B2 are listed in Table 5.

Table 5. Freestream conditions of Case B2.

M_∞	15.0
ρ_∞^*	$0.00764\ \mathrm{kg/m^3}$
T_∞^*	20.0 K
T_o^*	920 K
T_{wall}^*	637.4 K
γ	1.4
Pr	0.72
R^*	$287.04\ \mathrm{N \cdot m / kg \cdot K}$ (air)
μ_r^*	$1.7894 \times 10^{-5} \mathrm{kg/m \cdot s}$ (sea level)
T_r^*	288 K (sea level)
T_s^*	110.3 K
Re_∞^*	$1.026 \times 10^7\ \mathrm{m}^{-1}$

In both Cases B1 and B2, the cone has a zero angle of attack to the freestream, the flow around the cone is axisymmetric, and the wall of the cone is smooth, rigid, and isothermal.

4.2 Freestream Hotspot Parameters

Similar to the standard case, namely Case 1, we consider the axisymmetric flow field with the axisymmetric freestream hotspot that is initially aligned with the centerline of the cone. The freestream hotspot has a radius of approximately $0.003\,\mathrm{m}$. The radial Gaussian temperature profile of the hotspot in the freestream is similar to the one shown in Figure 30. At the center of the hotspot, the temperature is maximal and the radial coordinate is zero. The hotspot is initially placed at a location not far upstream from the bow shock along the centerline of cone. The hotspot radius is controlled by a dimensionless Gaussian factor, σ. In the current study, the dimensionless Gaussian factor is 0.001. The shape parameters of the freestream hotspot perturbations are based on the laser spot experiments of Salyer *et al.* [96, 97].

In the current study, the receptivity process is focused within the linear regime, thus a hotspot with very weak amplitude is imposed in the freestream. Previously, Ma *et al.* [4] and Zhong *et al.* [36] chose their freestream relative perturbation amplitudes as $O\left(10^{-4}\right)$, in order to keep the development of boundary-layer disturbances within the linear regime. Therefore, the freestream maximum relative amplitude of temperature perturbations at the center of hotspot , ε , is chosen to be 10^{-4} for all five cases, as expressed in Eq. (71).

The procedures of both the steady and unsteady simulation are very similar to those of Case 1. Based on the steady base flow, the unsteady numerical simulation is performed by imposing hotspot perturbations into the freestream in front of the bow shock. The Gaussian formulations given by Eqs. (39) to (42) are used to analytically model a three-dimensional hotspot that convects with the freestream. Moreover, this freestream hotspot is imposed onto the computational domain as an unsteady shock boundary condition.

4.3 Simulation Results for Nose Bluntness Effects

Nose bluntness has significant effects on the characteristics of the flow around the cone. Balakumar *et al.* [73, 88] carried out a numerical receptivity and stability study on nose bluntness effects over straight cones. However, their conclusions are drawn based on the comparisons between the results of different single sampling frequencies in each case. Lei *et al.* [48] performed an LST study on the bluntness effects over straight cones. More specifically, they aimed to investigate the transition reversal phenomenon when the nose became too blunt. Their results were based on several discrete frequencies. In the current study, the nose bluntness effects on the boundary-layer receptivity and stability are investigated over a wide continuous frequency spectrum, which can draw a more systematic and complete conclusion about nose bluntness effects.

Unless specified, all flow variables shown in the figures are dimensionless, which are normalized by the corresponding freestream values. For all contour plots, the upper boundary is the location of the shock, the lower boundary is the cone-wall, the left boundary is the flow inlet, and the right boundary is the flow exit. Since the cone is at a zero degree angle of attack, only the upper half of the cone is demonstrated. The lower half is the mirror image of the upper half due to the axis symmetry of the flow. Figure 11 shows the partial view of the computational grid structure around the cone. Due to the limited computer power for computing almost a million grid points at once, the simulation is divided into roughly 20 zones. Zone 1 is the computation domain that wraps around the hemispherical cone nose and Zones 2 through 20 wrap around the compression wall of the cone.

4.3.1 Steady Base Flow Solutions

In the current parametric study, the final goal is to study the nose bluntness effects over the boundary-layer receptivity to freestream hotspot perturbations and the linear growth of boundary-layer disturbances. The boundary-layer receptivity and linear growth study are carried out from the results of unsteady flow simulation. Moreover, the unsteady flow simulation is carried out based on the steady base flow. Hence, the initial step prior to all the subsequent analyses is investigating the nose bluntness effects on the steady base flow.

Steady base flow contours provide an overview of the distribution of a flow variable throughout the flow field. In Figure 58 to Figure 61, the Mach number contours and the entropy contours are presented. Figure 58 and Figure 59 show the Mach number contours of Case A1 and A2. For Case A1, the flow field extends to almost $x^* = 0.3\text{ m}$, and in Case A2, the flow field extends to $x^* = 0.22\text{ m}$. Both cases have very similar observations: there is a thin boundary layer that is blue in color above the wall, and the Mach number is very low in the nose region since there is a stagnation flow region where the viscous interaction is very significant. Shortly behind the nose region, the Mach number outside the boundary layer rises drastically for a very short distance. In contrast to the short rise of the Mach number immediately behind the nose region, the gradual decrease of Mach number throughout the rest of the cone is due to the adverse pressure gradient that is produced by the concavity of the flared cone surface. Eventually, a region of relatively low Mach number appears above the wall near the bottom of the cone. This trend of Mach number in the steady base flow field is similar to Case 1, which is discussed in Section 3.2.1. One of the main differences between the two cases of sharper cones (Case A1 and A2) and the standard case (Case 1) is as follows: the boundary-layer thickness behind the nose region is almost constant in Case 1. Cases A1 and A2, however, do not have constant boundary layer thicknesses.

According to Crocco's theorem, the curvature of bow shock in the nose region of a blunt cone generates a gradient of entropy, which is related to an entropy layer. In Figure 60 and Figure 61, the entropy contours of the steady base flow of Case A1 and A2 are shown. There is no gradient of entropy generated from the straight oblique shock far behind the nose region. However, there is a thin layer of entropy gradient next to the wall in both cases. This layer of entropy gradient is the resulting boundary layer that has swallowed the entropy layer generated by the curved shock in the nose region and shortly behind it. A more detailed study on the interactions between the entropy and boundary layers of the steady base flow are presented in the latter part of this section.

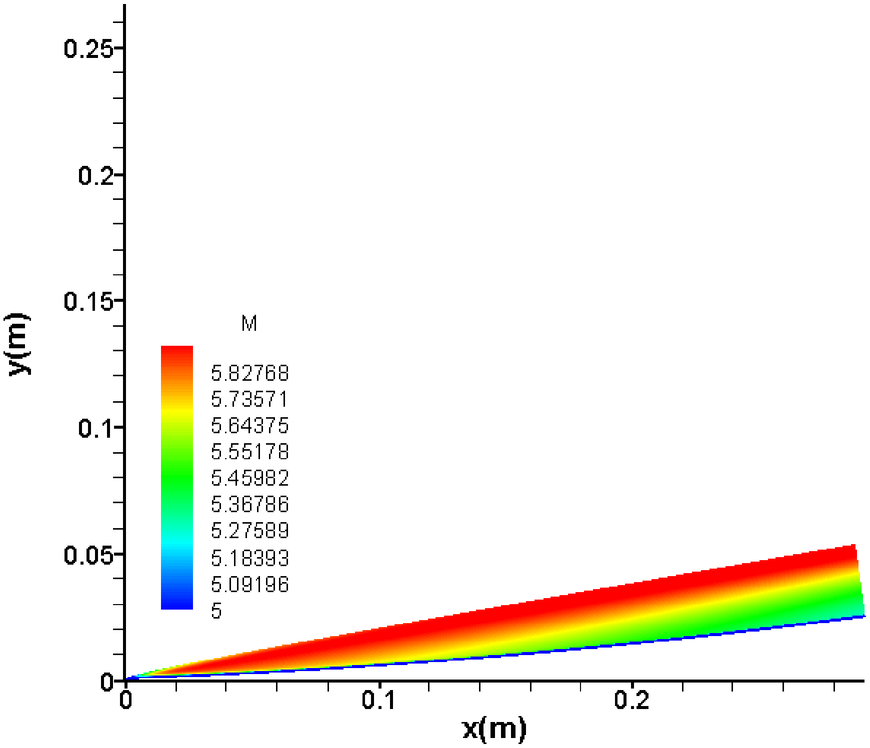

Figure 58. Mach number contours of Case A1 steady base flow.

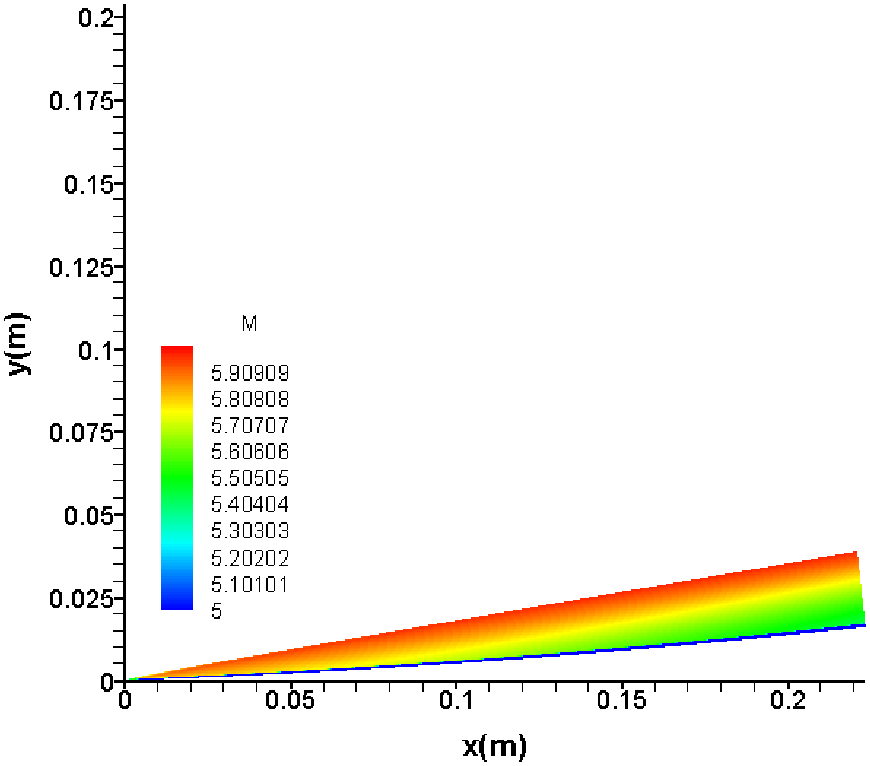

Figure 59. Mach number contours of Case A2 steady base flow.

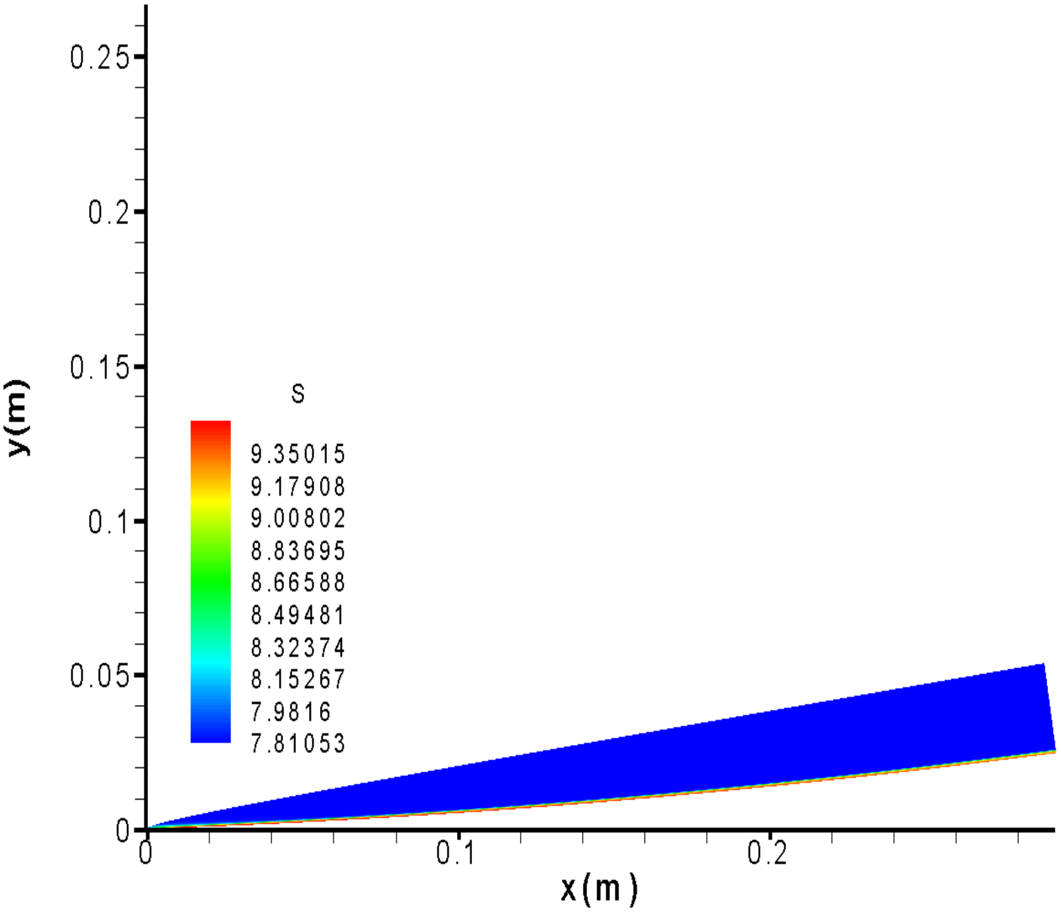

Figure 60. Entropy contours of Case A1 steady base flow.

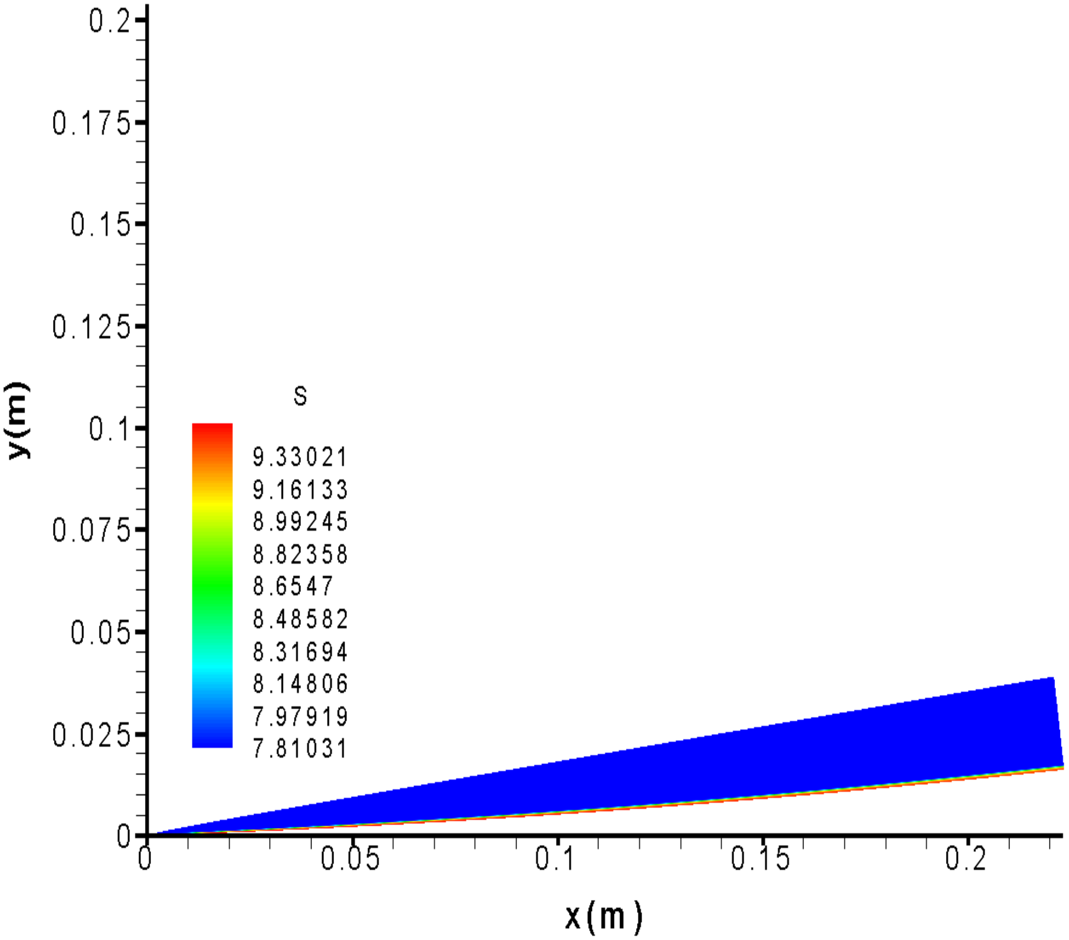

Figure 61. Entropy contours of Case A2 steady base flow.

In the parametric study, it is necessary to make comparisons between cases of differing parameters. While making comparisons, the common features or similarities between different cases are required. Therefore, expressing the dimensions in self-similarity or dimensionless variables is convenient in parametric study. Figure 62 shows the comparison of wall-normal profiles of velocity shortly behind the nose region between all three cases of different nose bluntness (Case 1, A1 and A2). Noticeably, the wall-normal height is normalized by the local boundary-layer thickness, and the velocity immediately behind the shock normalizes the velocity. Since the dimensional streamwise locations of all three cases are irrelevant due to the difference in cone geometry, the local Reynolds numbers are taken as a referencing common characteristic between all three cases. In Figure 62, the Reynolds number of 323 is chosen as a location in the upstream region shortly behind the nose. Moreover, the dimensional locations of all three cases are different. The velocity profiles outside the boundary layer are mostly uniform. However, the curvatures of the profiles at the edge of boundary layer are different for all three cases. More specifically, Case A2 has the largest curvature and Case 1 has the smallest curvature. The profile with a smaller curvature at the edge of the boundary layer has stronger nose effects. In other words: the flow field is closer to the nose and therefore the effects of the bow-shock curvature cause the variation of wall-normal velocity gradient in the shock layer and thus the boundary layer. In addition, the nose effects of the wall-normal profile imply that the less self-similar is the flow field in the early upstream region near the nose. From the comparison of the curvatures of the profiles at the edge of the boundary layer at the same local Reynolds number, the steady base flow field of the blunter cone has stronger nose effects at the same local Reynolds number.

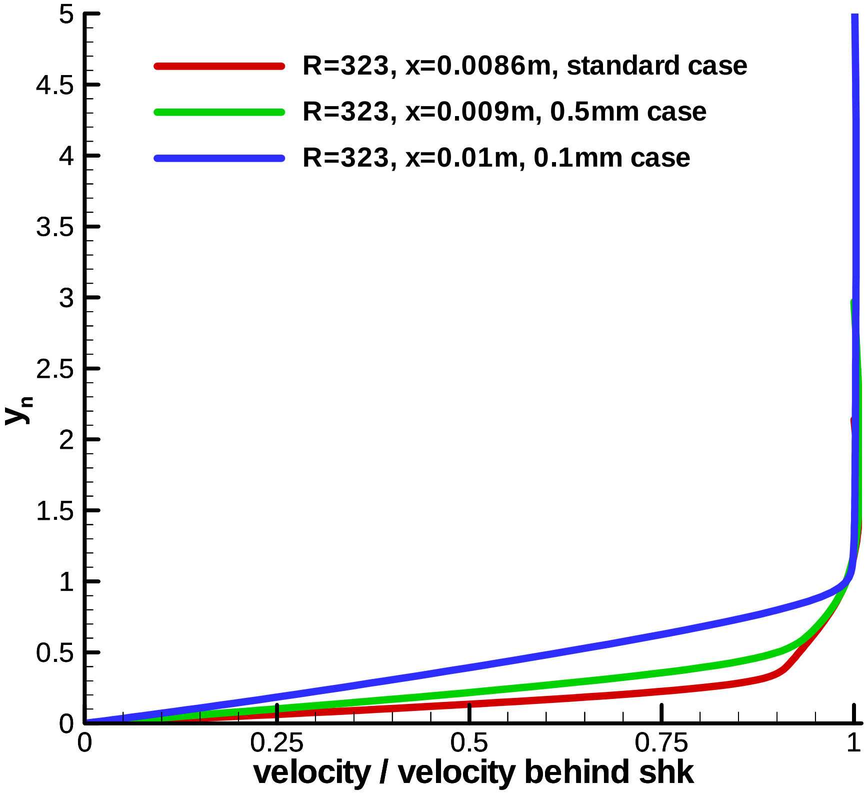

Figure 62. Comparison of the steady base wall-normal velocity profiles at the same local Reynolds number shortly behind the nose region between the cases of different nose bluntness (Case 1, A1 and A2).

In addition to velocity profiles, the wall-normal temperature profiles of Case 1, A1, and A2 are shown in Figure 63. Noticeably, the wall-normal height is normalized by the local boundary layer thickness, and the freestream temperature normalizes the local temperature. All profiles have the same local Reynolds number but not the dimensional spatial locations. Since the wall has an isothermal condition, the temperature profiles converge to a fixed value of around 5.8 at the wall for all three cases. It is obvious that the thickness proportion of boundary layer in the shock layer of Case 1 and A1 is far higher than that of Case A2. Moreover, the boundary-layer thickness proportion of Case 1 is higher than Case A1. The reason for having the higher boundary-layer thickness proportion is that the curvature of the bow shock in the nose region creates significant variation of temperature gradient in the shock layer and thus the boundary layer. In other words, the flow field has stronger nose effects. In addition, the nose effects of the wall-normal profile imply that the less self-similar is the flow field in the early upstream region nearby the nose. Based on the comparison of boundary-layer thickness proportions at the same local Reynolds number, the steady base flow field of blunter cone has stronger nose effects at the same local Reynolds number.

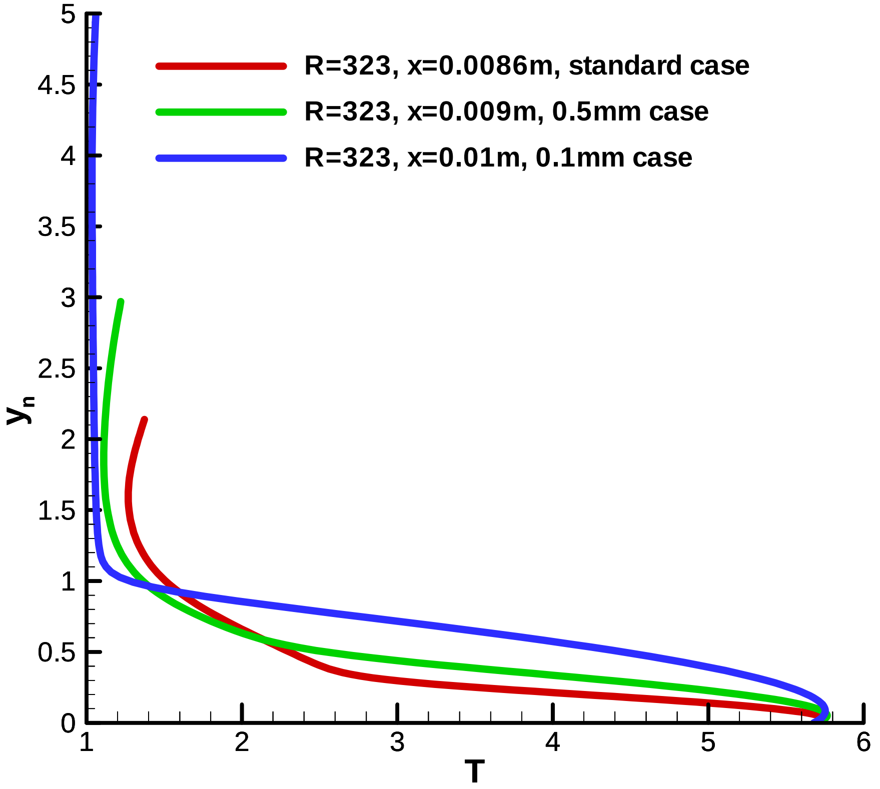

Figure 63. Comparison of the steady base wall-normal temperature profiles at the same local Reynolds number shortly behind the nose region between the cases of different nose bluntness (Case 1, A1 and A2).

The wall-normal profiles of velocity in the middle region of the cone between all three cases of different nose bluntness (Case 1, A1, and A2) are shown in Figure 64. Noticeably, the wall-normal height is normalized by the local boundary-layer thickness and the velocity immediately behind the shock normalizes the velocity. Since the dimensional streamwise locations of all three cases are irrelevant due to the difference in cone geometry, the local Reynolds numbers are taken as a referencing common characteristic between all three cases. In Figure 64, the local Reynolds number of 1015 is chosen as a location in the middle region of the cone. The velocity profiles outside the boundary layer are uniform, however, the curvatures of the profiles at the edge of boundary layer are different for all three cases. Specifically, Case A2 has the largest curvature, Case 1 has the smallest curvature, and Case A1 has the curvature that is only slightly smaller than Case A2. The profiles of Case A1 and A2 are close to similarity; however Case 1 is still far away from the cases of sharper cones. The profile with a smaller curvature at the edge of the boundary layer has stronger nose effects, in other words, the flow field is nearer the nose, and therefore, the effects of the bow-shock curvature would cause the variation of wall-normal velocity gradient in the shock layer and thus the boundary layer. In addition, the nose effects of the wall-normal profile imply that the flow field in the middle region of the cone is more self-similar than the one in the early upstream region. From the comparison of the curvatures of the profiles at the edge of the boundary layer at the same local Reynolds number, the steady base flow field of blunter cone has stronger nose effects at the same local Reynolds number.

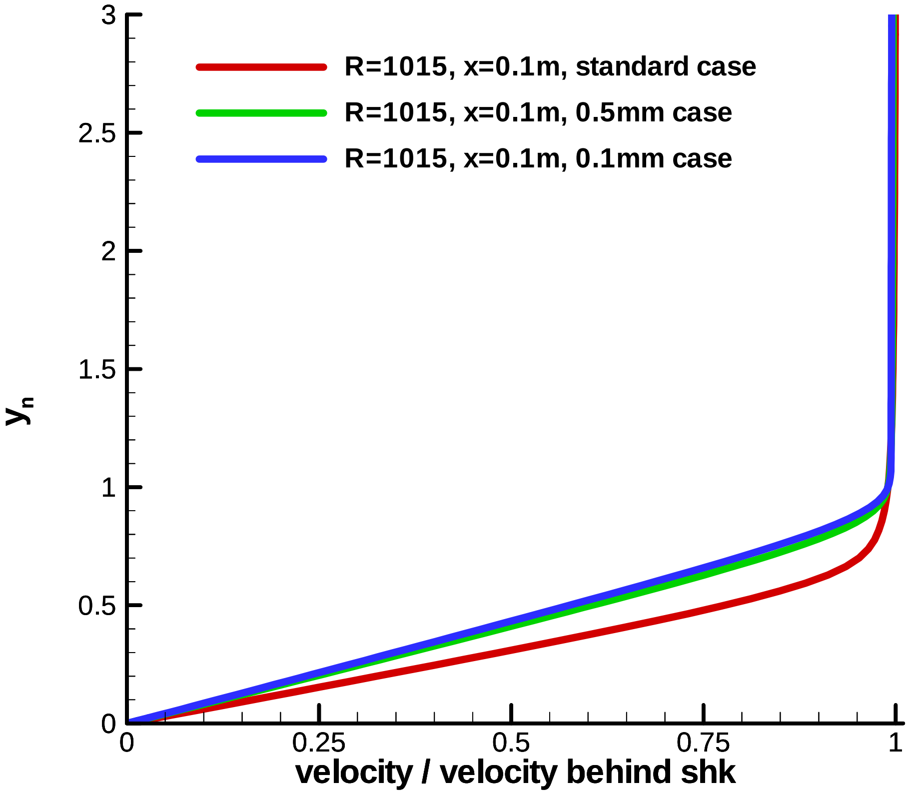

Figure 64. Comparison of the steady base wall-normal velocity profiles at the same local Reynolds number in the middle region of the cone between the cases of different nose bluntness (Case 1, A1 and A2).

In addition to velocity profiles, the wall-normal temperature profiles of Case 1, A1, and A2 in the middle region are shown in Figure 65. Noticeably, the wall-normal height is normalized by the local boundary layer thickness and the freestream temperature normalizes the local temperature. All profiles have the same local Reynolds number of 1015. Since the wall has the isothermal condition, the temperature profiles converge to a fixed value of around 5.8 at the wall for all three cases. It is obvious that the profile curvature at the edge of the boundary layer of Case A1 and A2 is larger than that of Case 1. Meanwhile, the profile curvatures of the boundary-layer edge of Case A1 and A2 are nearly similar. The reason for having lower profile curvature at the boundary-layer edge for Case 1 is that the curvature of the bow shock in the nose region distorts temperature gradient significantly in the shock layer and thus the boundary layer, in other words, the flow field has stronger nose effects. In addition, the nose effects of the wall-normal profile imply that the flow field in the middle region of the cone is more self-similar than the one in the early upstream region. From the comparison of curvatures of the profiles at the edge of boundary layer at the same local Reynolds number, one can conclude that the nose effects in the middle region of Case A1 and A2 are insignificant, and thus Case A1 and A2 has achieved self-similarity, while Case 1 still has the significant nose effects in the middle region.

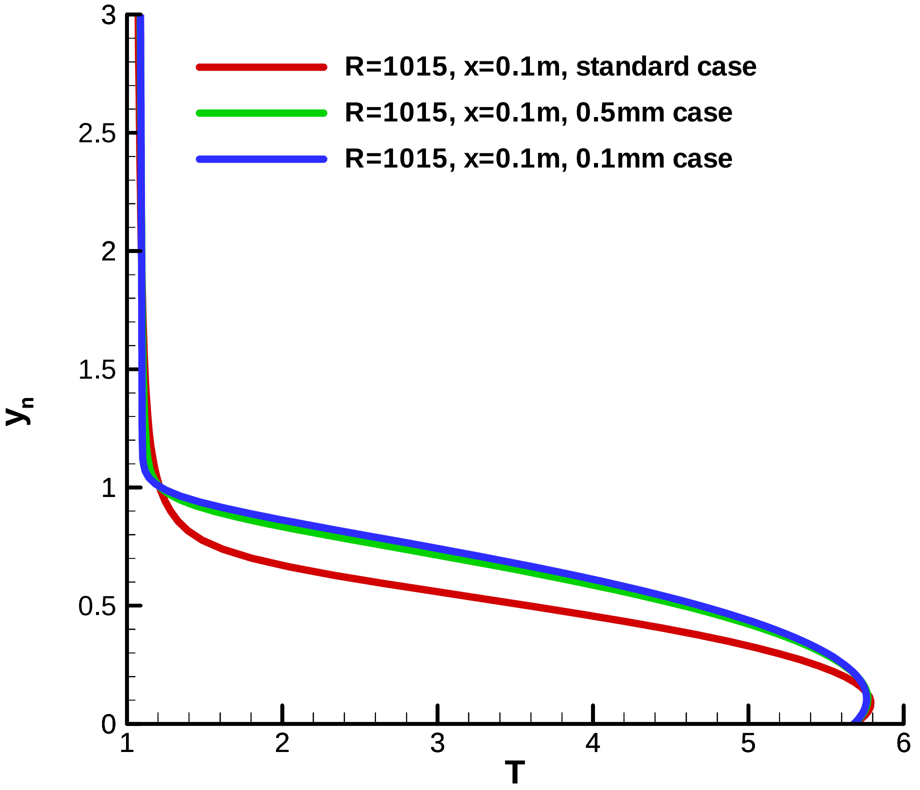

Figure 65. Comparison of the steady base wall-normal temperature profiles at the same local Reynolds number in the middle region of the cone between the cases of different nose bluntness (Case 1, A1 and A2).

Figure 66 shows the wall-normal profiles of velocity between all three cases of different nose bluntness (Case 1, A1, and A2) in the downstream region. Noticeably, the wall-normal height is normalized by the local boundary-layer thickness, and the velocity immediately behind the shock normalizes the velocity. Since the dimensional streamwise locations of all three cases are irrelevant due to the difference in cone geometry, the local Reynolds numbers are taken as a referencing common characteristic between all three cases. In

Figure 66, the local Reynolds number of 1506 is the chosen location in the downstream region of the cone. The velocity profiles outside the boundary layer are uniform. Different to the profiles in the earlier regions, those in the downstream region are very close to each other, excepting the profile curvature of the boundary-layer edge of Case 1, which is only slightly less than those of Cases A1 and A2. By comparing the observation in the downstream region to the earlier regions, the similarity of the profiles of all the cases of nose bluntness effects (Case 1, A1, and A2) in the downstream region implies that the nose effects are insignificant in the downstream region for Case 1, A1, and A2, and thus self-similarity is achieved in the flow field of the downstream region.

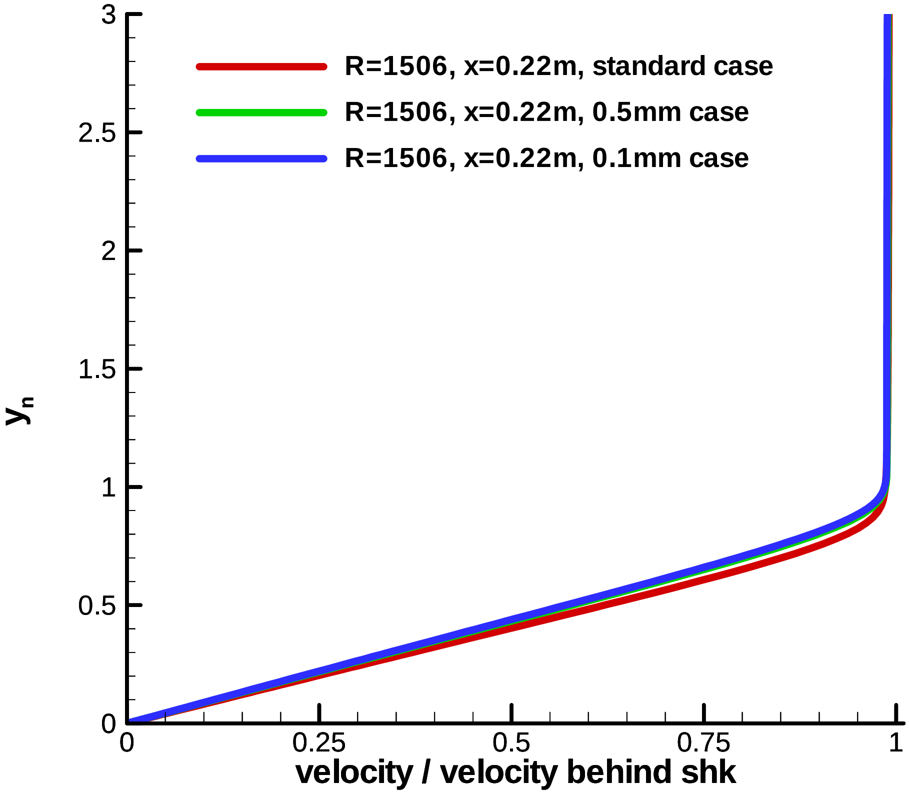

Figure 66. Comparison of the steady base wall-normal velocity profiles at the same local Reynolds number in the downstream region of the cone between the cases of different nose bluntness (Case 1, A1 and A2).

The wall-normal temperature profiles of Case 1, A1, and A2 in the downstream region are shown in Figure 67. Noticeably, the wall-normal height is normalized by the local boundary layer thickness and the freestream temperature normalizes the local temperature. All profiles have the same local Reynolds number of 1506. Since the wall has the isothermal condition, the temperature profiles converge to a fixed value of around 5.8 at wall for all three cases. The temperature profiles outside the boundary layer are uniform.

In contrast to the profiles in the earlier regions, those in the downstream region are in close proximity to each other, excepting the profile curvature of the boundary-layer edge of Case 1, which is only slightly less than those of Cases A1 and A2. By comparing the observation in the downstream region to those in the earlier regions, the similarity of the profiles of all the cases of nose bluntness effects (Case 1, A1, and A2) in the downstream region implies that the nose effects are insignificant in the downstream region for these cases and thus self-similarity is achieved in the flow field of the downstream region.

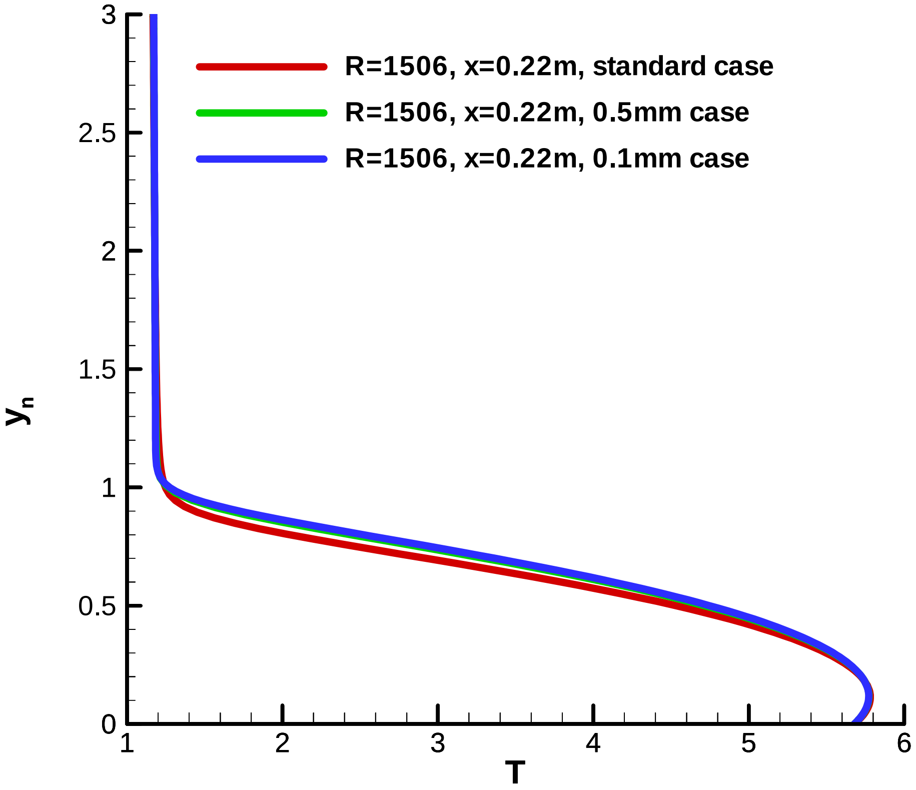

Figure 67. Comparison of the steady base wall-normal temperature profiles at the same local Reynolds number in the downstream region of the cone between the cases of different nose bluntness (Case 1, A1 and A2).

In the nose region, the curved shock generates inviscid vorticity in the flow field behind the shock. According to Crocco's Theorem, the gradient of entropy—which is related to entropy layer—is also generated due to the generation of vorticity by the shock curvature. As previously discussed in the results of Case 1, we characterize the entropy layer effects by a parameter named generalized velocity gradient, $\rho\left(du_t/dy_n\right)$, and the peak of such parameter within a compressible boundary layer is defined as a generalized inflection point. Lees and Lin [104] showed that the existence of generalized inflection point is a necessary and sufficient condition for the existence of inviscid instability in a compressible boundary layer.

In Figure 68 and Figure 69, the evolution of the generalized inflection point that involves the interaction of entropy layer and boundary layer is demonstrated for the Case A1 and A2. The dimensionless wall-normal height, y_n, is normalized by the local thickness of boundary layer in both figures for maintaining self-similarity. The generalized velocity gradient is shown in the abbreviated mathematical notation, ρDU. Both local Reynolds numbers and the corresponding x-coordinates of various locations are shown in the legend.

In Figure 68 (a), the wall-normal profiles of generalized velocity gradient of Case A1 at various locations upstream near by the nose region are shown. The viscous effects from the wall occur throughout the entire upstream flow field near the nose region. The earliest location of R=90.2 is immediately behind the nose region. At this location, a peak of generalized velocity gradient initially enters the flow field from shock. In the subsequent locations of R=101.7 to 194.7, the peak moves towards the wall, meanwhile, its amplitude attenuates. These observations imply that the entropy layer generated by the bow shock moves toward the wall, while the entropy layer moves downstream. Additionally, the entropy layer is gradually swallowed by the boundary layer during this movement.

The wall-normal profiles of generalized velocity gradient of Case A1 at further downstream locations are demonstrated in Figure 68 (b). At the location of R=250.2, the peak is completely swallowed by the boundary layer. A turning point appears around the local boundary-layer normalized height of 0.3, which is near the wall. At the location of R=323, a peak of generalized velocity gradient, which is the generalized inflection point, first appears below the turning point at the local boundary-layer normalized height of 0.3. According to Mack [24], and Lees and Lin [104], the inviscid neutral waves exist at the generalized inflection point, where the discontinuity of Reynolds stress appears. This is the sufficient condition for the existence of inviscid instability in the boundary layer. Mack [24], and Lees and Lin [104] also pointed out that the phase velocity of the neutral inviscid wave is the same as the mean velocity at the generalized inflection point. From the subsequent locations from R=323 to 1015, the generalized inflection point moves toward the edge of the boundary-layer. As mentioned in Mack [24], this is the result of increasing the Mach number of the flow above the boundary layer at those subsequent locations, which causes the mean velocity at the generalized inflection point and the phase velocity of the neutral inviscid wave to increase. The outward movement of the generalized inflection point leads to a more unstable boundary layer. In Figure 68 (b), the generalized inflection point stays at the almost constant self-similar wall-normal height of 0.8, which is near the edge of the boundary layer at the locations downstream from R=1015.

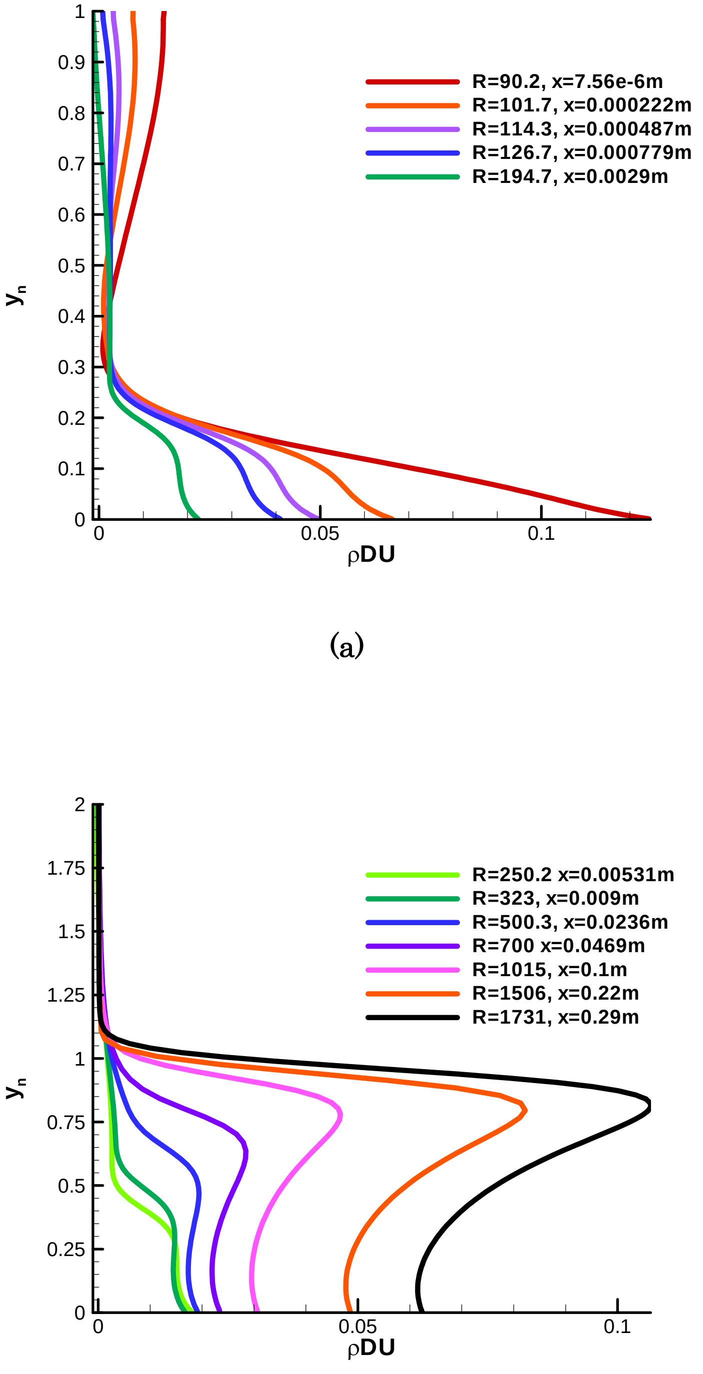

(a)

(b)

Figure 68. Wall-normal generalized velocity gradient at various (a) upstream and (b) downstream locations of Case A1.

In Figure 69 (a), the wall-normal profiles of generalized velocity gradient of Case A2 at various locations upstream near the nose region are shown. The viscous effects from the wall occur throughout the entire upstream flow field near the nose region. The earliest location of R=40.3 is immediately behind the nose region and at this location, a peak of generalized velocity gradient initially enters the flow field from shock. In the subsequent locations of R=45.5 to 75, the peak moves towards the wall, meanwhile, its amplitude attenuates. These observations imply that the entropy layer generated by the bow shock moves toward the wall, while the entropy layer is moving downstream. Additionally, the entropy layer is gradually swallowed by the boundary layer during this movement.

The wall-normal profiles of generalized velocity gradient of Case A2 at further downstream locations are demonstrated in Figure 69 (b). At the location of R=100.5, the peak is completely swallowed by the boundary layer. There is a turning point which appears around the local boundary-layer normalized height of 0.5, which is near by the wall. At the location of R=120.5, a peak of generalized velocity gradient, which is the generalized inflection point, first appears below the turning point at the local boundary-layer normalized height of 0.45. According to Mack [24], and Lees and Lin [104], the inviscid neutral waves exist at the generalized inflection point, where the discontinuity of Reynolds stress appears, and this is the sufficient condition for the existence of inviscid instability in the boundary layer. Mack [24], and Lees and Lin [104] also pointed out that the phase velocity of the neutral inviscid wave is the same as the mean velocity at the generalized inflection point. From the subsequent locations from R=120.5 to 323, the generalized inflection point moves toward the edge of the boundary-layer. As mentioned in Mack [24], this is a result of increasing Mach number of the flow above the boundary layer at those subsequent locations, which causes the mean velocity at the generalized inflection point as well as the phase velocity of the neutral inviscid wave increases. The outward movement of the generalized inflection point leads to a more unstable boundary layer. In Figure 69 (b), the generalized inflection point stays at the almost constant self-similar wall-normal height of 0.8, which is near the edge of the boundary layer, at the locations downstream from R=323.

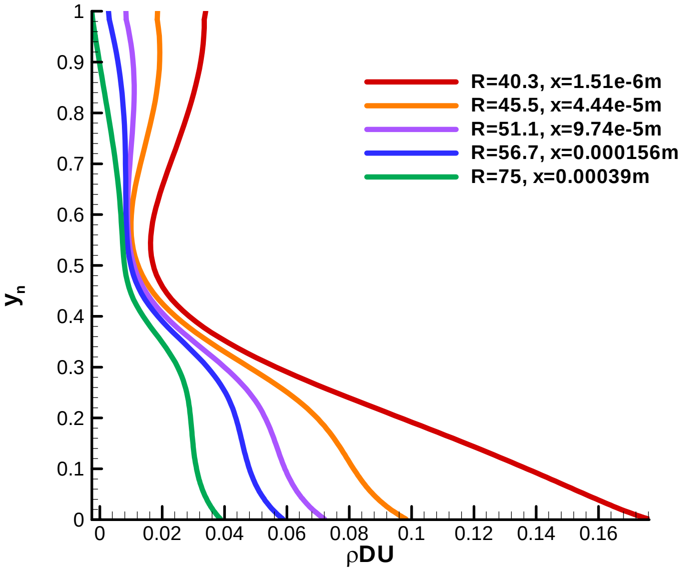

(a)

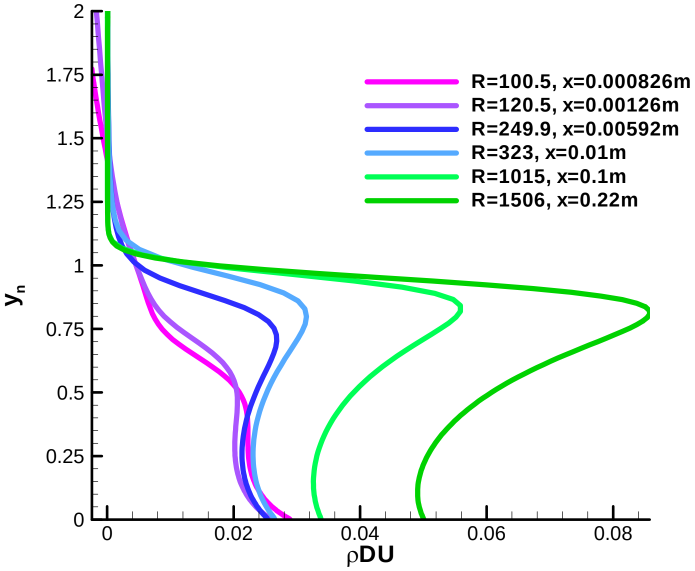

(b)

Figure 69. Wall-normal generalized velocity gradient at various (a) upstream and (b) downstream locations of Case A2.

From the above observations of the sharper cases (Case A1 and A2) and the earlier observations of Case 1, the overall evolution of the entropy-layer/boundary-layer interaction is similar among Cases A1, A2 and 0. More specifically, the entropy layer is first created by the curved shock in the nose region, then gradually moves toward the wall and diffuses into the boundary layer, while moving downstream. Eventually the entropy layer is completely swallowed by the boundary layer and a generalized inflection point follows. The generalized inflection point, a sufficient condition of having inviscid instability in the boundary layer, then gradually moves toward the edge of the boundary layer.

Although the overall evolution of the entropy-layer/boundary-layer interaction is similar for Cases A1, A2 and 0, the local Reynolds numbers for evolving into each stage of the evolution are different between different nose bluntness based on the above quantified observations in the generalized velocity profiles of Cases 1, A1 and A2. Specifically, the sharper cone has smaller local Reynolds numbers for evolving into each stage because of the smaller length scale of the boundary layer. In other words, the sharper cone has an earlier occurrence of inviscid instability.

In addition to the trend of local Reynolds numbers, the self-similar wall-normal heights for the initial appearance of the generalized inflection point of Cases 1, A1 and A2 are different. More specifically, the sharper cone has a higher initially appearing generalized inflection point. Conversely, the final constant heights of the generalized inflection point downstream are almost the same for all cases of differing nose bluntness (Cases 1, A1 and A2).

4.3.2 Analyses of Boundary-Layer Disturbances and Stability

The previous parametric comparison discussion is based on the steady base flow over cones with different nose bluntness. One of the main goals of the current parametric study is to investigate the nose bluntness effects in the boundary-layer receptivity to the freestream disturbances and the subsequent linear growth of the boundary-layer disturbances. Prior to performing these receptivity and linear growth studies, the unsteady simulations of the hotspot perturbed flow based on the steady base flow behind the shock over the compression cones with different nose radii are completed.

Identical to the set up of Case 1, we consider the axisymmetric flow field with the axisymmetric freestream hotspot that is initially aligned with the centerline of the cone. The freestream hotspot has a radius of about $0.003\,\mathrm{m}$, and the radial Gaussian temperature profile of the hotspot in the freestream is shown in Figure 30. At the center of the hotspot, the temperature is maximal and the radial coordinate is zero. The hotspot is initially placed at a location not far upstream from the bow shock along the centerline of cone. The hotspot core radius is controlled by a dimensionless Gaussian factor, σ, and in the current study, the dimensionless Gaussian factor is 0.001. The shape parameters of the freestream hotspot perturbations are based on the laser spot experiments of Salyer *et al.* [96, 97].

The receptivity process and the boundary-layer disturbances' growth studied in this work fall into the linear regime. Hence, the amplitude of the hotspot imposed in the freestream should be very weak. Previously, Ma *et al.* [4] and Zhong *et al.* [36] chose their freestream relative perturbation amplitudes as $O\left(10^{-4}\right)$ in order to keep the development of boundary-layer disturbances within the linear regime. Therefore, the freestream maximum relative amplitude of temperature perturbations at the center of hotspot, ε, is chosen to be 10^{-4} as expressed in Eq. (71).

After obtaining the steady base flow solution, the unsteady numerical simulation with a freestream hotspot is carried out. The Gaussian formulations that are given by Eqs. (39) to (42), are used to analytically model a three-dimensional hotspot that convects with the freestream. Furthermore, the freestream hotspot is imposed onto the computational domain as an unsteady shock boundary condition.

When performing the simulations in the parallel computers, the simulated time history of the pressure perturbations in boundary layer is recorded at every grid point along the cone surface, and the subsequent receptivity and disturbance growth studies are carried out based on this time history. The recording time steps are very small in order to obtain a sufficiently high resolution in the recorded time-history that carries the high frequency components of the simulated boundary-layer disturbances. The details of the recording procedures are very similar to Case 1, which are described earlier in Section 3.2.4.

Figure 70 to Figure 73 present the time-history traces of wall-pressure perturbations of Case A1 and A2 at some sampling locations throughout the upstream and downstream part of the cones. Noticeably, the amplitudes of the pressure perturbations are normalized with respect to the value of freestream pressure.

Figure 70 shows the wall-pressure perturbations travelling through the upstream part of the sharper cone in Case A1. At the stagnation point in the nose region at $x^* = -0.0005\ \text{m}$, the perturbation time-history profile initially has a pure Gaussian shape. Shortly behind the nose region from $x^* = 0.0058\ \text{m}$ to $0.08\ \text{m}$, the profile becomes more complicated containing many peaks. Simultaneously, the overall amplitude of the perturbations decays while travelling downstream. In the range from $x^* = 0.08\ \text{m}$ to $0.125\ \text{m}$, the wave profile is split into two parts that have different waveforms: a faster part and a slower part. The faster part is the part of the wave packet that arrives at the sampling location at an earlier time. In other words, it travels faster between these sampling locations. Vice versa, the slower part is the part of the wave packet that travels slower between these sampling locations. The faster part on the left of the wave packet is more oscillatory, while conversely, the slower part on the right of the wave packet has a monotonic shape. Their overall amplitudes are comparable with each other. The faster part has the frequency of around 167 kHz. This is the stable mode F that is excited by the fast acoustic waves inside and near the nose region, while mode S is excited by the slow acoustic waves.

In order to characterize the growth of the wave packet in the current parametric study, the average growth rate of the overall wave packet is introduced in Section 3.2.4 by Eq. (72). By following this equation, the calculated average growth rate of the stable wave packet from $x^* = 0.0058\ \text{m}$ to $0.08\ \text{m}$ is $-11.8\ \text{m}^{-1}$. Noticeably, there is a new waveform that has very small amplitudes first appearing at the right side of the slower part behind $0.0002\ \text{s}$ at $x^* = 0.125\ \text{m}$. The new waveform at this location has a frequency of approximately 333 kHz.

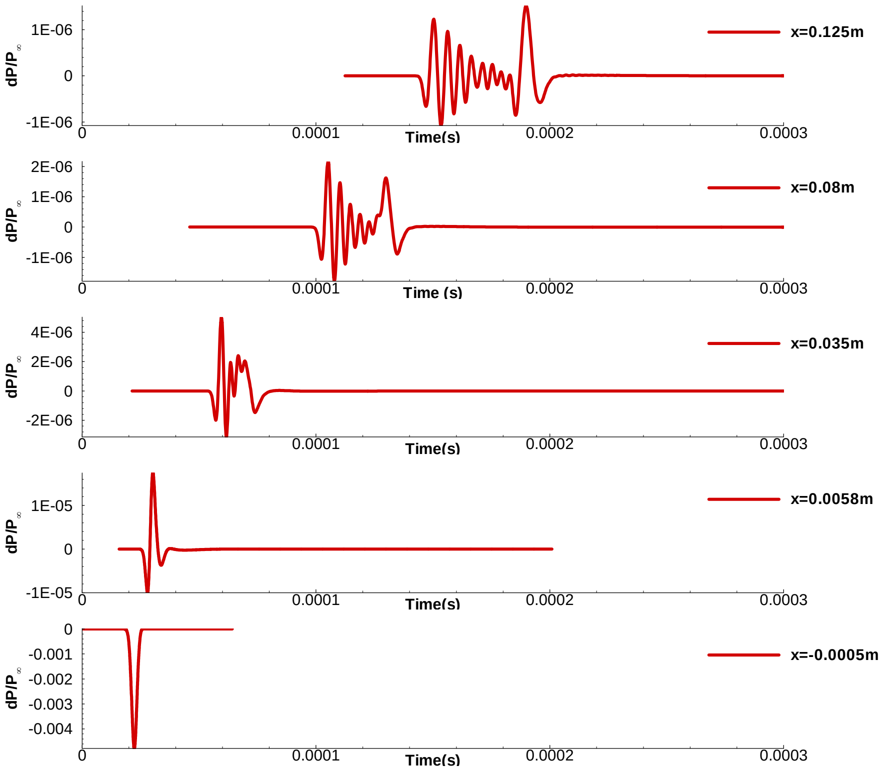

Figure 70. Time-history traces of pressure perturbations at wall at various streamwise locations over the upstream part of the cone in Case A1.

Figure 71 shows the wall-pressure perturbations in the downstream part of the sharper cone in Case A1. In this part of the cone, the new waveform of higher frequency that appears at the right end of the wave packet catches up and combines with the slower part. As a result, the slower part becomes oscillatory with the higher frequency. The faster part at the left-hand-side of the wave packet continuously attenuates throughout all the sampling locations, while the amplitudes of the newly combined slower part is growing so rapidly, thus it soon surpasses those of the decaying faster part, and becomes the dominant instability in the boundary layer. Eventually, the faster part becomes insignificant. The combined dominantly growing new waveform is relevant to the mode S related second mode instability. The frequency of the maximum amplitude of the dominantly growing waveform is found to be around 317 kHz at $x^* = 0.26\ \text{m}$. The similar approach to quantify the growth of the wave packet in the upstream part of the cone is to calculate the average growth rate of the overall second mode dominated wave packet. The calculated average growth rate of the overall second mode dominated wave packet from $x^* = 0.2\ \text{m}$ to $0.26\ \text{m}$ is $112\ \text{m}^{-1}$. The latter discussion of receptivity mechanisms in Section 4.3.3 supports the findings from the analysis of the time-history traces.

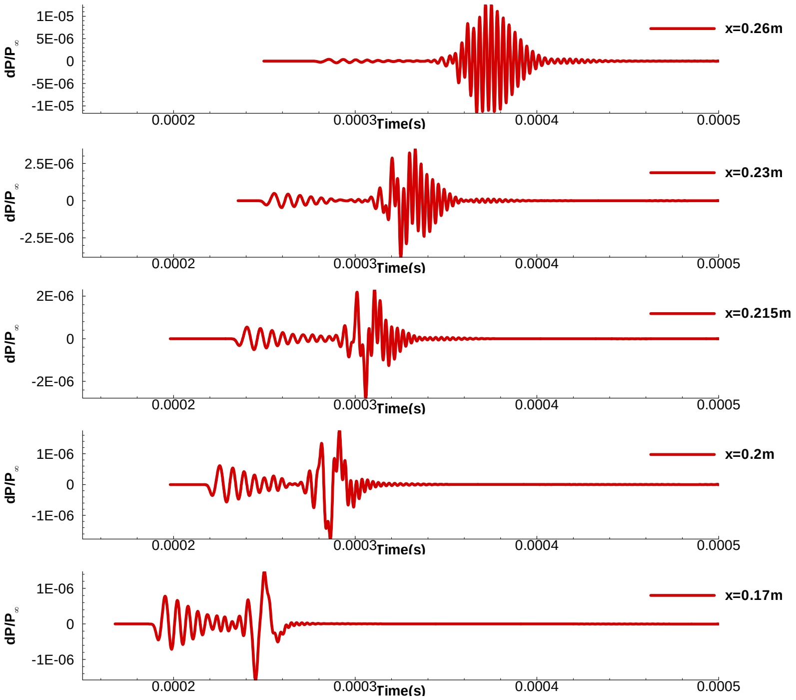

Figure 71. Time-history traces of pressure perturbations at wall at various streamwise locations over the downstream part of the cone for Case A1.

Figure 72 shows the wall-pressure perturbations travelling through the upstream part of the sharpest cone in Case A2. At the stagnation point in the nose region at $x^* = -0.0001\ \text{m}$, the perturbation time-history profile initially have a pure Gaussian shape. Behind the nose region from $x^* = 0.00115$ m to 0.03 m, the profile gradually becomes more complicated and containing many peaks. At the same time while the wave packet is travelling downstream, the overall amplitude of the perturbations decays. The average growth rate of the overall wave packet amplitude from $x^* = 0.00115$ m to 0.03 m is $-32.8\ \text{m}^{-1}$. Similar to the blunter cases, the faster part of the wave packet and the slower part, or mode F and mode S still exist. However, the profiles for both parts are not distinguishable, and their amplitudes are also comparable to each other in a stable range.

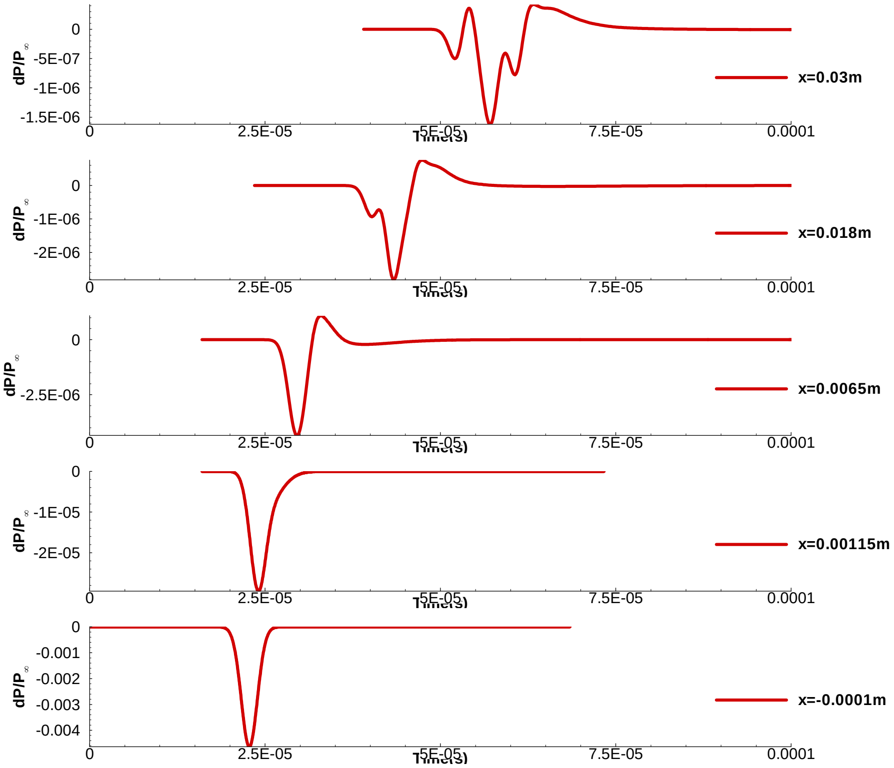

Figure 72. Time-history traces of pressure perturbations at wall at various streamwise locations over the upstream part of the cone for Case A2.

Figure 73 shows the wall-pressure perturbations in the downstream part of the sharpest cone in Case A2. At $x^* = 0.054$ m, the overall wave packet amplitudes still attenuate, and the faster part and the slower part are still not distinguishable. A new unstable waveform first appears on the right end of the wave packet at $x^* = 0.078$ m. At this location, the faster part and the slower part of the wave packet merely become distinguishable by the obvious amplitude difference at 0.00012 s. The faster part on the left-hand-side of the wave packet has smaller amplitude. Conversely, the slower part on the right-hand-side of the wave packet possesses stronger and rapidly growing amplitude at the same time as the appearance of the new unstable waveform at around 0.00013 s at $x^* = 0.078$ m. At this location, the new waveform has a frequency of approximately 550 kHz.

From $x^* = 0.078$ m to 0.197 m, the new waveform of higher frequency that appears at the right end of the wave packet catches up and merges into the slower part. As a result, the slower part becomes more oscillatory. The stable faster part at the left side of the wave packet continuously attenuates throughout all sampling locations, while the amplitudes of the newly combined slower part grow rapidly. Thus, it soon surpasses those of the decaying faster part and becomes the dominant instability in the boundary layer. Eventually, the faster part becomes insignificant. The combined dominantly growing new waveform is relevant to the mode S related second mode instability. The frequency of the maximum amplitude of the dominantly growing waveform is found to be around 340 kHz at $x^* = 0.197$ m. The calculated average growth rate of the overall second mode dominated wave packet from $x^* = 0.078$ m to 0.197 m is 472 m^{-1}. The latter discussion of receptivity mechanisms in Section 4.3.3 supports the findings from the analysis of the time-history traces.

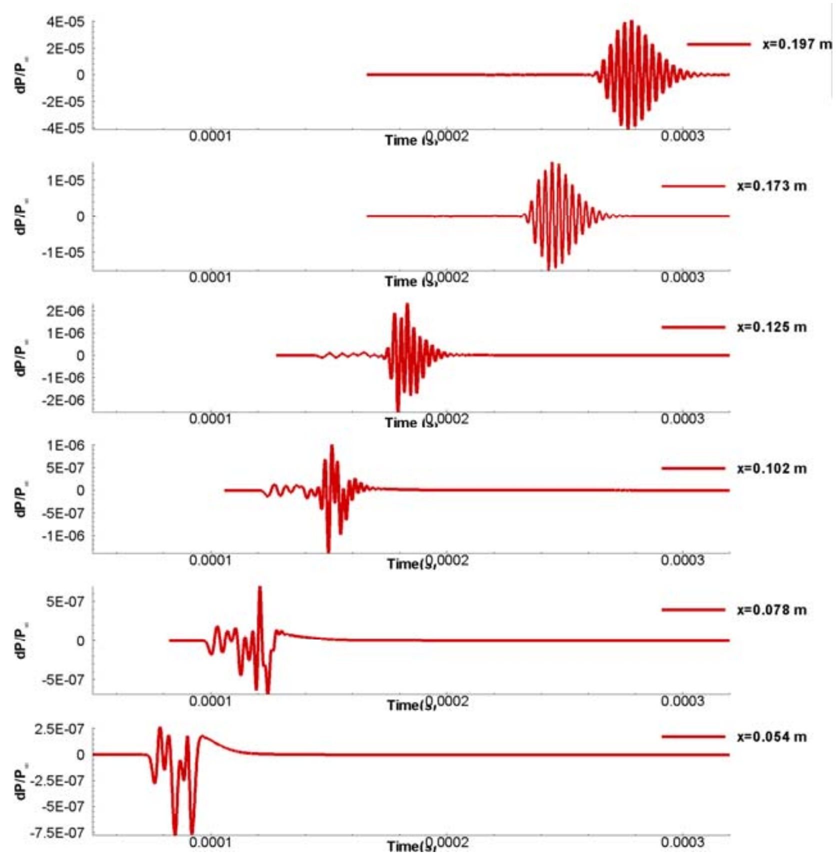

Figure 73. Time-history traces of pressure perturbations at wall at various streamwise locations over the downstream part of the cone for Case A2.

By comparing the observation and results in the time history of the boundary-layer wave packet between the cases of different nose bluntness (Case 1, A1 and A2), one can see that there are trends of the locations of the new unstable waveform appearance with respect to different nose bluntness. Specifically, a location of the initial appearance of the new unstable waveform is more upstream for a sharper cone. Such trend implies that the dominant boundary-layer instability appear earlier as the cone becomes sharper.

In addition to the locations of the initial appearance of the new unstable waveform, the frequency of the stable and unstable waveform and the shift of such frequency throughout the growth of the unstable wave also have a trend with respect to the nose bluntness. Specifically, a sharper cone has a higher stable waveform frequency. Moreover, a sharper cone also has a higher initial frequency of the unstable waveform at its initial appearance location. The reason for having higher frequencies of both the stable and unstable waveforms over a sharper cone is due to the boundary-layer over a sharper cone being thinner. Also, the downshift of frequency over a unit distance during the growth of the unstable waveform is found to be larger for a sharper cone. This implies that the growth of boundary-layer thickness is faster over a sharper cone.

Finally, the average growth or decay rate of the wave packet also varies with respect to different nose bluntness. To be specific, the decay rate of the stable waveform in the upstream part of the sharper cone is larger, and the growth rate in the downstream part of the sharper cone is also larger. This observation implies that the decay and the growth of the wave packet are more vigorous over a sharper cone.

After investigating the nose bluntness effects on the overall development of the wave packet in the boundary layer, the following stage is to carry out a detailed parametric study of the nose bluntness effects on the frequency component behavior in the boundary-layer disturbances along the cone. In order to study the frequency components, the Fourier transformation based on the time history of wall-pressure perturbations is carried out at various surface locations. The formulations of the Fourier transformation are shown in Section 2.5. The simulated perturbations are single impulse, which is temporally "transient", i.e. they do not continue to repeat in time at a given location. The transient perturbed flow at a location eventually returns back to its steady base flow after the passage of the perturbations. When conducting the Fourier transformation, the time history of single impulse is windowed with no more perturbations existing on both sides.

More specifically, the Fourier transformed amplitudes in the current study are independent of the width of the time-window as long as the relative amplitudes of the pressure perturbations at both end are $O(10^{-9})$. In this way, a periodicity of the signal is assumed in the time domain. The maximum recording time-step size of the time histories is 1.4×10^{-7} s, which is sufficient to resolve the second mode instability at the high end of the studied frequency range. Our Fourier transformed results are confirmed to be independent of the time step used when we were post-processing the data from the simulation using the current windowed-Fourier transformation.

It is shown in Figure 40 that the amplitudes of the freestream forcing disturbances are not uniform at different frequencies. Hence, in order to include such frequency effects in the analyses of boundary-layer receptivity and instability growth, it is necessary to normalize the amplitudes of the wall-pressure-perturbations by those of the freestream forcing disturbances. The expression of the normalized amplitude is shown in Eq. (73), and the details are explained in the paragraph around such equation in Section 3.2.4.

The normalized amplitude frequency spectra of behind-shock acoustic waves and entropy waves in the nose region of Case A1 and A2 are shown in Figure 74 and Figure 75. In order to compare the relative strength in the local flow field between the pressure and entropy perturbations, the local perturbation amplitude is divided by the local steady base value immediately behind the shock. Both pressure and entropy waves are the result of the combined interactions of the shock with the freestream hotspot perturbations, and the reflected acoustic waves behind the shock. Each line represents the spectrum at a shock location that has a specific angle between the stagnation line in front of the cone nose and the line that connects the shock location and the origin.

In the spectra of Case A1 in Figure 74, the maximum generated acoustic waves behind the shock appear on the stagnation line where the angle is 0. These generated waves mainly decay at downstream shock locations in the nose region. The normalized amplitudes of the acoustic wave spectra or pressure perturbations have local maxima at the frequency from 340 to 260 kHz at the angles from 0 to 40 degrees. These maxima are caused by the resonance of the acoustic waves that bounces between the shock and the wall in the nose region. Moreover, the downshift of the resonance frequency downstream is due to the increasing shock-layer thickness downstream in the nose region. However, the angle of 0 degree on the stagnation line has the minimum generated entropy waves behind the shock. These generated entropy waves mainly increase at downstream shock locations in the nose region. The generated waves reach the maximum generated entropy waves behind the shock around the end of the nose region at the angles of 80 and 88 degrees for the frequency components under 480 kHz. For the frequency components above 480 kHz, the angle of 60 degrees has the maximum generated entropy waves behind the shock. The amplitudes of entropy waves have the local minima from 190 kHz to 110 kHz at the angles from 0 to 40 degrees. From Figure 74 (a), the maximum normalized amplitude of the pressure disturbances just behind the shock is 1.09 at 0 degree with the frequency of 340 kHz. Such maximum relative strength of pressure perturbations immediately behind the shock is slightly higher than the relative strength of freestream perturbations due to the resonance interaction around the stagnation line. The overall amplitudes fall in the range from 0.61 to 1.09. The mean value of amplitude in this range is 0.85. From Figure 74 (b), the maximum strength of the entropy perturbations is 0.0665 at 60 degrees with the frequency of 520 kHz. The overall amplitudes fall in the range from 0.0425 to 0.0665. The mean value of amplitude in this range is 0.0545. By comparing the amplitudes of both perturbations, one can see that the normalized amplitudes of the acoustic waves or pressure perturbations are more than an order of magnitude higher than the entropy perturbations. Such observation indicates that after the hotspot/shock interaction in the nose region, the perturbations are mainly acoustic waves.

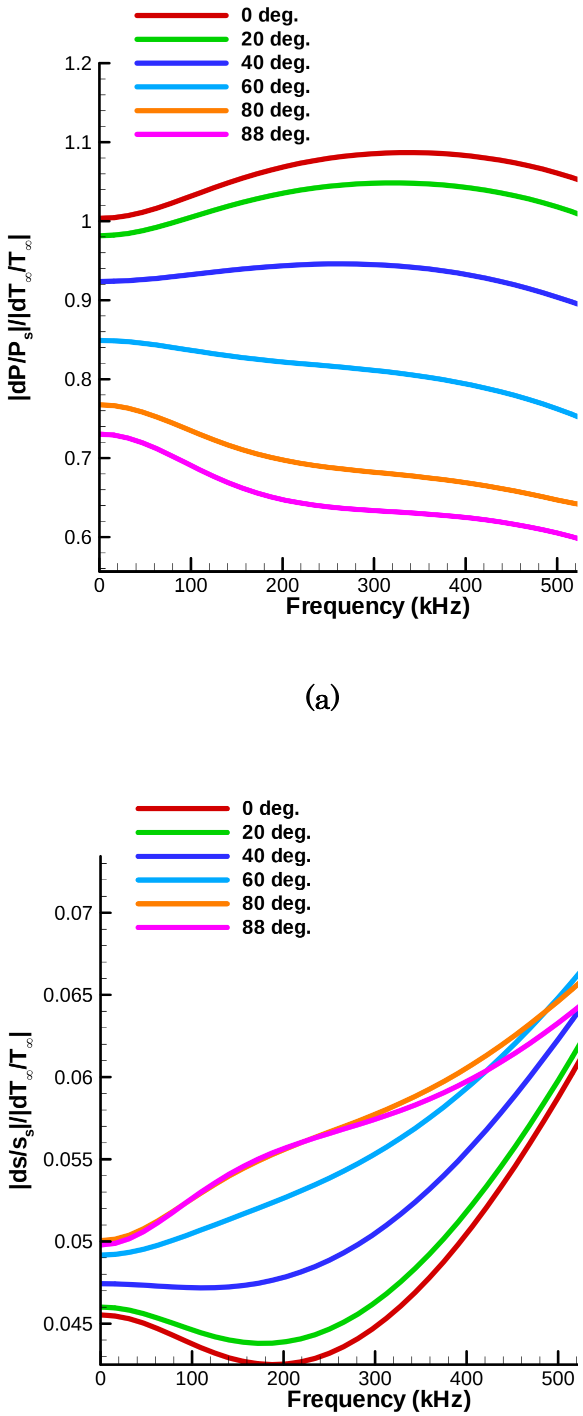

(a)

(b)

Figure 74. Frequency spectrum of normalized amplitudes of (a) pressure perturbations and (b) entropy perturbations immediately behind the shock in the nose region of Case A1.

In the spectra of Case A2 in Figure 75, the maximum generated acoustic waves behind the shock appear on the stagnation line where the angle is 0. These generated waves mainly decay at downstream shock locations in the nose region. Conversely, the angle of 0 degree on the stagnation line has the minimum generated entropy waves behind the shock. These generated entropy waves mainly increase at downstream shock locations in the nose region. The generated waves reach the maximum generated entropy waves behind the shock at the end of the nose region that has the angle of 88 degrees. From Figure 75 (a), the maximum normalized amplitude of the pressure disturbances just behind the shock is 1.04 at 0 degree with the frequency of 520 kHz. Such maximum relative strength of pressure perturbations immediately behind the shock is slightly higher than the relative strength of freestream perturbations due to the resonance interaction near the stagnation line. The overall amplitudes fall in the range from 0.83 to 1.04. The mean value of amplitude in this range is 0.935. From Figure 75 (b), the maximum strength of the entropy perturbations is 0.078 at 88 degrees with the frequency of 520 kHz. The overall amplitudes fall in the range from 0.0435 to 0.078. The mean value of amplitude in this range is 0.06075. By comparing the amplitudes of both perturbations, one can see that the normalized amplitudes of the acoustic waves or pressure perturbations are more than an order of magnitude higher than the entropy perturbations. Such observation indicates that after the hotspot/shock interaction in the nose region, the perturbations are mainly acoustic waves.

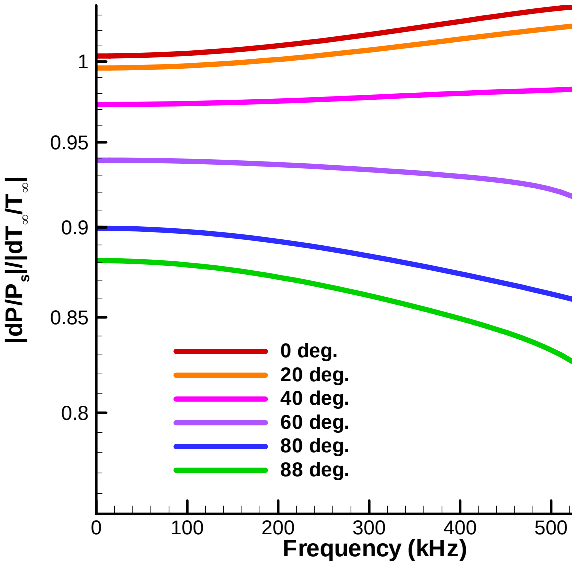

(a)

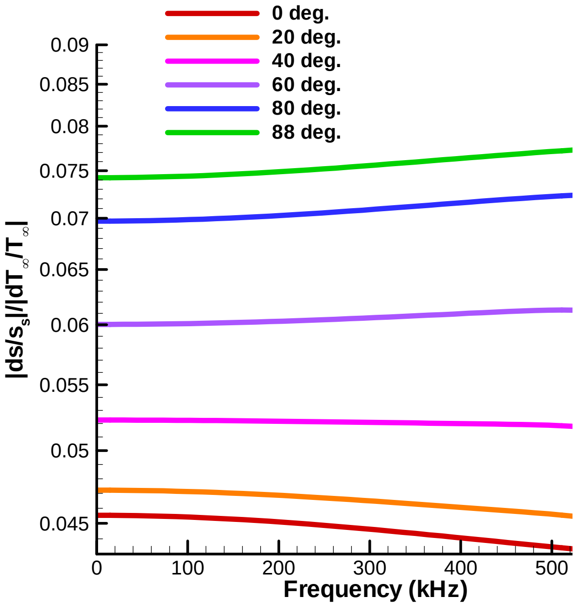

(b)

Figure 75. Frequency spectrum of normalized amplitudes of (a) pressure perturbations and (b) entropy perturbations immediately behind the shock in the nose region of Case A2.

By comparing the above observations on the normalized amplitude frequency spectra of behind-shock acoustic waves and entropy waves in the nose region of Case 1, A1 and A2, one can see that there are a few similarities, difference between these cases of different nose bluntness, and thus some trends can be concluded from the comparisons.

Specifically, the maximum normalized amplitude of the generated acoustic waves behind the shock for all the cases of different nose bluntness (Case 1, A1 and A2) always appear on the stagnation line where the angle is 0, and these generated acoustic waves decay at further downstream shock locations in the nose region. However, the trends of maximum normalized amplitudes of the generated entropy waves behind the shock for all the cases of different nose bluntness (Case 1, A1 and A2) are different. The maximum normalized amplitude of entropy waves in Case 1 of 1 mm in nose radius is at the stagnation line or 0 degree angle. In Case A1 of a blunter nose of 0.5 mm in nose radius, the maximum normalized amplitude of entropy waves is at the angle of 60 degrees. Moreover, for Case A2 of 0.1 mm nose radius, the maximum normalized amplitude of entropy waves is at the angle of 88 degrees, which is at the end of the nose region. From these comparisons, one can see that the sharper the cone is, the maximum normalized amplitude of the generated entropy waves appears at further downstream locations. The reason is that the size of the freestream hotspot is the same, which is 3 mm in hotspot radius, for all cases of different nose bluntness, thus the ratio of the hotspot radius over the nose radius are different; the sharper the cone is, the larger the ratio of radius is. The larger radius ratio implies that the nose of the cone is hit by a freestream hotspot with a relatively larger portion of the hotspot center, which the Gaussian variation in the incoming plane of the freestream hotspot (the plane that has the stagnation line as its normal) is less significant. Noticeably, the entropy perturbation amplitude is the maximum at the hotspot center. When the Gaussian variation effects in the incoming plane are significant, for example Case 1, the maximum amplitude of the generated or transmitted entropy waves intuitively appears at the angle of 0 degree. However, according to the theoretical study of the interaction between a freestream two-dimensional Gaussian entropy spot and shocks of different normal incident Mach numbers by Fabre *et al.* [109], the shock with a lower normal incident Mach number has the stronger transmitted entropy perturbations behind the shock. In the current study, since the ratio of radius for Case A2 is 30 (by comparing to 6 for Case A1, and 3 for Case 1), the relatively very large freestream hotspot hits the sharp nose with a very large portion of its central entropy amplitude, plus the fact that the shock becomes more oblique downstream (the normal incident Mach number becomes lower with a more oblique shock), the variation of the normalized amplitude of the generated entropy waves in the nose region of Case A2 agrees with the trend studied by Fabre *et al.* [109].

The frequency of the local maximum of the generated acoustic waves caused by the resonance in the shock layer depends on the shock-layer thickness. The resonance frequencies from 0 to 40 degrees in Case 1 are 180 to 160 kHz. Those of Case A1 is from 340 to 260 kHz, and those of A2 is out of the frequency range. The trend from this observation is that the sharper cone has the higher resonance frequencies. This is owing to the fact that the shock layer thickness is less over a sharper cone, thus the resonance frequencies are higher, vice versa for the blunter cones. Moreover, the downshift of the frequency downstream in the nose region is due to the increase of shock-layer thickness downstream in the nose region. The observation that Case A1 has the larger downshift than Case 1 implies that the growth of the shock-layer thickness is more vigorous in a sharper cone.

As discussed previously, the mean value of the overall amplitude of acoustic waves or pressure perturbations for Case 1 is 0.67, the one for Case A1 is 0.85, and the one for Case A2 is 0.935. The trend is obvious that the case of sharper cone has the higher overall normalized amplitude of the generated acoustic waves behind the shock in the nose region. The greater ratio of the hotspot radius over the nose radius in the case of sharper cone is the cause of such trend. However, for the generated entropy waves, the mean values of the overall normalized amplitudes are 0.063 for Case 1, 0.0545 for Case A1, and 0.06075 for Case A2. Obviously, there is no trend between the cases of different nose bluntness, and these mean values are close to each other.

Figure 76 shows the normalized frequency spectra at wall from the nose tip to the end of the cone in Case A1. In the figure, there is a large peak of spatial growth of amplitudes with the frequency ranging from about 237 kHz to 368 kHz. The mean frequency of this range is 302.5 kHz, and the width of this range is 131 kHz. This growing peak is the instability dominated by the second mode. The frequency corresponding to the maximum amplitude is about 305 kHz at $x^* = 0.289 \text{ m}$, and the frequency at the peak downshifts from 348 kHz at $x^* = 0.125 \text{ m}$ to 305 kHz at $x^* = 0.289 \text{ m}$. The frequency shift rate is -262 kHz/m. This downshift of frequency is due to the growth of boundary-layer thickness downstream. The second mode dominated peak grows from the initial maximum normalized amplitude of 2.07×10^{-2} at $x^* = 0.125 \text{ m}$ to 36.3 at $x^* = 0.289 \text{ m}$. Thus, the average growth rate of the second mode dominated growing peak from $x^* = 0.125 \text{ m}$ to 0.289 m is $1.07 \times 10^4 \text{ m}^{-1}$, and the average spatial gradient of the 10-based logarithm of the growing peak is 19.8 m^{-1}.

In Figure 76, the bump, which is within the frequency range from 190 kHz to 500 kHz, decays spatially from $x^* = 0.018 \text{ m}$ to 0.11 m. The mean frequency of the range is 345 kHz.

The boundary layer disturbances within this spatial range have relatively strong stable mode F that is discussed in the next section of parametric study of receptivity mechanisms. The maximum normalized amplitude within the bump decays from 0.551 with the frequency of 385 kHz at $x^* = 0.018\ \mathrm{m}$ to 0.0892 with the frequency of 208 kHz at $x^* = 0.11\ \mathrm{m}$. Thus, the average growth rate of the bump from $x^* = 0.018\ \mathrm{m}$ to $0.11\ \mathrm{m}$ is $-9.1\ \mathrm{m}^{-1}$, and the average spatial gradient of the 10-based logarithm of the maximum amplitudes is $-8.6\ \mathrm{m}^{-1}$. The oscillations in the spectra are caused by multi-mode wave modulations, which are complex physical process with a co-existence of many wave modes. Noticeably, there is no such oscillation appearing over the peaks that are dominated by the second mode.

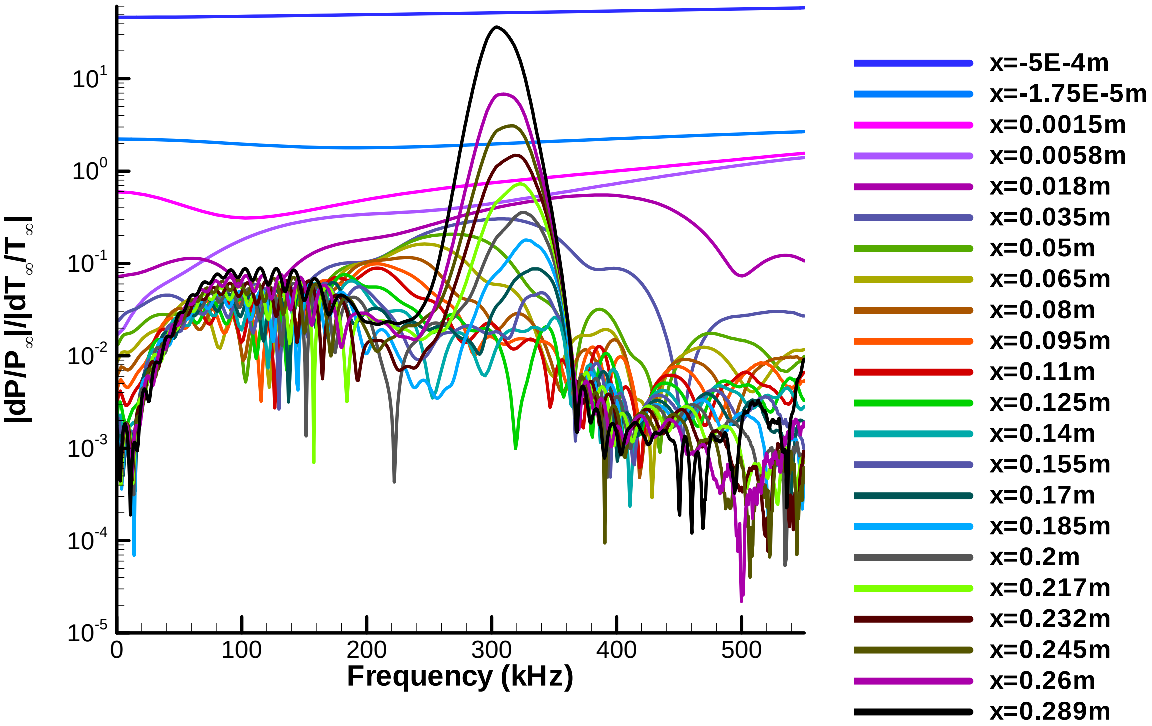

Figure 76. Normalized frequency spectra of the wall-pressure disturbances from the nose tip to the end of the cone in Case A1.

Figure 77 shows the normalized frequency spectra at wall from the nose tip to the end of the cone in Case A2. In the figure, there is a large peak of spatial growth of amplitudes with the frequency ranging from about 200 kHz to 640 kHz. The mean frequency of this range is 420 kHz, and the width of this range is 440 kHz. This growing peak is the instability dominated by the second mode. The frequency corresponding to the maximum amplitude is about 334 kHz at $x^* = 0.221\text{ m}$, and the frequency at the peak downshifts from 518 kHz at $x^* = 0.054\text{ m}$ to 334 kHz at $x^* = 0.221\text{ m}$. The frequency shift rate is -1102 kHz/m. This downshift of frequency is due to the growth of boundary-layer thickness downstream. The second mode dominated peak grows from the initial maximum normalized amplitude of 0.283 at $x^* = 0.054\text{ m}$ to 83.6 at $x^* = 0.221\text{ m}$. Thus, the average growth rate of the second mode dominated growing peak from $x^* = 0.054\text{ m}$ to 0.221 m is $1.77 \times 10^3\text{ m}^{-1}$, and the average spatial gradient of the 10-based logarithm of the growing peak is 14.8 m^{-1}. The oscillations in the spectra are caused by multi-mode wave modulations, which are complex physical process with a co-existence of many wave modes. Noticeably, there is no such oscillation appears over the peaks that are dominated by the second mode.

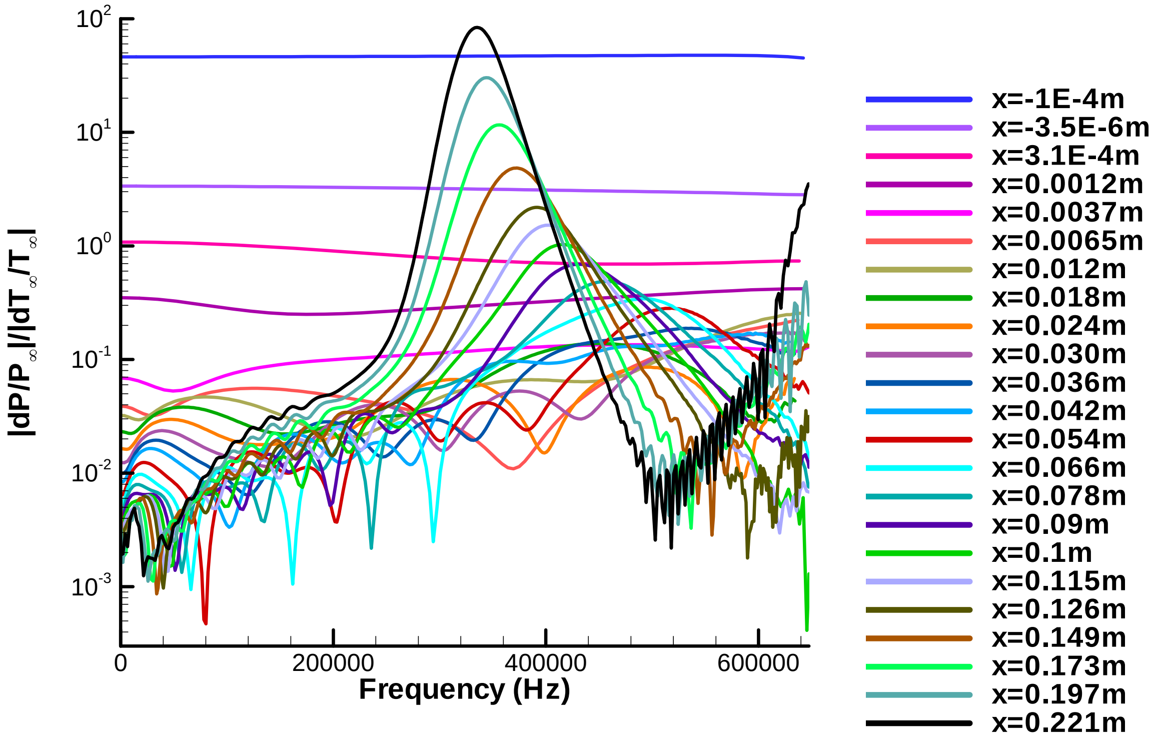

Figure 77. Normalized frequency spectra of the wall-pressure disturbances from the nose tip to the end of the cone in Case A2.

From the observations of the normalized amplitude spectra of the pressure disturbances at wall of Case 1, A1 and A2, we found that there are many trends under the variation of nose bluntness. The mean frequency of the second mode dominant range is higher for the sharper cone, since the boundary-layer thickness over a sharper cone is lower, and the wavelength of the second mode instability is shorter. The bandwidth of the second mode dominant range is wider over the sharper cone. The initial location of the second mode dominant boundary-layer disturbances growth is earlier for the sharper cone. The initial maximum normalized amplitude within the second mode dominant frequency range is larger for the sharper cone. Such trend implies that the sharper cone has the stronger waves from the boundary-layer receptivity process. The frequency downshift rate of the second mode dominant peak is higher throughout the growth of the disturbances over the sharper cone. Such trend reveals that the streamwise growth of the boundary-layer thickness is faster over the sharper cone. Although the cone with larger nose bluntness has the lower initial amplitude of the second mode dominant growth and the later beginning location of the growth, the second mode dominant average growth rate of the blunter cone is found to be higher from the comparisons of the average growth rates and the average logarithm gradients. Noticeably, in the earlier parametric study of the time-history traces, the average growth rate of the sharper cone is found to be larger. However, due to the fact that the growth of the amplitude of the second mode waves is exponential, only having the average growth rate is insufficient to measure the strength of the exponential growth. Therefore, in the analyses of the normalized amplitude spectra, we use the average gradient of the amplitude logarithm to measure the growth. From the comparison between the cases of different nose bluntness, the average logarithm gradient of the second mode dominant growth over the blunter cone is found to be larger.

In order to compare the maximum normalized amplitudes at a fixed distance downstream from the initial location of the growth of the second mode dominant boundary-layer disturbances, a downstream sampling location in each case of the nose bluntness effects study is chosen. The fixed distance downstream from the initial location in each case is chosen to be around $0.16\ \mathrm{m}$. Hence, the downstream sampling location for Case 1 is chosen to be $x^* = 0.33\ \mathrm{m}$, and the corresponding maximum normalized amplitude is 4.68. Secondly, the one for Case A1 is chosen to be $x^* = 0.289\ \mathrm{m}$, and the corresponding maximum normalized amplitude is 36.2. Lastly, the one for Case A2 is chosen to be $x^* = 0.221\ \mathrm{m}$, and the corresponding maximum normalized amplitude is 84. This amplitude comparison shows an obvious trend that the sharper cone has the significantly higher amplitudes in the boundary-layer disturbances after a certain distance of second mode dominant growth. Such trend is the evidence of the significant destabilizing impact created by the sharper nose of a cone.

The stable mode F is relatively strong (though far weaker than the second mode) in the boundary-layer disturbances upstream from the second mode dominant growth region. From the observations of the small decaying bump that has relatively strong stable mode F at the lower frequencies from the second mode dominant frequency range in Case 1 and A1, a few trends are also found. Similar to the trend of the second mode dominant range, the mean frequency of the range that has relatively strong stable mode F is higher for the sharper cone. The spatial average decay rate and the average decay logarithm gradient of the maximum normalized amplitude of the bump are higher for the sharper cone.

A neutral stability curve indicates the locations of the boundary-layer wave modes at each frequency becoming unstable in the linear flow regime. However, it does not include the effects of freestream forcings in the boundary-layer disturbances. Recording the Branch-I and II neutral locations of many sampling frequency components generates the neutral stability curve. As discussed in Section 3.2.2 of LST, since the neutral locations are different between frequencies, one need to run spatial LST for each sampling frequency, and then record the first and second neutral locations encountered in each run. A large amount of sampling frequency is necessary to enhance the smoothness of the neutral stability curve, and thus the accuracy of interpolation between the adjacent sampling frequencies in future use.

The neutral stability curve of Case A1 is shown in Figure 78 (a) in order to demonstrate the general stability properties of this flow in linear regime. The critical location is

$s^* = 0.0575\ \mathrm{m}$ at a frequency of 390 kHz. The second mode instability, which is the dominant instability in the current boundary-layer waves, only appears at the locations of $s^* > 0.0575\ \mathrm{m}$. The overall frequency range of the second mode instability appearance is from around 260 kHz to 400 kHz. The mean frequency of this range is 330. Its bandwidth is 140 kHz. The wave components of $F^* > 400\ \mathrm{kHz}$ do not have second mode instability. The median of the second mode frequency range at $s^* = 0.156\ \mathrm{m}$ is 320 kHz. Thus, the median frequency shifting rate from the critical point to $s^* = 0.156\ \mathrm{m}$ is $-711\ \mathrm{kHz/m}$. Notice that the Branch-II neutral locations appear as the trailing edge of the unstable region.

Figure 78 (a) is shown in the dimensional form, which reveals more practical aspects of the flow. However, when analyzing the theoretical aspects of the boundary-layer receptivity and stability in a parametric study, expressing the quantities in self-similarity is convenient when comparing the flow characteristics between cases of various parameters. The dimensional flow quantities are normalized by the freestream variables according to the formulations discussed in Section 3.2.2 of LST. In detail, the dimensional frequency is normalized by the freestream density, velocity and viscosity. The streamwise coordinate can be expressed in terms of local Reynolds number that is based on the boundary-layer thickness length scale.

Figure 78 (b) shows the neutral stability curve in self-similar variables. Owing to the square root over the s^* in the Eq. (63), the shape is different to the one in dimensional variables, however, it reveals the similar pattern as the dimensional one. The critical Reynolds number is 760, and the corresponding dimensionless frequency is 2.72×10^{-4}. The median of the second mode frequency range at $R = 1280$ is 2.22×10^{-4}. Thus, the dimensionless median frequency shifting rate from the critical point to $R = 1280$ is

-9.6×10^{-8}. The second mode instability, which is the dominant instability in the current boundary-layer waves, only appears at the Reynolds number above 760. The wave components of $F > 2.8 \times 10^{-4}$ do not have second mode instability.

In LST, each dimensionless circular frequency, ω, corresponds to a unique eigenvalue for each normal mode in a perfectly self-similar flow field. Figure 78 (c) shows the corresponding dimensionless circular frequencies for the eigenvalues at the neutral location. In a perfectly self-similar flow field, the dimensionless circular frequency that is correspondent to the unique Branch-I neutral eigenvalue of mode S, is a constant value regardless of the frequency and local Reynolds number. However, in the flow field around a blunt cone, the self-similarity cannot be held due to the geometry of the blunt nose. As a result, the dimensionless circular frequencies at the neutral locations are not constant for all frequency components in Figure 78 (c). However, the variation range of the dimensionless circular frequencies at the neutral locations is from 0.202 to 0.23, which is small. This reveals the proximity of self-similarity in the flow field around the neutral locations. The mean of the dimensionless circular frequency at the neutral locations is 0.216.

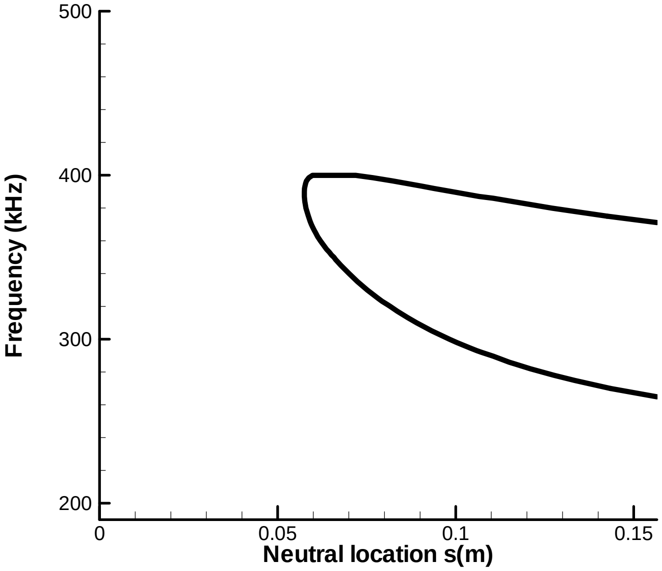
Frequency (kHz)
500
400
300
200
0
0.05
0.1
0.15
Neutral location s(m)

(a)

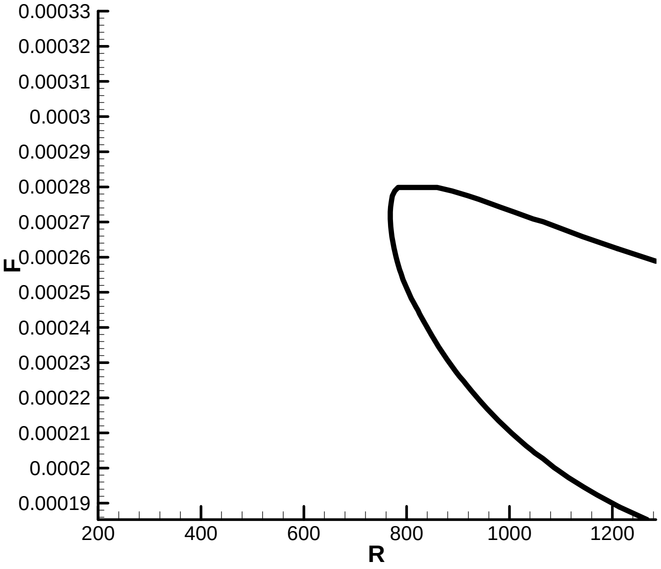
F
0.00033
0.00032
0.00031
0.0003
0.00029
0.00028
0.00027
0.00026
0.00025
0.00024
0.00023
0.00022
0.00021
0.0002
0.00019
200
400
600
800
1000
1200
R

(b)

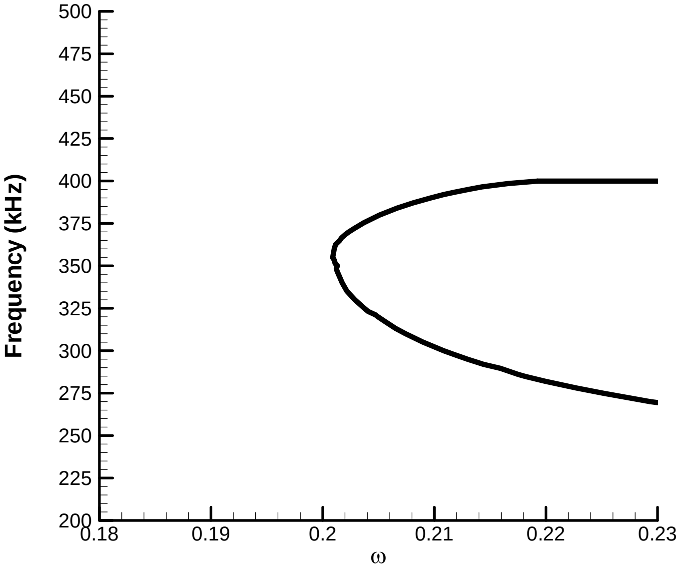

(c)

Figure 78. Neutral stability curve of the second mode in (a) dimensional form and (b) self-similar variables, and (c) the corresponding dimensionless circular frequencies along the neutral stability curve in Case A1.

The LST generated neutral stability curve of Case A2 is shown in Figure 79 (a). The critical location is $s^* = 0.0214$ m at a frequency of 670 kHz. The second mode instability, which is the dominant instability in the current boundary-layer waves, only appears at the locations of $s^* > 0.0214$ m. The overall frequency range of the second mode instability appearance is from 260 kHz to 680 kHz. The mean frequency of this range is 470. Its bandwidth is 420 kHz. The wave components of $F^* > 680$ kHz do not have second mode instability. The median of the second mode frequency range at $s^* = 0.19$ m is 330 kHz. Thus, the median frequency shifting rate from the critical point to $s^* = 0.19$ m is

$-2020\ \text{kHz/m}$. Notice that the Branch-II neutral locations appear as the trailing edge of the unstable region.

Figure 79 (b) shows the neutral stability curve in self-similar variables. Even though the observed shape is different to the one in dimensional variables, it reveals the similar pattern as the dimensional one. The critical Reynolds number is 480, and the corresponding dimensionless frequency is 4.65×10^{-4}. The median of the second mode frequency range at $R=1200$ is 2.5×10^{-4}. Thus, the dimensionless median frequency shifting rate from the critical point to $R=1200$ is -3.0×10^{-7}. The second mode instability, which is the dominant instability in the current boundary-layer waves, only appears at the Reynolds number above 480. The wave components of $F>4.75\times10^{-4}$ do not have second mode instability.

Figure 79 (c) shows the corresponding dimensionless circular frequencies for the eigenvalues at the neutral location. The variation range of the dimensionless circular frequencies at the neutral locations is from 0.208 to 0.26, which is small. This reveals the proximity of self-similarity in the flow field around the neutral locations. The mean of the dimensionless circular frequency at the neutral locations is 0.234.

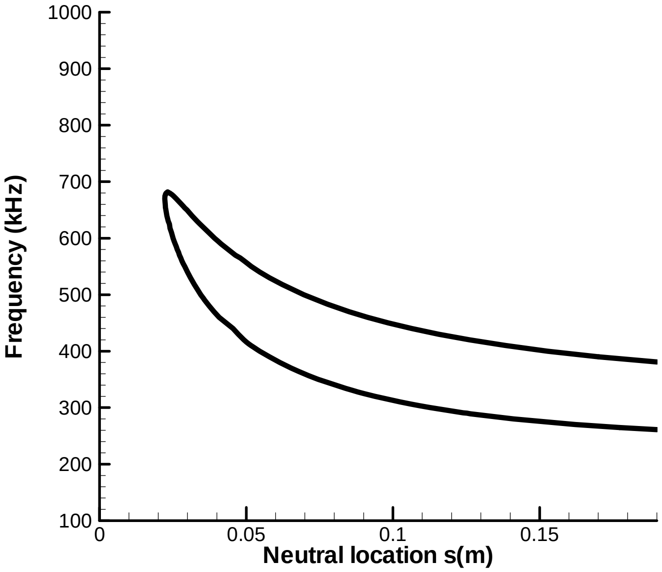
Frequency (kHz)
1000
900
800
700
600
500
400
300
200
100
0
0.05
0.1
0.15
Neutral location s(m)

(a)

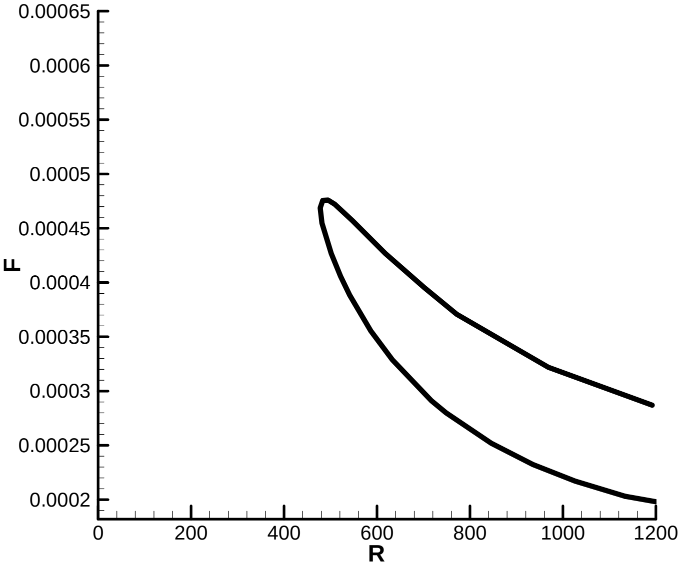
F
0.00065
0.0006
0.00055
0.0005
0.00045
0.0004
0.00035
0.0003
0.00025
0.0002
0
200
400
600
800
1000
1200
R

(b)

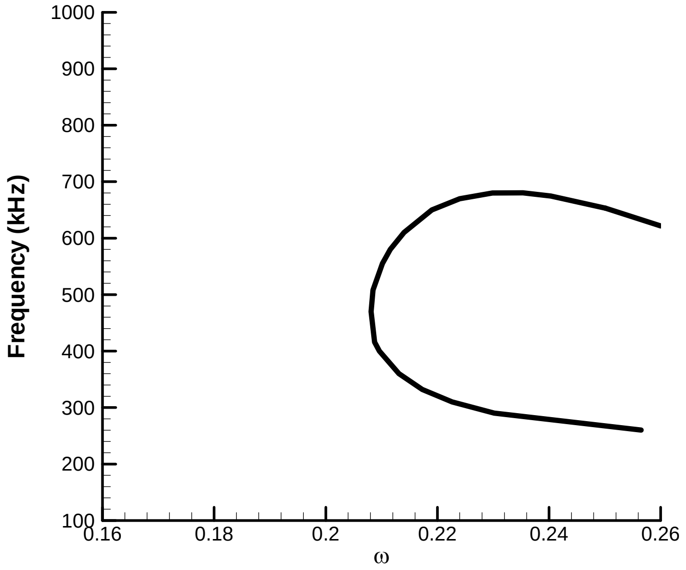

(c)

Figure 79. Neutral stability curve of the second mode in (a) dimensional form and (b) self-similar variables, and (c) the corresponding dimensionless circular frequencies along the neutral stability curve in Case A2.

By comparing the observations of both the dimensional and dimensionless neutral stability curves of Case 1, A1 and A2, we can see there are common characteristics and trended differences between the cases of different nose bluntness. The critical location is earlier or the critical Reynolds number is less, and the corresponding critical frequency is higher for the sharper cone. Due to the growth of the boundary-layer thickness downstream, all the cases of different nose bluntness have downshift of the second mode median frequency downstream from the critical point. Moreover, the sharper cone has the higher median frequency downshifting rate, which implies the faster growth of boundary-layer thickness downstream over the sharper cone. The mean frequency of the overall second mode frequency range is higher for the sharper cone, which implies that the boundary-layer thickness of a sharper cone is less than the blunter cone. The bandwidth of the overall second mode frequency range is also larger for the sharper cone. All of these concluded trends are consistent with the trends of the boundary-layer disturbances frequency aspects and the growth locations found in the second mode dominant boundary-layer perturbations analyses that are presented earlier in this section. Finally, the mean values of the dimensionless circular frequency at the neutral locations for all the cases of different nose bluntness are very close to each other. This observation implies that a high degree of self-similarity is being held between the cases of different nose bluntness.

The stability topography of the second mode is discussed previously. However, the overall spatial behaviors of the normal modes in the boundary layer under the nose bluntness effects are not yet revealed. Hence, the investigation of the mode F and mode S for both Case A1 and A2 are presented next.

The LST predicted spatial dimensionless phase speeds of the mode F and mode S along the dimensionless circular frequency over the cone are calculated from α_r by Eqs. (63), (67), and (68). The plot of the dimensionless phase speeds at the sampling frequency of 337 kHz in Case A1 is shown in Figure 80. The three horizontal lines are the dimensionless phase speeds of fast acoustic, slow acoustic and entropy/vorticity waves determined using freestream flow conditions in front of the bow shock. As a result, they only serve as qualitative references to show the existence of the three wave modes. The actual phase speeds depend on local non-constant flow conditions.

The upstream fast acoustic waves synchronized mode F has the phase speed decrease from the phase speed of the fast acoustic waves upstream to the phase speed of 0.82 downstream. There is a break in the phase speeds of mode F from $\omega = 0.19$ to 0.23. It is due to the synchronization between mode F and the entropy/vorticity waves. Specifically, the eigenvalue of the discrete mode F merges into the entropy/vorticity spectrum and reappears while moving downstream. As a result, the trace of the eigenvalue of mode F is interrupted by the entropy/vorticity spectrum. Since the actual phase speed of entropy/vorticity waves depends on local flow conditions, the break appears below the freestream phase speed of entropy/vorticity waves.

The upstream slow acoustic waves synchronized mode S has the phase speed that changes from the phase speed of the slow acoustic waves upstream to the phase speed of around 0.89 downstream. The mode S synchronizes with the mode F at $\omega = 0.26$.

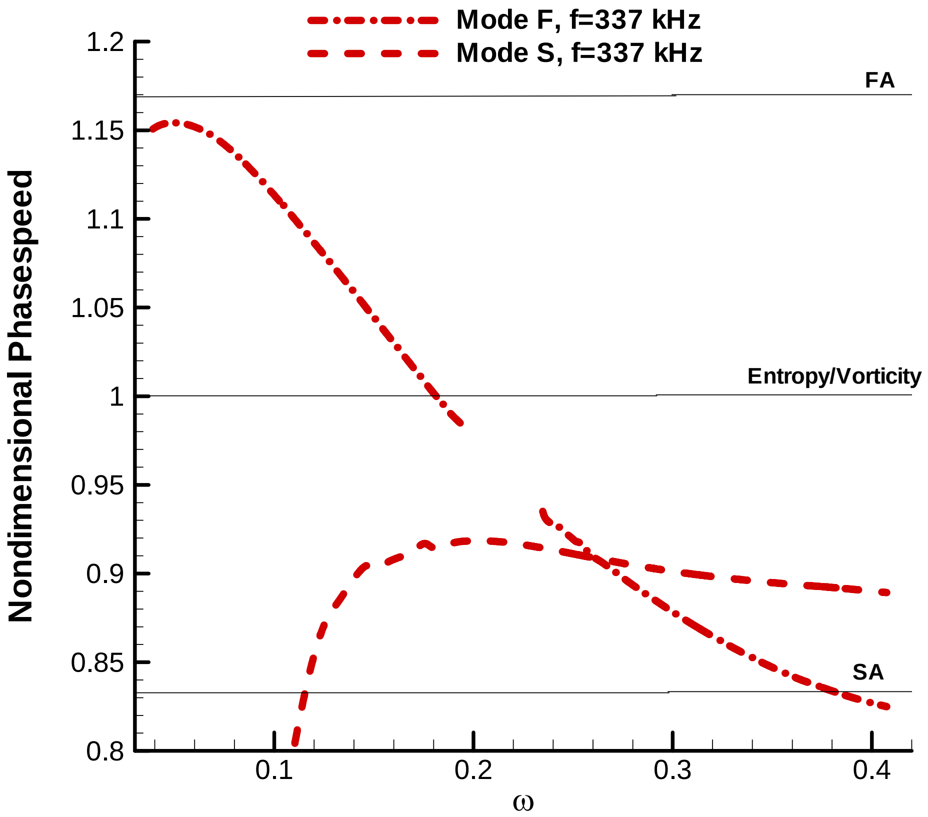

Figure 80. Streamwise phase speeds of mode F and mode S at the frequency of 337 kHz along the dimensionless circular frequency in Case A1.

The plot of the dimensionless phase speeds at the sampling frequency of 400 kHz in Case A2 is shown in Figure 81. The upstream fast acoustic waves synchronized mode F has the phase speed that decreases from the phase speed of the fast acoustic waves upstream to the phase speed of 0.76 downstream. There is a break in the phase speeds of mode F from $\omega = 0.21$ to 0.25. It is due to the synchronization between mode F and the entropy/vorticity waves. Specifically, the eigenvalue of the discrete mode F merges into the entropy/vorticity spectrum and reappears while moving downstream. As a result, the trace of the eigenvalue of mode F is interrupted by the entropy/vorticity spectrum. Since the actual phase speed of entropy/vorticity waves depends on local flow conditions, the break appears below the freestream phase speed of entropy/vorticity waves.

The upstream slow acoustic waves synchronized mode S has the phase speed that changes from the phase speed of the slow acoustic waves upstream to the phase speed of around 0.9 downstream. The mode S synchronizes with the mode F at $\omega = 0.26$.

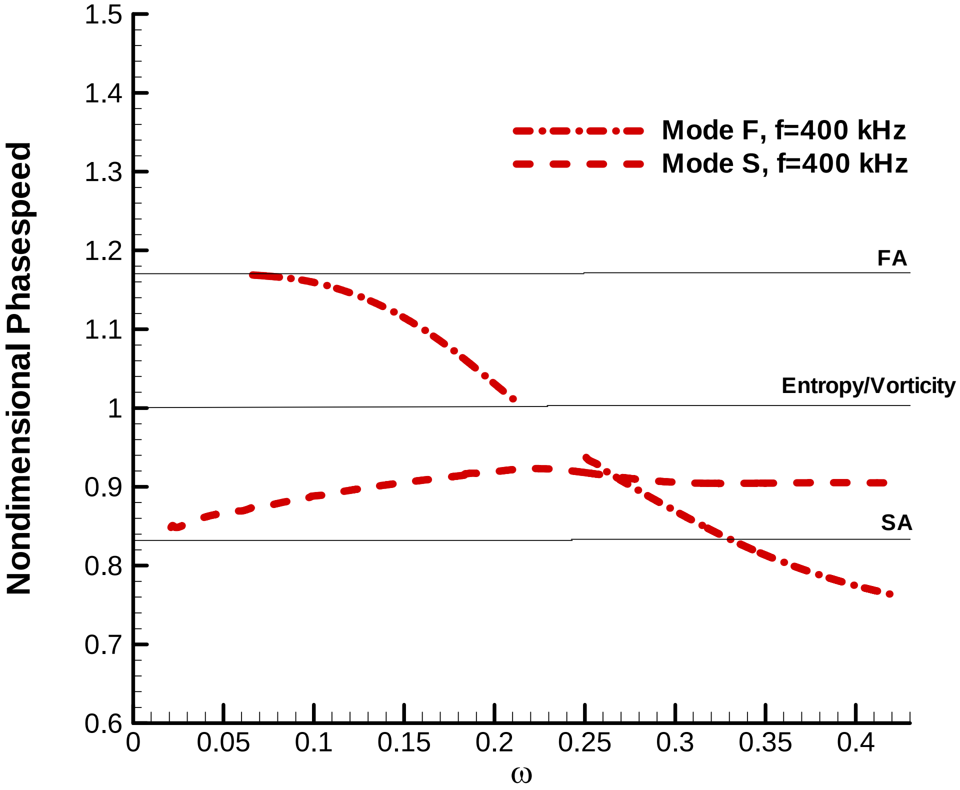

Figure 81. Streamwise phase speeds of mode F and mode S at the frequency of 400 kHz along the dimensionless circular frequency in Case A2.

In addition to the streamwise phase speeds, the streamwise dimensional growth rates are also calculated from α_i by Eqs. (62) and (66). The streamwise dimensional growth rates along the dimensionless circular frequency at 337 kHz in Case A1 are shown in Figure 82. The mode F is stable everywhere while mode S is stable before the Branch-I neutral point at $\omega = 0.205$, and it becomes the unstable second Mack mode behind this location. These observations indicate that the unstable second mode is related to mode S. Moreover, the unstable second mode begins shortly upstream from the synchronization of mode F and mode S at $\omega = 0.26$. Within the break due to the synchronization of the mode F and the entropy/vorticity waves, the growth rate of the mode F has a drop, in other words, a jump in α_i, which indicates the stabilizing effects to mode F from the synchronization between mode F and entropy/vorticity waves. Such jump in α_i is also found in Fedorov *et al.* [78, 80].

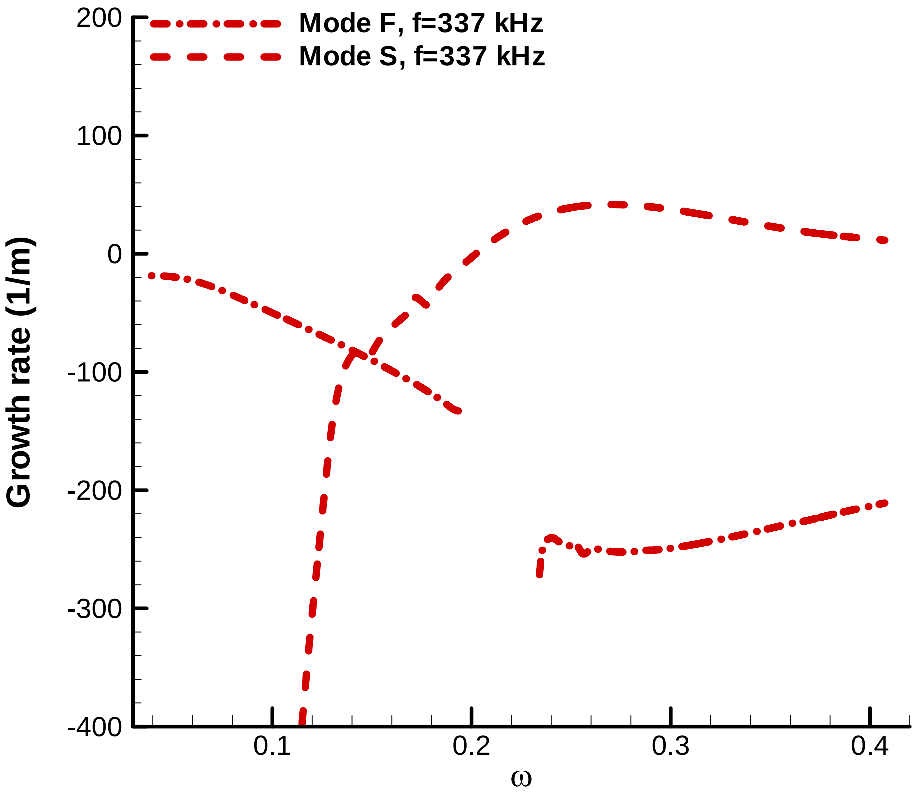

Figure 82. Streamwise growth rates of mode F and mode S at the frequency of 337 kHz along the dimensionless circular frequency in Case A1.

The streamwise dimensional growth rates along the dimensionless circular frequency at 400 kHz in Case A2 are shown in Figure 83. The mode S is stable before the Branch-I neutral point at $\omega = 0.21$, and it only becomes unstable behind this dimensionless circular frequency. The mode F is stable everywhere throughout the cone. These observations indicate that the unstable second mode is related to mode S. Moreover, the unstable second mode begins shortly upstream from the synchronization of mode F and mode S at $\omega = 0.26$. Within the break due to the synchronization of the mode F and the entropy/vorticity waves, the growth rate of the mode F has a drop, in other words, a jump in α_i, which indicates the stabilizing effects to mode F from the synchronization between mode F and entropy/vorticity waves. Such jump in α_i is also found in Fedorov *et al.* [78, 80].

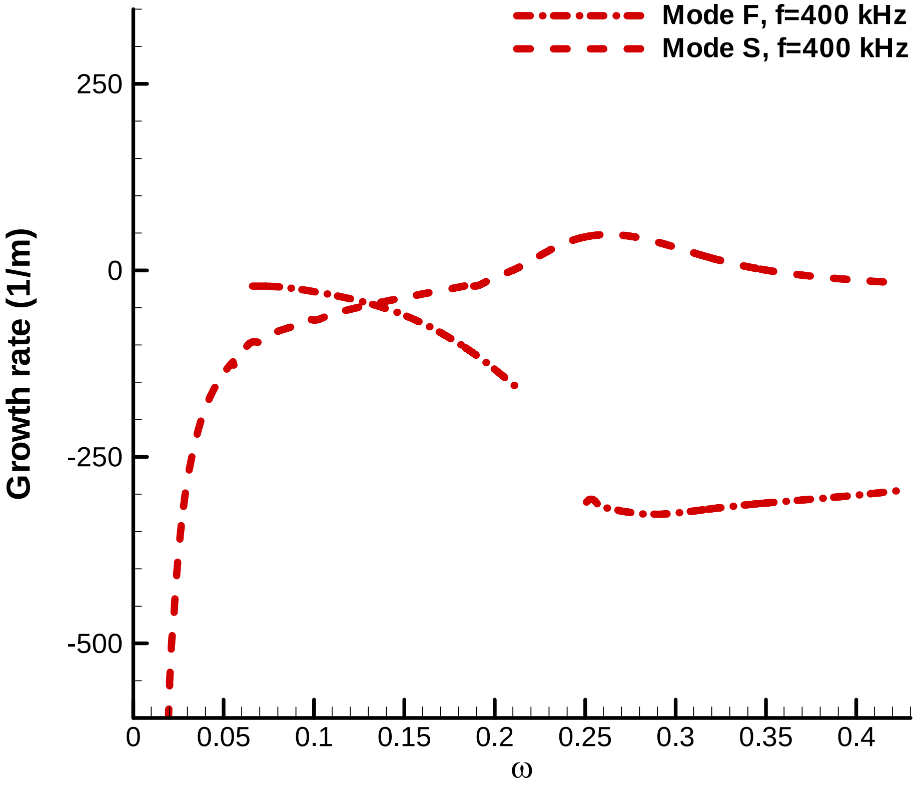

Figure 83. Streamwise growth rates of mode F and mode S at the frequency of 400 kHz along the dimensionless circular frequency in Case A2.

From the analyses of the streamwise phase speeds and growth rates of mode F and mode S in all three cases of different nose bluntness (Case 1, A1 and A2), we found that the dimensionless circular frequency of the synchronization point of mode F and mode S are the same between all three cases. Moreover, the Branch-I neutral point of each case of the different nose bluntness is also very close to others in terms of the dimensionless circular frequency, and all these Branch-I neutral points are shortly upstream from the synchronization points of mode F and mode S. The proximities of the synchronization points and the Branch-I neutral points between the cases of different nose bluntness are due to the high degree of self-similarity in the steady base flow field of these cases. More importantly, all three cases of different nose bluntness have the second mode instability relevant to mode S.

Other than the above mentioned proximity and similarity, the dimensionless circular frequencies of the synchronization "breaks" of the entropy/vorticity waves and mode F are different between the cases of nose bluntness effects. Specifically, the break appears slightly ($O\left(10^{-2}\right)$) earlier over the blunter cone. These LST predicted mode F and mode S phase speeds and growth rates are compared with the simulated unsteady boundary-layer disturbances in Section 4.3.3, in order to study the effects of nose bluntness in the boundary-layer receptivity mechanism.

The disturbances in the boundary layer contain discrete spectrum wave modes such as mode F and mode S, and continuous spectrum wave modes such as fast acoustic, slow acoustic and entropy/vorticity waves. The amplitudes in the frequency spectra that are shown earlier in this section, are the total sum of the co-existing discrete and continuous wave modes. Boundary-layer receptivity process is the process of having the disturbances from outside of the boundary-layer evolve to the final form within the boundary layer before the dominant modal growth. In order to study the receptivity process, the receptivity strength of each mode is one of the important features to investigate. Specifically, for characterizing the strength of receptivity prior to the growth of the boundary-layer disturbances, there is a receptivity coefficient which is defined as the ratio of the wave amplitude of a specific mode and frequency at the Branch-I neutral location that is immediately behind the receptivity process, to the perturbation amplitude of the specific frequency in freestream. In fact, the normalized amplitude defined in Eq. (73) at the Branch-I neutral location is the receptivity coefficient. In the earlier discussion of the receptivity coefficient approximation method in Section 3.2.4, the receptivity coefficient of the single dominant unstable mode is approximated by Eq. (75). Such approximate method requires the N-factors from LST calculations, and the simulated normalized spectra of the overall disturbances that are presented in Figure 76.

The N-factors over the cone in Case A1 is shown in Figure 84. They are generated from LST calculations that are discussed in Section 3.2.2 of LST analysis over the steady base flow. The sampling frequencies span from 265 kHz to 350 kHz, which is within the second-mode dominant frequency range that is observed in Figure 76. From the N-factors at the end of the computation domain, 305 kHz is found to be the most amplified frequency, which reaches the N-factor of 8.8. This frequency is also found to be the peak frequency at $x^* = 0.289\ \mathrm{m}$ in Figure 76. Thus, from the earliest neutral location in the plot, $x^* = 0.0622\ \mathrm{m}$, to the end of the computation domain, $x^* = 0.291\ \mathrm{m}$, the overall gradient of N-factor is $38.5\ \mathrm{m}^{-1}$. From 275 kHz to 340 kHz, the N-factors are around 5 or higher. From our experience of using the receptivity coefficient method, one needs to use the sampling frequencies with the N-factor equal to or more than 5 to make qualitative reasonable approximations. Moreover, for the accurate approximations, the N-factor needs to be 8 or higher. Therefore, the approximation of mode S receptivity coefficients in the Case A1 is only of the sampling frequencies from 275 kHz to 340 kHz. The use of smaller N-factors will results in the over-estimation of the receptivity coefficient due to the significance of impurity of other modes in the second mode dominant boundary-layer disturbances.

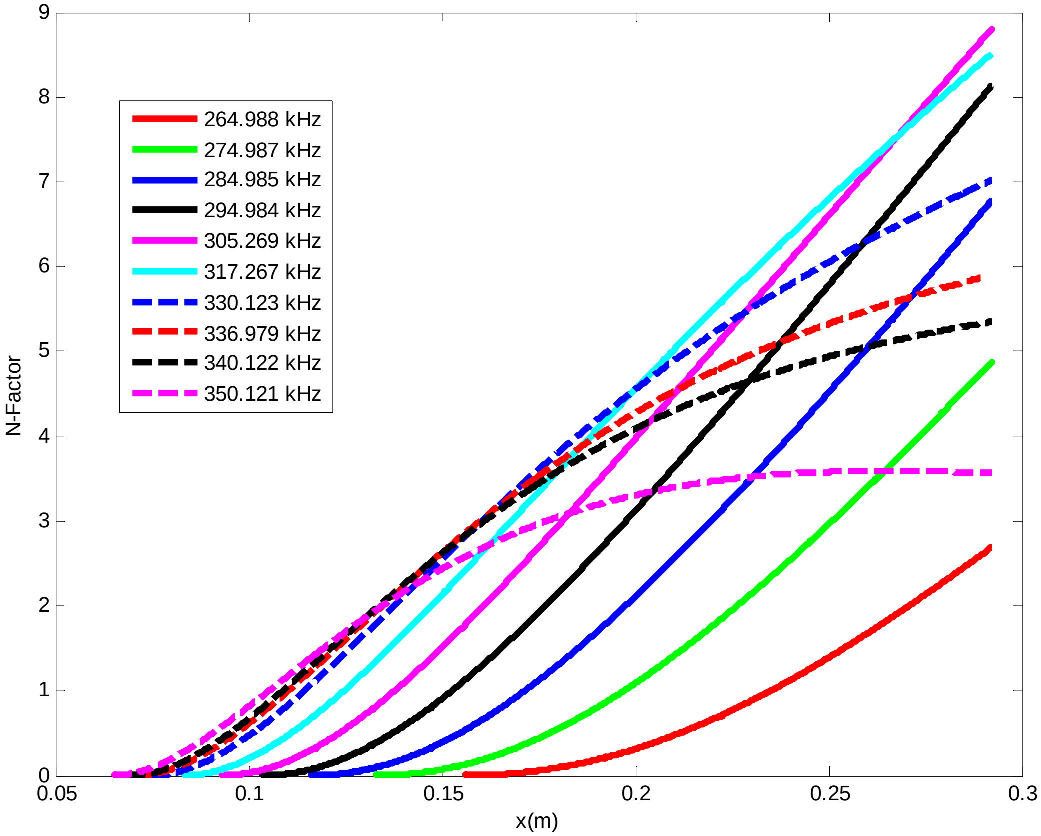

Figure 84. Second mode N-factors in Case A1.

Figure 85 shows the frequency spectra of simulated overall boundary-layer disturbances and the receptivity coefficient of the unstable mode S at the Branch-I neutral location for Case A1. Such frequency spectra are shown within the frequency range of the dominant growth. The amplitudes of the simulated boundary-layer disturbances that contains all wave modes, are recorded at the LST predicted Branch-I neutral locations which are shown as the neutral stability curve in Figure 78 (a). The solid line in Figure 85 represents such overall boundary-layer disturbances. At the locations of Branch-I neutral stability, there is no dominant mode appeared yet, in other words, the amplitudes of each modes are comparable. Therefore, the modulation between each mode waves occurs, and it results in the oscillatory amplitude curve for the overall boundary-layer disturbances. The receptivity coefficient of mode S is shown in the dash line. It is approximated by Eq. (75) for many sampling frequencies, and the curve is far smoother than the one of the overall boundary-layer disturbances because the receptivity coefficient only represents a single mode. The minor oscillation on the curve is due to the difference between the LST predicted pure mode S solution and the simulated overall wave solution at the selected downstream location near the end of the computation zone. The largest peak in the amplitude of the overall disturbances is from 298 kHz to 350 kHz. The maximum value of this peak is 0.0295. The general pattern of the overall disturbance amplitude seems ascending over lower frequencies, since the valleys and the peaks beside the largest one of the overall disturbance amplitude is ascending while the frequency is becoming lower. The mode S has the minimum amplitudes behind 318 kHz, and the small rise of the amplitude behind 318 kHz is the result of over-estimation from using the smaller N-factors ($N < 8$) that has the sampling frequency away from the most amplified frequency of 305 kHz in Figure 84. The frequency of 305 kHz is also the peak frequency of the second mode dominant frequency range at $x^* = 0.289$ m in Figure 76. The amplitude of mode S demonstrates a pattern that is consistent with the pattern of the overall disturbances: the lower frequencies have higher amplitudes and the maximum is located further left outside the plotted range. In addition, the amplitudes of mode S at the Branch-I neutral locations are well-contained under the overall disturbances amplitudes. In the frequency range from 275 kHz to 340 kHz, the overall disturbances have the amplitudes from 0.0103 to 0.0295, and the median amplitude is 0.0199. The amplitudes of mode S are from 0.0055 to 0.0156, and the median amplitude is 0.0106. The ratio of the median amplitude of mode S to the one of the overall boundary-layer disturbances is 53%.

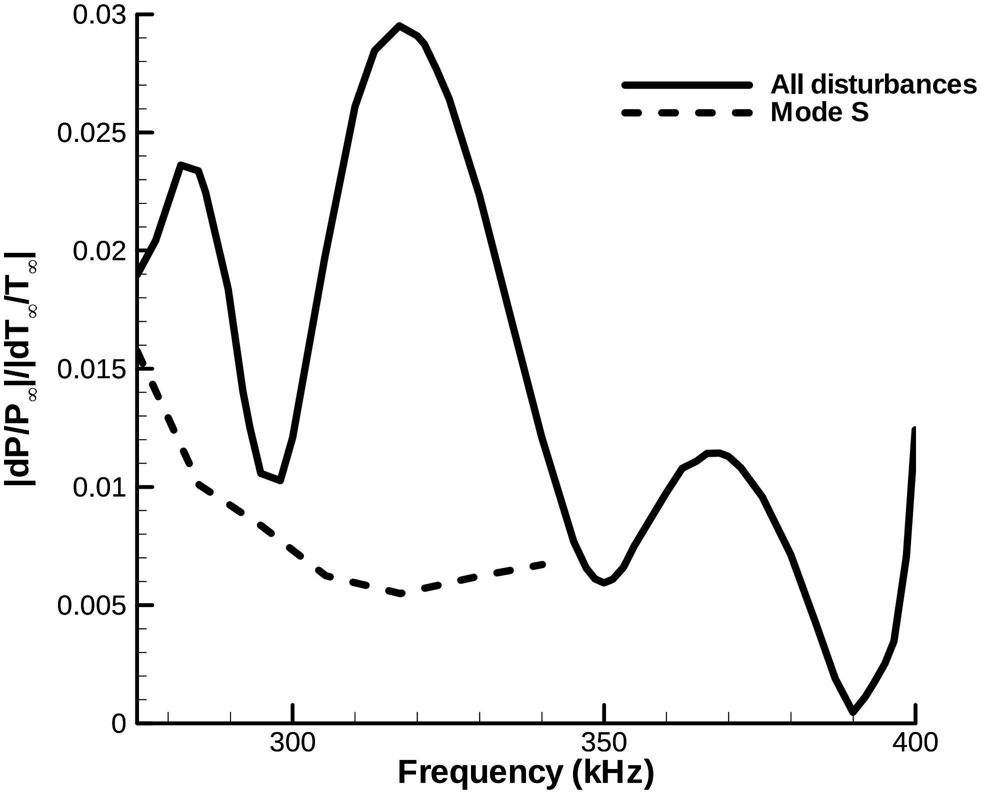

Figure 85. Frequency spectra of the simulated overall boundary-layer disturbances and the approximated receptivity coefficient of the unstable mode S at the Branch-I neutral location in Case A1.

Figure 86 shows the frequency spectra of simulated overall boundary-layer disturbances for Case A2. The amplitudes of the simulated boundary-layer disturbances that contains all wave modes, are recorded at the LST predicted Branch-I neutral locations which are shown as the neutral stability curve in Figure 79 (a). At the locations of Branch-I neutral stability, there is no dominant mode appeared yet, in other words, the amplitudes of each modes are comparable. Therefore, the modulation between each mode waves occurs, and it results in the oscillatory amplitude curve for the overall boundary-layer disturbances. The largest peak in the amplitude of the overall disturbances is from 410 kHz to 650 kHz. The maximum value of this peak is 0.166 at 495 kHz. In the frequency range from 410 kHz to 650 kHz, the overall disturbances have the amplitudes from 0.03 to 0.166, and the median amplitude is 0.098. In the Case 1 and A1, we computed the receptivity coefficients of mode S in order to investigate the dominant wave mode amplitudes at its initial neutral location over the second mode dominant frequency range. However, since the downshift of the second mode dominant frequency range is very large throughout the growth in Case A2 as revealed in Figure 77, and the frequency range of the peak with high second mode dominancy only covers a small fraction of the entire second mode dominant frequency range, the receptivity coefficients throughout the second mode dominant frequency range for Case A2 is not available in this work. The curve roughness beyond 600 kHz is due to having not enough streamwise grid resolution to resolve the higher frequency components.

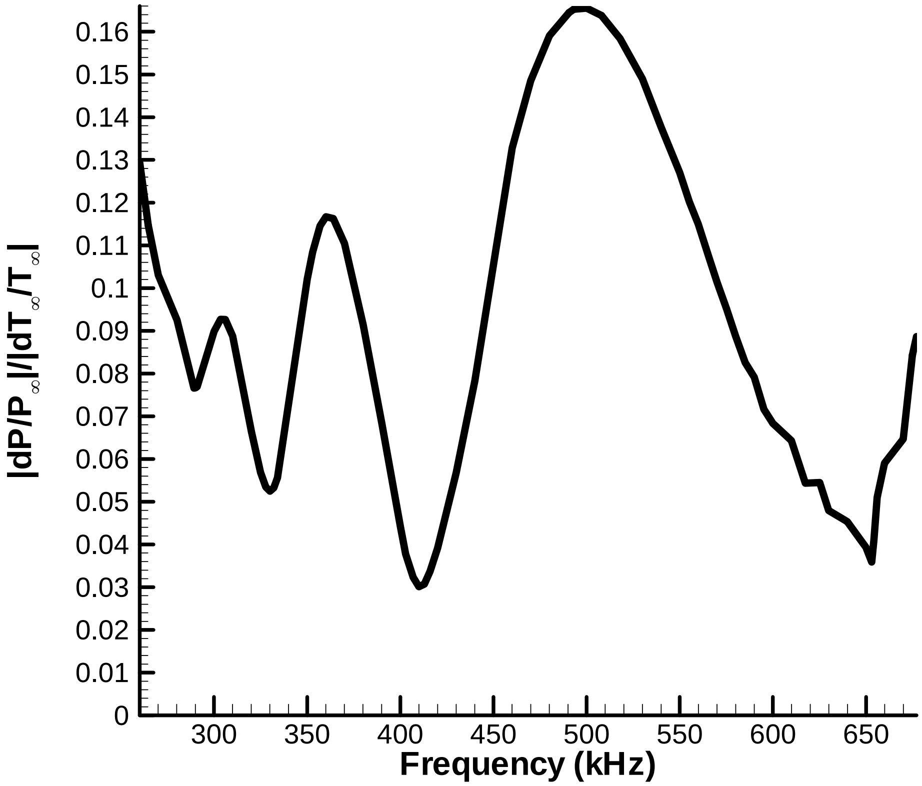

Figure 86. Frequency spectrum of the simulated overall boundary-layer disturbances at the Branch-I neutral location of the second mode in Case A2.

From the observations of the LST predicted N-factor plots in Case 1 and A1, the overall gradient of N-factor of the second mode in Case 1 is larger than the one in Case A1, which implies that the blunter cone has the faster growing second mode. Such finding is consistent with the finding in the earlier discussion of the normalized amplitude spectra of the pressure disturbances at wall for the cases of different nose bluntness: the average growth rate of the second mode dominant boundary-layer disturbances over the blunter cone is found to be higher from the comparisons of the average growth rates and the average logarithm gradients.

From the observations of the receptivity coefficients of the mode S in the Case 1 and A1, the median amplitude of receptivity coefficients of mode S in Case A1 is higher than Case 1, which implies that the receptivity coefficient of the mode S at the Branch-I neutral location is larger over the sharper cone. Moreover, the ratio of the median amplitude of mode S to the one of the overall boundary-layer disturbances in Case A1 is also larger than the one of Case 1. Such finding implies that the initial boundary-layer disturbances at the Branch-I neutral locations over the sharper cone have the higher proportion of mode S.

In addition to the trends of mode S, from the observations of the amplitude of the overall boundary-layer disturbances in Case 1, A1 and A2, the median amplitude of the initial overall boundary-layer disturbances at the Branch-I neutral locations over the sharper cone is also higher.

4.3.3 Mechanism of Boundary-Layer Receptivity

After the parametric study of the nose bluntness effects in the receptivity and the growth of the boundary-layer disturbances from the earlier frequency spectra of Case 1, A1 and A2, an investigation of the nose bluntness effects in spatial modal evolution of the boundary-layer disturbances throughout the cone is conducted next. It is a crucial step in understanding the receptivity mechanism under the effects of nose bluntness.

Figure 87 shows the spatial development of wall-pressure-perturbation amplitude from the upstream region to the downstream region in Case A1 and A2. In each case of different nose bluntness, a frequency near the amplitude peak in the second mode dominant ranges that are shown in Figure 76 and Figure 77, is chosen as the sampling frequency to be investigated in this section. Both Case A1 and A2 start with high initial amplitudes where the hotspot has just passed through the shock and excites the boundary-layer disturbances in the upstream region. Then the perturbations decay through the receptivity process while moving downstream. When the perturbations reach $s^* = 0.116\ \text{m}$ in Case A1, and $s^* = 0.052\ \text{m}$ in Case A2, they begin to grow exponentially downstream. In Figure 78 (a) and Figure 79 (a), the LST predicted Branch-I neutral location of 337 kHz in Case A1 is $s^* = 0.07\ \text{m}$, and the one of 400 kHz in Case A2 is $s^* = 0.055\ \text{m}$. Noticeably, the boundary-layer disturbance growth beginning location for Case A1 is further downstream than the Branch-I neutral location of mode S. This is due to the fact that mode S is not dominant yet around the Branch-I neutral location, thus even though the mode S is unstable at such location, the overall disturbances amplitude can be other than growing. The boundary-layer disturbance growth beginning location for Case A2 is almost the same as the Branch-I neutral location of mode S. This observation reveals that the initial mode S is relatively strong at such location in Case A2. The trend of the ratio of the receptivity coefficient of mode S over the one of the overall boundary-layer disturbances found in the earlier parametric study of the receptivity coefficients at the Branch-I neutral locations supports this revealing. Additionally, the oscillatory features of the curves are the results of the modulation of multiple wave modes when there is no single dominant instability mode. This multi-mode modulation phenomenon is expected in the synchronization zone. They are commonly seen in many numerical studies [4, 28, 31, 35, 36, 94].

In Figure 87, the growth of amplitude for both cases eventually slows down after reaching certain location downstream. In Case A2, the growth slows down until

$s^* = 0.16$ m where the Branch-II neutral location of mode S is (shown in the neutral stability curve of Case A2 in Figure 79 (a)), then the amplitude start to decay.

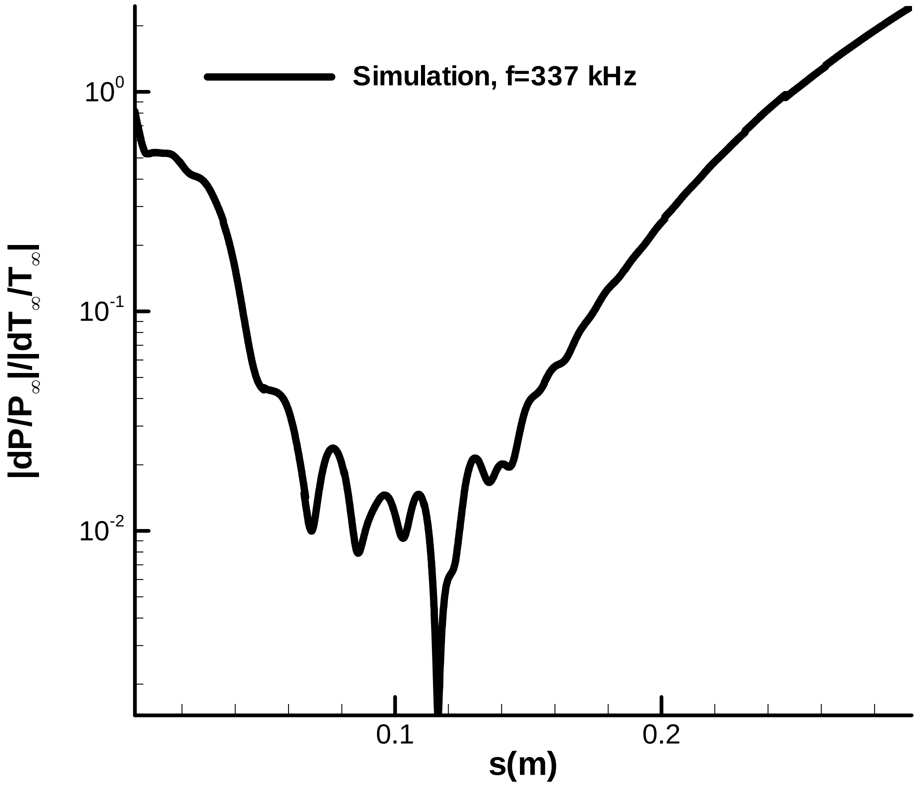

(a)

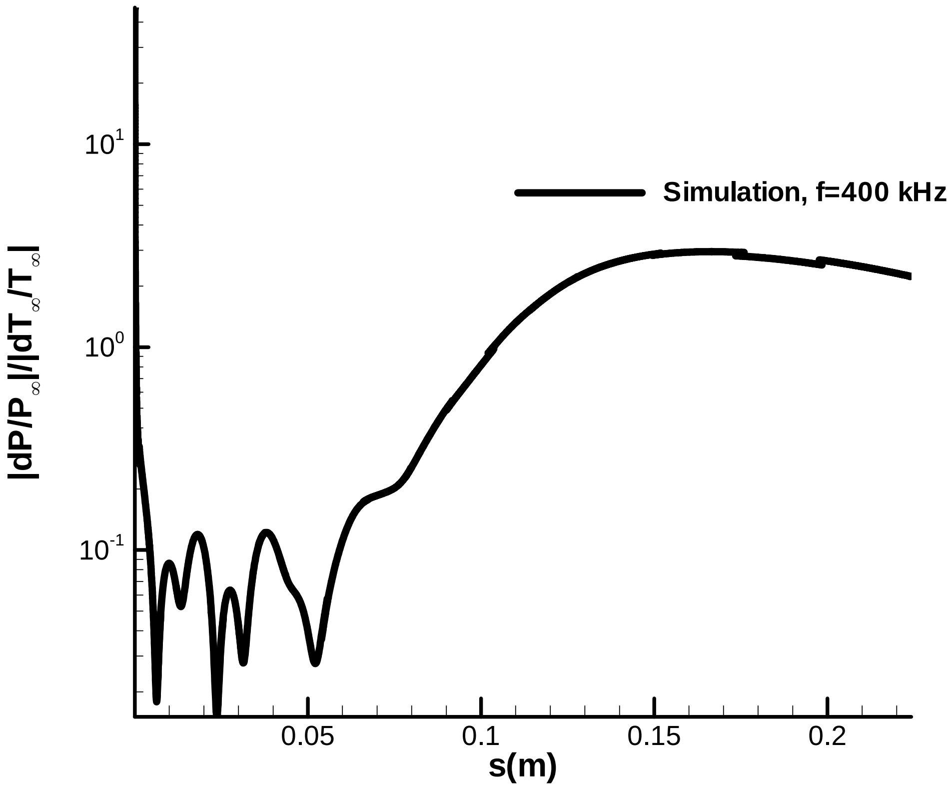

(b)

Figure 87. The spatial amplitude development of the simulated wall-pressure perturbations at the frequency of (a) 337 kHz in Case A1, and (b) 400 kHz in Case A2.

We cannot determine the modal evolution in the boundary layer from the simulated overall boundary-layer disturbance amplitudes along the cone. Therefore, we have to compare the results of the simulated overall disturbances to the LST predicted results of the pure boundary-layer modes in order to identify the dominant wave modes in the boundary layer. The sampling frequency to be analyzed in each case of different nose bluntness is the one near the peak amplitude in the second mode dominant ranges that are shown in Figure 76 and Figure 77. The simulated dimensionless phase speed is computed by Eqs. (45), (66), and (68). The comparison between the phase speed of the simulated overall disturbances and the LST predicted mode S and mode F phase speeds in Case A1 is shown in Figure 88 (a). The three horizontal lines are the dimensionless phase speeds of fast acoustic, slow acoustic and entropy/vorticity waves determined using freestream flow conditions in front of the bow shock. As a result, they only serve as qualitative references to show the existence of the three continuous wave modes. The actual phase speeds depend on local non-constant flow conditions. Figure 88 (a) shows a trend of the phase speed of the simulated disturbances decreases from the phase speed of the fast acoustic wave in the nose region. The simulated phase speed closely matches the LST predicted mode F with small wiggles until $s^* = 0.05\ \mathrm{m}$. The comparison shows that the disturbances are likely to be initially excited in the boundary layer by the fast acoustic waves near the nose. The comparison also shows that mode F is relatively strong in the boundary-layer disturbances before $s^* = 0.05\ \mathrm{m}$. The large oscillations begin after the phase speed of the simulated disturbances reaches the one of entropy/vorticity waves. The phase speed of the simulated disturbances vigorous oscillate between the phase speeds of entropy/vorticity waves, mode F and mode S between $0.05\ \mathrm{m} < s^* < 0.12\ \mathrm{m}$, and the phase speed of the simulated disturbances jumps up to the one of the fast acoustic waves at $s^* = 0.115\ \mathrm{m}$. The modulation between many wave modes causes the strong oscillations in that region. More specifically, there are many wave modes existing in the simulated boundary-layer disturbances, while the LST results are based on a single mode only. Consequently, the co-existence of other modes with comparable strengths results in the modulations of the simulated results. The same phenomenon was also discussed by Ma and Zhong [4, 35, 36].

In Figure 88 (a), the simulated disturbance phase speed in the modulation region is mainly close to the phase speeds of entropy/vorticity waves, mode F and mode S. It indicates that the entropy/vorticity waves, mode F and mode S have the outstanding strengths relative to the other modes in the boundary-layer disturbances in that region. As the waves propagate further downstream, the phase speed decreases and becomes almost the same as the mode S behind the synchronization point of mode S and mode F at $s^* = 0.12\ \mathrm{m}$. This observation indicates that the dominance of mode S in the boundary-layer disturbances begins after the synchronization between mode S and mode F.

In Fedorov *et al.* [80, 108], a branch point is where both the real and imaginary parts of the phase speed are equal for mode F and mode S. The second mode instability is excited downstream from the branch point. The branch point, however, does not exist in most practical flows with a real x axis (or Reynolds numbers) only, except for a very specific disturbance frequency with a very cold wall. Instead, the branch point appears along complex Reynolds number with a non-zero imaginary part. In the case of practical flow, mode F and mode S have resonance interaction when the real part of the wave number and frequency are the same near the branch point, even though the growth rates are different. Therefore, we define the synchronization point, which is also the resonant point, between mode F and mode S as the point where the real parts of the phase speed are equal for mode F and mode S. Ma and Zhong [4, 35, 36] have shown that this synchronization point plays an important role in receptivity process.

In Figure 88 through Figure 91, there is a break in the phase speeds and growth rates of mode F before the synchronization point. It is due to that the eigenvalue of the discrete mode F merges into the entropy/vorticity spectrum and reappears while moving downstream before reaching the synchronization point. As a result, the eigenvalue of mode

F is interrupted by the entropy/vorticity spectrum. Since the actual phase speed of entropy/vorticity waves depends on local flow conditions, the break appears below the freestream phase speed of entropy/vorticity waves in Figure 88 (a). This break is typical for hypersonic flow over a cone.

The plot of dimensionless phase speed in Figure 88 (a) is expressed in terms of dimensional streamwise coordinate along the surface of the compression cone. It provides intuitive idea and practical information by referring to the spatial location along the cone. It is especially convenient when comparing with the experiment results, or providing guidance to experimental study or vehicle design process. In parametric studies, it is more convenient to express results in terms of dimensionless parameters such as self-similarity parameters, because self-similarity parameters allow comparison of common characteristics between different cases regardless to the dimensional differences. The horizontal axis in Figure 88 (b) has the dimensionless circular frequency, ω, instead of the dimensional streamwise location along the cone surface, s^*. According to Eq. (67), the dimensionless circular frequency contains both the factors of local Reynolds number and frequency.

In Figure 88 (b), the synchronization point of mode F and mode S is at $\omega = 0.26$. From $\omega = 0.04$ to 0.17, both the phase speeds of mode F and the simulated disturbances decrease from the one of the fast acoustic waves to around the one of the entropy/vorticity waves, and the simulated phase speed is in the proximity of the one of mode F. This observation implies that the boundary-layer disturbances have relatively strong mode F, and it is most likely being initially excited by the fast acoustic waves in the earlier region near the nose. The earlier results in Figure 74, which show that there are mainly acoustic waves carried into the shock layer in the nose region, also confirm this implication. The oscillation in the simulated phase speed is due to the modulation of different wave modes in the boundary layer, when various wave modes are having comparable amplitudes as explained previously. From $\omega = 0.17$ to 0.26, the simulated phase speed oscillates between mode F, mode S and entropy/vorticity waves. This observation indicates that mode S, mode F and entropy/vorticity waves are relatively strong between $\omega = 0.17$ to 0.26. At $\omega = 0.255$, the simulated phase speed jumps up to the phase speed of the fast acoustic waves. This observation indicates that the fast acoustic waves are relatively strong shortly before the synchronization point. Immediately behind the synchronization point, the simulated phase speed drops down and converges to the one of mode S. Simultaneously, the oscillation gradually disappears behind the synchronization point, and the simulated phase speed curve eventually becomes smooth downstream. These observations indicate the domination of mode S in the boundary-layer disturbances after the synchronization between mode F and mode S.

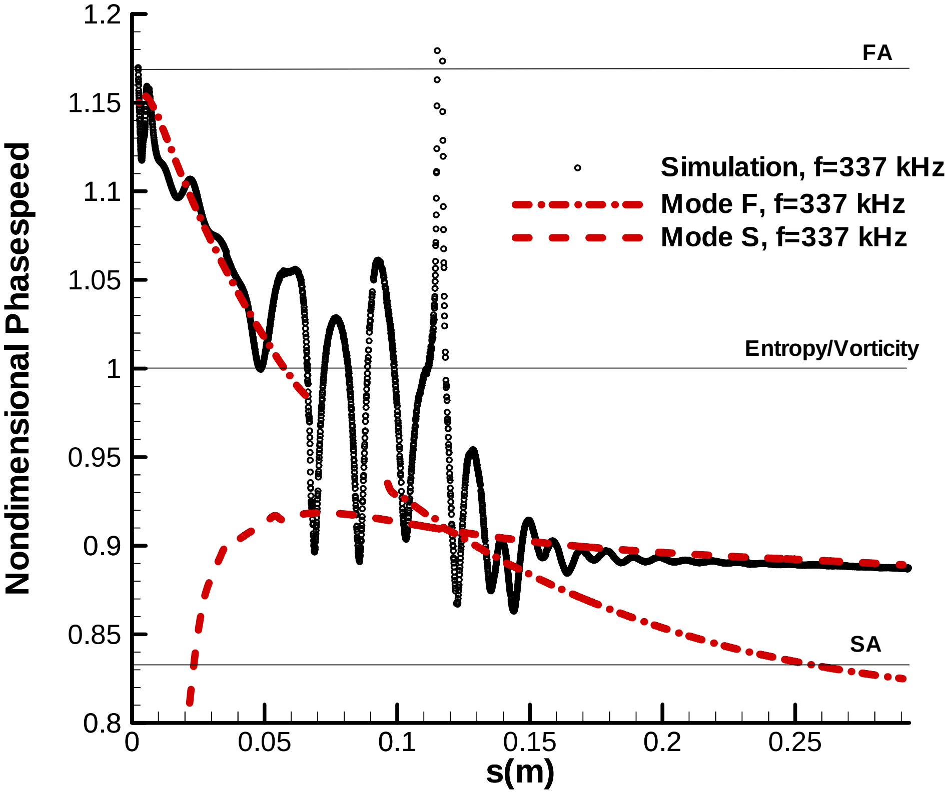
Nondimensional Phasespeed
1.2
1.15
1.1
1.05
1
0.95
0.9
0.85
0.8
0
0.05
0.1
0.15
0.2
0.25
s(m)
FA
Entropy/Vorticity
SA
Simulation, f=337 kHz
Mode F, f=337 kHz
Mode S, f=337 kHz

(a)

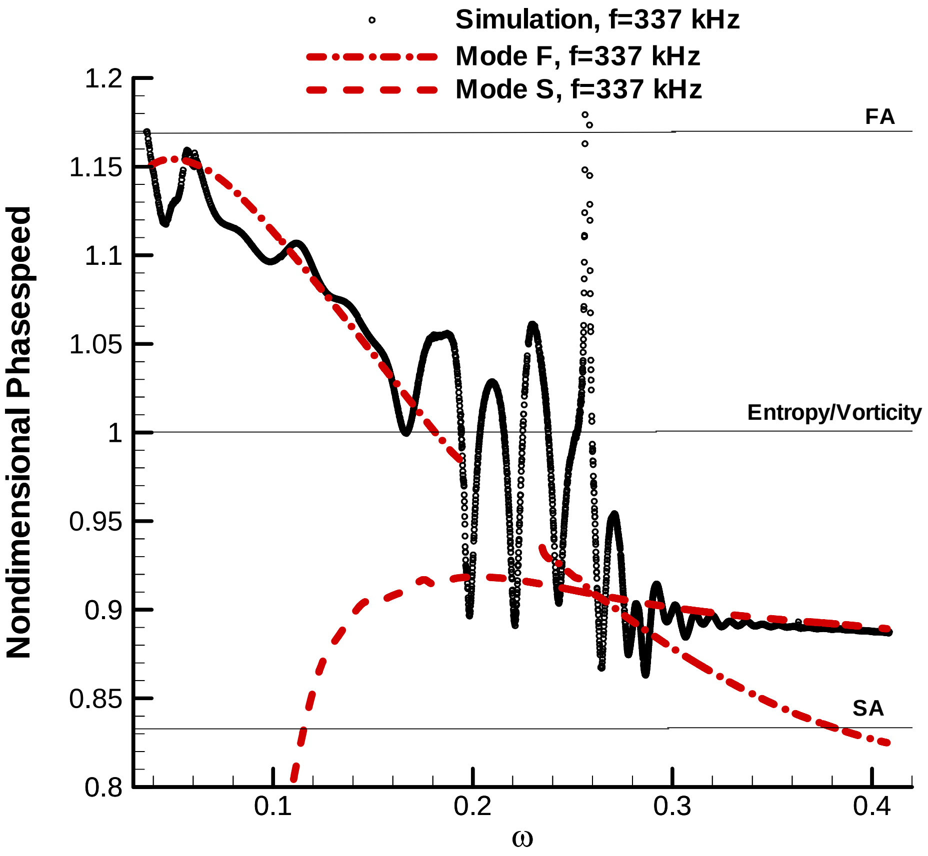

(b)

Figure 88. Comparison of the streamwise phase speeds of the simulated wall pressure disturbances with those of the LST predicted mode F and mode S at the frequency of 337 kHz along (a) the dimensional body surface coordinate and (b) the dimensionless circular frequency in Case A1.

The comparison between the phase speed of the simulated overall disturbances and the LST predicted mode S and mode F phase speeds in Case A2 is shown in Figure 89 (a). The phase speed of the simulated disturbances vigorously oscillate around the phase speeds of the fast acoustic wave and decrease with the mode F behind the nose region until

$s^* = 0.018$ m . This observation implies that the boundary-layer disturbances are originated from the fast acoustic waves near the nose, and the fast acoustic waves have also the outstanding relative strength beside the mode F after the excitation of the mode F until $s^* = 0.018$ m . After the phase speed of the simulated disturbances decrease to the one of entropy/vorticity waves at $s^* = 0.018$ m , the phase speed of the simulated disturbances vigorously oscillates around the phase speeds of all the modes shown between $0.018 \text{ m} < s^* < 0.035$ m . Then, the phase speed of the simulated disturbances oscillates around the slow acoustic waves and begins to converge to mode S between $0.042 \text{ m} < s^* < 0.085$ m . Behind the synchronization point of mode S and mode F at $s^* = 0.085$ m , the simulated phase speed matches the one of the mode S very well. This observation reveals that the dominance of the mode S in the boundary-layer disturbances begins earlier than the synchronization point of mode S and mode F.

The plot of dimensionless phase speed expressed in the variable of self-similarity is shown in Figure 89 (b). The horizontal axis in Figure 89 (b) has the dimensionless circular frequency, ω , instead of the dimensional streamwise location along the cone surface, s^*. According to Eq. (67), the dimensionless circular frequency contains both the factors of local Reynolds number and frequency.

In Figure 89 (b), the synchronization point of mode F and mode S is at $\omega = 0.26$. From shortly behind the nose region at $\omega = 0.02$ to 0.12, the simulated phase speed of the boundary-layer disturbances oscillates vigorously around the phase speeds of the fast acoustic wave and decrease with the one of the mode F. This observation implies that the boundary-layer disturbances are originated from the fast acoustic waves near the nose, and the fast acoustic waves have also the outstanding relative strength beside the mode F after the excitation of the mode F until $\omega = 0.12$. The earlier results in Figure 75, which shows that there are mainly acoustic waves carried into the shock layer in the nose region, also confirm this implication. From $\omega = 0.12$ to 0.17, the simulated phase speed oscillates between all the modes shown in the plot. This observation indicates the strong modulation between all the shown wave modes between $\omega = 0.12$ to 0.17. From $\omega = 0.185$ to 0.26, the phase speed of the simulated disturbances oscillates around the slow acoustic waves and begins to converge to mode S. Immediately behind the synchronization point, the simulated phase speed matches the one of the mode S very well. This observation indicates that the dominance of mode S in the boundary-layer disturbances appears earlier than the synchronization point between mode F and mode S.

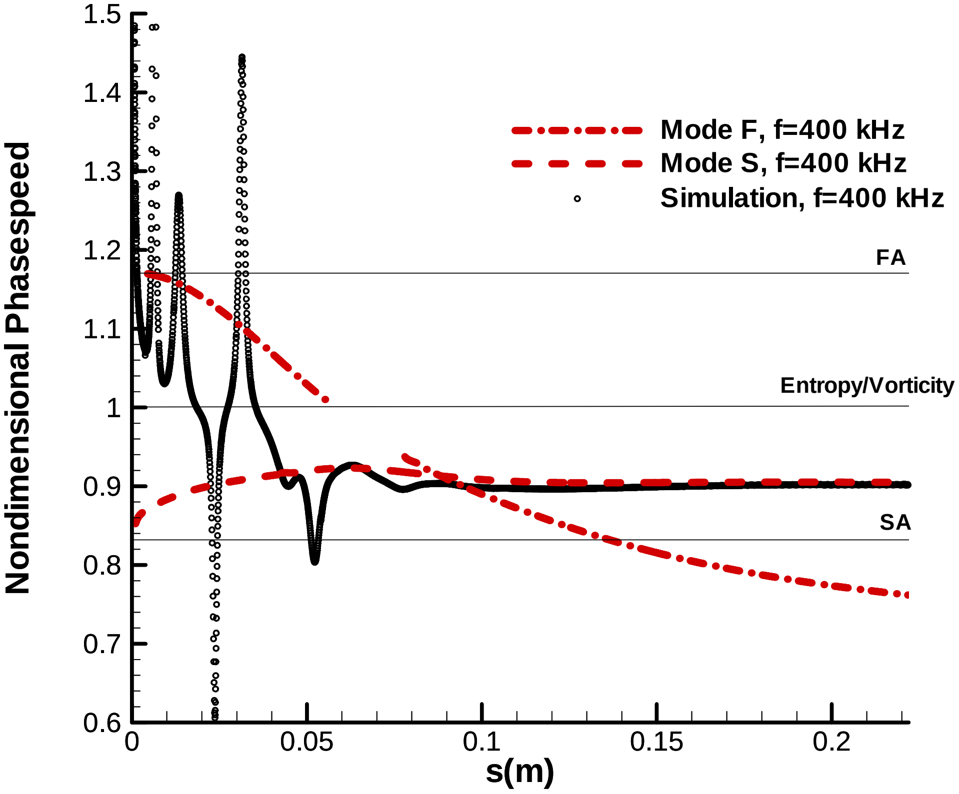

(a)

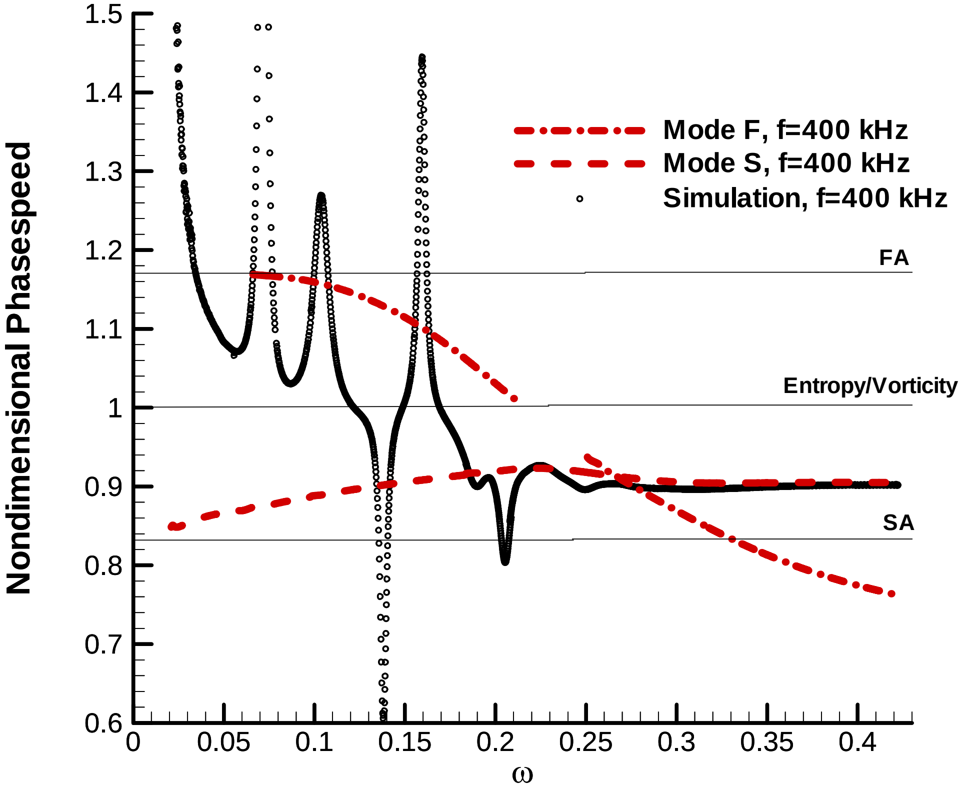

(b)

Figure 89. Comparison of the streamwise phase speeds of the simulated wall pressure disturbances with those of the LST predicted mode F and mode S at the frequency of 400 kHz along (a) the dimensional body surface coordinate and (b) the dimensionless circular frequency in Case A2.

From the observations of the cases of different nose bluntness, it is obvious that the receptivity paths of all these cases are similar: the boundary layer disturbances are initially carried in as the fast acoustic waves near the nose region. The fast acoustic wave excited mode F in the boundary-layer disturbances has the relative large strength behind the nose region until the boundary-layer disturbance phase speed reaches the one of the entropy/vorticity waves. Then it is followed by the occurrence of the strong multi-wave-mode modulations in the middle of the cone. Finally, the synchronization of the mode F and mode S causes the dominance of the mode S in the boundary-layer disturbances in the downstream part of the cone.

From the earlier investigation of the nose-bluntness effects on the normalized amplitude spectra in the nose region in Figure 41, Figure 74 and Figure 75, the sharper cone has the stronger acoustic perturbations that are carried in by the freestream hotspot in the nose region. Therefore, Case A2 has the longer spatial region that bears the relatively stronger fast acoustic waves in the boundary-layer disturbances after the excitation of the mode F behind the nose region. Different to Case 1 and A1, Case A2 has the dominance of mode S in the boundary-layer disturbances first appears shortly before the synchronization point of mode S and mode F.

Moreover, in the earlier parametric study of the nose bluntness effects on the neutral stability curves in Figure 27, Figure 78 (c) and Figure 79 (c), a high degree of similarity of instability locations are held between the cases of different nose bluntness. Therefore, the mode S and mode F synchronization points of all three cases of different nose bluntness have almost the same dimensionless circular frequency.

The stability of the boundary-layer disturbances at different locations is determined by their growth rates. The simulated growth rate is calculated by Eq. (44). The comparisons between the growth rates of the simulated boundary-layer disturbances and those of mode S and mode F obtained by LST in Case A1 and A2 are shown in Figure 90 and Figure 91.

In the comparison of Case A1 in Figure 90 (a), there are oscillations in the simulated growth rate as a result of multi-mode wave modulations. The simulated growth rate oscillates around the mode F from $s^* = 7.5 \times 10^{-3}$ m to 0.065 m. This observation implies that the mode F is relatively strong shortly behind the nose region. The LST predicted mode F is stable everywhere while mode S is stable before the Branch-I neutral location of $s^* = 0.069$ m, and it becomes the unstable second Mack mode behind this location. Such neutral location is earlier than the synchronization point of mode S and mode F, $s^* = 0.12$ m, which is discussed and shown earlier in the phase speed comparison of Case A1 in Figure 88 (a). From the earlier discussion of the spatial development of the boundary-layer disturbances with the frequency of 337 kHz in Case A1, which is shown in Figure 87 (a), the boundary-layer disturbances only exponentially grow behind $s^* = 0.116$ m, which is shortly earlier than the synchronization point of mode S and mode F. In Figure 90 (a), the simulated growth rate converges to the unstable growth rate of mode S behind $s^* = 0.116$ m. Both growth rates of the simulation and the mode S compare very well further downstream. These combined observations of the earlier results and the growth rate comparison implies that the boundary-layer disturbances only begin to grow exponentially at the location where the dominancy of the mode S related second mode in the boundary-layer disturbances first appears.

Figure 90 (b) shows the comparison in Case A1 between the simulated growth rate and the one obtained from LST in self-similar variable, which allows comparison of common characteristics between different cases regardless to the dimensional differences. The horizontal axis in Figure 90 (b) has the dimensionless circular frequency, ω, instead of the dimensional streamwise location along the cone surface, s^*.

In Figure 90 (b), there are oscillations in the simulated growth rate as a result of multi-mode wave modulations. The simulated growth rate oscillates around the mode F from $\omega = 0.07$ to 0.19. This observation implies that the mode F is relatively strong shortly behind the nose region. The LST predicted mode F is stable everywhere while mode S is stable before the Branch-I neutral location of $\omega = 0.205$, and it becomes the unstable second Mack mode behind this location. Such neutral location is earlier than the synchronization point of mode S and mode F, $\omega = 0.26$, which is discussed and shown earlier in the phase speed comparison of Case A1 in Figure 88 (b). In Figure 90 (b), the simulated growth rate converges to the unstable growth rate of mode S behind $\omega = 0.258$. Both growth rates of the simulation and the mode S compare very well further downstream. These combined observations of the earlier results and the growth rate comparison implies that even though the Branch-I neutral location of mode S related second mode instability appears earlier than the synchronization point of mode S and mode F, the boundary-layer disturbances in Case A1 become dominant by the mode S related second mode instability shortly earlier than the synchronization point of mode S and mode F.

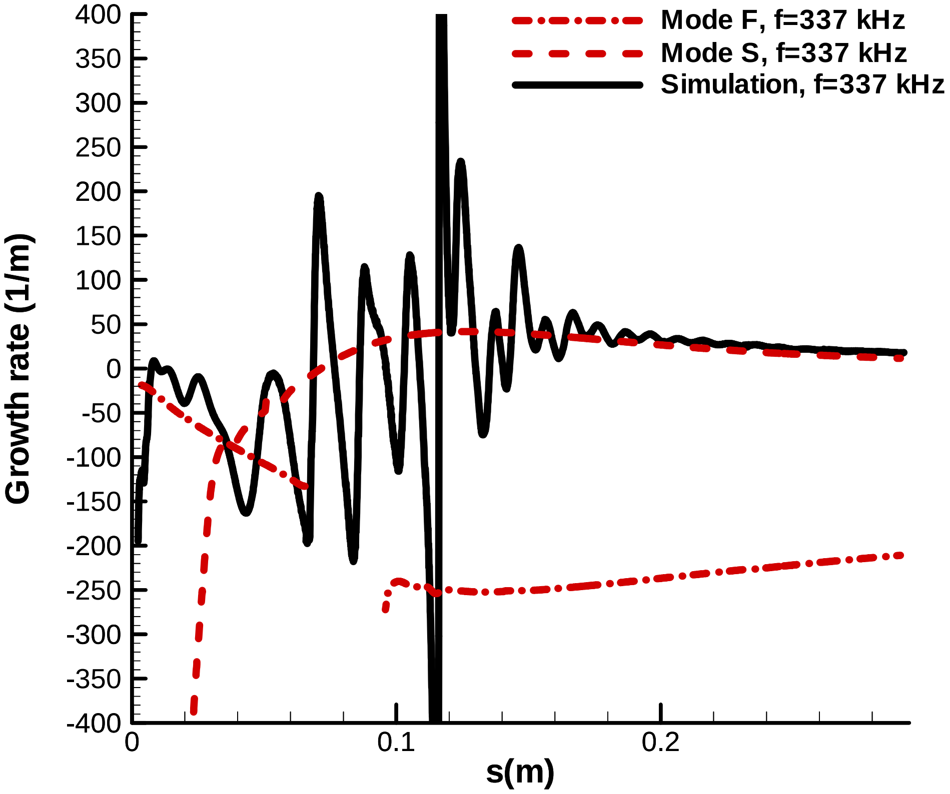
Mode F, f=337 kHz
Mode S, f=337 kHz
Simulation, f=337 kHz
Growth rate (1/m)
400
350
300
250
200
150
100
50
0
-50
-100
-150
-200
-250
-300
-350
-400
0
0.1
0.2
s(m)

(a)

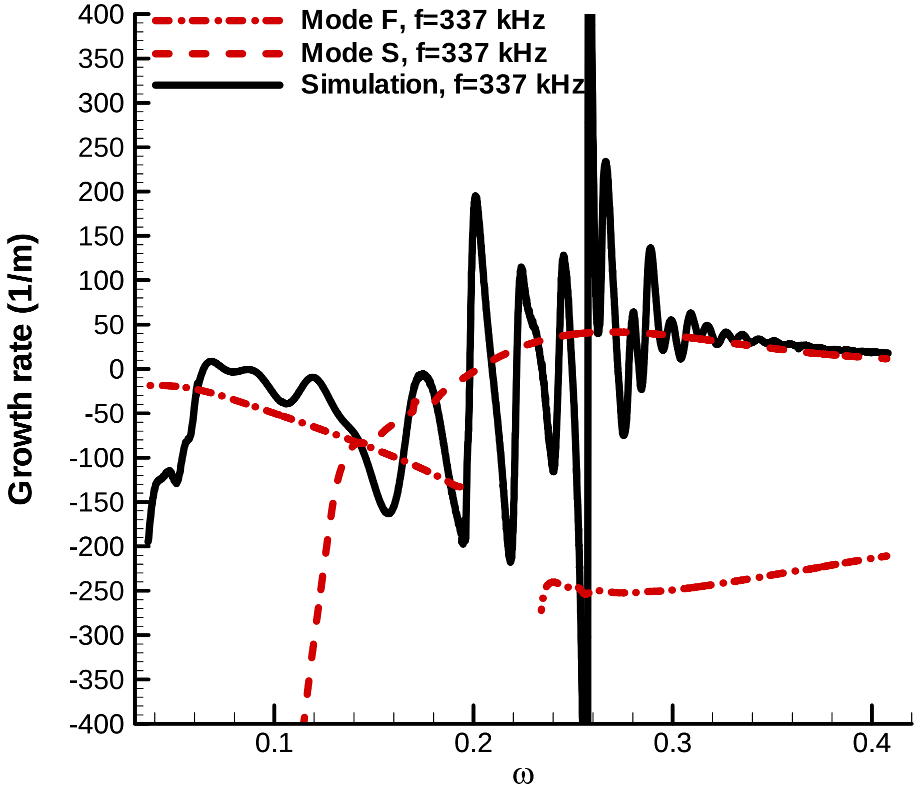

(b)

Figure 90. Comparison of the spatial growth rates of the simulated wall-pressure disturbances with those of the LST predicted mode F and mode S at the frequency of 337 kHz along (a) the dimensional body surface coordinate and (b) the dimensionless circular frequency in Case A1.

The comparison of growth rates between the simulated boundary-layer disturbances and the LST-predicted mode S and mode F at the sampling frequency of 400 kHz for Case A2 is shown in Figure 91 (a). The oscillations in the simulated growth rate as a result of multi-mode wave modulations. The simulated growth rate oscillates vigorously over both mode S and mode F before reaching $s^* = 0.055$ m. This observation is unable to reveal which mode has the outstanding strength before $s^* = 0.055$ m. Then, the simulated growth rate converges to mode S from $s^* = 0.055$ m to 0.09 m. Such observation reveals that the mode S begins to be the dominant mode in the boundary-layer disturbances from $s^* = 0.055$ m to 0.09 m. The LST predicted mode F is stable everywhere while mode S is stable before the Branch-I neutral location of $s^* = 0.055$ m, and it becomes the unstable second Mack mode behind this location. Such neutral location is earlier than the synchronization point of mode S and mode F, $s^* = 0.085$ m, which is discussed and shown earlier in the phase speed comparison of Case A2 in Figure 89 (a). From the earlier discussion of the spatial development of the boundary-layer disturbances with the frequency of 400 kHz in Case A2, which is shown in Figure 87 (b), the boundary-layer disturbances only exponentially grow behind $s^* = 0.052$ m, which is around the Branch-I neutral location. In Figure 91 (a), both growth rates of the simulation and the mode S compare very well downstream from $s^* = 0.09$ m. This observation reveals that the mode S is fully dominant in the boundary-layer disturbances behind $s^* = 0.09$ m, which is around the synchronization point of mode S and mode F. These combined observations of the earlier results and the growth rate comparison implies that the boundary-layer disturbances only begin to grow exponentially at the location where the dominancy of the mode S related second mode in the boundary-layer disturbances first appears. Different to Case 1 and A1, the dominancy of the mode S related second mode instability in Case A2 first appears at the Branch-I neutral location, which is earlier than the synchronization point of mode S and mode F. Such difference is likely caused by the higher initial strength of the mode S related second mode at the Branch-I neutral location in Case A2. The trend of the ratio of the receptivity coefficient of mode S over the one of the overall boundary-layer disturbances found in the earlier parametric study of the receptivity coefficients at the Branch-I neutral locations in Section 4.3.2 supports this explanation.

Figure 91 (b) shows the comparison in Case A2 between the simulated growth rate and the one obtained from LST in self-similar parameter, which allows comparison of common characteristics between different cases regardless to the dimensional differences. The horizontal axis in Figure 91 (b) has the dimensionless circular frequency, ω, instead of the dimensional streamwise location along the cone surface, s^*.

In Figure 91 (b), there are oscillations in the simulated growth rate as a result of multi-mode wave modulations. The simulated growth rate oscillates vigorously over both mode S and mode F before reaching $\omega = 0.21$. This observation is unable to reveal which mode has the outstanding strength before $\omega = 0.21$. Then, the simulated growth rate converges to mode S from $\omega = 0.21$ to 0.27. Such observation reveals that the mode S begins to be the dominant mode in the boundary-layer disturbances from $\omega = 0.21$ to 0.27. The LST predicted mode F is stable everywhere while mode S is stable before the Branch-I neutral location of $\omega = 0.21$, and it becomes the unstable second Mack mode behind this location. Such neutral location is earlier than the synchronization point of mode S and mode F, $\omega = 0.26$, which is discussed and shown earlier in the phase speed comparison in self-similarity variable of Case A2 in Figure 89 (b). In the growth rate comparison along dimensionless circular frequency in Figure 91 (b), both growth rates of the simulation and the mode S compare very well downstream from $\omega = 0.27$. This observation reveals that the mode S is fully dominant in the boundary-layer disturbances behind $\omega = 0.27$, which is shortly behind the synchronization point of mode S and mode F. These combined observations of the earlier phase speed comparison and the growth rate comparison implies that the dominancy of the mode S related second mode in the boundary-layer disturbances first appears at the Branch-I neutral location, which is different to Case 1 and A1. Moreover, the synchronization of the phase speeds of mode S and mode F further contributes to the dominancy of the mode S related second mode in the boundary-layer disturbances. The difference in the initial location of dominance is likely caused by the higher initial strength of the mode S related second mode at the Branch-I neutral location in Case A2. The trend of the ratio of the receptivity coefficient of mode S over the one of the overall boundary-layer disturbances found in the earlier parametric study of the receptivity coefficients at the Branch-I neutral locations in Section 4.3.2 supports this explanation. This conclusion is consistent with the conclusion in the earlier receptivity mechanism analyses of Case A2.

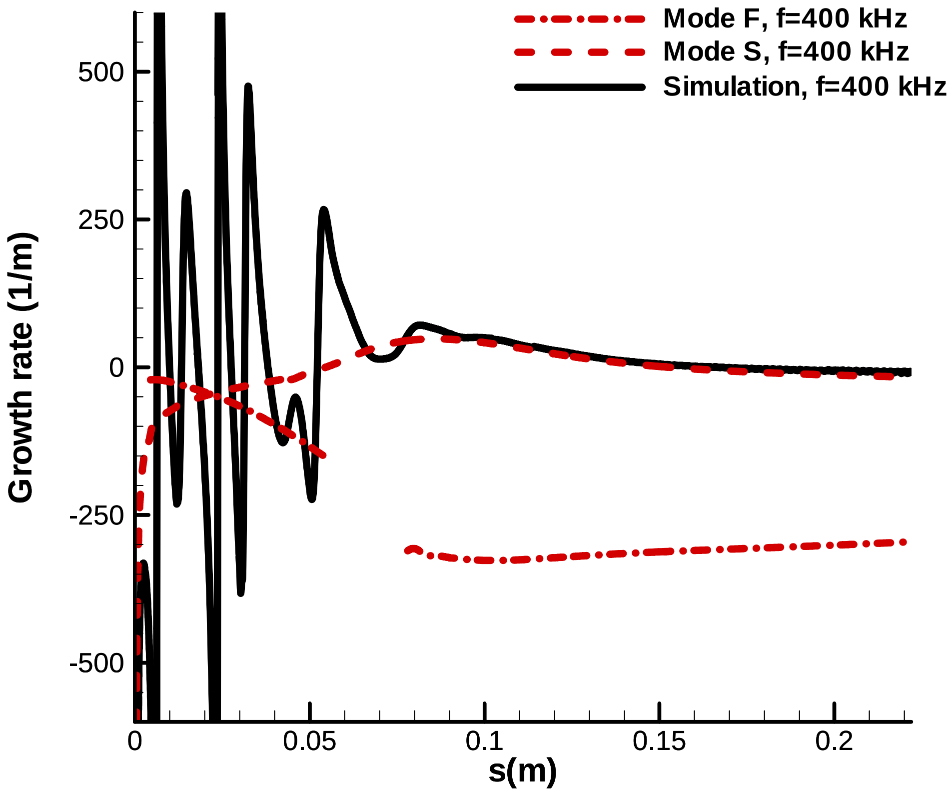
Mode F, f=400 kHz
Mode S, f=400 kHz
Simulation, f=400 kHz
Growth rate (1/m)
500
250
0
-250
-500
0
0.05
0.1
0.15
0.2
s(m)

(a)

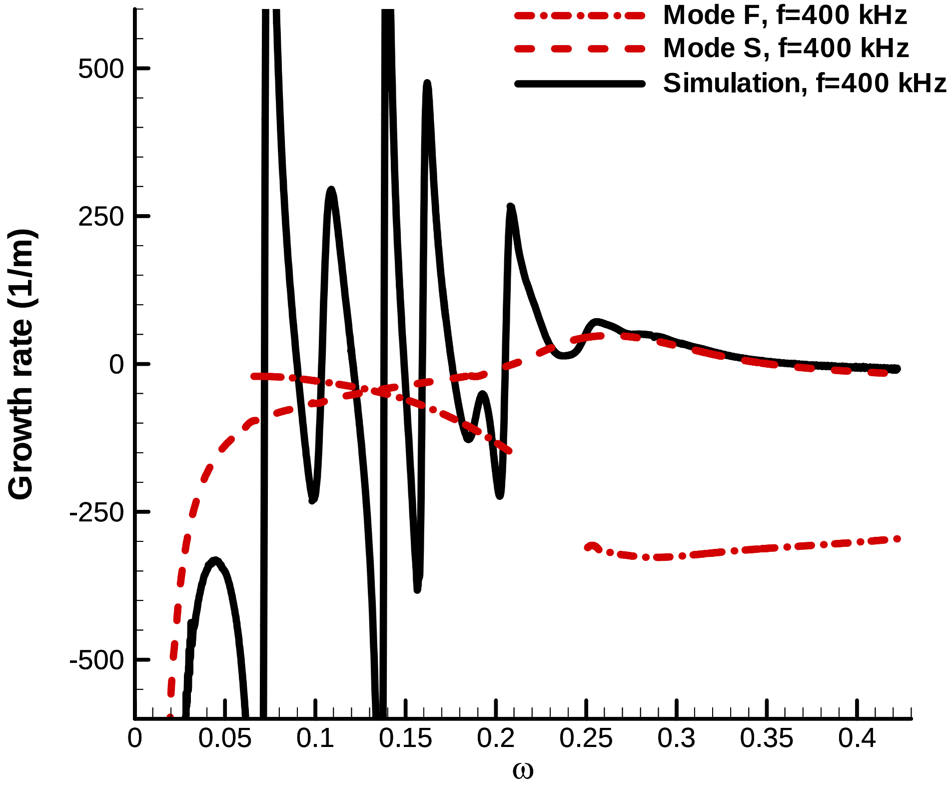

(b)

Figure 91. Comparison of the spatial growth rates of the simulated wall-pressure disturbances with those of the LST predicted mode F and mode S at the frequency of 400 kHz along (a) the dimensional body surface coordinate and (b) the dimensionless circular frequency in Case A2.

From the observations of all three cases of different nose bluntness, the receptivity modal evolution paths for all the cases observed are consistent with the one found in the earlier phase speed comparison study. Moreover, by combining the earlier observations from the spatial amplitude development study of the boundary-layer disturbances at the sampling frequencies and the phase speed comparison study with the current observations from the growth rate comparison, the boundary-layer disturbances are found to be only beginning to grow exponentially at the location where the dominancy of the mode S related second mode in the boundary-layer disturbances first appears. Furthermore, the beginning locations of the mode S related second mode dominance in the boundary-layer disturbances are found to be different for different nose bluntness. The sharper cone has the beginning location more upstream and closer to the Branch-I neutral location of the mode S related second mode. For the blunter cone, the beginning location can be further downstream from the Branch-I neutral location, and can even pass the synchronization point of mode S and mode F. Such trend is likely due to the higher initial strength of the mode S related second mode at the Branch-I neutral location over the sharper cone. The trend of the ratio of the receptivity coefficient of mode S over the one of the overall boundary-layer disturbances found in the earlier parametric study of the receptivity coefficients at the Branch-I neutral locations in Section 4.3.2 supports this explanation.

Owing to the high degree of similarity that are previously found to be held between the cases of different nose bluntness, similar to the synchronization point of mode S and mode F, the dimensionless circular frequencies of Branch-I neutral point of the mode S related second mode in all the cases are found to be very close to each other.

In order to confirm the previous identification of modal evolution in the induced boundary-layer disturbances during the receptivity process, we compare the mode shapes or the eigenfunctions at the sampling frequencies between the simulated boundary-layer disturbances and the mode S and the mode F calculated by LST at locations in the upstream region and the downstream region. These are shown in Figure 92 and Figure 93 for Case A1 and A2 respectively. Noticeably, the vertical axis is the dimensional wall-normal height, and the horizontal axis is the pressure perturbation amplitude that is normalized by the maximum amplitude in the current mode shape.

In Figure 92 (a), at the location of $s^* = 0.0356\ \mathrm{m}$ in the upstream region before the major multi-mode modulations shown in the phase speeds comparison in Figure 88 (a), the mode shape of the simulated boundary-layer disturbances within the boundary layer below $H^* = 0.0008\ \mathrm{m}$ is very close to the one of mode F. However, the mode shape outside the boundary layer is deviated away from the mode F. This comparison shows that in such upstream location, the mode F is relatively strong in the disturbances within the boundary layer. However, there are transient forcings exist outside the boundary layer at that location.

In Figure 92 (b), at the location of $s^* = 0.275\ \mathrm{m}$ further downstream from the synchronization point, the comparisons shows that the simulated mode shape compares very well to the one of mode S both inside and outside of the boundary layer. This comparison shows that the mode S is dominant in the boundary-layer disturbances at such downstream location after the synchronization of mode S and mode F, and there is no transient forcings outside the boundary layer. The current modal identifications obtained from the mode shape analyses at the upstream and downstream locations are consistent with the receptivity modal path found in the earlier phase speeds and growth rates comparisons.

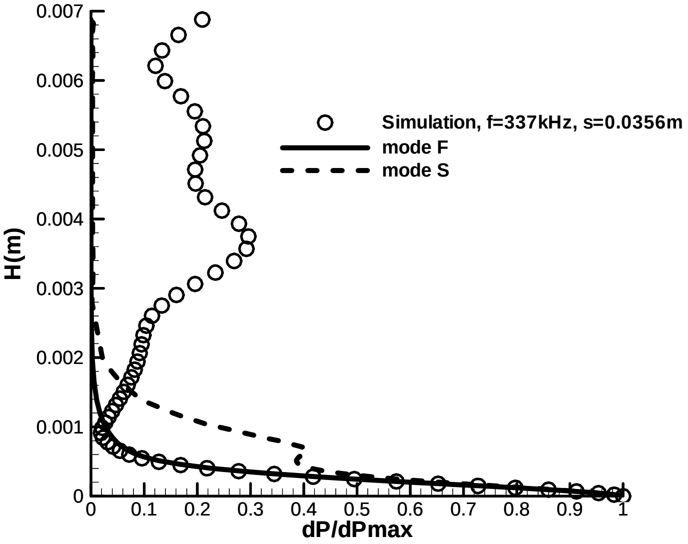

(a)

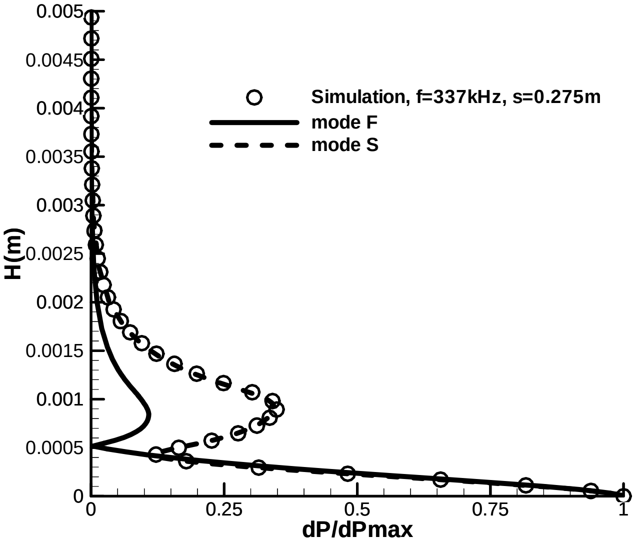

(b)

Figure 92. Comparisons of wall-normal mode shapes of pressure perturbations between the simulation and LST with the frequency of 337 kHz at (a) an upstream location, and (b) a downstream location in Case A1.

In Figure 93 (a), at the location of $s^* = 0.012\text{ m}$ in the upstream region shortly after the excitation of mode F from the fast acoustic waves shown in the phase speeds comparison in Figure 89 (a), the mode shape of the simulated boundary-layer disturbances within the boundary layer below $H^* = 0.00023\text{ m}$ is close to the one of mode F. However, the mode shape at the edge of boundary layer around $H^* = 0.0003\text{ m}$ and outside the boundary layer is deviated away from the mode F. This comparison shows that in such upstream location, the mode F is relatively strong in the disturbances within the boundary layer. However, there are transient forcings exist at the edge of the boundary layer and outside the boundary layer at that location. The existence of transient forcings at the edge of the boundary layer is most likely related to the modulations of the simulated phase speed between the mode F and the fast acoustic waves in the upstream region in Figure 89 (a).

In Figure 93 (b), at the location of $s^* = 0.22\text{ m}$ further downstream from the synchronization point, the comparisons shows that the simulated mode shape compares very well to the one of mode S both inside and outside of the boundary layer. This comparison shows that the mode S is dominant in the boundary-layer disturbances at such downstream location after the synchronization of mode S and mode F, and there is no transient forcings outside the boundary layer. The current modal identifications obtained from the mode shape analyses at the upstream and downstream locations are consistent with the receptivity modal path found in the earlier phase speeds and growth rates comparisons.

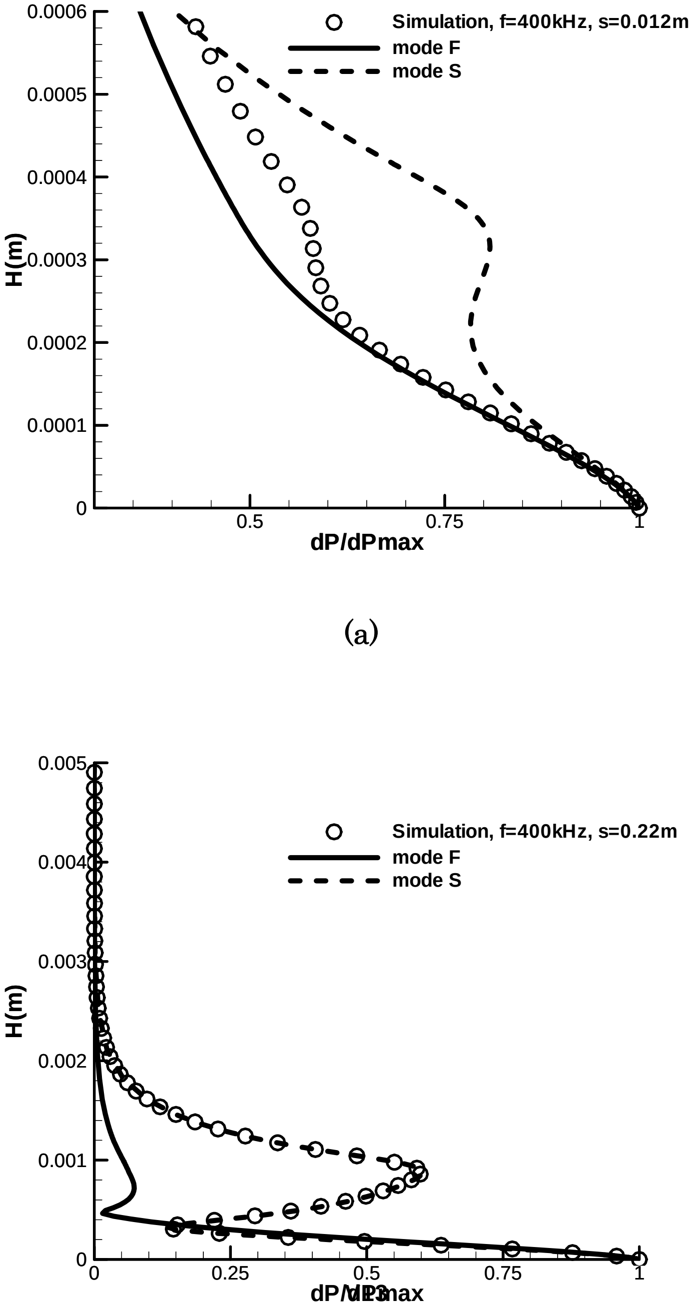

(a)

(b)

Figure 93. Comparisons of wall-normal mode shapes of pressure perturbations between the simulation and LST with the frequency of 400 kHz at (a) an upstream location, and (b) a downstream location in Case A2.

4.4 Simulation Results for Effects of Freestream Mach Number

The boundary-layer linear receptivity and stability mechanisms with the effects of nose bluntness are studied up to this point. Other than nose bluntness effects, the freestream Mach number effects are chosen in the current study, since freestream Mach number effects are frequently encountered during a flight in the atmosphere. In the following sections, the receptivity and stability mechanisms with freestream Mach number effects will be discussed.

Unless specified, all flow variables shown in the figures are dimensionless, which are normalized by the corresponding freestream values. For all contour plots, the upper boundary is the location of the shock, the lower boundary is the cone-wall, the left boundary is the flow inlet, and the right boundary is the flow exit. Since the cone is at zero degree angle of attack, only the upper half of the cone is demonstrated, and the lower half is the mirror image of the upper half due to the axis-symmetry of the flow. Figure 11 shows the partial view of the computational grid structure around the cone. Due to the limiting computer power for computing almost a million grid points at once, the simulation is divided into around 20 zones. Zone 1 is the computation domain that wraps around the hemispherical cone nose, Zone 2 to 20 wrap around the compression wall of the cone.

4.4.1 Steady Base Flow Solutions

Freestream Mach number has significant effects on the characteristics of the flow around the cone. In this work, the effects on steady base flow, boundary-layer receptivity and linear growth of boundary-layer disturbances are studied.

In the current parametric study, the final goal is to study the freestream Mach number effects over the boundary-layer receptivity to freestream hotspot perturbations and the linear growth of boundary-layer disturbances. The boundary-layer receptivity and linear growth study are carried out from the results of unsteady flow simulation. Moreover, the unsteady flow simulation is carried out based on the steady base flow. Hence, the initial step prior to all the subsequent analyses is to carry out the numerical simulations with different freestream Mach number over the same compression cone geometry and to conduct the parametric study on the freestream Mach number effects in the steady base flow.

Steady base flow contours provide an overview of the distribution of a flow variable throughout the flow field. In Figure 94, Figure 95, Figure 98 and Figure 99, the Mach number contours and the entropy contours are presented. Figure 94 and Figure 95 show the Mach number contours of Case B1 and B2. For Case A1, the flow field extended to around $x^* = 0.36\ \text{m}$. For Case B2, the flow field is extended to $x^* = 0.46\ \text{m}$. Both cases have similar observations. There is a thin boundary layer that is blue in color above the wall. The Mach number is very low in the nose region, since there is a stagnation flow region where the viscous interaction is very significant. Shortly behind the nose region, the Mach number outside the boundary layer rises drastically for a short distance. In contrast to the short rise of the Mach number immediately behind the nose region, the gradual decreasing of Mach number throughout the rest of the cone is due to the adverse pressure gradient that is produced by the concavity of the flared cone surface. Eventually, a region of relatively low Mach number appears above the boundary layer near the end of the cone. This trend of Mach number in the steady base flow field is similar to Case 1, which is discussed in Section 3.2.1. There are several main differences between the two cases of different freestream Mach number (Case B1 and B2) and the standard case (Case 1). Firstly, the boundary layer thickness behind the nose region is almost constant in Case 1. However, Case B1 and B2 do not have constant boundary layer thicknesses along the cone. Secondly, the shock front of the case of the higher freestream Mach number is closer to the surface of the cone. Thirdly, near the end of the cone in Case B2, besides the yellow colored lower Mach number region immediately above the boundary layer, there is another light green colored lower Mach number region behind the shock. There are Mach waves developed in the flow field by the flaring of the cone, and the flow behind the shock boundary decelerates by passing through the Mach waves downstream. Thus, the light green colored lower Mach number region formed as the result of such deceleration.

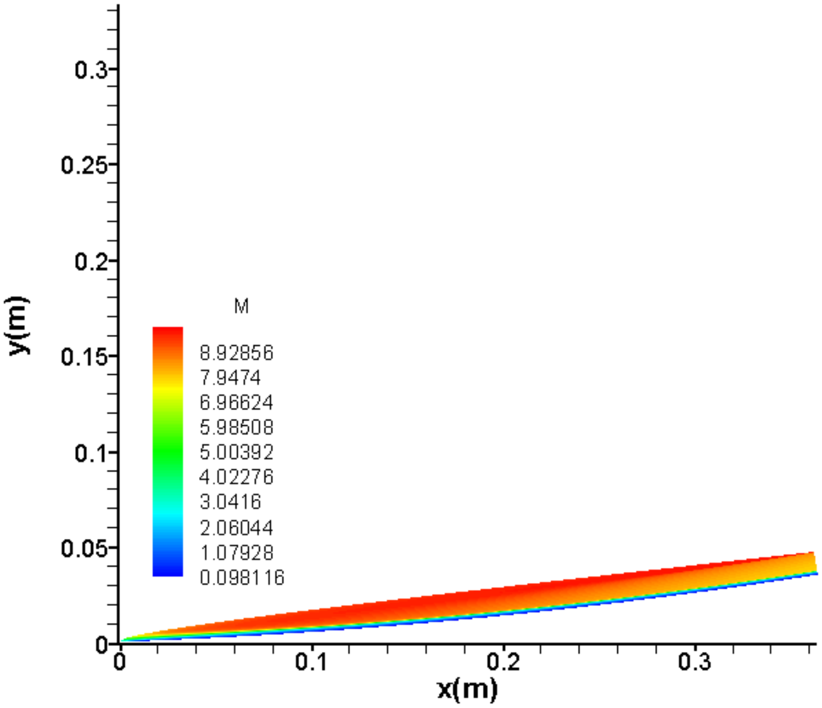

Figure 94. Mach number contours of Case B1 steady base flow.

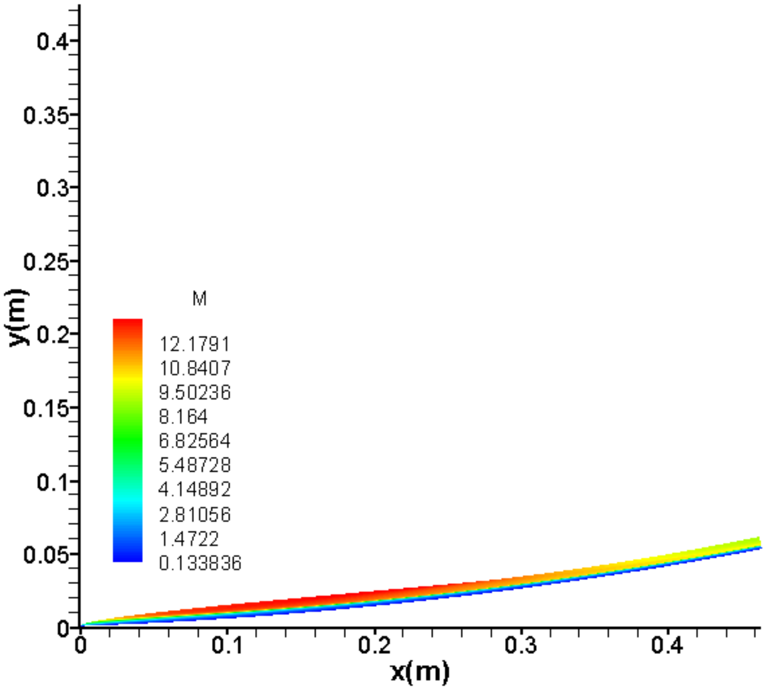

Figure 95. Mach number contours of Case B2 steady base flow.

In Figure 96, the shock shapes of all three cases of freestream Mach number effects are compared. Noticeably, the geometry of the cone is identical in these cases. One can see that the shock angle is smaller for the higher freestream Mach number case. For Case 1 and B1, the shock shape downstream is almost straight. Only Case B2 has the downstream part of the shock shape concaving upward behind $x^* = 0.26$ m, and the shock shape before this location is nearly straight behind the nose region. Since the higher freestream Mach number will lead to closer shock front to the cone body, the straight portion of the shock shape, which is the portion between the bow shock near the nose and the concaved portion downstream, ends earlier. Due to the Mach waves developed along the flared wall, the shock downstream are being forced to curve upward rather than touching the wall after a certain distance away from the nose. If we assume the flared cones are sufficiently long in the other cases, the concaved portion of the shock shape will eventually appear as well.

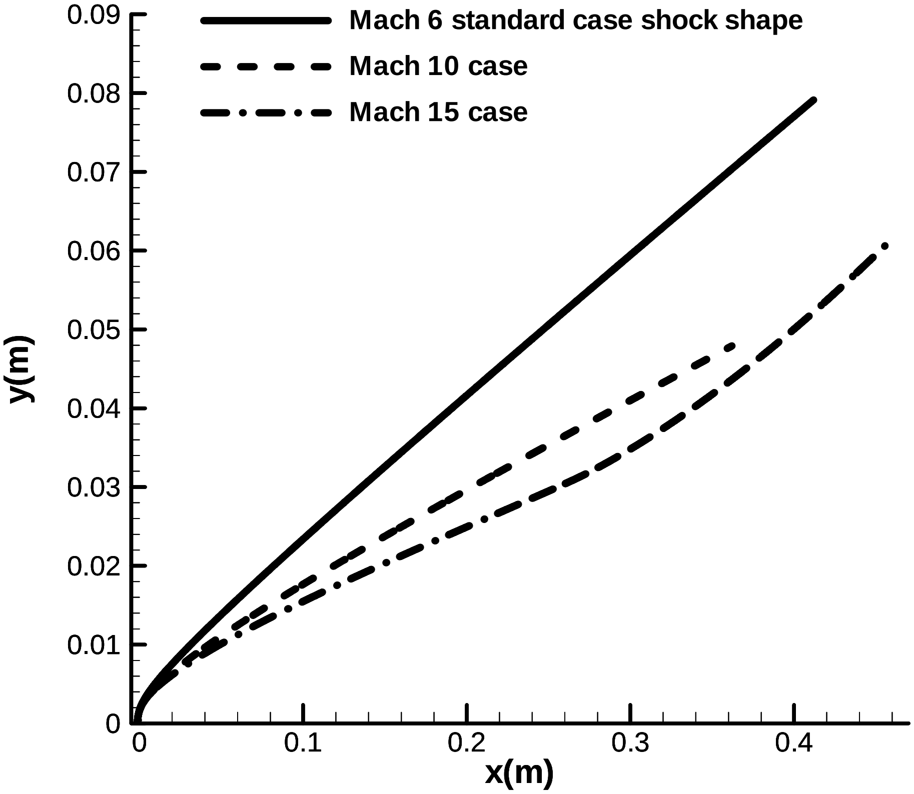

Figure 96. Comparison of the shock shape between the cases of different freestream Mach number (Case 1, B1 and B2).

In Figure 97, the local Mach number immediately behind the shock relative to the freestream Mach number for all three cases of freestream Mach number effects are compared. The Mach number rises from the stagnation line in the nose region to the middle of the cone where the nose effects are less significant. For the Cases 0 and B1, the relative Mach number is asymptotically approaching 1 along the finite-length flared cone while the shock is attenuating downstream. For Case B2, there is a significant decrease initially appears around $x^* = 0.26 \text{ m}$. This decrease of Mach number begins about the same location as the concaved portion of the shock shape initially appears. The Mach waves developed in the flow field by the concavity of the wall causes the decrease of the Mach number behind the shock. Moreover, the current comparison shows that the higher freestream Mach number leads to the lower relative Mach number behind the shock. Such observation reveals that the shock with a higher freestream Mach number is stronger.

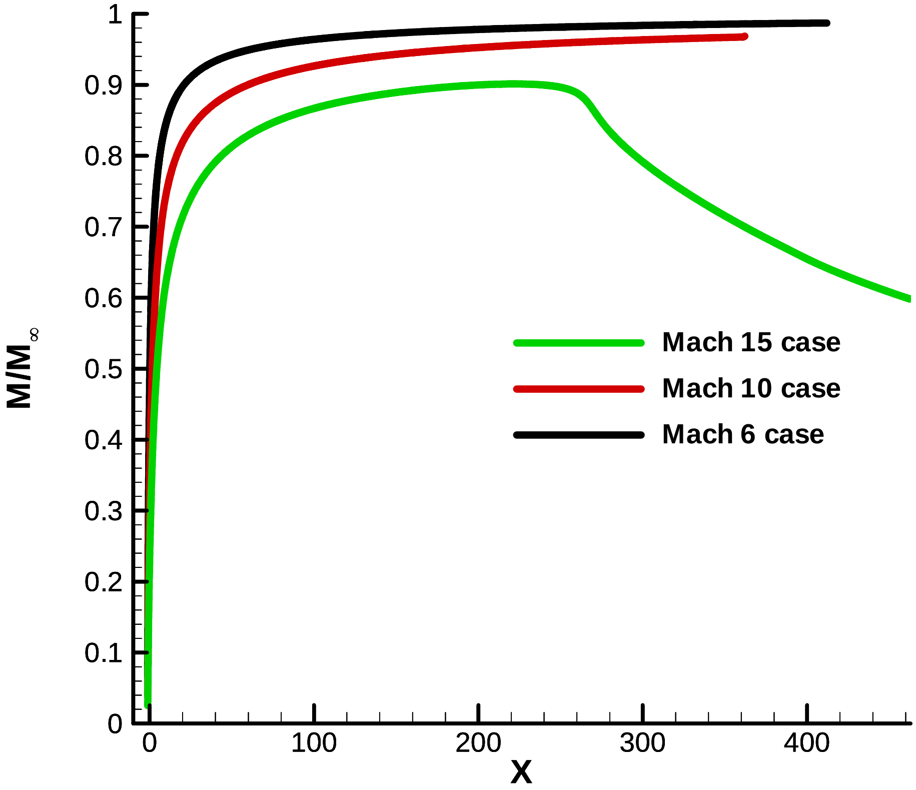

Figure 97. Comparison of Mach number streamwise distribution behind the shock between the cases of different freestream Mach number (Case 1, B1 and B2).

In the nose region of a blunt cone, according to Crocco's theorem, the curvature of bow shock generates a gradient of entropy, which is related to an entropy layer. In Figure 98 and Figure 99, the entropy contours of the steady base flow of Case B1 and B2 are shown. There is no gradient of entropy generated from the straight oblique shock far behind the nose region. However, there is a thin layer of entropy gradient next to the wall in both cases. Such layer of entropy gradient is the resulting boundary layer that has swallowed the entropy layer generated by the curved shock in the nose region and shortly behind it. More detailed study on the interactions between entropy layer and boundary layer of the steady base flow is presented in the latter part of this section.

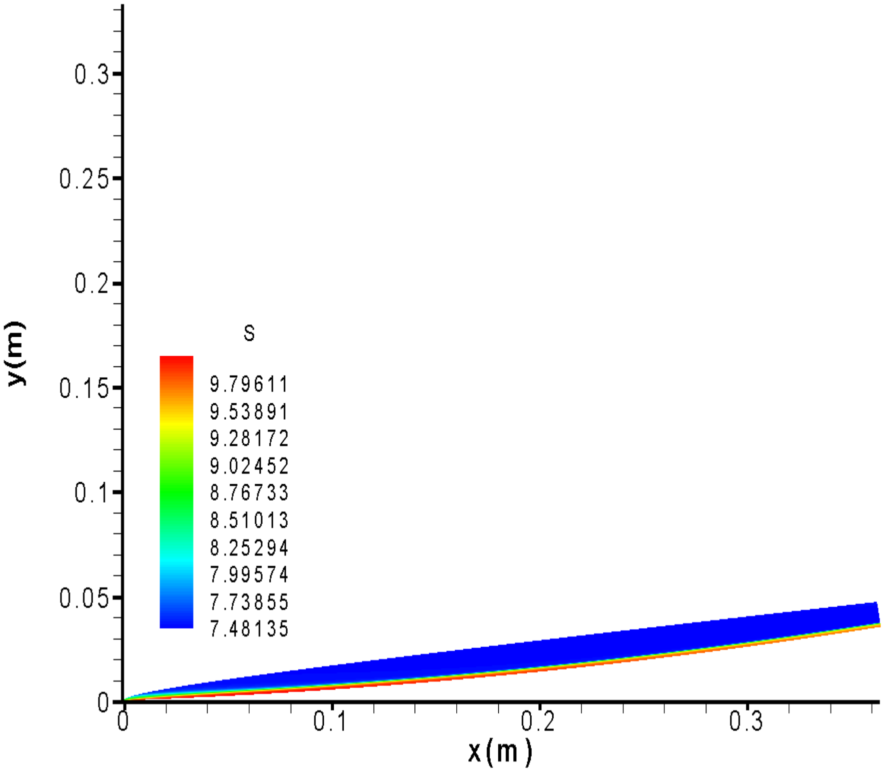

Figure 98. Entropy contours of Case B1 steady base flow.

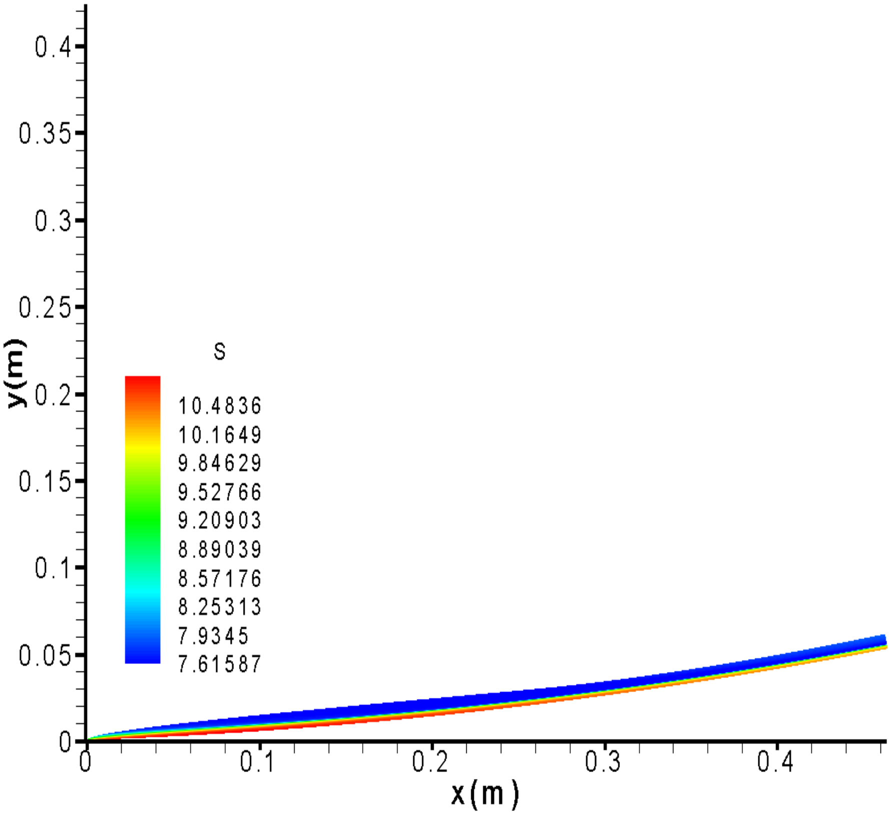

Figure 99. Entropy contours of Case B2 steady base flow.

In parametric study, it is necessary to make comparisons between cases of different parameters. While making comparisons, the common features or similarities between different cases are required. Therefore, expressing the dimensions in self-similarity or dimensionless variables is convenient in parametric study. Figure 100 shows the comparison of wall-normal profiles of velocity shortly behind the nose region between all three cases of different freestream Mach number (Case 1, B1 and B2). Noticeably, the wall-normal height is normalized by the local boundary-layer thickness, and the velocity immediately behind the shock normalizes the velocity. Since the dimensional streamwise locations of all three cases are relevant due to the same freestream Reynolds number per unit length and the same cone geometry are used, both the local Reynolds numbers and the dimensional streamwise locations are viable to be taken as a referencing common characteristic between all three cases.

In Figure 100, the Reynolds number around 221 is chosen as a location in the upstream region shortly behind the nose. Noticeably, the velocity profiles of Case B1 and B2 have the boundary layer extends up to the shock boundary due to the strong nose effects. The velocity profile of Case 1 outside the boundary layer is mostly uniform. The curvatures of the turning profiles around the edge of boundary layer are different for all three cases. Specifically, Case 1 has the largest curvature, and Case B2 has the smallest curvature. The profile with a smaller curvature around the edge of boundary layer has the stronger nose effects, and therefore, the effects of the bow-shock curvature would cause the variation of wall-normal velocity gradient in the shock layer and thus the boundary layer. In addition, the nose effects of the wall-normal profile imply that the less self-similar is the flow field in the early upstream region nearby the nose. From the comparison of the curvatures of the profiles around the edge of boundary layer at the same local Reynolds number, the steady base flow field of the higher freestream Mach number has the stronger nose effects at the same local Reynolds number in the upstream region.

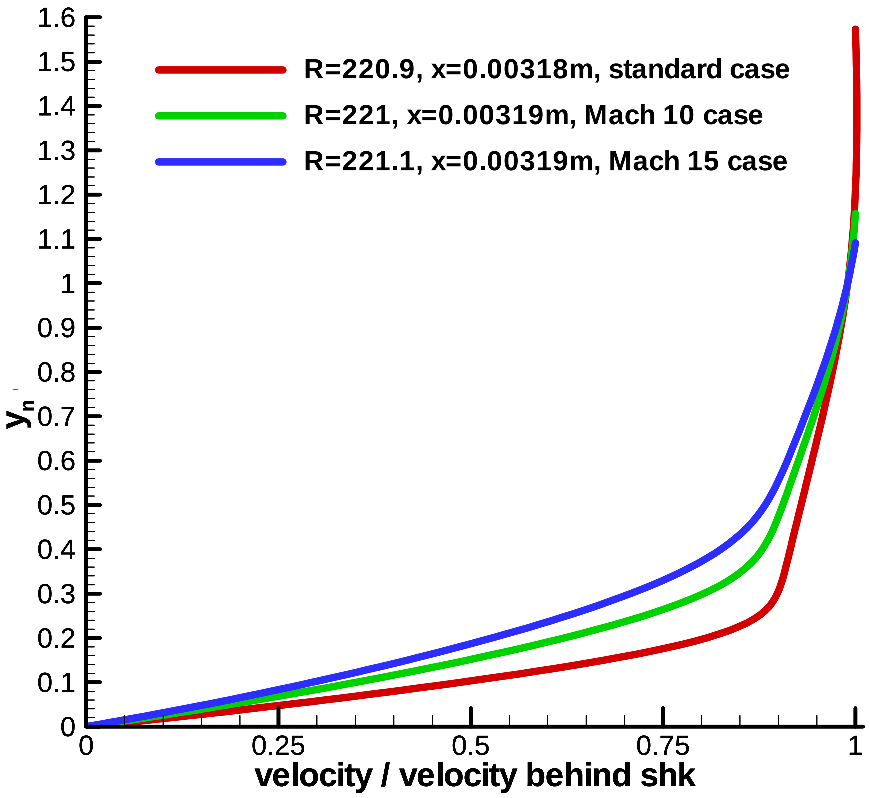

Figure 100. Comparison of the steady base wall-normal velocity profiles at the same local Reynolds number shortly behind the nose region between the cases of different freestream Mach number (Case 1, B1 and B2).

In addition to the velocity profiles, the wall-normal temperature profiles of Case 1, B1 and B2 shortly behind the nose region are shown in Figure 101. Since the isothermal wall temperatures for each case are different, we compare only the shape of the temperature profile for each case by taking the normalized relative temperature, $(T - T_{shk})/(T_{wall} - T_{shk})$. The normalized relative temperature is zero at the shock boundary, and it is equal to 1 at wall. All these profiles have almost the same local Reynolds number and the dimensional spatial locations. It is obvious that the thickness proportions of boundary layer in the shock layer of Case B1 and B2 are higher than the one of Case 1. The reason of having the higher boundary-layer thickness proportion is that the curvature of the bow shock in the nose region creates significant variation of temperature gradient in the shock layer and thus the boundary layer, in other words, the flow field has stronger nose effects. In addition, the nose effects of the wall-normal profile imply that the less self-similar is the flow field in the early upstream region nearby the nose. From the comparison of the boundary-layer thickness proportions at the same local Reynolds number, the steady base flow field with the higher freestream Mach number has the stronger nose effects at the same local Reynolds number.

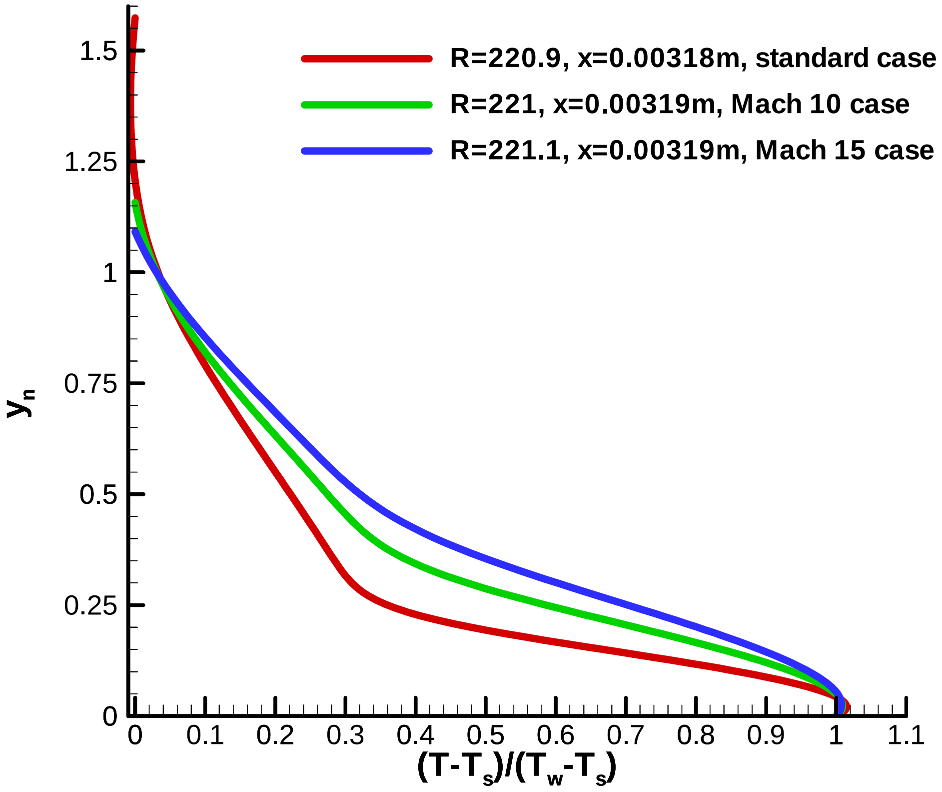

Figure 101. Comparison of the steady base wall-normal temperature profiles at the same local Reynolds number shortly behind the nose region between the cases of different freestream Mach number (Case 1, B1 and B2).

The wall-normal profiles of velocity in the middle region of the cone between all three cases of different freestream Mach number (Case 1, B1 and B2) are shown in Figure 102. Noticeably, the wall-normal height is normalized by the local boundary-layer thickness, and the velocity is normalized by the velocity immediately behind the shock. Since the cone geometry and the freestream Reynolds number per unit length for all three cases are the same, both the local Reynolds numbers and the dimensional streamwise locations can be taken as a referencing common characteristic between all three cases. In Figure 102, the local Reynolds number of 900 is chosen as a sampling location in the middle region of the cone. The velocity profiles outside the boundary layer are uniform. However, the curvatures of the profiles at the edge of boundary layer are different for all three cases. Specifically, Case B2 has the largest curvature, Case 1 has the smallest curvature, and Case B1 has the curvature that is only slightly smaller than Case B2. The profiles of Case B1 and B2 are close to similarity. However, Case 1 is still far away from the cases of higher freestream Mach numbers. The profile with a smaller curvature at the edge of the boundary layer has stronger nose effects, and therefore, the effects of the bow-shock curvature would cause the variation of wall-normal velocity gradient in the shock layer and thus the boundary layer. In addition, the nose effects of the wall-normal profile imply that the flow field in the middle region of the cone is more self-similar than the one in the early upstream region. From the comparison of the curvatures of the profiles at the edge of boundary layer at the same local Reynolds number, the steady base flow field of the lower freestream Mach number has the stronger nose effects at the same local Reynolds number in the middle region of the cone.

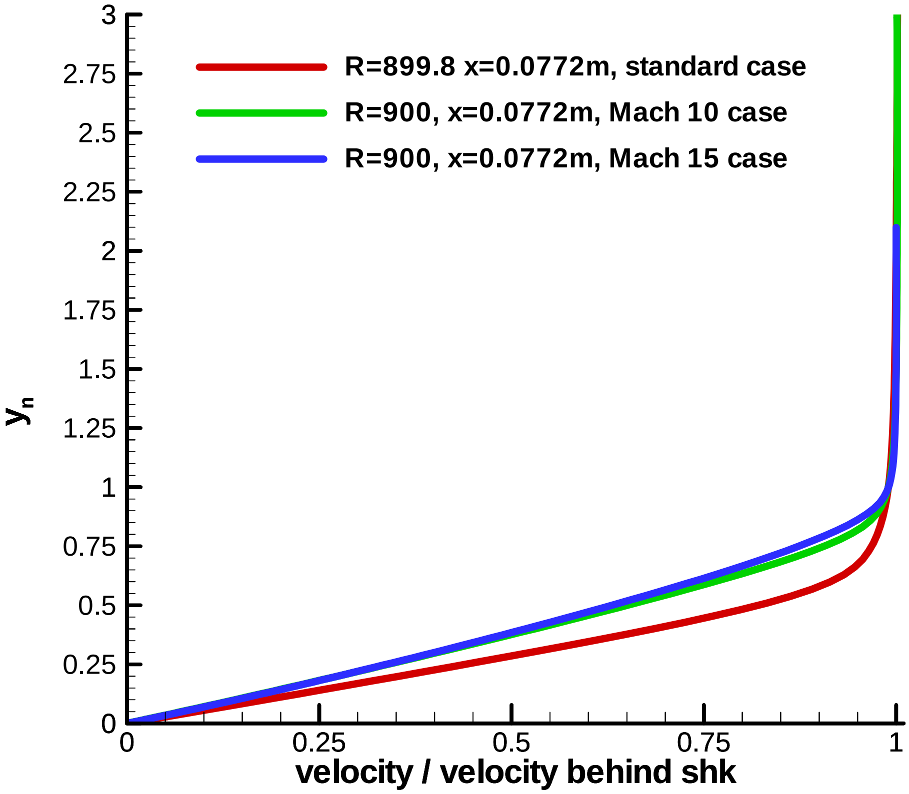

Figure 102. Comparison of the steady base wall-normal velocity profiles at the same local Reynolds number in the middle region of the cone between the cases of different freestream Mach number (Case 1, B1 and B2).

Other than the velocity profiles, the wall-normal temperature profiles of Case 1, B1 and B2 in the middle region are shown in Figure 103. Since the isothermal wall temperatures for each case are different, we compare only the shape of the temperature profile for each case by taking the normalized relative temperature, $\left(T-T_{shk}\right)/\left(T_{wall}-T_{shk}\right)$. The normalized relative temperature is zero at the shock boundary, and it is equal to 1 at wall. All these profiles have the same local Reynolds number of 900. It is obvious that the profile curvature at the edge of the boundary layer of Case B1 and B2 is larger than the one of Case 1. Meanwhile, the profile curvatures of boundary-layer edge of Case B1 and B2 are nearly similar. The reason of having lower profile curvature at the boundary-layer edge for Case 1 is that the curvature of the bow shock in the nose region distorts temperature gradient significantly in the shock layer and thus the boundary layer, in other words, the flow field has the stronger nose effects than Case B1 and B2. In addition, the weaker nose effects relative to those in the early upstream region imply that the flow field in the middle region of the cone is more self-similar than the one in the early upstream region. From the comparison of curvatures of the profiles at the edge of boundary layer at the same local Reynolds number, one can conclude that the nose effects in the middle region of Case B1 and B2 are less significant, and thus Case B1 and B2 has archived some degree of self-similarity, while Case 1 is still far from self-similarity in the middle region.

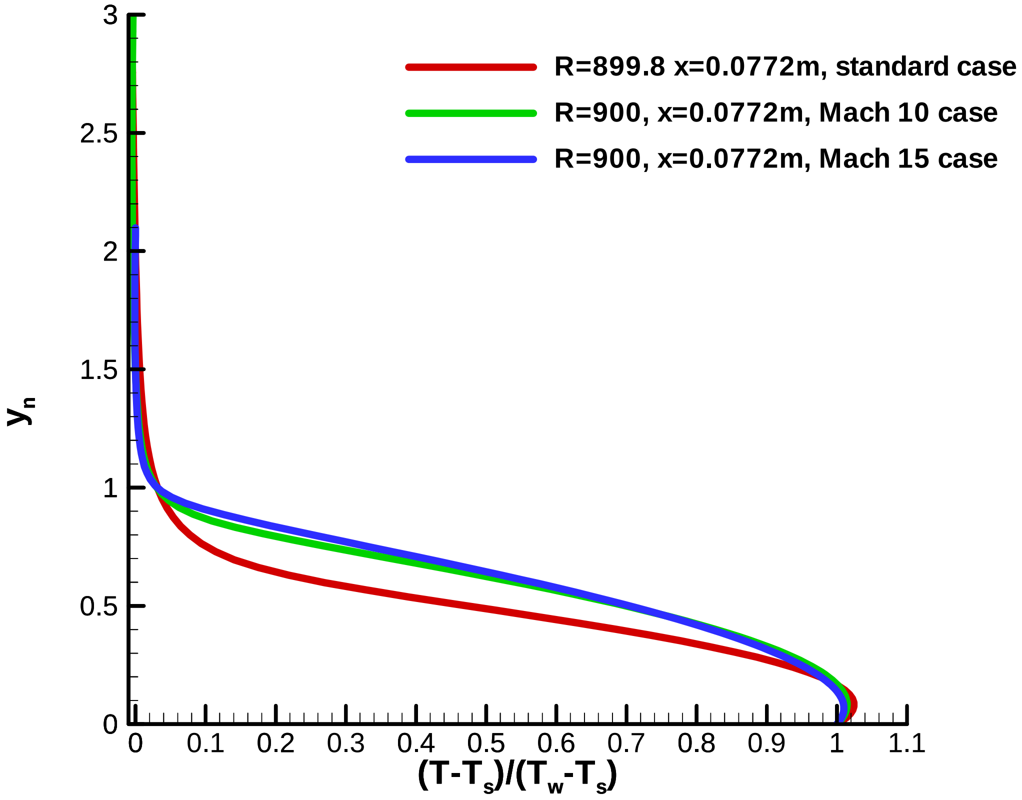

Figure 103. Comparison of the steady base wall-normal temperature profiles at the same local Reynolds number in the middle region of the cone between the cases of different freestream Mach number (Case 1, B1 and B2).

Figure 104 shows the wall-normal profiles of velocity between all three cases of different freestream Mach number (Case 1, B1 and B2) in the downstream region. Noticeably, the wall-normal height is normalized by the local boundary-layer thickness, and the velocity is normalized by the velocity immediately behind the shock. Since the cone geometry and the freestream Reynolds number per unit length for all three cases are the same, both the local Reynolds numbers and the dimensional streamwise locations can be taken as a referencing common characteristic between all three cases. In Figure 104, the local Reynolds number of 1704 is chosen as a location in the downstream region of the cone. The velocity profiles outside the boundary layer are uniform. Different to the profiles in the earlier regions, those in the downstream region are much closer to each other. Particularly, the profiles of Case B1 and B2 are very similar. However, the profile curvature of the boundary-layer edge of Case 1 is still less than those of Case B1 and B2. By comparing the observation in the downstream region to the earlier regions, the proximity of the profiles of all the cases of freestream Mach number effects (Case 1, B1 and B2) in the downstream region implies that the nose effects are less significant in the downstream region for Case 1, B1 and B2. However, the degree of self-similarity in the flow field of the downstream region in the cases of freestream Mach number effects is not as high as the one in the earlier study of the nose bluntness effects.

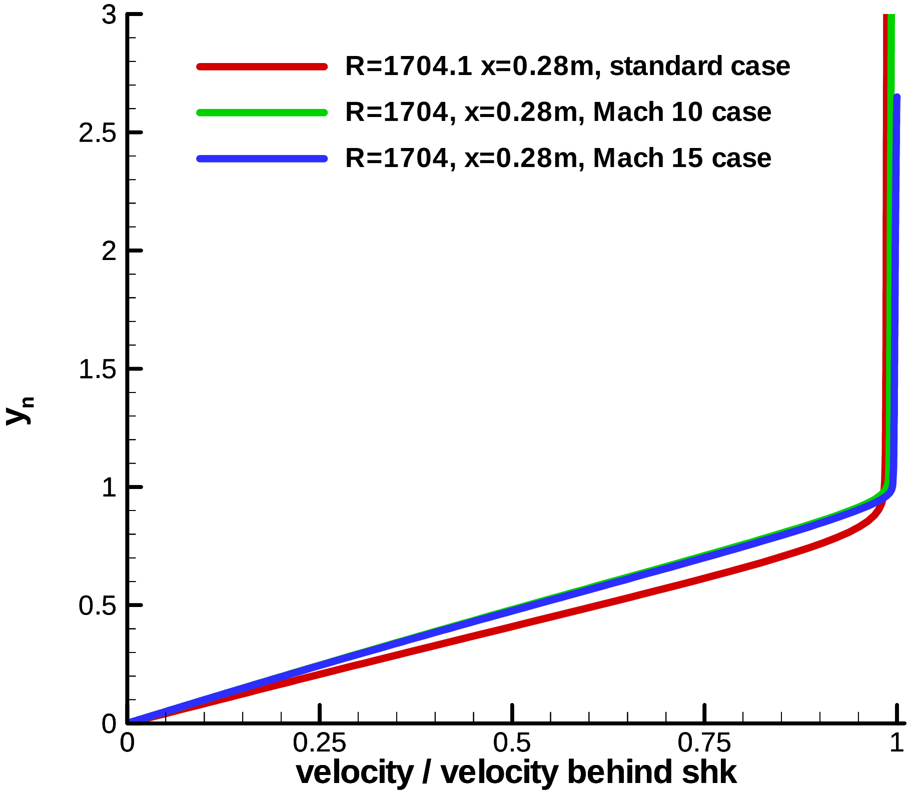

Figure 104. Comparison of the steady base wall-normal velocity profiles at the same local Reynolds number in the downstream region of the cone between the cases of different freestream Mach number (Case 1, B1 and B2).

The wall-normal temperature profiles of Case 1, B1 and B2 in the downstream region are shown in Figure 105. All these profiles have the same local Reynolds number of 1704. Noticeably, the uniform normalized relative temperatures outside the boundary layer are slightly different between each case, because of the Mach waves appearing near the shock boundary and affecting the temperature behind the shock. However, the temperature profiles inside the boundary layer are not affected accordingly. In contrast to the profiles in the earlier regions, those in the downstream region are in close proximity to each other, except the profile curvature of the boundary-layer edge of Case 1 is still less than those of Case B1 and B2. By comparing the observations in the downstream region to those in the earlier regions, the proximity of the profiles of all the cases of freestream Mach number effects (Case 1, B1 and B2) in the downstream region implies that the nose effects are less significant in the downstream region for Case 1, B1 and B2. However, the degree of self-similarity in the flow field of the downstream region in the cases of different freestream Mach numbers is not as high as the one in the earlier study of the nose bluntness effects. Moreover, only Case B1 and B2 have reached a certain degree of self-similarity, Case 1 is still not similar to Case B1 and B2 even in the downstream region.

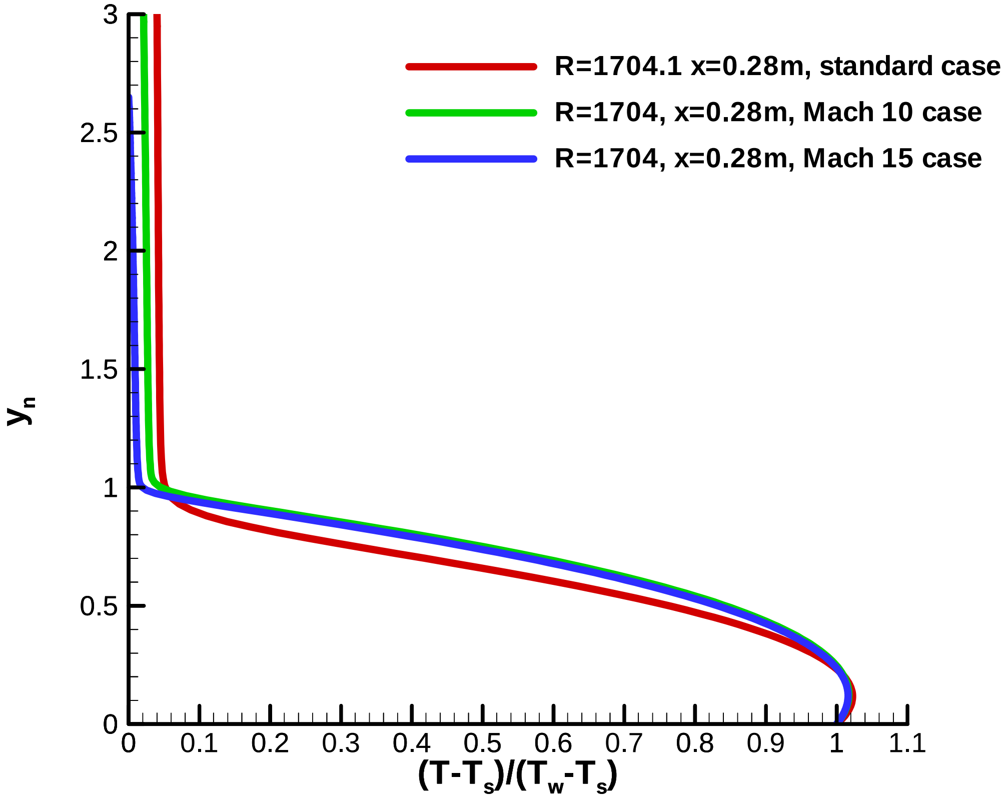

Figure 105. Comparison of the steady base wall-normal temperature profiles at the same local Reynolds number in the downstream region of the cone between the cases of different freestream Mach number (Case 1, B1 and B2).

From the observations of the steady base flow variable profiles between the cases of different freestream Mach numbers, one can see that the nose effects in the early upstream region of the cone is stronger with the higher freestream Mach number. However, the nose effects last further downstream with the lower freestream Mach number. Moreover, the self-similarity of the flow field downstream is not as high as the one in the earlier study of the nose bluntness effects. Hence, we would expect a lower degree of self-similarity being found in the latter parametric studies of the freestream Mach number effects in the boundary-layer receptivity and stability.

In the nose region, the curved shock generates inviscid vorticity in the flow field behind the shock. According to Crocco's Theorem, the gradient of entropy, which is related to entropy layer, is also generated due to the generation of vorticity by the shock curvature. As previously discussed in the results of Case 1, we characterize the entropy layer effects by a parameter named generalized velocity gradient, $\rho\left(du_t/dy_n\right)$, and the peak of such parameter within a compressible boundary layer is defined as a generalized inflection point. Lees and Lin [104] showed that the existence of generalized inflection point is a necessary and sufficient condition for the existence of inviscid instability in a compressible boundary layer.

In Figure 106 and Figure 107, the evolution of the generalized inflection point that involves the interaction of entropy layer and boundary layer is demonstrated for the Case B1 and B2. The dimensionless wall-normal height, y_n, is normalized by the local thickness of boundary layer in both figures for maintaining self-similarity. The generalized velocity gradient is shown in the abbreviated mathematical notation ρDU. Both local Reynolds numbers and the corresponding x-coordinates of various locations are shown as the legend.

In Figure 106 (a), the wall-normal profiles of generalized velocity gradient of Case B1 at various locations upstream near by the nose region are shown. The viscous effects from the wall occur throughout the entire upstream flow field near by the nose region. The earliest location of R=161.7 is immediately behind the nose region. At this location, a peak of generalized velocity gradient initially enters the flow field from the shock. In the subsequent locations of R=177.7 to 240.8, the peak moves towards the wall, meanwhile, its amplitude attenuates. These observations imply that the entropy layer generated by the bow shock moves toward the wall, while the entropy layer is moving downstream. Additionally, the entropy layer is gradually swallowed by the boundary layer during this movement. At the location of R=395.8, the peak is mainly swallowed by the boundary layer. There is a peak of generalized velocity gradient, which is the generalized inflection point, first appears at the local boundary-layer normalized height of 0.22. According to Mack [24], and Lees and Lin [104], the inviscid neutral waves exist at the generalized inflection point, where the discontinuity of Reynolds stress appears, and this is the sufficient condition for the existence of inviscid instability in the boundary layer. Mack [24], and Lees and Lin [104] also pointed out that the phase velocity of the neutral inviscid wave is the same as the mean velocity at the generalized inflection point.

The wall-normal profiles of generalized velocity gradient of Case B1 at further downstream locations are demonstrated in Figure 106 (b). From R=470 to 1289, the generalized inflection point moves toward the edge of the boundary-layer. As mentioned in Mack [24], this is a result of increasing Mach number of the flow above the boundary layer at those subsequent locations, which causes the mean velocity at the generalized inflection point as well as the phase velocity of the neutral inviscid wave increases. The outward movement of the generalized inflection point leads to a more unstable boundary layer. In Figure 106 (b), the generalized inflection point stays at the almost constant self-similar wall-normal height of 0.9, which is near the edge of the boundary layer, at the locations downstream from R=1289.

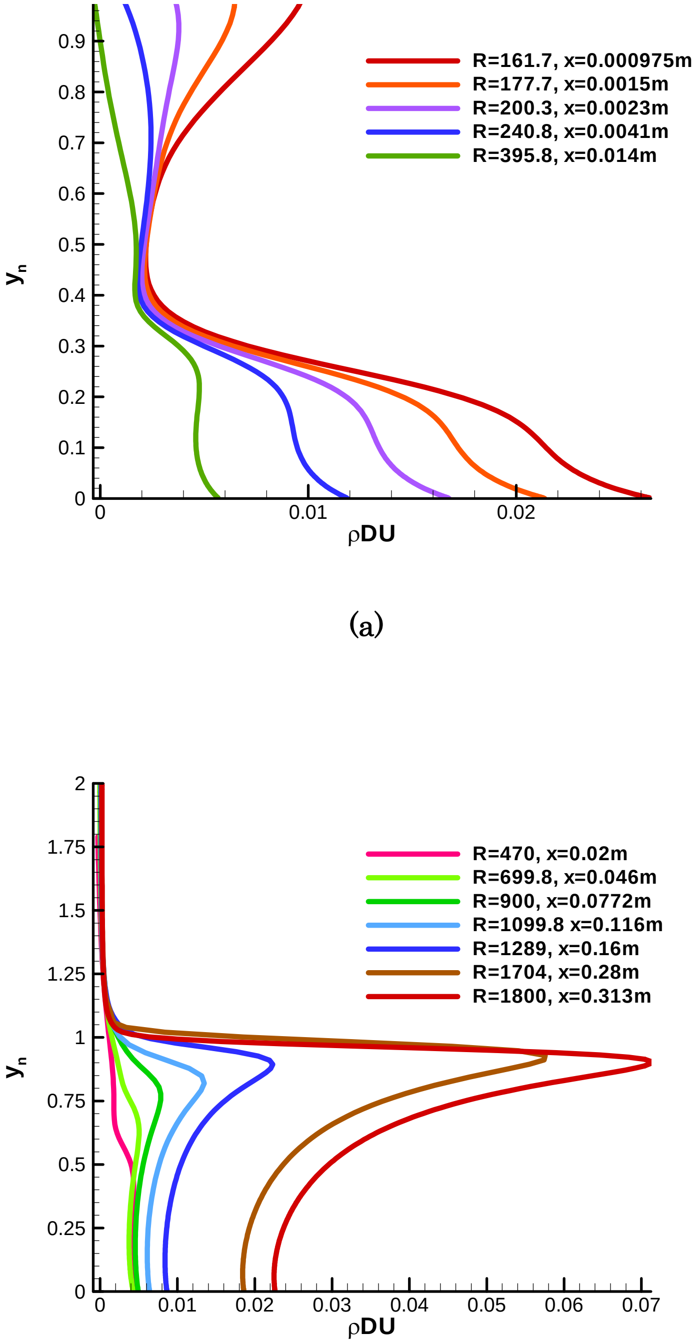

(a)

(b)

Figure 106. Wall-normal generalized velocity gradient at various (a) upstream and (b) downstream locations in Case B1.

In Figure 107 (a), the wall-normal profiles of generalized velocity gradient of Case B2 at various locations upstream near by the nose region are shown. The viscous effects from the wall occur throughout the entire upstream flow field near by the nose region. The earliest location of R=200.3 is shortly behind the nose region. At this location, a peak of generalized velocity gradient initially enters the flow field from the shock. In the subsequent locations of R=221.1 to 278.7, the peak moves towards the wall, meanwhile, its amplitude attenuates. These observations imply that the entropy layer generated by the bow shock moves toward the wall, while the entropy layer is moving downstream. Additionally, the entropy layer is gradually swallowed by the boundary layer during this movement. At the location of R=399.6, the peak is mainly swallowed by the boundary layer, and there is a peak of generalized velocity gradient, which is the generalized inflection point, first appears at the local boundary-layer normalized height of 0.34. According to Mack [24], and Lees and Lin [104], the inviscid neutral waves exist at the generalized inflection point, where the discontinuity of Reynolds stress appears, and this is the sufficient condition for the existence of inviscid instability in the boundary layer. Mack [24], and Lees and Lin [104] also pointed out that the phase velocity of the neutral inviscid wave is the same as the mean velocity at the generalized inflection point.

The wall-normal profiles of generalized velocity gradient of Case B2 at the further locations in the middle region are shown in Figure 107 (b). From R=470 to 1099.8, the generalized inflection point moves toward the edge of the boundary layer. As mentioned in Mack [24], this is a result of increasing Mach number of the flow above the boundary layer at those subsequent locations, which causes the mean velocity at the generalized inflection point as well as the phase velocity of the neutral inviscid wave increases. The outward movement of the generalized inflection point leads to a more unstable boundary layer. In

Figure 107 (b), the generalized inflection point stays at the almost constant self-similar wall-normal height of 0.92, which is near the edge of the boundary layer, at the locations downstream from R=1099.8.

The wall-normal profiles of generalized velocity gradient of Case B2 at the locations in the downstream region where the shock shape is concaved upward are shown in Figure 107 (c). Throughout these locations, the generalized inflection point stays at the almost constant self-similar wall-normal height of 0.92, which is near the edge of the boundary layer. Noticeably, there is a small negative peak of generalized velocity gradient developed in this region outside the boundary layer. This negative peak is the result of the upward concavity of the shock in this region. However, until the last location, the negative peak outside the boundary layer has not yet affected the generalized inflection point inside the boundary layer.

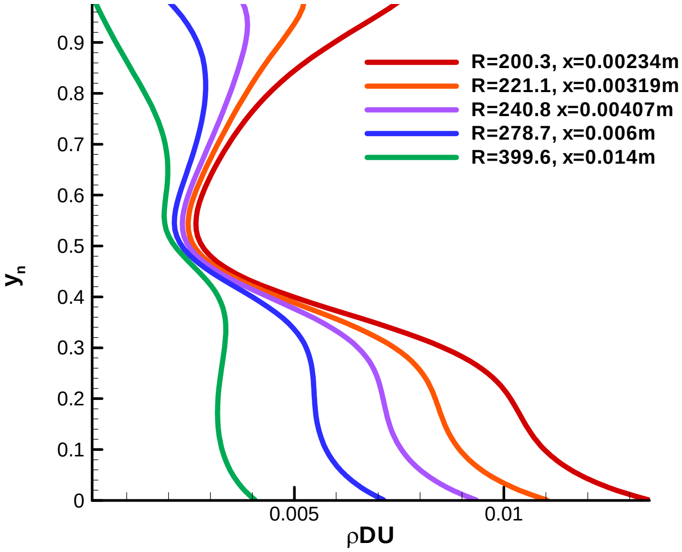

R=200.3, x=0.00234m
R=221.1, x=0.00319m
R=240.8 x=0.00407m
R=278.7, x=0.006m
R=399.6, x=0.014m
y_n
0
0.1
0.2
0.3
0.4
0.5
0.6
0.7
0.8
0.9
0.005
0.01
ρDU

(a)

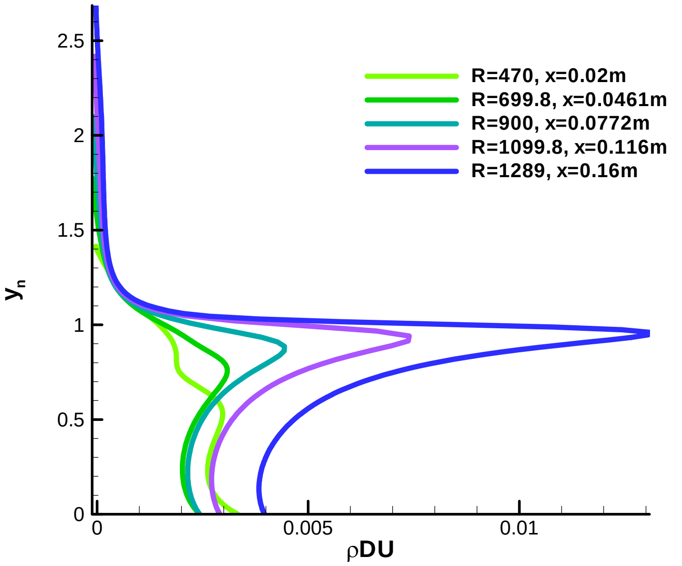

R=470, x=0.02m
R=699.8, x=0.0461m
R=900, x=0.0772m
R=1099.8, x=0.116m
R=1289, x=0.16m
y_n
0
0.5
1
1.5
2
2.5
0
0.005
0.01
ρDU

(b)

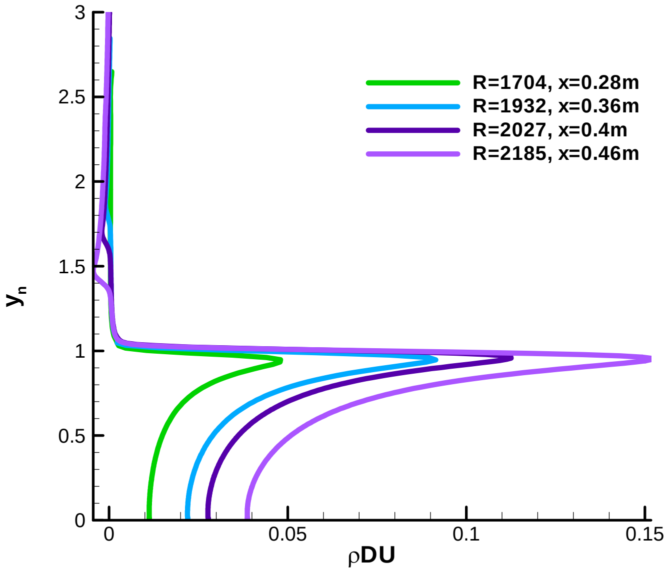

(c)

Figure 107. Wall-normal generalized velocity gradient at various (a) upstream, (b) middle and (c) downstream locations of Case B2.

From the above observations of the higher freestream Mach number cases (Case B1 and B2) and the earlier observations of Case 1, the overall evolution of the entropy-layer/boundary-layer interaction is similar for Case B1, B2 and 0. Specifically, the entropy layer is first created by the curved shock in the nose region, then it gradually moves toward the wall, and diffuse into the boundary layer, while it is moving downstream. Eventually the entropy layer is swallowed by the boundary layer, and a generalized inflection point appears as followed. The generalized inflection point then gradually moves toward the edge of the boundary layer, which is a sufficient condition of having inviscid instability in the boundary layer.

Although the overall evolution of the entropy-layer/boundary-layer interaction is similar for Case B1, B2 and 0, the local Reynolds numbers for evolving into each stage of the evolution are different between different freestream Mach number based on the above quantified observations in the generalized velocity profiles of Case 1, B1 and B2. However, there is no clear trend found in the locations of the generalized inflection point initial appearance between these three cases. The ending location of the outward movement of the generalized inflection point is found to be more upstream when the freestream Mach number is higher.

In addition to the trend of local Reynolds numbers, the self-similar wall-normal heights for the initial appearance of the generalized inflection point of Case 1, B1 and B2 are different. More specifically, the flow field with the higher freestream Mach number has a higher initially appeared generalized inflection point. Similarly, the final constant height of the generalized inflection point downstream is also higher for the flow field with the higher freestream Mach number.

4.4.2 Analyses of Boundary-Layer Disturbances and Stability

The previous parametric comparison discussion is based on the steady base flow over the same compression cone with different freestream Mach numbers. One of the main goals of the current parametric study is to investigate the freestream Mach number effects in the boundary-layer receptivity to the freestream disturbances and the subsequent linear growth of the boundary-layer disturbances. Prior to performing these receptivity and linear growth studies, the unsteady simulations of the hotspot perturbed flow based on the steady base flow behind the shock over the compression cone with different freestream Mach numbers are completed.

Identical to the set up of Case 1, we consider the axisymmetric flow field with the axisymmetric freestream hotspot that is initially aligned with the centerline of the cone. The freestream hotspot has a radius of about $0.003\ \mathrm{m}$. The radial Gaussian temperature profile of the hotspot in the freestream is similar to the one shown in Figure 30, except the magnitude of the temperature perturbations is different under different freestream Mach numbers. At the center of the hotspot, the temperature is maximal and the radial coordinate is zero. The hotspot is initially placed at a location not far upstream from the bow shock along the centerline of cone. The hotspot core radius is controlled by a dimensionless Gaussian factor, σ. In the current study, the dimensionless Gaussian factor is 0.001. The shape parameters of the freestream hotspot perturbations are based on the laser spot experiments of Salyer *et al.* [96, 97]

The receptivity process and the boundary-layer disturbances growth to be studied in this work fall in linear regime. Hence, the hotspot imposed in the freestream should be of a very weak one in amplitude. Previously, Ma *et al.* [4] and Zhong *et al.* [36] chose their freestream relative perturbation amplitudes to be $O\left(10^{-4}\right)$ in order to keep the development of boundary-layer disturbances within the linear regime. Therefore, the freestream maximum relative amplitude of temperature perturbations at the center of hotspot, ε, is chosen to be 10^{-4} as expressed in Eq. (71).

After obtaining the steady base flow, the unsteady numerical simulation with a freestream hotspot can be carried out. The Gaussian formulations that are given by Eqs. (39) to (42), are used to analytically model a three-dimensional hotspot that convects with the freestream. Furthermore, the freestream hotspot is imposed onto the computational domain as an unsteady shock boundary condition.

When performing the simulations in the parallel computers, the simulated time history of the pressure perturbations in boundary layer is recorded at every grid point along the cone surface, and the subsequent receptivity and disturbance growth studies are carried out based on these time history. The recording time steps are taken to be very small in order to obtain a sufficient high resolution in the recorded time-history that carries the high frequency components of the simulated boundary-layer disturbances. The details of the recording procedures are described earlier in Section 3.2.4 for Case 1.

Figure 108 to Figure 111 present the time-history traces of wall-pressure perturbations of Case B1 and B2 at some sampling locations throughout the upstream and downstream part of the cones. Noticeably, the amplitudes of the pressure perturbations are normalized with respect to the value of freestream pressure.

Figure 108 shows the wall-pressure perturbations travelling through the upstream part of the compression cone in Case B1. At the stagnation point in the nose region at $x^* = -0.001\ \mathrm{m}$, the perturbation time-history profile initially have a pure Gaussian shape. Shortly behind the nose region from $x^* = 0.00076\ \mathrm{m}$ to $0.16\ \mathrm{m}$, the profile becomes more complicated that contains many peaks. At $x^* = 0.16\ \mathrm{m}$, the profile of the wave packet clearly contains two parts that have different waveforms: a faster part and a slower part. The faster part means the part of wave packet that arrives at the sampling location at an earlier time, which is on the left side of the wave packet. Vice versa, the slower part is the part of wave packet that arrives at a later time, which is on the right side of the wave packet. The faster part of the wave packet has only the first two peaks on the left. The slower part of the wave packet is more oscillatory, which contains all the peaks behind the faster part. From $x^* = 0.04$ m to 0.16 m, the amplitudes of the faster part decay, and those of the slower part grow while travelling downstream. At $x^* = 0.04$ m, the overall amplitude of the faster part is much larger than the slower part. However, at $x^* = 0.16$ m, the overall amplitude of the slower part is much larger than the faster part. At $x^* = 0.04$ m, the faster part has the frequency of around 127.5 kHz. It is the stable mode F that is excited by the fast acoustic waves within and nearby the nose region. At $x^* = 0.16$ m, the slower part has the frequency of around 112 kHz. The slower part is the mode S that is excited by the slow acoustic waves.

In order to characterize the growth of the wave packet in the current parametric study, the average growth rate of the overall wave packet is introduced in Section 3.2.4 by Eq. (72). By following this equation, the calculated average growth rate of the stable wave packet from $x^* = 0.00076$ m to 0.1 m is $-9.54\ \mathrm{m}^{-1}$.

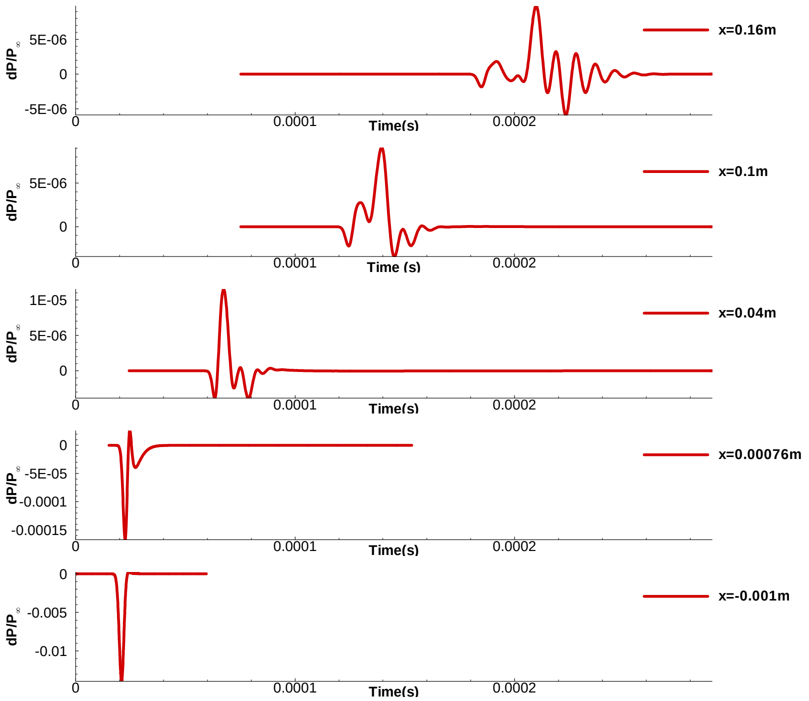

Figure 108. Time-history traces of pressure perturbations at wall at various streamwise locations over the upstream part of the cone for Case B1.

Figure 109 shows the wall-pressure perturbations in the downstream part of the sharper cone in Case B1. In this part of the cone, the faster part at the left-hand-side of the wave packet continuously attenuates throughout all the sampling locations, while the amplitudes of the slower part is growing so rapidly and becomes the dominant instability in the boundary layer. Eventually, the faster part becomes insignificant. The dominantly growing slower part is relevant to the mode S related second mode instability. The frequency of the maximum amplitude of the dominantly growing waveform is found to be around 125 kHz at $x^* = 0.34$ m. The up-shift rate of frequency throughout the dominant growth is 72.2 kHz/m. The similar approach to quantify the growth of the wave packet in the upstream part of the cone is used to calculate the average growth rate of the overall second mode dominated wave packet. The calculated average growth rate of the overall second mode dominated wave packet from $x^* = 0.16$ m to 0.34 m is $224\ \text{m}^{-1}$. The latter discussion of receptivity mechanisms in Section 4.4.3 supports the findings from the current analysis of the time-history traces.

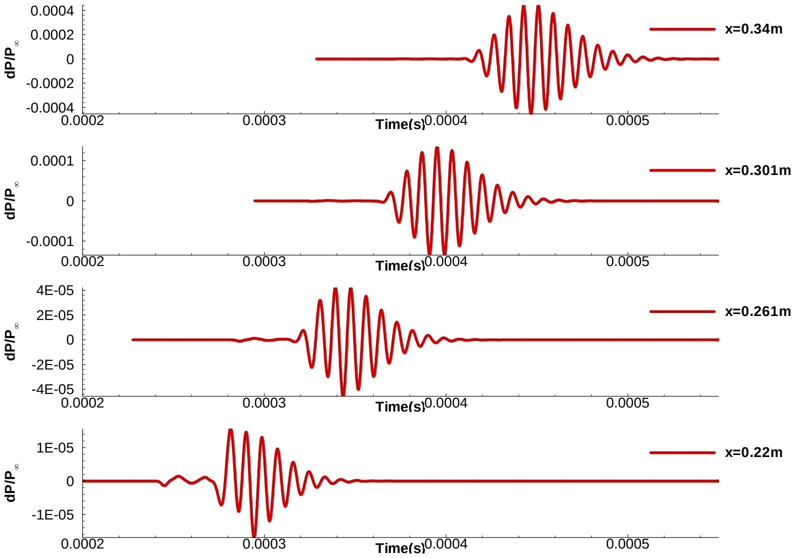

Figure 109. Time-history traces of pressure perturbations at wall at various streamwise locations over the downstream part of the cone for Case B1.

Figure 110 shows the wall-pressure perturbations travelling through the upstream part of the compression cone in Case B2. At the stagnation point in the nose region at $x^* = -0.001$ m, the perturbation time-history profile initially have a pure Gaussian shape. Shortly behind the nose region from $x^* = 0.00076$ m to 0.16 m, the profile evolves and becomes more complicated that contains many peaks. From $x^* = 0.00076$ m to 0.1 m, the amplitudes of the first trough and the first peak from the left side of the wave packet decay, and the wave amplitudes to the right of the first peak, (i.e. the second trough and second peak, etc.) grow while travelling downstream. At $x^* = 0.16$ m, the previously decaying first peak splits into two parts: the part at the left side is still decaying, while the part at the right side is growing. At this point, the profile of the wave packet contains two parts, namely, a decaying faster part and a growing slower part. The faster part means that the part of wave packet that arrives at the sampling location at an earlier time, which is on the left side of the wave packet. Vice versa, the slower part is the part of wave packet that arrives at a later time, which is on the right side of the wave packet. The decaying faster part of the wave packet has only the first trough and the left side of the split first peak. The growing slower part of the wave packet is more oscillatory, which contains all the peaks and troughs behind the faster part. At $x^* = 0.04$ m, the decaying faster part has the frequency of around 150 kHz. The decaying faster part contains the stable mode F that is excited by the fast acoustic waves within and nearby the nose region. At $x^* = 0.16$ m, the growing slower part has the frequency of around 109 kHz. The slower part is the mode S that is excited by the slow acoustic waves.

In order to characterize the growth of the wave packet in the current parametric study, the average growth rate of the overall wave packet is introduced in Section 3.2.4 by Eq. (72). By following this equation, the calculated average growth rate of the stable wave packet from $x^* = 0.00076$ m to 0.1 m is $-9.64\ \text{m}^{-1}$.

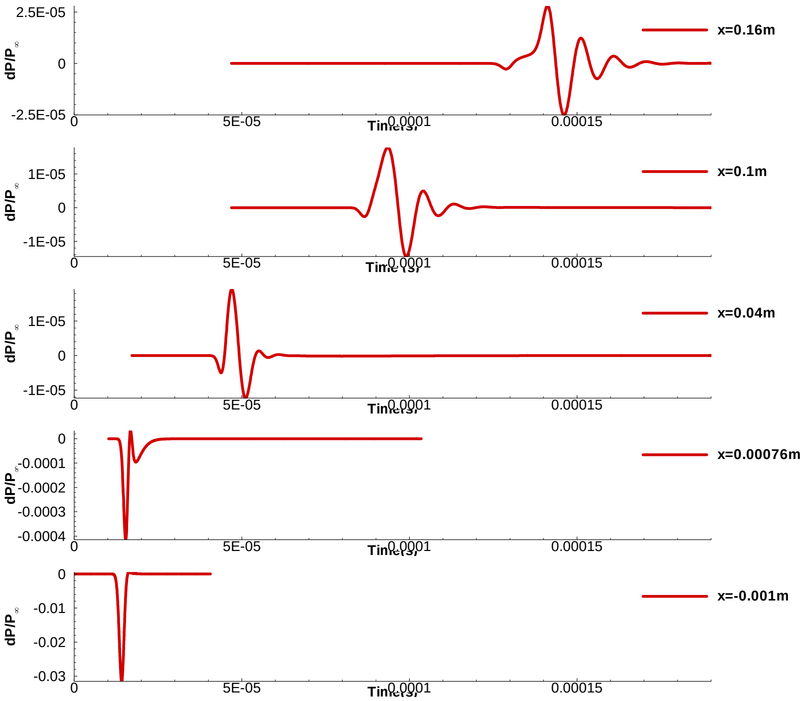

Figure 110. Time-history traces of pressure perturbations at wall at various streamwise locations over the upstream part of the cone for Case B2.

Figure 111 shows the wall-pressure perturbations in the downstream part of the sharper cone in Case B2. In this part of the cone, the faster part at the left side of the splitting peak continuously attenuates and separates from the growing slower part throughout all the sampling locations, while the amplitudes of the slower part is growing so rapidly and becomes the dominant instability in the boundary layer. Eventually, the faster part becomes insignificant. The dominantly growing slower part is relevant to the mode S related second mode instability. The frequency of the maximum amplitude of the dominantly growing waveform is found to be around 133 kHz at $x^* = 0.42\ \text{m}$. The up-shift rate of frequency throughout the dominant growth is $92.3\ \text{kHz/m}$. The similar approach to quantify the growth of the wave packet in the upstream part of the cone is used to calculate the average growth rate of the overall second mode dominated wave packet. The calculated average growth rate of the overall second mode dominated wave packet from $x^* = 0.16$ m to 0.42 m is $304\ \mathrm{m}^{-1}$. The latter discussion of receptivity mechanisms in Section 4.4.3 supports the findings from the current analysis of the time-history traces.

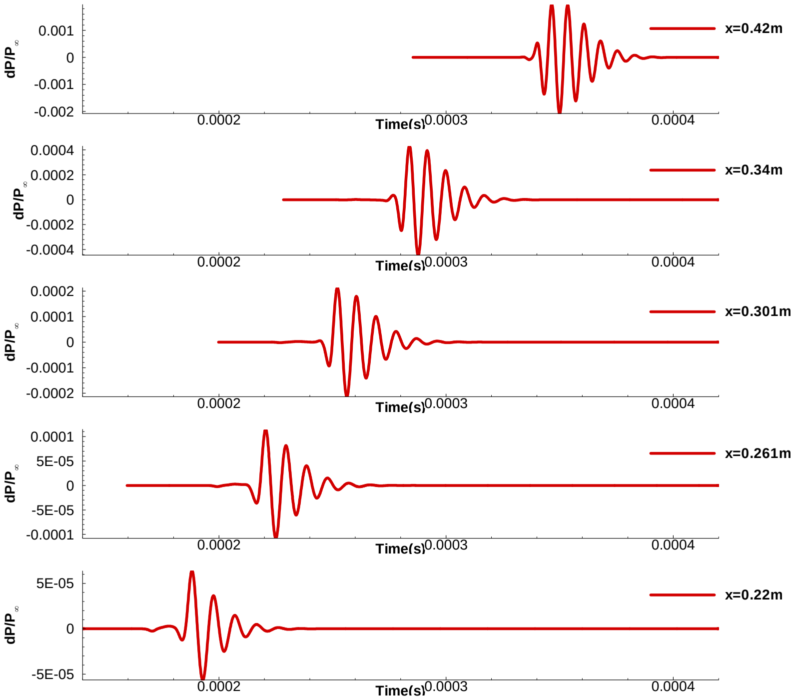

Figure 111. Time-history traces of pressure perturbations at wall at various streamwise locations over the downstream part of the cone for Case B2.

By comparing the observation and results in the time history of the boundary-layer wave packet between the cases of Freestream Mach number effects (Case 1, B1 and B2), one can see that there are trends of the locations of the new unstable waveform appearance with respect to different freestream Mach numbers. Specifically, a location of the initial appearance of the unstable slower part is more upstream with a higher freestream Mach number. Such trend implies that the dominant boundary-layer instability appear earlier as the freestream Mach number becomes higher.

In addition to the locations of the initial appearance of the unstable slower part, the frequency of the unstable slower part and the shift of such frequency throughout the growth of the unstable wave also have a trend with respect to the freestream Mach number. Specifically, the case with a higher freestream Mach number has a lower initial frequency of the unstable waveform at its initial appearance location. The reason for having the initial frequency of the unstable waveform to be lower for the case with a higher freestream Mach number is that the boundary layer is thicker at such location with a higher freestream Mach number. Moreover, the up-shift of frequency over a unit distance or the up-shift rate during the dominant growth of the unstable waveform is found to be larger with a higher freestream Mach number. This implies that the decrease of boundary-layer thickness is faster with a higher freestream Mach number.

Finally, the average growth or decay rate of the wave packet also varies with respect to different freestream Mach number. To be specific, the decay rate of the stable waveform in the upstream part of the cone with a higher freestream Mach number is larger, and the growth rate in the downstream part of the cone with a higher freestream Mach number is also larger. This observation implies that the decay and the growth of the wave packet are more vigorous with a higher freestream Mach number.

After investigating the freestream Mach number effects on the overall development of the wave packet in the boundary layer, the following stage is to carry out a detailed parametric study of the freestream Mach number effects on the frequency component behavior in the boundary-layer disturbances along the cone. In order to study the frequency components, the Fourier transformation based on the time history of wall-pressure perturbations is carried out at various surface locations. The formulations of the Fourier transformation are shown in Section 2.5. The simulated perturbations are single impulse which is temporally "transient", i.e. they do not continue to repeat in time at a given location. The transient perturbed flow at a location eventually returns back to its steady base flow after the passage of the perturbations. When conducting the Fourier transformation, the time history of single impulse is windowed with no more perturbations existing on both sides. More specifically, the Fourier transformed amplitudes in the current study are independent of the width of the time-window as long as the relative amplitudes of the pressure perturbations at both end are $O(10^{-9})$. In this way, a periodicity of the signal is assumed in the time domain. The maximum recording time-step size of the time-histories is 1.12×10^{-7} s, which is sufficient to resolve the second mode instability at the high end of the studied frequency range. Our Fourier transformed results are confirmed to be independent of the time-step used when we were post-processing the data from the simulation using the current windowed-Fourier transformation.

It is shown in Figure 40 that the amplitudes of the freestream forcing disturbances are not uniform at different frequencies. Hence, in order to include such frequency effects in the analyses of boundary-layer receptivity and instability growth, it is necessary to normalize the amplitudes of the wall-pressure-perturbations by those of the freestream forcing disturbances. The expression of the normalized amplitude are shown in Eq. (73), and the details are explained in the paragraph around the equation in Section 3.2.4.

The normalized amplitude frequency spectra of behind-shock acoustic waves and entropy waves in the nose region of Case B1 and B2 are shown in Figure 112 and Figure 113. In order to compare the relative strength in the local flow field between the pressure and entropy perturbations, the local perturbation amplitude is divided by the local steady base value immediately behind the shock. Both pressure and entropy waves are the result of the combined interactions of the shock with the freestream hotspot perturbations, and the reflected acoustic waves behind the shock. Each line represents the spectrum at a shock location that has a specific angle between the stagnation line in front of the cone nose and the line that connects the shock location and the origin.

Under the flow conditions of Case B1, the maximum generated acoustic and entropy waves behind the shock appear on the stagnation line where the angle is 0. These generated waves mainly decay at downstream shock locations in the nose region. The normalized amplitudes of the acoustic wave spectra or pressure perturbations have local maxima at the frequency from 200 to 180 kHz at the angles from 0 to 40 degrees. These maxima are caused by the resonance of the acoustic waves that bounces between the shock and the wall in the nose region. Moreover, the downshift of the resonance frequency downstream is due to the increasing shock-layer thickness downstream in the nose region. The amplitudes of entropy waves mainly increase with the increasing frequency. From Figure 112 (a), the maximum normalized amplitude for the pressure disturbances just behind the shock is 1.09 at the stagnation line or 0 degree with the frequency of 200 kHz. Such maximum relative strength of pressure perturbations immediately behind the shock is slightly higher than the relative strength of freestream perturbations due to the resonance interaction around the stagnation line. The overall amplitudes fall in the range from 0.26 to 1.09. The mean value of amplitude in this range is 0.675. From Figure 112 (b), the maximum strength of the entropy perturbations is 0.104 at 0 degrees with the frequency of 520 kHz. The overall amplitudes fall in the range from 0.001 to 0.104. The mean value of amplitude in this range is 0.0525. By comparing the amplitudes of both perturbations, one can see that the normalized amplitudes of the acoustic waves or pressure perturbations are around an order of magnitude higher than the entropy perturbations. Such observation indicates that after the hotspot/shock interaction in the nose region, the perturbations are mainly acoustic waves.

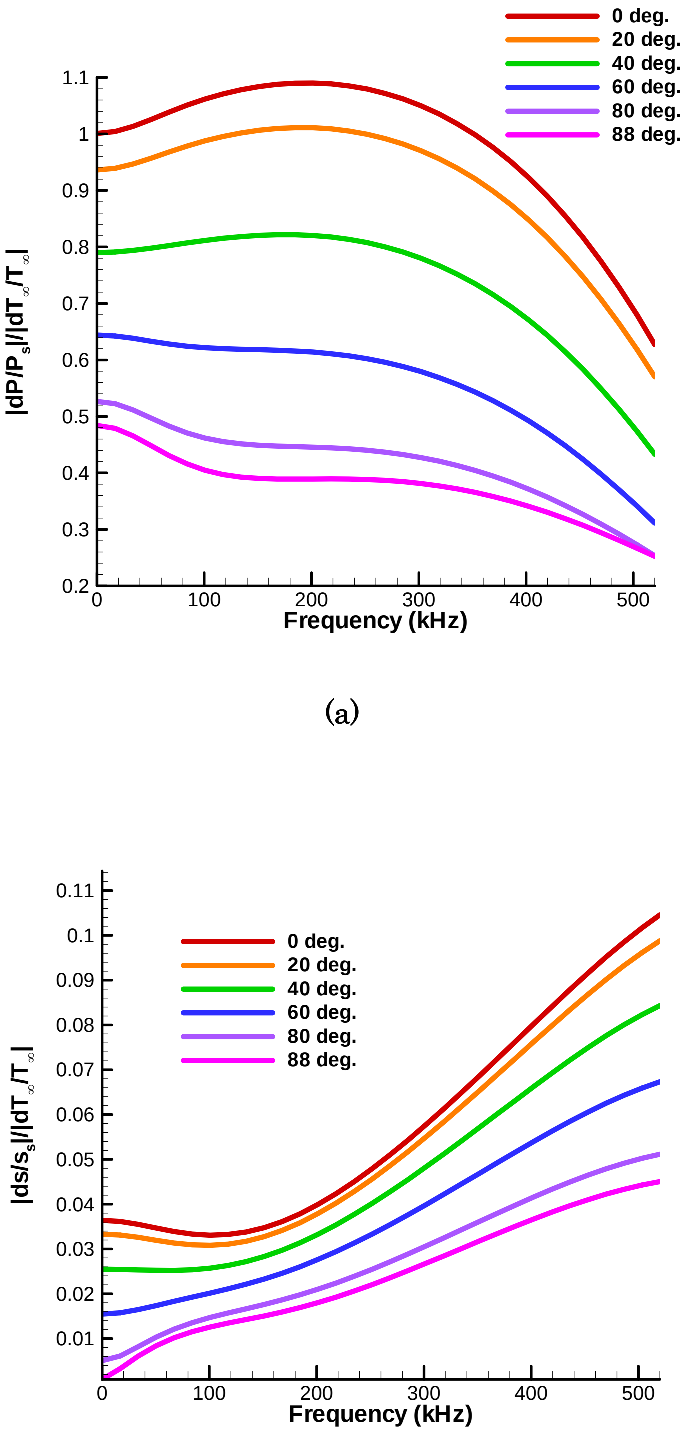

(a)

(b)

Figure 112. Frequency spectra of normalized amplitudes of (a) pressure perturbations and (b) entropy perturbations immediately behind the shock in the nose region of Case B1.

From the normalized amplitude frequency spectra of behind-shock acoustic waves and entropy waves in the nose region of Case B2 that is shown in Figure 113, the maximum generated acoustic and entropy waves behind the shock appear on the stagnation line where the angle is 0. These generated waves mainly decay at downstream shock locations in the nose region. The normalized amplitudes of the acoustic wave spectra or pressure perturbations have local maxima at the frequency from 290 to 260 kHz at the angles from 0 to 40 degrees. These maxima are caused by the resonance of the acoustic waves that bounces between the shock and the wall in the nose region. Moreover, the downshift of the resonance frequency downstream is due to the increasing shock-layer thickness downstream in the nose region. The amplitudes of entropy waves mainly increase with the increasing frequency. From Figure 113 (a), the maximum normalized amplitude for the pressure disturbances just behind the shock is 1.09 at the stagnation line or 0 degree with the frequency of 290 kHz. Such maximum relative strength of pressure perturbations immediately behind the shock is slightly higher than the relative strength of freestream perturbations due to the resonance interaction around the stagnation line. The overall amplitudes fall in the range from 0.36 to 1.09. The mean value of amplitude in this range is 0.725. From Figure 113 (b), the maximum strength of the entropy perturbations is 0.065 at 0 degrees with the frequency of 520 kHz. The overall amplitudes fall in the range from 0.001 to 0.065. The mean value of amplitude in this range is 0.033. By comparing the amplitudes of both perturbations, one can see that the normalized amplitudes of the acoustic waves or pressure perturbations are more than an order of magnitude higher than the entropy perturbations. Such observation indicates that after the hotspot/shock interaction in the nose region, the perturbations are mainly acoustic waves.

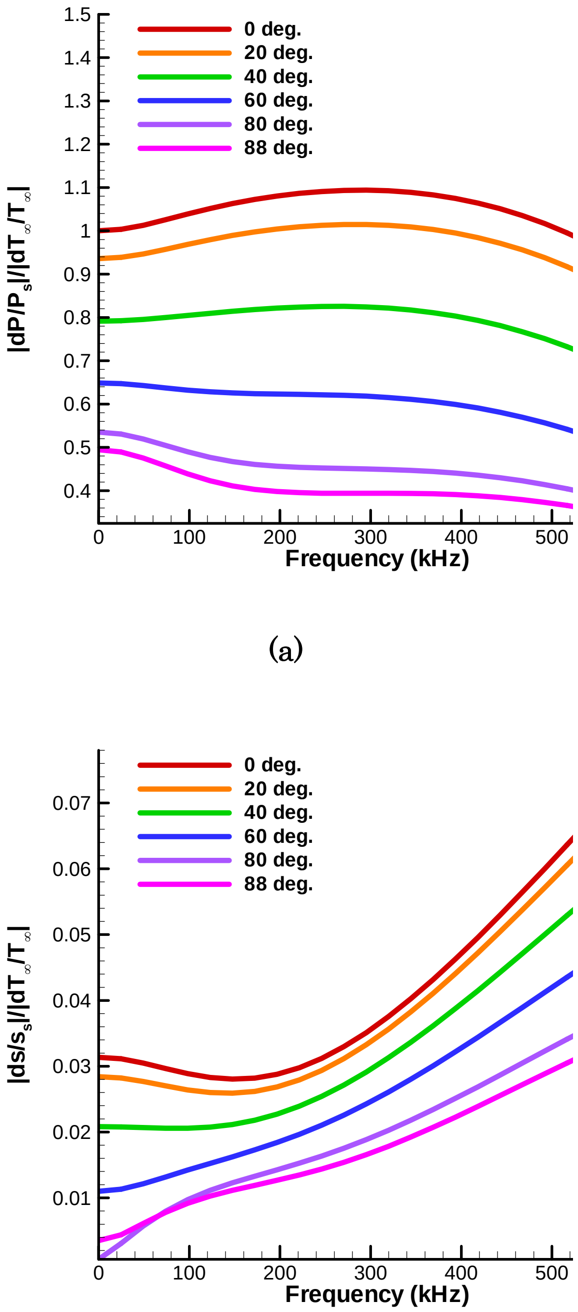

(a)

(b)

Figure 113. Frequency spectra of normalized amplitudes of (a) pressure perturbations and (b) entropy perturbations immediately behind the shock in the nose region of Case B2.

By comparing the observations on the normalized amplitude frequency spectra of behind-shock acoustic waves and entropy waves in the nose region of Case 1, B1 and B2, one can see that there are a few similarity and difference between these cases of different freestream Mach numbers, and thus some trends can be concluded from the comparisons.

Specifically, the maximum normalized amplitude of both the generated acoustic and entropy waves behind the shock for all the cases of different freestream Mach numbers (Case 1, B1 and B2) always appear on the stagnation line where the angle is 0, and these generated waves decay at further downstream shock locations in the nose region. The frequency of the local maximum of the generated acoustic waves caused by the resonance in the shock layer depends on the shock-layer thickness. The resonance frequencies from 0 to 40 degrees in Case 1 is 180 to 160 kHz, those of Case B1 is from 200 to 180 kHz, and those of B2 is from 290 to 260 kHz. The trends from this observation are that the higher freestream Mach number leads to the higher resonance frequencies and the larger resonance frequency downshift in the shock layer of the nose region. The trend in the resonance frequency is owing to the fact that the shock-layer thickness is less with a higher freestream Mach number, thus the resonance frequencies are higher. The trend in the streamwise downshift of the resonance frequency implies that the streamwise growth of the shock-layer thickness is faster with a higher freestream Mach number.

As discussed previously, the mean value of the overall amplitude of acoustic waves or pressure perturbations for Case 1 is 0.67, the one for Case B1 is 0.675, and the one for Case B2 is 0.725. The trend is obvious that the case of higher freestream number has the higher overall normalized amplitude of the generated acoustic waves behind the shock in the nose region. Conversely, for the generated entropy waves, the mean values of the overall normalized amplitudes are 0.063 for Case 1, 0.0525 for Case B1, and 0.033 for Case B2.

Obviously, the trend is that the case of higher freestream number has the lower overall normalized amplitude of the generated entropy waves behind the shock in the nose region.

Figure 114 shows the normalized frequency spectra at wall from the nose tip to the end of the cone in Case B1. In the figure, there is a large peak of spatial growth of amplitudes with the frequency ranging from about 30 kHz to 200 kHz. The mean frequency of this range is 115 kHz, and the width of this range is 170 kHz. This growing peak is the instability dominated by the second mode. The frequency corresponding to the maximum amplitude is about 125 kHz at $x^* = 0.367\text{ m}$, and the frequency at the peak upshifts from 109.5 kHz at $x^* = 0.16\text{ m}$ to 125 kHz at $x^* = 0.367\text{ m}$. The frequency shift rate is 74.9 kHz/m. This upshift of frequency is due to the decrease of boundary-layer thickness downstream. The second mode dominated peak grows from the initial maximum normalized amplitude of 0.358 at $x^* = 0.16\text{ m}$ to 113.4 at $x^* = 0.367\text{ m}$. Thus, the average growth rate of the second mode dominated growing peak from $x^* = 0.16\text{ m}$ to 0.367 m is 1525 m^{-1}, and the average spatial gradient of the 10-based logarithm of the growing peak is 12.1 m^{-1}. The oscillations in the spectra are caused by multi-mode wave modulations which are complex physical process with a co-existence of many wave modes. Noticeably, there is no such oscillation appears over the peaks that are dominated by the second mode.

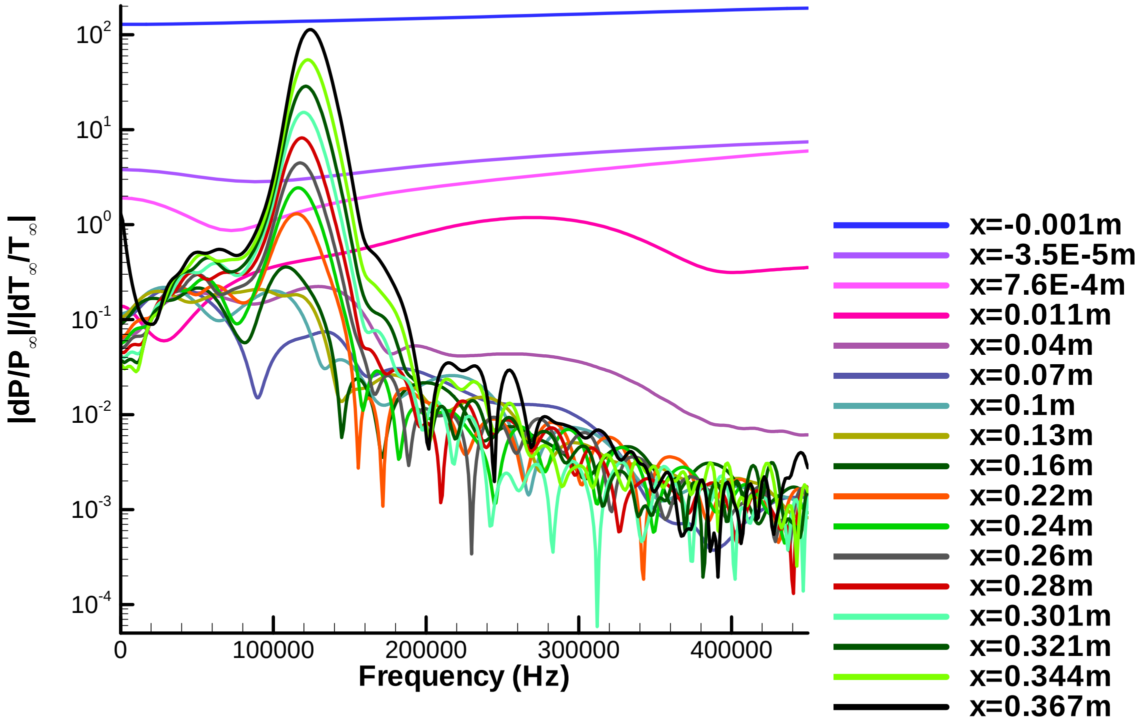

Figure 114. Normalized frequency spectra of the wall-pressure disturbances from the nose tip to the end of the cone in Case B1.

Figure 115 shows the normalized frequency spectra at wall from the nose tip to the end of the cone in Case B2. In the figure, there is a large peak of spatial growth of amplitudes with the frequency ranging from about 28 kHz to 537 kHz. The mean frequency of this range is 283 kHz, and the width of this range is 509 kHz. This growing peak is the instability dominated by the second mode. Owing to the unique abrupt change in the shock shape downstream from around $x^* = 0.26$ m (previously shown in Figure 96), this growing peak is so different to those in the other cases of this work. The higher frequency components from 240 kHz to 537 kHz grow with the second mode dominant peak downstream from around $x^* = 0.22$ m . The frequency corresponding to the maximum amplitude is about 143 kHz at $x^* = 0.441\ \mathrm{m}$. The frequency at the peak upshifts from 99.4 kHz at $x^* = 0.16$ m to 143 kHz at $x^* = 0.441\ \mathrm{m}$. The frequency shift rate is $155\ \mathrm{kHz/m}$. This upshift of frequency is due to the decrease of boundary-layer thickness downstream. The second mode dominated peak grows from the initial maximum normalized amplitude of 1.13 at $x^* = 0.16$ m to 248 at $x^* = 0.441\ \mathrm{m}$. Thus, the average growth rate of the second mode dominated growing peak from $x^* = 0.16$ m to $x^* = 0.441\ \mathrm{m}$ is $777\ \mathrm{m}^{-1}$, and the average spatial gradient of the 10-based logarithm of the growing peak is $8.33\ \mathrm{m}^{-1}$. The oscillations in the spectra are caused by multi-mode wave modulations which are a complex physical process with a co-existence of many wave modes. Noticeably, there is no such oscillation appears over the peaks that are dominated by the second mode.

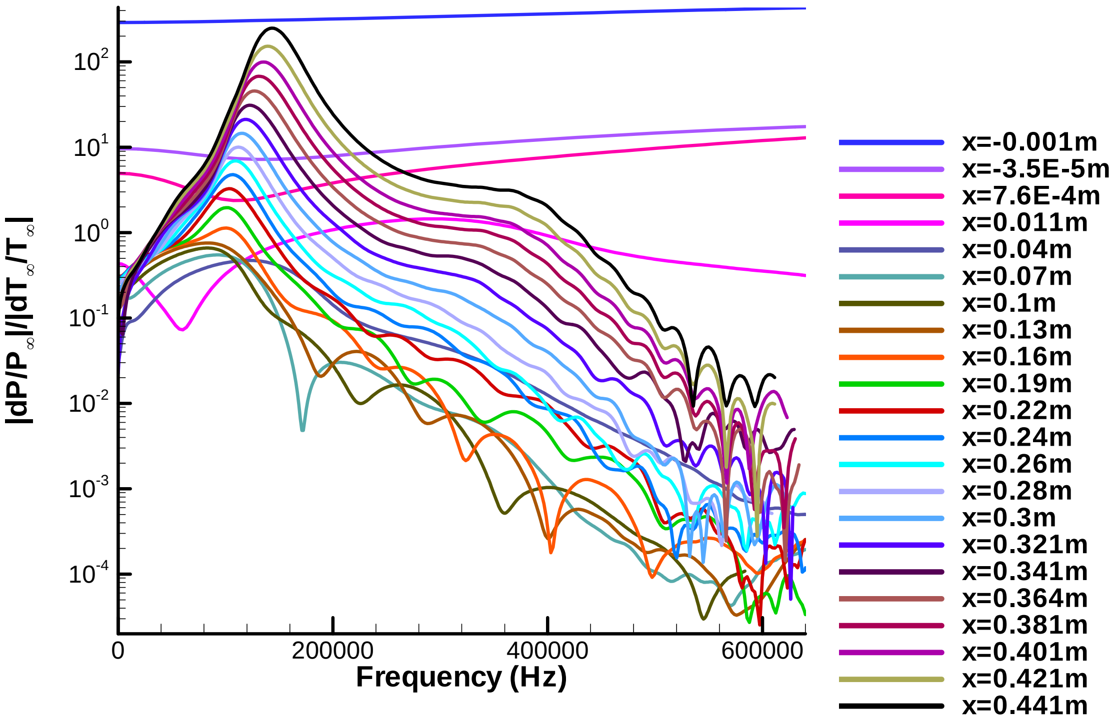

Figure 115. Normalized frequency spectra of the wall-pressure disturbances from the nose tip to the end of the cone in Case B2.

From the observations of the normalized amplitude spectra of the pressure disturbances at wall of Case 1, B1 and B2, we found that there are many trends under the variation of freestream Mach number. Owing to the unique abrupt change in the shock shape downstream in Case B2, the mean frequency of the second mode dominant range is not conclusive to show a trend, however, the initial second mode dominant peak frequency are found to be lower with the higher freestream Mach number, which indicates that the boundary-layer thickness at the initial growing location is higher with the higher freestream Mach number, and the wavelength of the initial second mode wave is longer. The bandwidth of the second mode dominant range is found to be wider with a higher freestream Mach number. The initial locations of the second mode dominant boundary-layer disturbances growth of all the cases of different freestream Mach number are very close to each other. Thus, the variation of the initial locations is not significant under different freestream Mach numbers. The initial maximum normalized amplitude within the second mode dominant frequency range is larger for the case of higher freestream Mach number. Such trend implies that the waves generated from the boundary-layer receptivity process are stronger with a higher freestream Mach number. The frequency upshift rate of the second mode dominant peak is higher throughout the growth of the disturbances with a higher freestream Mach number. Such trend reveals that the streamwise decay of the boundary-layer thickness is faster over the cone with a higher freestream Mach number. Although the case with the lower freestream Mach number has the lower initial amplitude of the second mode dominant growth, the overall growth rate of the second mode dominant waves is found to be higher from the comparisons of the average growth rates and the average logarithm gradients. Noticeably, in the earlier parametric study of the time-history traces, the average growth rate of the case with a higher freestream Mach number is found to be larger. However, due to the fact that the growth of the amplitude of the second mode waves is exponential, only having the average growth rate is insufficient to measure the strength of the exponential growth. Therefore, in the analyses of the normalized amplitude spectra, we use the average gradient of the amplitude logarithm to measure the growth. From the comparison between the cases of different freestream Mach number, the average logarithm gradient of the second mode dominant growth with a lower freestream Mach number is found to be larger.

Finally, a downstream sampling location in each case of the freestream Mach number effects study is chosen, in order to compare the maximum normalized amplitudes at a fixed distance downstream from the initial location of the growth of the second mode dominant boundary-layer disturbances. The fixed distance downstream from the initial location in each case is chosen to be around 0.2 m . Hence, the downstream sampling location for Case 1 is chosen to be $x^* = 0.394\text{ m}$, and the corresponding maximum normalized amplitude is 181.3. Secondly, the one for Case B1 is chosen to be $x^* = 0.367\text{ m}$, and the corresponding maximum normalized amplitude is 113.2. Lastly, the one for Case B2 is chosen to be $x^* = 0.364\text{ m}$, and the corresponding maximum normalized amplitude is 44.4. This amplitude comparison shows a trend that the higher freestream Mach number leads to the lower amplitudes in the boundary-layer disturbances after a certain distance of second mode dominant growth. Such trend is the evidence of the stabilizing impact from having a higher freestream Mach number.

A neutral stability curve indicates the locations of the boundary-layer wave modes at each frequency becoming unstable in the linear flow regime. However, it does not include the effects of freestream forcings in the boundary-layer disturbances. Recording the Branch-I and II neutral locations of many sampling frequency components generates the neutral stability curve. As discussed in Section 3.2.2 of LST, since the neutral locations are different between frequencies, one need to run spatial LST for each sampling frequency, and then record the first and second neutral locations encountered in each run. A large amount of sampling frequency is necessary to enhance the smoothness of the neutral stability curve, and thus the accuracy of interpolation between the adjacent sampling frequencies in future use.

The neutral stability curve of the second mode waves within the dominant boundary-layer disturbance growth frequency range of Case B1 is shown in Figure 116 (a) in order to demonstrate the general stability properties of this flow in linear regime. The critical location is $s^* = 0.0825\ \mathrm{m}$ at a frequency of 114 kHz. The second mode instability, which is the dominant instability in the current boundary-layer waves, only appears at the locations of $s^* > 0.0825\ \mathrm{m}$. The median of the second mode frequency range at $s^* = 0.171\ \mathrm{m}$ is 145.5 kHz. Thus, the median frequency shifting rate from the critical point to $s^* = 0.171\ \mathrm{m}$ is $356\ \mathrm{kHz/m}$.

Figure 116 (a) is shown in the dimensional form which reveals more practical aspects of the flow. However, when analyzing the theoretical aspects of the boundary-layer receptivity and stability in a parametric study, expressing the quantities in self-similarity is convenient when comparing the flow characteristics between cases of various parameters. The dimensional flow quantities are normalized by the freestream variables according to the formulations discussed in Section 3.2.2 of LST. In detail, the dimensional frequency is normalized by the freestream density, velocity and viscosity. The streamwise coordinate can be expressed in terms of local Reynolds number that is based on the boundary-layer thickness length scale.

Figure 116 (b) shows the neutral stability curve in self-similar variables. Owing to the square root over the s^* in the Eq. (63), the shape is different to the one in dimensional variables, however, it reveals the similar pattern as the dimensional one. The critical Reynolds number is 920, and the corresponding dimensionless frequency is 7.72×10^{-5}. The median of the second mode frequency range at $R=1327$ is 9.78×10^{-5}. Thus, the dimensionless median frequency shifting rate from the critical point to $R=1327$ is 5.06×10^{-8}. The second mode instability, which is the dominant instability in the current boundary-layer waves, only appears at the Reynolds number above 920.

In LST, each dimensionless circular frequency, ω, corresponds to a unique eigenvalue for each normal mode in a perfectly self-similar flow field. Figure 116 (c) shows the corresponding dimensionless circular frequencies for the eigenvalues at the neutral location. In a perfectly self-similar flow field, the dimensionless circular frequency that is correspondent to the unique Branch-I neutral eigenvalue of mode S, is a constant value regardless of the frequency and local Reynolds number. However, in the flow field around a blunt cone, the self-similarity cannot be held due to the geometry of the blunt nose. As a result, the dimensionless circular frequencies at the neutral locations are not constant for all frequency components in Figure 116 (c). The variation range of the dimensionless circular frequencies at the neutral locations is from 0.067 to 0.18, which is small. This reveals the proximity of self-similarity in the flow field around the neutral locations. The mean of the dimensionless circular frequency at the neutral locations is 0.1235.

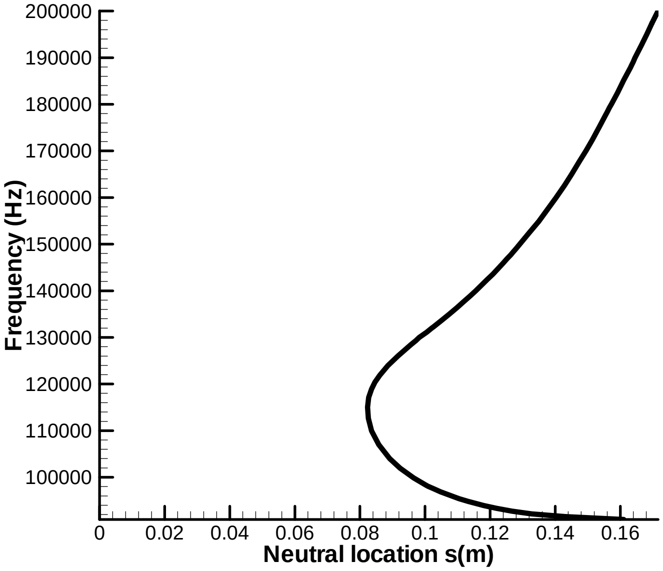
Frequency (Hz)
200000
190000
180000
170000
160000
150000
140000
130000
120000
110000
100000
0
0.02
0.04
0.06
0.08
0.1
0.12
0.14
0.16
Neutral location s(m)

(a)

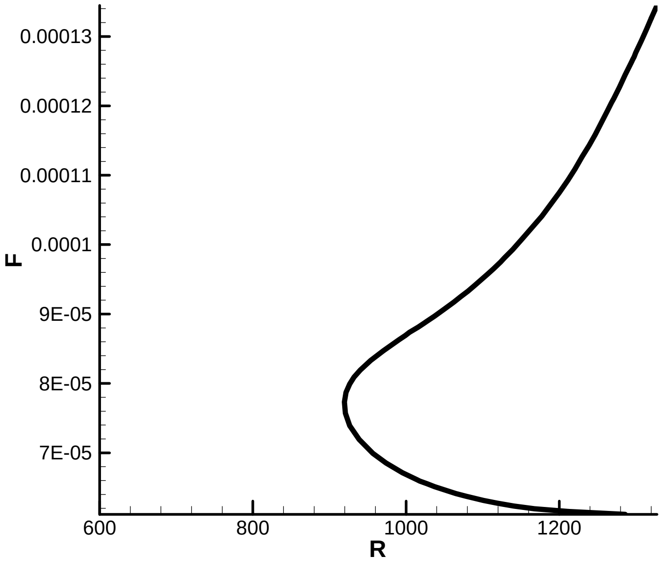
F
0.00013
0.00012
0.00011
0.0001
9E-05
8E-05
7E-05
600
800
1000
1200
R

(b)

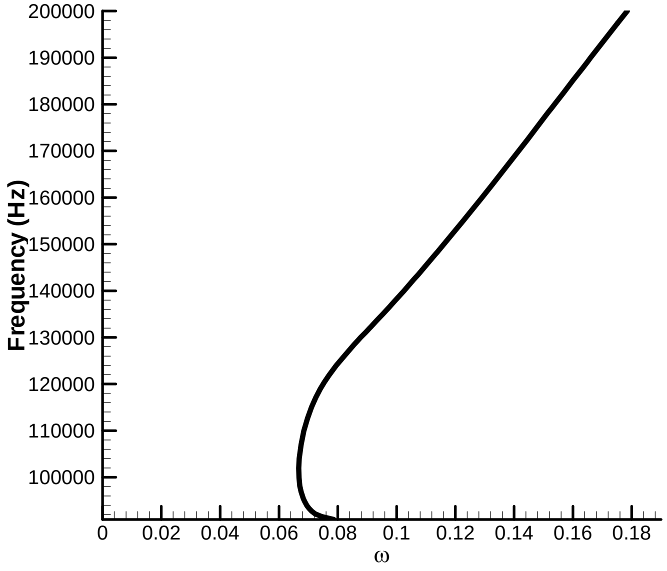

(c)

Figure 116. Neutral stability curve of the second mode in (a) dimensional form and (b) self-similar variables, and (c) the corresponding dimensionless circular frequencies along the neutral stability curve in Case B1.

The neutral stability curve of the second mode waves within the dominant boundary-layer disturbance growth frequency range of Case B2 is shown in

Figure 117 (a). The critical location is $s^* = 0.121\,\mathrm{m}$ at a frequency of 105 kHz. The second mode instability, which is the dominant instability in the current boundary-layer waves, only appears at the locations of $s^* > 0.121\,\mathrm{m}$. The neutral stability curve of the second mode instability is expected to cover further lower frequencies than 95 kHz, since the frequency spectra of the simulated boundary-layer disturbances in Figure 115 have the second-mode dominant growth below 95 kHz. However, the frequency components lower than 95 kHz cannot be determined due to the low-end frequency limitation of the current LST solver. The median of the second mode frequency range at $s^* = 0.136$ m is 109 kHz. Thus, the median frequency shifting rate from the critical point to $s^* = 0.136$ m is 267 kHz/m. Unlike the other cases in this work, the shifting rate up to $s^* = 0.136$ m is only averaged over a small fraction of streamwise distance of the entire neutral stability curve in Case B2, thus, this median frequency shifting rate up to $s^* = 0.136$ m is not sufficient to reflect the overall shifting rate. The overall shifting rate is much larger, since there are much more frequency components above the critical frequency having the second mode unstable region behind $s^* = 0.136$ m.

Figure 117 (b) shows the neutral stability curve in self-similar variables. Owing to the square root over the s^* in the Eq. (63), the shape is different to the one in dimensional variables, however, it reveals the similar pattern as the dimensional one. The critical Reynolds number is 1116, and the corresponding dimensionless frequency is 4.75×10^{-5}. The second mode instability, which is the dominant instability in the current boundary-layer waves, only appears at the Reynolds number above 1116.

In LST, each dimensionless circular frequency, ω, corresponds to a unique eigenvalue for each normal mode in a perfectly self-similar flow field.

Figure 117 (c) shows the corresponding dimensionless circular frequencies for the eigenvalues at the neutral location. In a perfectly self-similar flow field, the dimensionless circular frequency that is correspondent to the unique Branch-I neutral eigenvalue of mode S, is a constant value regardless of the frequency and local Reynolds number. However, in the flow field around a blunt cone, the self-similarity cannot be held due to the geometry of the blunt nose. As a result, the dimensionless circular frequencies at the neutral locations are not constant for all frequency components in

Figure 117 (c). The variation range of the dimensionless circular frequencies at the neutral locations is from 0.05 to 0.14, which is small. This reveals the proximity of self-similarity in the flow field around the neutral locations. The mean of the dimensionless circular frequency at the neutral locations is 0.095.

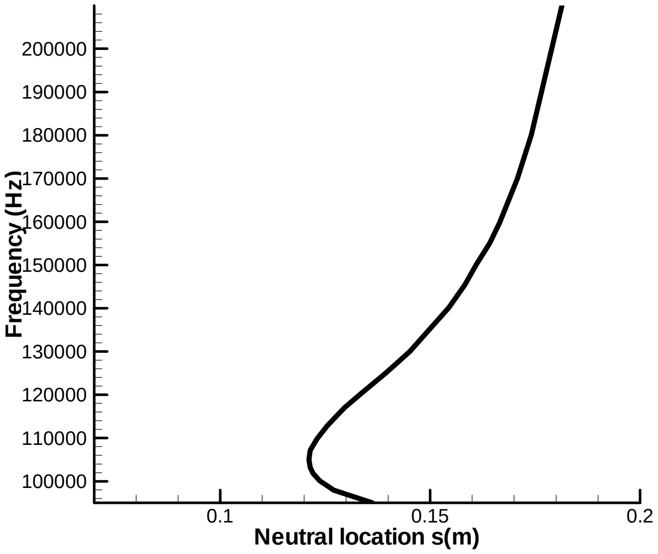

(a)

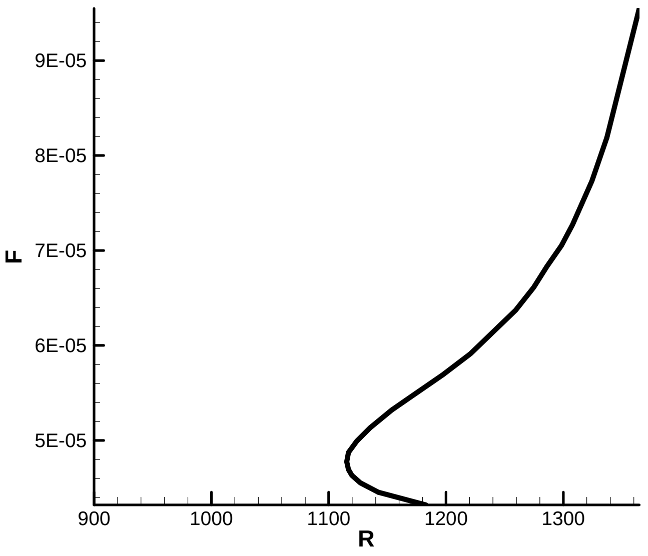

(b)

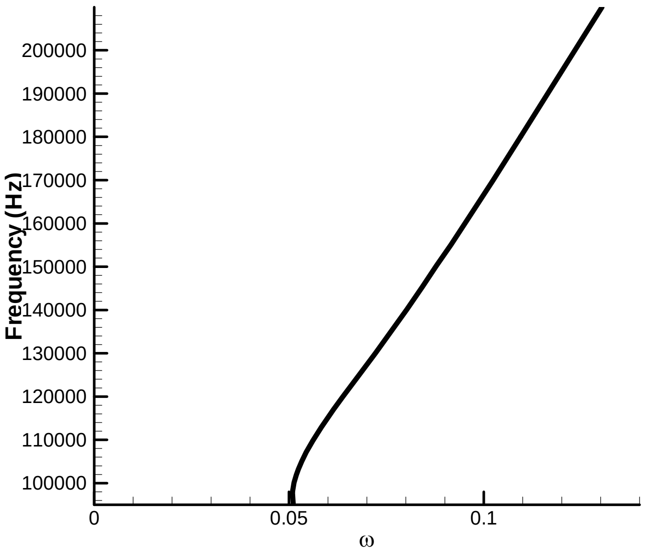

(c)

Figure 117. Neutral stability curve of the second mode in (a) dimensional form and (b) self-similar variables, and (c) the corresponding dimensionless circular frequencies along the neutral stability curve in Case B2.

By comparing the observations of both the dimensional and dimensionless neutral stability curves of Case 1, B1 and B2, we can see that there are common characteristics and trended differences between the cases of different freestream Mach number. The critical locations and the critical Reynolds numbers for all these cases have no trend being found, however, they are very close to each other. Therefore, the freestream Mach number effects do not have a significant impact on the critical location of the second mode instability. Only Case 1 has the streamwise downshifting median frequency, and the Case B1 and B2 all have upshifting median frequencies. Such observations indicate that the boundary-layer thickness in Case 1 has streamwise growth, though not significantly as discussed in the earlier Section 3.2.1. Conversely, Case B1 and B2 have the boundary-layer thickness decay in streamwise direction. The critical frequency is lower for the case of higher freestream Mach number, which indicates that the boundary-layer thickness at the Branch-I neutral location of second mode is larger with the higher freestream Mach number, and the wavelength of the initial second mode wave is longer. All of these discovered similarity and trends are consistent with those of the overall boundary-layer disturbances frequency aspects and the initial growth locations found in the second mode dominant boundary-layer perturbations analyses that are presented earlier in this section.

Finally, the initial and mean values of the dimensionless circular frequency at the neutral locations for Case B1 and B2 are near each other. However, those of Case 1 are very different to those of Case B1 and B2. This observation implies that there is a certain degree of similarity between Case B1 and B2. However, Case 1 is not similar to Case B1 and B2. The similarity between the cases of different freestream Mach number is low when compare to the similarity between the cases of nose bluntness effects. Moreover, the initial or the lowest dimensionless circular frequency of the Branch-I neutral locations is less with a higher freestream Mach number.

The topography of linear instability region of the second mode in the boundary layer is discussed previously. However, the overall spatial behaviors of the normal modes in the boundary layer under the freestream Mach number effects are not yet revealed. Hence, the investigation of the mode F and mode S for both Case B1 and B2 are presented next.

The LST predicted spatial dimensionless phase speeds of the mode F and mode S along the dimensionless circular frequency over the cone are calculated from α_r by Eqs. (63), (67) and (68). The plot of the dimensionless phase speeds at the sampling frequency of 130 kHz in Case B1 are shown in Figure 118. Those three horizontal lines are the dimensionless phase speeds of fast acoustic, slow acoustic and entropy/vorticity waves determined using freestream flow conditions in front of the bow shock. As a result, they only serve as qualitative references to show the existence of the three wave modes. The actual phase speeds depend on local non-constant flow conditions.

The upstream fast acoustic waves synchronized mode F has the phase speed that changes from the phase speed of the fast acoustic waves upstream to the phase speed of 0.93 downstream. There is a break in the phase speeds of mode F from $\omega = 0.068$ to 0.078. It is due to the synchronization between mode F and the entropy/vorticity waves. Specifically, the eigenvalue of the discrete mode F merges into the entropy/vorticity spectrum and reappears while moving downstream. As a result, the trace of the eigenvalue of mode F is interrupted by the entropy/vorticity spectrum. Since the actual phase speed of entropy/vorticity waves depends on local flow conditions, the break appears below the freestream phase speed of entropy/vorticity waves.

The upstream slow acoustic waves synchronized mode S has the phase speed that changes from the phase speed of 0.81 upstream to the phase speed of around 0.93 downstream. The mode S first synchronizes with the mode F at $\omega = 0.078$, then they synchronize again at $\omega = 0.17$.

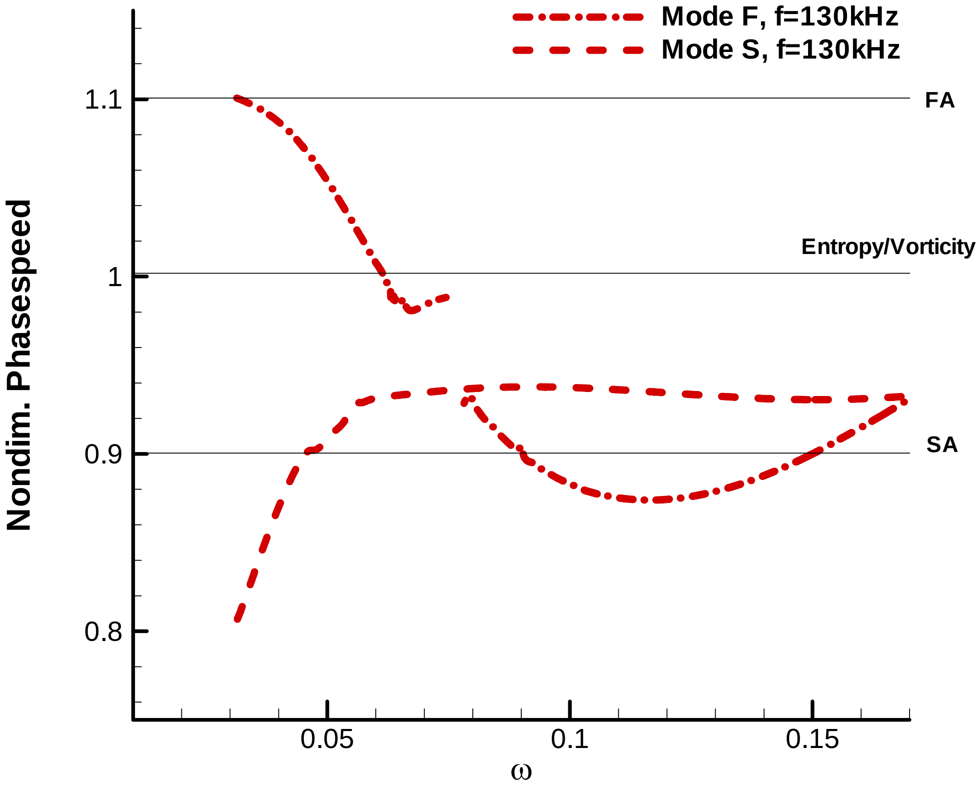

Figure 118. Streamwise phase speeds of mode F and mode S at the frequency of 130 kHz along the dimensionless circular frequency in Case B1.

The plot of the dimensionless phase speeds at the sampling frequency of 130 kHz in Case B2 are shown in Figure 119. The upstream fast acoustic waves synchronized mode F has the phase speed that changes from around the phase speed of the fast acoustic waves upstream to the phase speed of 0.98 downstream. There is a break in the phase speeds of mode F from $\omega = 0.047$ to 0.055. It is due to the synchronization between mode F and the entropy/vorticity waves. Specifically, the eigenvalue of the discrete mode F merges into the entropy/vorticity spectrum and reappears while moving downstream. As a result, the trace of the eigenvalue of mode F is interrupted by the entropy/vorticity spectrum. Since the actual phase speed of entropy/vorticity waves depends on local flow conditions, the break appears below the freestream phase speed of entropy/vorticity waves.

The upstream slow acoustic waves synchronized mode S has the phase speed that changes from the phase speed of the 0.89 upstream to the phase speed of around 0.95 downstream. The mode S first synchronizes with the mode F at $\omega = 0.051$, which is within the break of the mode F curve, then they synchronize again at $\omega = 0.107$.

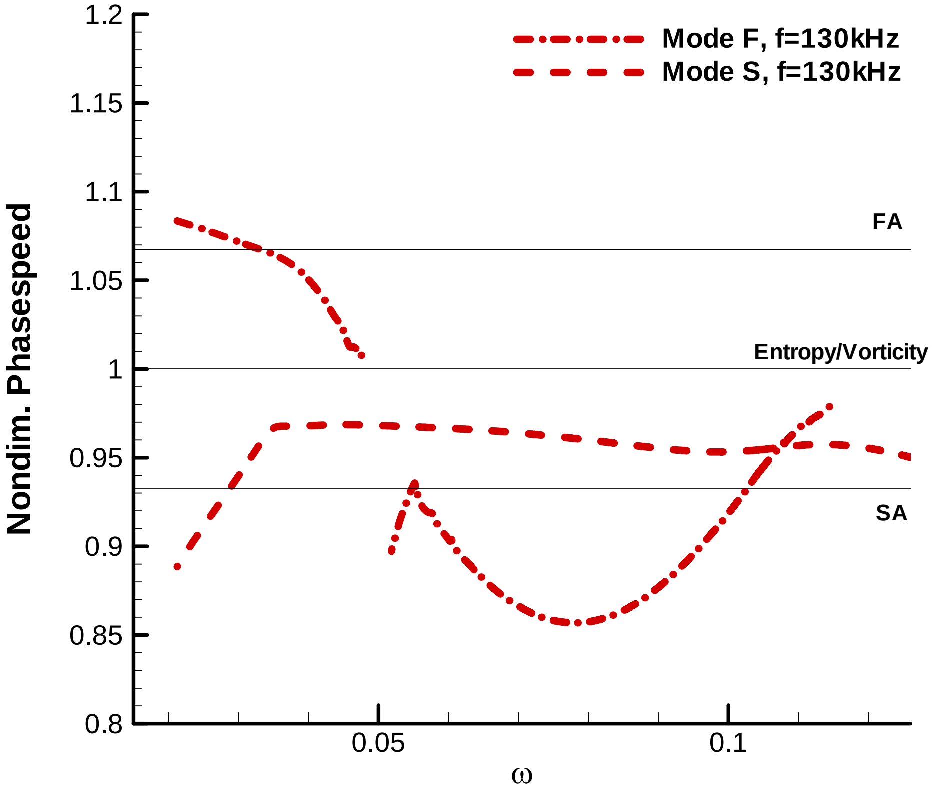

Figure 119. Streamwise phase speeds of mode F and mode S at the frequency of 130 kHz along the dimensionless circular frequency in Case B2.

In addition to the streamwise phase speeds, the streamwise dimensional growth rates are also calculated from α_i by Eqs. (62) and (66). The streamwise dimensional growth rates along the dimensionless circular frequency at 130 kHz in Case B1 are shown in Figure 120. The mode F is stable everywhere while mode S is stable before the Branch-I neutral point at $\omega = 0.088$, and it becomes the unstable second Mack mode behind this location. These observations indicate that the unstable second mode is related to mode S. Moreover, the unstable second mode begins shortly downstream from the synchronization of mode F and mode S at $\omega = 0.078$. Within the break due to the synchronization of the mode F and the entropy/vorticity waves, the growth rate of the mode F has a drop, in other words, a jump in α_i , which indicates the stabilizing effects to mode F from the synchronization between mode F and entropy/vorticity waves. Such jump in α_i is also found in Fedorov *et al.* [78, 80].

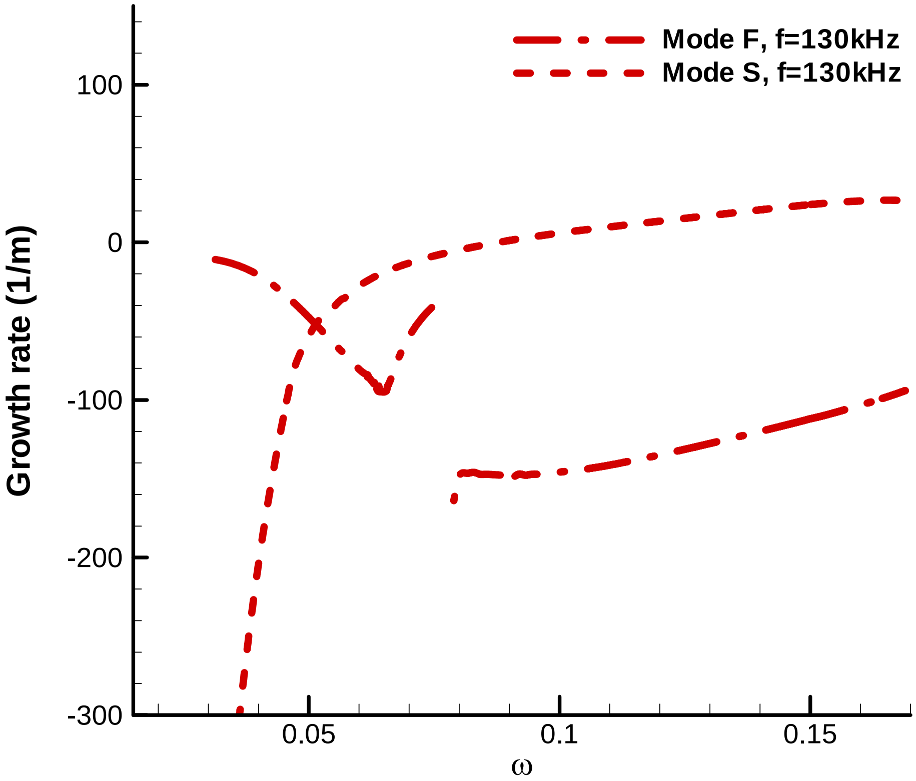

Figure 120. Streamwise growth rates of mode F and mode S at the frequency of 130 kHz along the dimensionless circular frequency in Case B1.

The streamwise dimensional growth rates along the dimensionless circular frequency at 130 kHz in Case B2 are shown in Figure 121. The mode S is stable before the Branch-I neutral point at $\omega = 0.0727$, and it only becomes unstable behind this dimensionless circular frequency. The mode F is stable everywhere throughout the cone. These observations indicate that the unstable second mode is related to mode S. Moreover, the unstable second mode begins shortly downstream from the synchronization of mode F and mode S at $\omega = 0.051$. Within the break due to the synchronization of the mode F and the entropy/vorticity waves, the growth rate of the mode F has a drop, in other words, a jump in α_i, which indicates the stabilizing effects to mode F from the synchronization between mode F and entropy/vorticity waves. Such jump in α_i is also found in Fedorov *et al.* [78, 80].

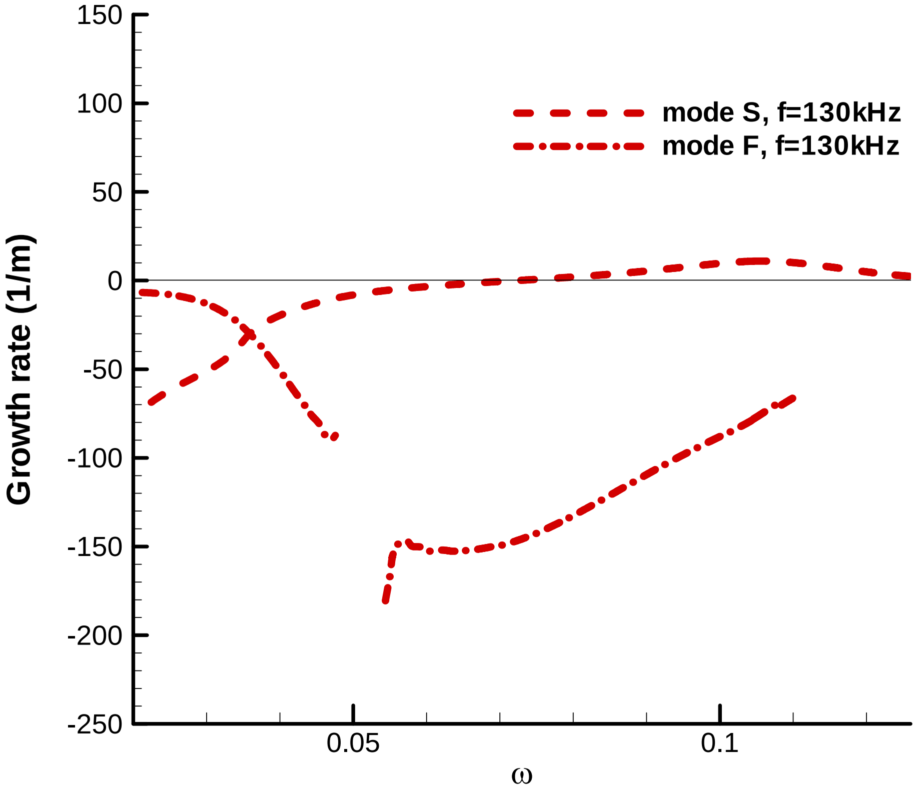

Figure 121. Streamwise growth rates of mode F and mode S at the frequency of 130 kHz along the dimensionless circular frequency in Case B2.

From the analyses of the streamwise phase speeds and growth rates of mode F and mode S in all three cases of freestream Mach number effects (Case 1, B1 and B2), we found that the synchronization points of mode F and mode S, Branch-I neutral points, the synchronization "breaks" of the mode F and entropy/vorticity waves, and the second synchronization points of mode F and mode S appear earlier in terms of dimensionless circular frequencies with a higher freestream Mach number. Such observation implies that the self-similarity is not well held in the steady base flow field between the cases of different freestream Mach numbers.

Moreover, except Case 1, the higher freestream Mach number cases of B1 and B2 have the synchronization points appear earlier than the Branch-I neutral points. The distance that is between the synchronization point and the Branch-I neutral point, is found to be longer with a higher freestream Mach number. The common feature between all the cases of freestream Mach number effects is that the second mode instability is always relevant to mode S.

The preceding LST predicted mode F and mode S phase speeds and growth rates are compared with the simulated unsteady boundary-layer disturbances in Section 4.4.3, in order to study the effects of freestream Mach number in the boundary-layer receptivity mechanism.

From LST predicted growth rates, the N-factors of the second mode are computed by Eq. (70), in order to prepare for the approximation of the receptivity coefficients at the Branch-I neutral stability locations, which is described in Section 3.2.4. The N-factors over the cone in Case B2 is shown in Figure 122. They are generated from LST calculations that are discussed in Section 3.2.2 of LST analysis over the steady base flow. The sampling frequencies span from 120 kHz to 180 kHz, which is around the maximum normalized amplitude within the second-mode dominant frequency range that is observed in Figure 115. From the N-factors at the end of the computation domain, 145.4 kHz is found to be the most amplified frequency, which reaches the N-factor of 2.6. This frequency is also found to be very close to the peak frequency of 143 kHz at $x^* = 0.441\ \mathrm{m}$ in Figure 115. Thus, from the earliest neutral location in the plot, $x^* = 0.132\ \mathrm{m}$, to the end of the computation domain, $x^* = 0.441\ \mathrm{m}$, the overall gradient of N-factor is $8.41\ \mathrm{m}^{-1}$. All of the sampling frequencies are equal to or below 2.6 in the computational domain. From our experience of using the receptivity coefficient method described earlier in Section 4.3.2, one needs to use the sampling frequencies with the N-factor equal to or more than 5 to make qualitative reasonable approximations. Moreover, for the accurate approximations, the N-factor needs to be 8 or higher. Therefore, the approximation of mode S receptivity coefficients in the Case B2 is not available due to the low N-factors with a higher freestream Mach number. The use of smaller N-factors will result in the over-estimation of the receptivity coefficient due to the significance of impurity of other modes in the second mode dominant boundary-layer disturbances.

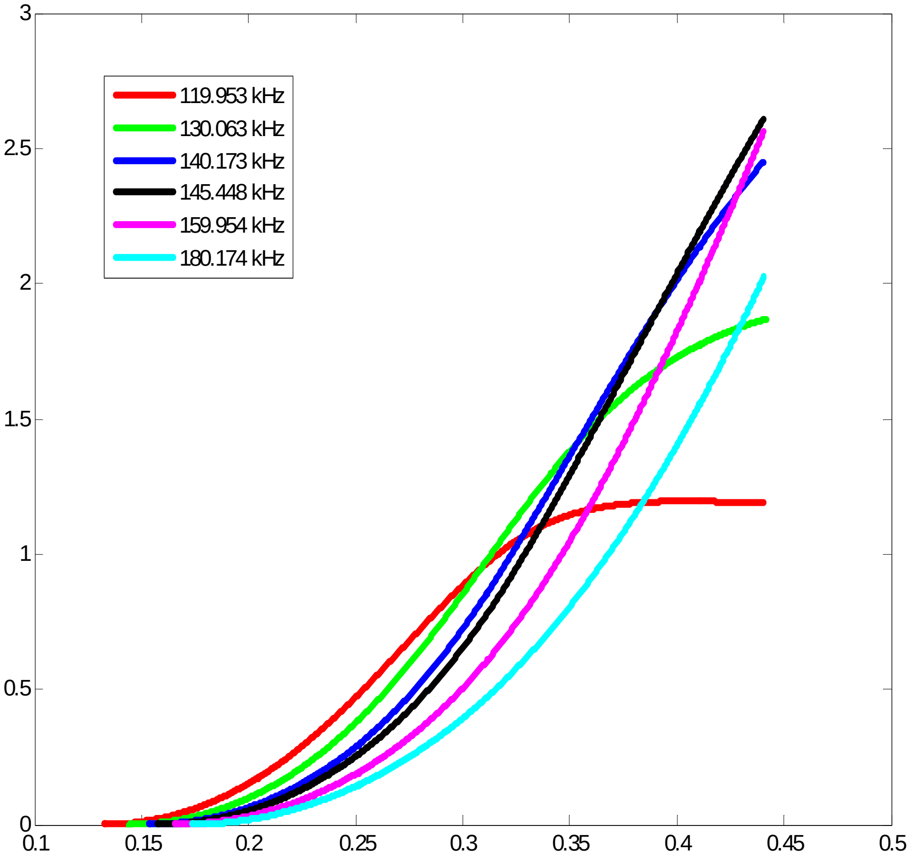

Figure 122. Second mode N-factors in Case B2.

From the observations of the LST predicted N-factor plots in Case 1 and B2, the overall gradient of N-factor of the second mode in Case 1 is far larger (five times) than the one in Case B2, which implies that the amplification rate of the second mode instability is significantly lower with a higher freestream Mach number. Such finding is consistent with the finding in the earlier discussion of the normalized amplitude spectra of the pressure disturbances at wall for the cases of different freestream Mach numbers: the average growth rate of the second mode dominant boundary-layer disturbances with a lower freestream Mach number is found to be higher from the comparisons of the average growth rates and the average logarithm gradients.

Boundary-layer receptivity process is the process of having the disturbances from outside of the boundary-layer evolve to the final form within the boundary layer before the dominant modal growth. In order to study the receptivity process, the receptivity strength is one of the important features to investigate. Specifically, for characterizing the strength of receptivity prior to the growth of the boundary-layer disturbances, there is a receptivity coefficient which is defined as the ratio of the wave amplitude at the Branch-I neutral location that is immediately behind the receptivity process, to the perturbation amplitude of the specific frequency in freestream. In fact, the normalized amplitude defined in Eq. (73) at the Branch-I neutral location is the receptivity coefficient. Due to the N-factors of mode S is significantly lower with a higher freestream Mach number, and the requirement of high N-factors in the single-mode receptivity coefficient approximation method discussed in Section 4.3.2, only the receptivity coefficients of the overall boundary-layer disturbances of the cases with the higher freestream Mach numbers are presented in Figure 123 and Figure 124.

Figure 123 shows the frequency spectrum of the simulated overall boundary-layer disturbances at the Branch-I neutral location for Case B1. Such frequency spectrum is shown within the frequency range of the dominant growth. The amplitudes of the simulated boundary-layer disturbances that contain all wave modes, are recorded at the LST predicted Branch-I neutral locations which are shown as the neutral stability curve in Figure 116 (a). At the locations of Branch-I neutral stability, there is no dominant mode appeared yet, in other words, the amplitudes of each modes are comparable. Therefore, the modulation between each mode waves occurs, and it results in the oscillatory amplitude curve for the overall boundary-layer disturbances. The largest peak in the amplitude of the overall disturbances is from 91 kHz to 115 kHz. The maximum value of this peak is 0.228. The general pattern of the overall disturbance amplitude seems ascending over lower frequencies, since the troughs and the peaks are ascending while the frequency is becoming lower. In the frequency range from 91 kHz to 200 kHz, the overall disturbances have the amplitudes from 0.0046 to 0.228, and the median amplitude is 0.116.

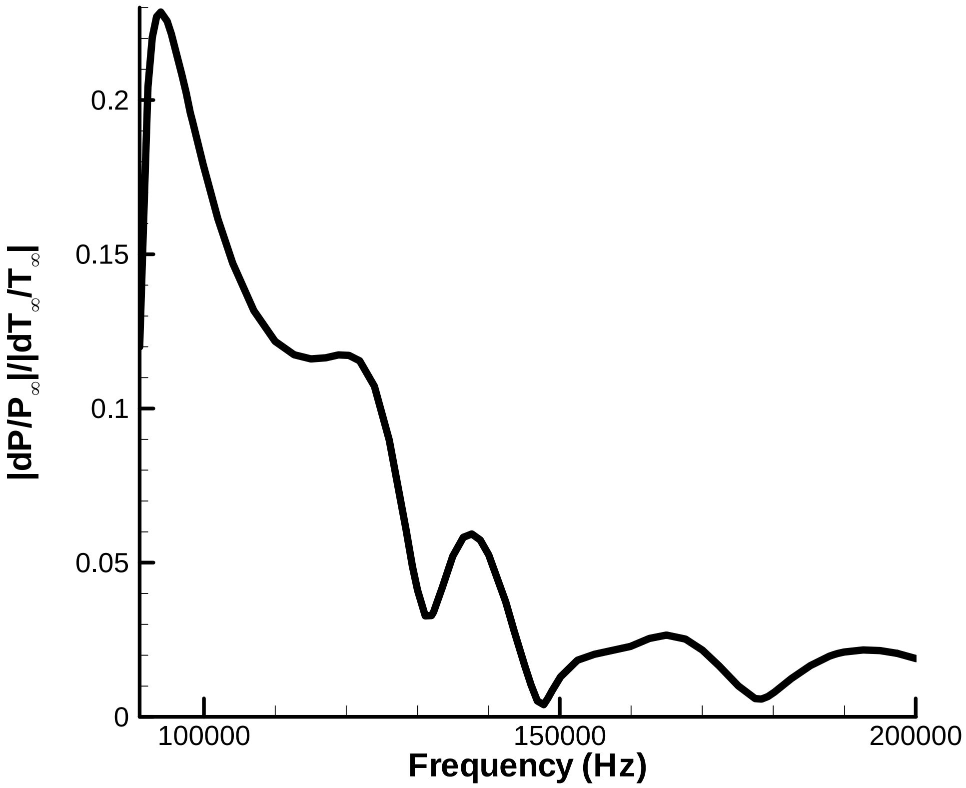

Figure 123. The spectrum of simulated overall boundary-layer disturbances at Branch-I neutral locations of Case B1.

Figure 124 shows the frequency spectrum of simulated overall boundary-layer disturbances for Case B2. The amplitudes of the simulated boundary-layer disturbances that contains all wave modes, are recorded at the LST predicted Branch-I neutral locations which are shown as the neutral stability curve in

Figure 117 (a). At the locations of Branch-I neutral stability, there is no dominant mode appeared yet, in other words, the amplitudes of each modes are comparable. Therefore, the modulation between each mode waves occurs, and it results in the oscillatory amplitude curve for the overall boundary-layer disturbances. However, the spectrum of Case B2 is much smoother than the Case 1 and B1. This is most likely due to having the relative stronger mode S in the boundary-layer disturbances initially in Case B2. The overall disturbance amplitude is ascending over lower frequencies. In the frequency range from 95 kHz to 210 kHz, the overall disturbances have the amplitudes from 0.067 to 0.754, and the median amplitude is 0.4105.

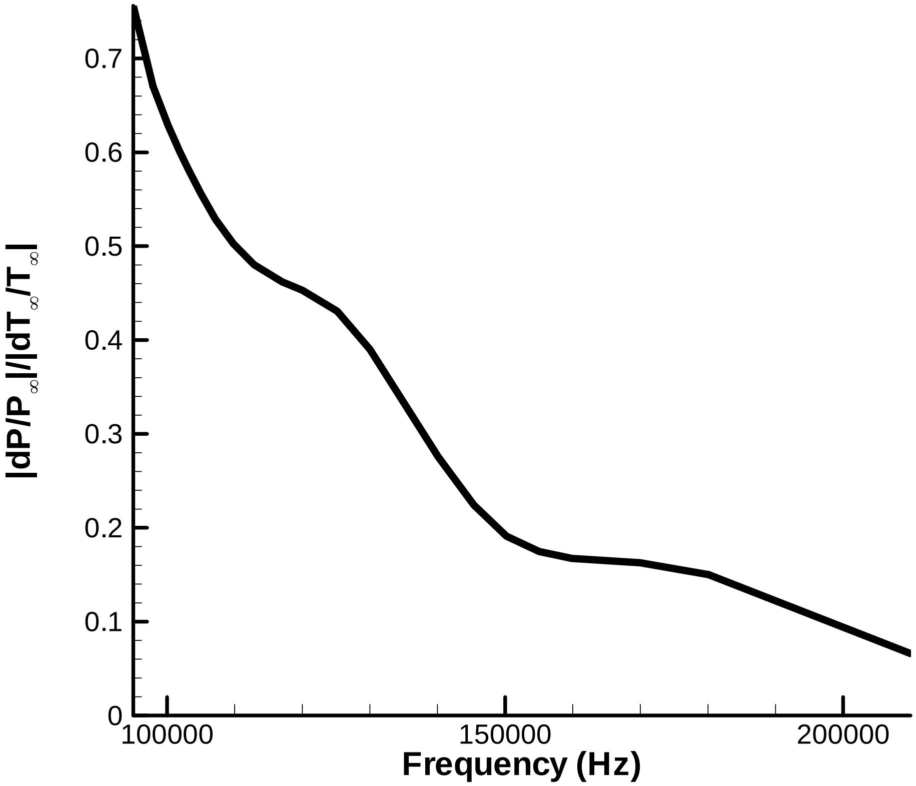

Figure 124. The spectrum of simulated overall boundary-layer disturbances at Branch-I neutral locations of Case B2.

From the observations of the receptivity coefficients of the overall boundary-layer disturbances in Case 1, B1 and B2, the median amplitude of the initial overall boundary-layer disturbances at the Branch-I neutral locations is found to be higher in the case of a higher freestream Mach number. This trend implies that the initial amplitude of the overall boundary-layer disturbances is higher before the second mode dominant growth with a higher freestream Mach number. Such finding is consistent with the finding in the earlier discussion of the normalized amplitude spectra of the pressure disturbances at wall for the cases of different freestream Mach numbers: the case with the lower freestream Mach number has the lower initial amplitude of the second mode dominant growth.

Additionally, the overall disturbance amplitude at the Branch-I neutral point of mode S is ascending over lower frequencies for the cases of B1 and B2. It is very different to Case 1, which no such clear pattern is found. Also, the modulations in the overall disturbance amplitude at the Branch-I neutral point of mode S are significantly weaker for the case of a higher freestream Mach number. Such trend implies that the initial boundary-layer disturbances with a higher freestream Mach number have the more outstanding mode S prior to the second mode dominant growth.

4.4.3 Mechanism of Boundary-Layer Receptivity

After the parametric study of the freestream Mach number effects in the receptivity and the growth of the boundary-layer disturbances from the earlier frequency spectra of Case 1, B1 and B2, an investigation of the freestream Mach number effects in the spatial modal evolution of the boundary-layer disturbances throughout the cone is conducted next. This is a crucial step to understand the receptivity mechanism under the effects of freestream Mach number.

Figure 125 shows the spatial development of wall-pressure-perturbation amplitude from the upstream region to the downstream region in Case B1 and B2. In each case of different freestream Mach number, the frequency of 130 kHz which is near the peak frequency in the second mode dominant ranges that are shown in Figure 114 and Figure 115 is chosen as the sampling frequency to be investigated in this section. Both Case B1 and B2 start with high initial amplitudes where the hotspot has just passed through the shock and excites the boundary-layer disturbances in the upstream region. Then the perturbations decay through the receptivity process while moving downstream. When the perturbations reach $s^* = 0.1\ \mathrm{m}$ in Case B1, and $s^* = 0.0954\ \mathrm{m}$ in Case B2, they begin to grow exponentially downstream. From this observation, one can see that the higher freestream Mach number results in the very slightly earlier beginning location of the boundary-layer disturbances growth. In Figure 116 (a) and

Figure 117 (a), the LST predicted Branch-I neutral location of 130 kHz in Case B1 is $s^* = 0.0983\ \mathrm{m}$, and the one in Case B2 is $s^* = 0.145\ \mathrm{m}$. Noticeably, the boundary-layer disturbance growth beginning location for Case B1 is almost the same as the Branch-I neutral location of mode S. However, the boundary-layer disturbance growth beginning location for Case B2 is earlier upstream than the LST predicted Branch-I neutral location of mode S. This phenomenon is further investigated in the latter part of this section. Moreover, the oscillatory or unsmooth features of the amplitude curves are the results of the modulation of multiple wave modes when there is no single dominant instability mode. This multi-mode modulation phenomenon is expected in the synchronization zone. It is commonly seen in many numerical studies [4, 28, 31, 35, 36, 94].

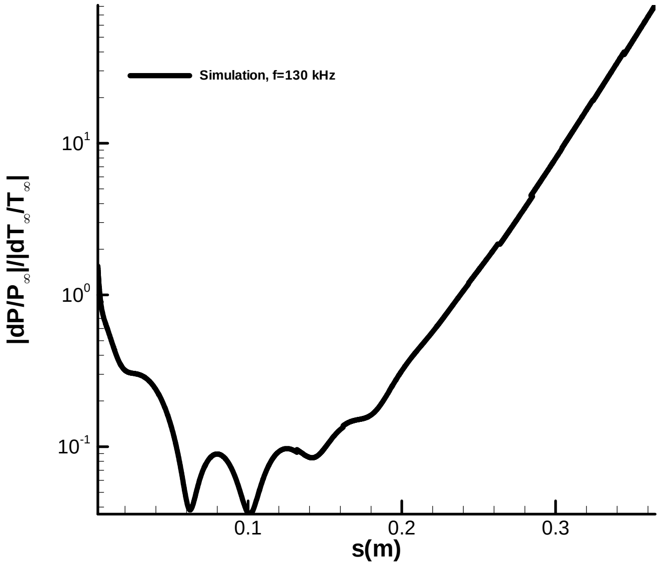

(a)

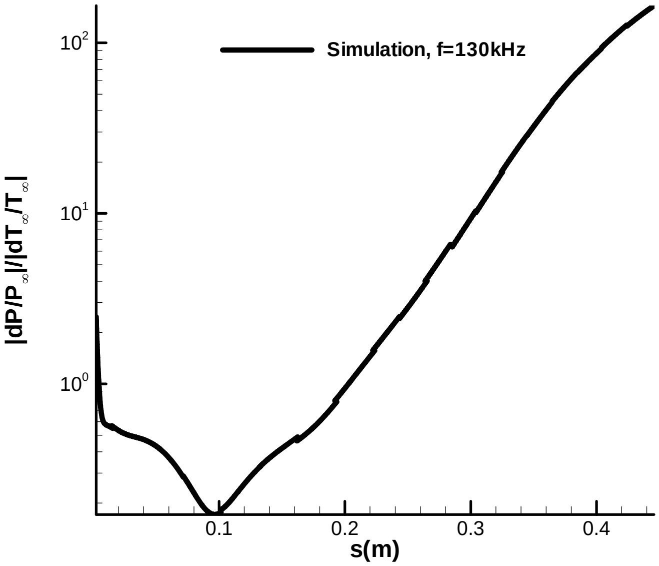

(b)

Figure 125. The spatial amplitude development of the simulated wall-pressure perturbations at the frequency of 130 kHz in (a) Case B1 and (b) Case B2.

The modal evolution in the boundary layer cannot be determined from the simulated overall boundary-layer disturbance amplitudes along the cone. Therefore, we have to compare the results of the simulated overall disturbances to the LST predicted results of the pure boundary-layer modes in order to identify the dominant wave modes in the boundary layer. The sampling frequency to be analyzed in each case of different freestream Mach number is the one near the peak amplitude in the second mode dominant ranges that are shown in Figure 114 and Figure 115. The simulated dimensionless phase speed is computed by Eqs. (45), (66), and (68). The comparison between the phase speed of the simulated overall disturbances and the LST predicted mode S and mode F phase speeds in Case B1 is shown in Figure 126 (a). The three horizontal lines are the dimensionless phase speeds of fast acoustic, slow acoustic and entropy/vorticity waves determined using freestream flow conditions in front of the bow shock. As a result, they only serve as qualitative references to show the existence of the three continuous wave modes. The actual phase speeds depend on local non-constant flow conditions. Figure 126 (a) shows a trend of the phase speed of the simulated disturbances decreases from the phase speed of the fast acoustic wave in the nose region. The simulated phase speed is below and following the LST predicted mode F with a small wiggle until $s^* = 0.038\ \text{m}$. The comparison shows that the disturbances are likely to be initially excited in the boundary layer by the fast acoustic waves near the nose. The comparison also shows that both mode F and the entropy/vorticity waves are relatively strong in the boundary-layer disturbances before $s^* = 0.038\ \text{m}$. The phase speed of the simulated disturbances jumps over the one of the fast acoustic waves after the simulated phase speed reaching the one of the entropy/vorticity waves, and then drops back to the phase speed of the entropy/vorticity waves between $0.038\ \text{m} < s^* < 0.08\ \text{m}$. Such jump indicates that the fast acoustic waves are relatively strong between $0.038\ \text{m} < s^* < 0.08\ \text{m}$. The modulation between many wave modes causes the wiggle and jump. More specifically, there are many wave modes existing in the simulated boundary-layer disturbances, while the LST results are based on a single mode only. Consequently, the co-existence of other modes with comparable strengths results in the modulations of the simulated results. The same phenomenon was also discussed by Ma and Zhong [4, 35, 36].

Within $0.08\ \text{m} < s^* < 0.1\ \text{m}$, the simulated phase speed drops below the phase speed of the slow acoustic waves . This drop implies that the slow acoustic waves, mode F and mode S are outstanding among the boundary-layer wave modes shortly behind the synchronization point of mode F and mode S at $s^* = 0.08\ \text{m}$. Behind $s^* = 0.1\ \text{m}$, the simulated phase speed converges to mode S. As the waves propagate further downstream, the simulated phase speed becomes almost the same as the mode S. This observation indicates the dominance of mode S in the boundary-layer disturbances after the synchronization between mode S and mode F.

In Fedorov *et al.* [80, 108], a branch point is where both the real and imaginary parts of the phase speed are equal for mode F and mode S. The second mode instability is excited downstream from the branch point. The branch point, however, does not exist in most practical flows with a real x axis (or Reynolds numbers) only, except for a very specific disturbance frequency with a very cold wall. Instead, the branch point appears along complex Reynolds number with a non-zero imaginary part. In the case of practical flow, mode F and mode S have resonance interaction when the real part of the wave number and frequency are the same near the branch point, even though the growth rates are different. Therefore, we define the synchronization point, which is also the resonant point, between mode F and mode S as the point where the real parts of the phase speed are equal for mode

F and mode S. Ma and Zhong [4, 35, 36] have shown that this synchronization point plays an important role in receptivity process.

In Figure 126 to Figure 129, there is a break in the phase speeds and growth rates of mode F before the synchronization point. It is due to that the eigenvalue of the discrete mode F merges into the entropy/vorticity spectrum and reappears while moving downstream before reaching the synchronization point. As a result, the eigenvalue of mode F is interrupted by the entropy/vorticity spectrum. Since the actual phase speed of entropy/vorticity waves depends on local flow conditions, the break appears below the freestream phase speed of entropy/vorticity waves in Figure 126 (a). This break is typical for hypersonic flow over a cone.

The plot of dimensionless phase speed in Figure 126 (a) is expressed in terms of dimensional streamwise coordinate along the surface of the compression cone. It provides intuitive idea and practical information by referring to the spatial location along the cone. It is especially convenient when comparing with the experiment results, or providing guidance to experimental study or vehicle design process. In parametric studies, it is more convenient to express results in terms of dimensionless parameters such as self-similarity parameters, because self-similarity parameters allow comparison of common characteristics between different cases regardless to the dimensional differences. The horizontal axis in Figure 126 (b) has the dimensionless circular frequency, ω, instead of the dimensional streamwise location along the cone surface, s^*. According to Eq. (67), the dimensionless circular frequency contains both the factors of local Reynolds number and frequency.

In Figure 126 (b), the synchronization point of mode F and mode S is at $\omega = 0.078$. From $\omega = 0.022$ to 0.056, both the phase speeds of mode F and the simulated disturbances decrease from the one of the fast acoustic waves to around the one of the entropy/vorticity waves, and the simulated phase speed is below and following the one of mode F. This observation implies that the boundary-layer disturbances have relatively strong mode F and entropy/vorticity modes, and it is being initially excited by the fast acoustic waves in the earlier region near the nose. The earlier results in Figure 112, which show that there are mainly acoustic waves carried into the shock layer in the nose region, also confirm this implication. The wiggles in the simulated phase speed is due to the modulation of different wave modes in the boundary layer, when various wave modes are having comparable amplitudes as explained previously. From $\omega = 0.056$ to 0.077, the simulated phase speed jumps over the fast acoustic waves and drops back to the phase speed of the entropy/vorticity waves. This observation indicates that the fast acoustic waves are relatively strong between $\omega = 0.056$ to 0.077, which is shortly before the synchronization point. Immediately behind the synchronization point, the simulated phase speed drops below the phase speed of slow acoustic waves until $\omega = 0.089$. Such drop implies that the slow acoustic waves, mode F and mode S are outstanding among the boundary-layer wave modes shortly behind the synchronization point of mode F and mode S. Further downstream, the simulated phase speed converges to the one of mode S. Simultaneously, the oscillation gradually disappears, and the simulated phase speed curve eventually becomes smooth downstream. These observations indicate the domination of mode S in the boundary-layer disturbances after the synchronization between mode F and mode S.

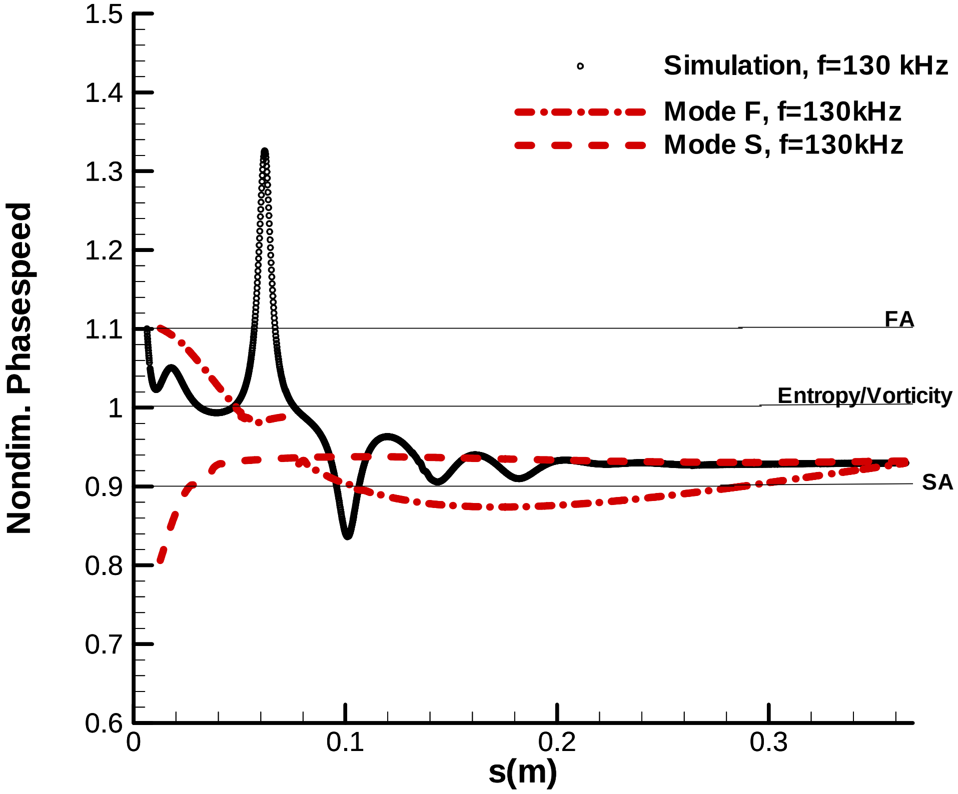
Simulation, f=130 kHz
Mode F, f=130kHz
Mode S, f=130kHz
FA
Entropy/Vorticity
SA
Nondim. Phasespeed
1.5
1.4
1.3
1.2
1.1
1
0.9
0.8
0.7
0.6
0
0.1
0.2
0.3
s(m)

(a)

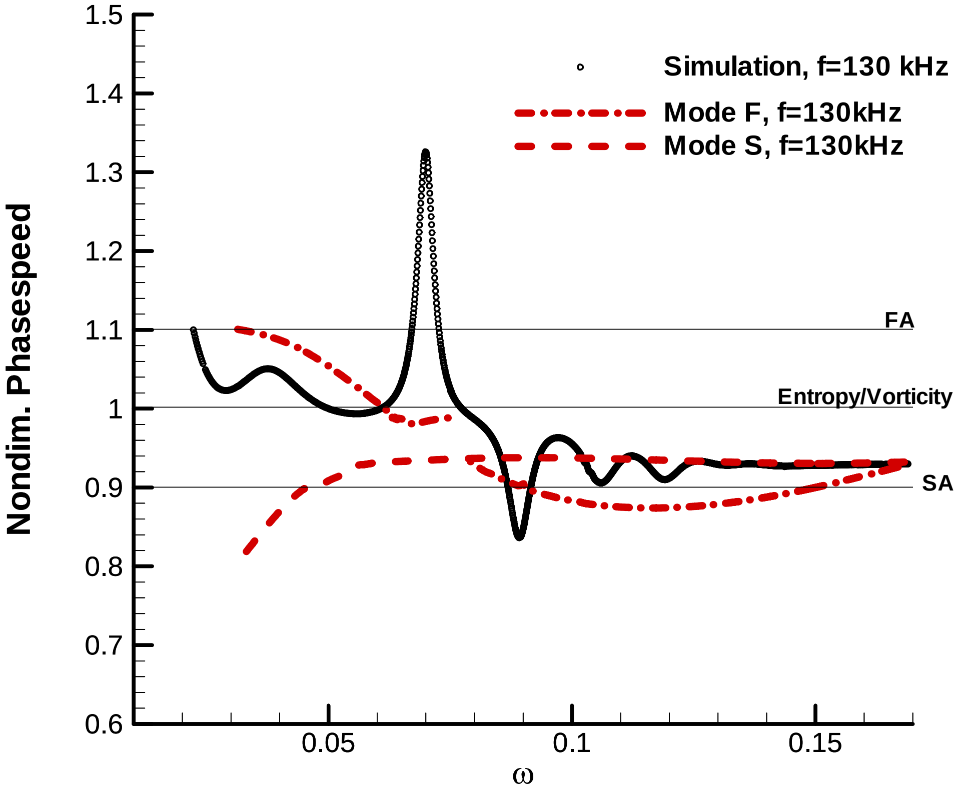

(b)

Figure 126. Comparison of the streamwise phase speeds of the simulated wall-pressure disturbances with those of the LST predicted mode F and mode S at the frequency of 130 kHz along (a) the dimensional body surface coordinate and (b) the dimensionless circular frequency in Case B1.

The comparison between the phase speed of the simulated overall disturbances and the LST predicted mode S and mode F phase speeds in Case B2 is shown in Figure 127 (a). The three horizontal lines are the dimensionless phase speeds of fast acoustic, slow acoustic and entropy/vorticity waves determined using freestream flow conditions in front of the bow shock. As a result, they only serve as qualitative references to show the existence of the three continuous wave modes. The actual phase speeds depend on local non-constant flow conditions. Figure 127 (a) shows a trend of the phase speed of the simulated disturbances drops to around the entropy/vorticity wave speed at $s^* = 0.02$ m from slightly above the phase speed of the fast acoustic wave shortly behind the nose region. This comparison shows that the disturbances are initially excited in the boundary layer by the fast acoustic waves near the nose. It also shows that both mode F and the entropy/vorticity waves are relatively strong in the boundary-layer disturbances before $s^* = 0.02$ m. The phase speed of the simulated disturbances continues decreasing to a point below the one of the slow acoustic waves at $s^* = 0.095$ m. Between $0.02\text{ m} < s^* < 0.095\text{ m}$, the modulations between mode S, mode F, slow acoustic waves and entropy/vorticity waves occur. There is no single outstanding mode. The synchronization point at around $s^* = 0.073$ m is within the break of the mode F curve.

In Figure 126 to Figure 129, there is a break in the phase speeds and growth rates of mode F before the synchronization point. It is due to that the eigenvalue of the discrete mode F merges into the entropy/vorticity spectrum and reappears while moving downstream before reaching the synchronization point. As a result, the eigenvalue of mode F is interrupted by the entropy/vorticity spectrum. Since the actual phase speed of entropy/vorticity waves depends on local flow conditions, the break appears below the freestream phase speed of entropy/vorticity waves in Figure 127 (a). This break is typical for hypersonic flow over a cone.

Behind $s^* = 0.095$ m, the simulated phase speed the simulated phase speed converges to mode S. As the waves propagate further downstream, the simulated phase speed becomes almost the same as the mode S. This observation indicates the dominance of mode S in the boundary-layer disturbances after the synchronization between mode S and mode F.

Figure 127 (b) is the comparison between the phase speed of the simulated overall disturbances and the LST predicted mode S and mode F phase speeds in Case B2 in terms of the dimensionless circular frequency. In the plot, the synchronization point of mode F and mode S is at $\omega = 0.051$, which is within the break of the mode F curve. From $\omega = 0.019$ to 0.026, the phase speeds of mode F drops from the one of the fast acoustic waves to around the one of the entropy/vorticity waves. This observation implies that the boundary-layer disturbances have relatively strong mode F and entropy/vorticity modes, and it is being initially excited by the fast acoustic waves in the earlier region near the nose. The earlier results in Figure 113 which shows that there are mainly acoustic waves carried into the shock layer in the nose region, also confirm this implication. From $\omega = 0.026$ to 0.059, the simulated phase speed continues decreasing to a point below the slow acoustic wave speed. This observation indicates the modulations between mode S, mode F, slow acoustic waves and entropy/vorticity waves between $\omega = 0.026$ to 0.059. Behind $\omega = 0.059$, the simulated phase speed converges to the one of mode S. Simultaneously, the oscillation gradually disappears, and the simulated phase speed curve eventually becomes smooth and matches mode S wave speed downstream. These observations indicate the domination of mode S in the boundary-layer disturbances after the synchronization between mode F and mode S.

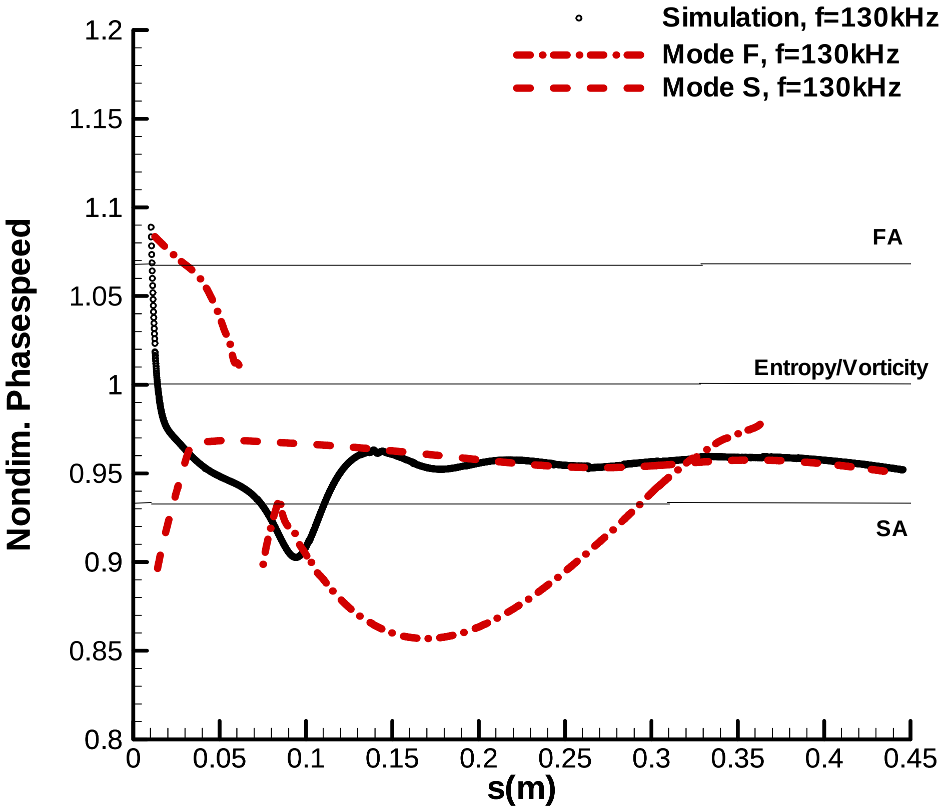
Simulation, f=130kHz
Mode F, f=130kHz
Mode S, f=130kHz
FA
Entropy/Vorticity
SA
Nondim. Phasespeed
s(m)
1.2
1.15
1.1
1.05
1
0.95
0.9
0.85
0.8
0
0.05
0.1
0.15
0.2
0.25
0.3
0.35
0.4
0.45

(a)

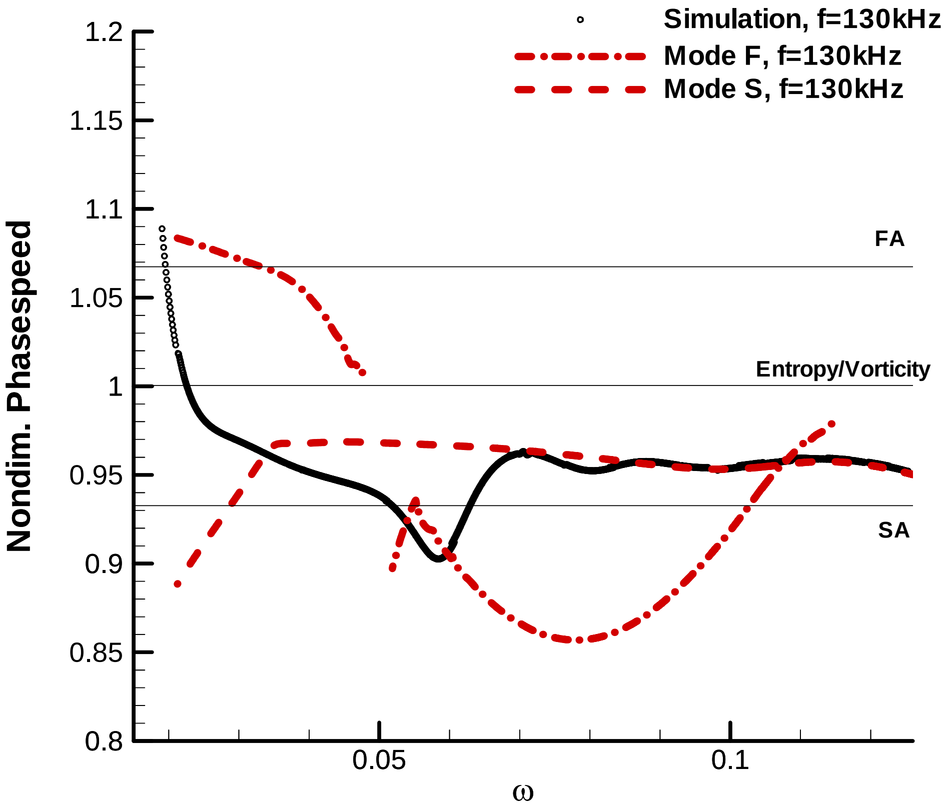

(b)

Figure 127. Comparison of the streamwise phase speeds of the simulated wall-pressure disturbances with those of the LST predicted mode F and mode S at the frequency of 130 kHz along (a) the dimensional body surface coordinate and (b) the dimensionless circular frequency in Case B2.

From the observations of the cases of different nose bluntness, it is obvious that the receptivity paths of all these cases are similar: the boundary layer disturbances are initially carried in as the fast acoustic waves near the nose region. The fast acoustic wave excited mode F in the boundary-layer disturbances has the relative large strength behind the nose region until the boundary-layer disturbance phase speed reaches the one of the entropy/vorticity waves. Then it is followed by the occurrence of the strong multi-wave-mode modulations in the middle of the cone. Finally, the synchronization of mode F and mode S causes the dominance of the mode S in the boundary-layer disturbances in the downstream part of the cone.

However, the dimensional streamwise synchronization location of mode F and mode S are very different for each case of the freestream Mach number effects. Specifically, under the same sampling frequency of 130 kHz in Case B1 and B2, the synchronization location of Case B2 is earlier than the one of Case B1. Such comparison shows that the higher freestream Mach number would leads to the earlier synchronization of mode F and mode S over a cone.

By comparing the phase speed plots of the cases of the different freestream Mach numbers, one can see that the simulated phase speed is lower than the mode F phase speed shortly behind the nose region. In addition, the higher freestream Mach number would leads to the faster dropping of the simulated phase speed to the entropy/vorticity wave speed. Therefore, such observation indicates that the higher freestream Mach number would leads to the more outstanding entropy/vorticity waves in the boundary-layer disturbances in the upstream part of the cone before the boundary-layer disturbance phase speed reaches the one of the entropy/vorticity waves. Different to Case 1 and B1, the fast acoustic waves are not outstanding in the boundary-layer disturbances during the strong multi-wave-mode modulations shortly before the synchronization point of mode S and mode F in Case B2.

Additionally, the dimensionless circular frequencies of the synchronization point in the cases of different freestream Mach numbers are significantly different, even under the same sampling frequency between Case B1 and B2. Therefore, such comparison implies that the similarity is not well held under different freestream Mach numbers. Moreover, the dimensionless circular frequency of the synchronization point is smaller with a higher freestream Mach number.

The stability of the boundary-layer disturbances at different locations is determined by their growth rates. The simulated growth rate is calculated by Eq. (44). The comparisons between the growth rates of the simulated boundary-layer disturbances and those of mode S and mode F obtained by LST in Case B1 and B2 are shown in Figure 128 and Figure 129.

In the comparison of Case B1 in Figure 128 (a), there are oscillations in the simulated growth rate as a result of multi-mode wave modulations. The simulated growth rate follows the mode F from $s^* = 0.025\text{ m}$ to 0.054 m. This observation implies that the mode F is relatively strong shortly behind the nose region. The LST predicted mode F is stable everywhere while mode S is stable before the Branch-I neutral location at $s^* = 0.0983\text{ m}$, and it becomes the unstable second Mack mode behind this location. The simulated growth rate vigorously oscillates around and begins to gradually converge to mode S from $s^* = 0.057\text{ m}$ to 0.21 m. Such observation shows the strong modulations between multiple boundary-layer wave modes, and the gradual dominance of mode S in the boundary-layer disturbances as it approaches and passes by the synchronization point of mode S and mode F at $s^* = 0.08\text{ m}$. Behind $s^* = 0.21\text{ m}$, the simulated growth rate eventually becomes converged to mode S, and there is no significant oscillation. This observation shows the dominance of the mode S related unstable second mode in the boundary-layer disturbances downstream of the synchronization point and the Branch-I neutral location.

Different to the cases in the parametric study of the nose bluntness effects, in Case B1, the synchronization point is earlier than the Branch-I neutral point. From the earlier discussion of the spatial development of the boundary-layer disturbances with the frequency of 130 kHz in Case B1, which is shown in Figure 125, the boundary-layer disturbances only exponentially grow behind $s^* = 0.1\text{ m}$, which is immediately behind the Branch-I neutral location.

Figure 128 (b) shows the comparison in Case B1 between the simulated growth rate and the one obtained from LST in self-similar variable, which allows comparison of common characteristics between different cases regardless to the dimensional differences. The horizontal axis in Figure 128 (b) has the dimensionless circular frequency, ω, instead of the dimensional streamwise location along the cone surface, s^*.

In Figure 128 (b), there are oscillations in the simulated growth rate as a result of multi-mode wave modulations. The simulated growth rate follows the mode F from $\omega = 0.045$ to 0.065. This observation implies that the mode F is relatively strong shortly behind the nose region. The LST predicted mode F is stable everywhere while mode S is stable before the Branch-I neutral location at $\omega = 0.088$, and it becomes the unstable second Mack mode behind this location. The simulated growth rate vigorously oscillates around and begins to gradually converge to mode S from $\omega = 0.068$ to 0.13. Such observation shows the strong modulations between multiple boundary-layer wave modes, and the gradual dominance of mode S in the boundary-layer disturbances as it approaches and passes by the synchronization point of mode S and mode F at $\omega = 0.078$. Behind $\omega = 0.13$, the simulated growth rate eventually becomes converged to mode S, and there is no significant oscillation. This observation shows the dominance of the mode S related unstable second mode in the boundary-layer disturbances downstream of the synchronization point and the Branch-I neutral location.

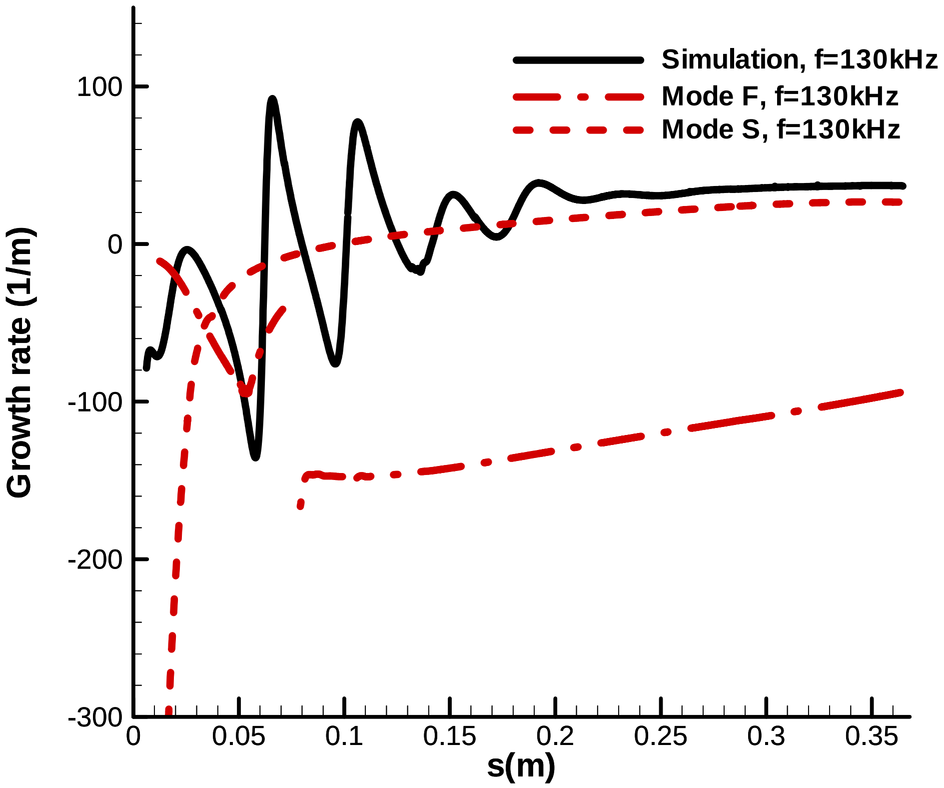
Simulation, f=130kHz
Mode F, f=130kHz
Mode S, f=130kHz
Growth rate (1/m)
100
0
-100
-200
-300
0
0.05
0.1
0.15
0.2
0.25
0.3
0.35
s(m)

(a)

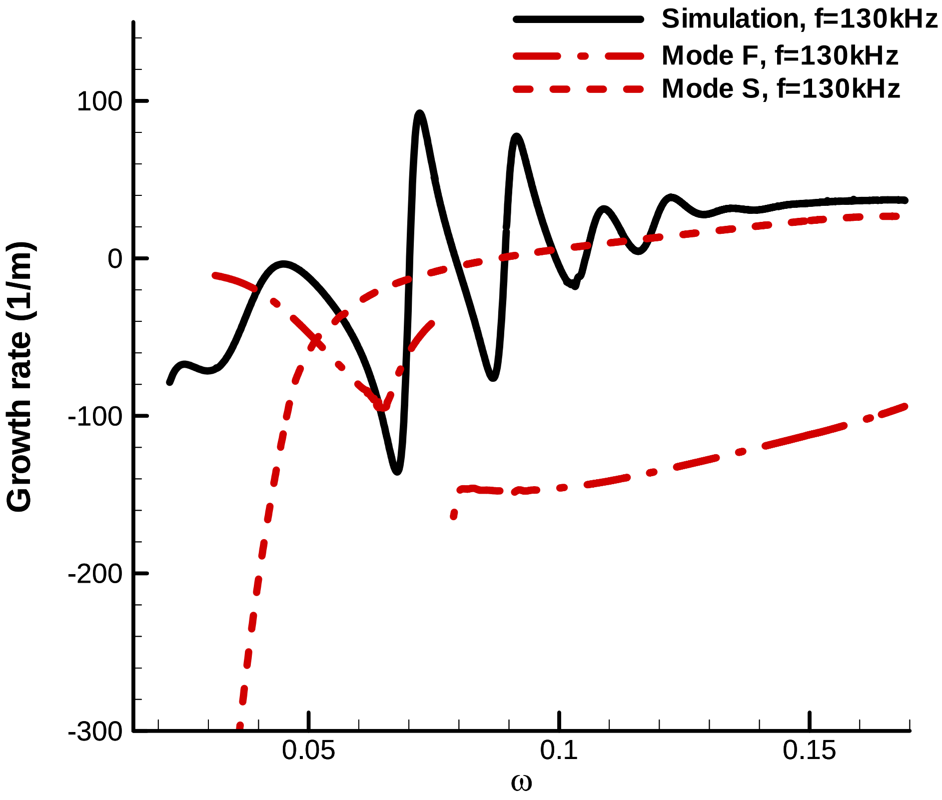

(b)

Figure 128. Comparison of the streamwise growth rates of the simulated wall-pressure disturbances with those of the LST predicted mode F and mode S at the frequency of 130 kHz along (a) the dimensional body surface coordinate and (b) the dimensionless circular frequency in Case B1.

In the growth rates comparison of Case B2 shown in Figure 129 (a), the simulated growth rate follows the mode F before $s^* = 0.02$ m. This observation implies that the mode F is relatively strong behind the nose region for a short distance. The LST predicted mode F is stable everywhere while mode S is stable before the Branch-I neutral location at

$s^* = 0.145\ \mathrm{m}$, and it becomes the unstable second Mack mode behind this location. The simulated growth rate deviates from mode F, oscillates around and begins to gradually converge to mode S from $s^* = 0.02\ \mathrm{m}$ to $0.16\ \mathrm{m}$. Such observation shows the strong modulations between multiple boundary-layer wave modes, and the gradual dominance of mode S in the boundary-layer disturbances as they approach and pass by the synchronization point of mode S and mode F that is within the break of the mode F curve around $s^* = 0.073\ \mathrm{m}$. Behind $s^* = 0.16\ \mathrm{m}$, the simulated growth rate eventually becomes converged to mode S, and there is no significant oscillation. This observation shows the dominance of the mode S related unstable second mode in the boundary-layer disturbances downstream of the synchronization point and the Branch-I neutral location.

Different to the cases in the parametric study of the nose bluntness effects, in Case B2, the synchronization point is earlier than the Branch-I neutral point. From the earlier discussion of the spatial development of the boundary-layer disturbances with the frequency of 130 kHz in Case B2, which is shown in Figure 125, the boundary-layer disturbances only exponentially grow behind $s^* = 0.0954\ \mathrm{m}$, which is between the synchronization point and the Branch-I neutral location.

Figure 129 (b) shows the comparison in Case B2 between the simulated growth rate and the one obtained from LST in self-similar variable, which allows comparison of common characteristics between different cases regardless to the dimensional differences. The horizontal axis in Figure 129 (b) has the dimensionless circular frequency, ω, instead of the dimensional streamwise location along the cone surface, s^*.

In Figure 129 (b), the simulated growth rate follows the mode F before $\omega = 0.0285$. This observation implies that the mode F is relatively strong behind the nose region for a short distance. The LST predicted mode F is stable everywhere while mode S is stable before the

Branch-I neutral location at $\omega = 0.0727$, and it becomes the unstable second Mack mode behind this location. The simulated growth rate deviates from mode F, oscillates around and begins to gradually converge to mode S from $\omega = 0.0285$ to 0.075. Such observation shows the strong modulations between multiple boundary-layer wave modes, and the gradual dominance of mode S in the boundary-layer disturbances as they approach and pass by the synchronization point of mode S and mode F that is within the break of the mode F curve around $\omega = 0.051$. Behind $\omega = 0.075$, the simulated growth rate eventually becomes converged to mode S, and there is no significant oscillation. This observation shows the dominance of the mode S related unstable second mode in the boundary-layer disturbances downstream of the synchronization point and the Branch-I neutral location.

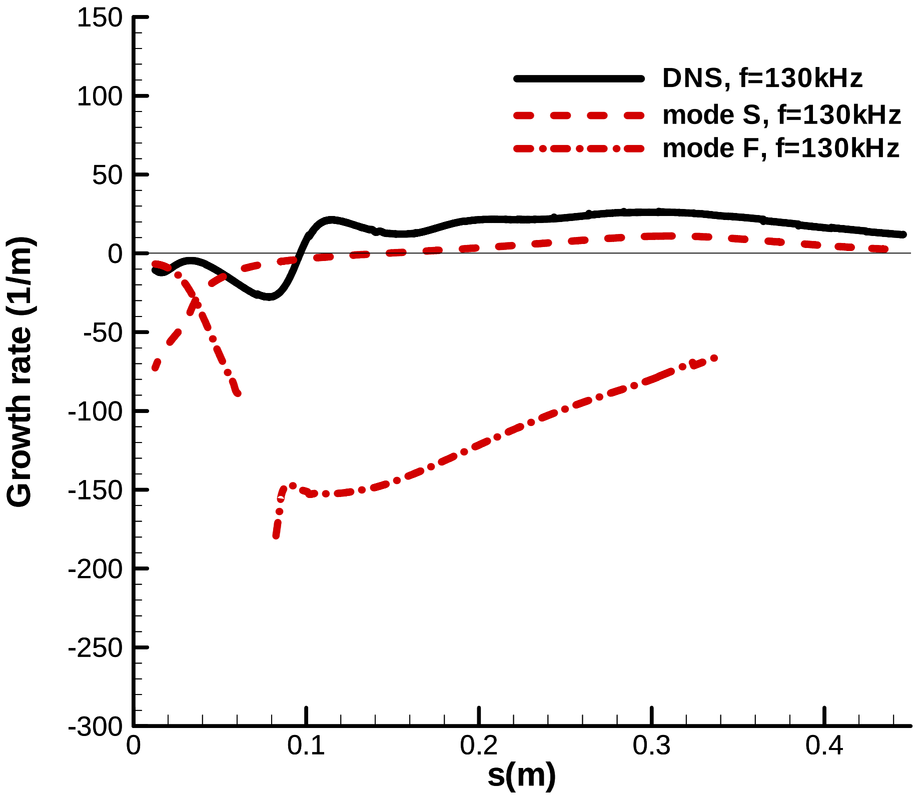

(a)

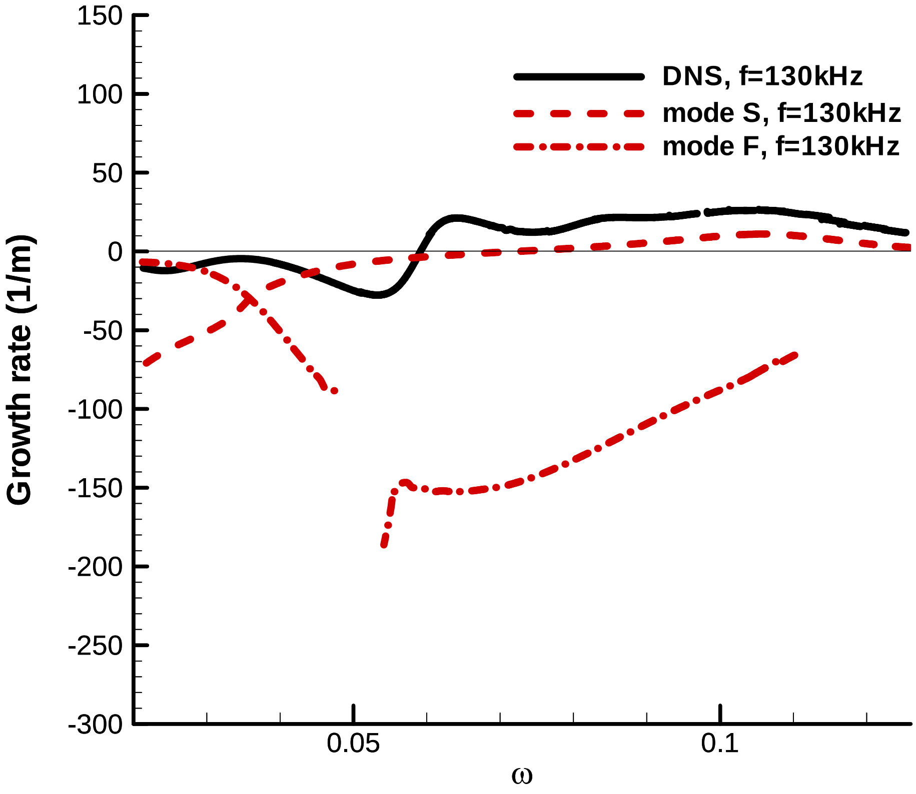

(b)

Figure 129. Comparison of the streamwise growth rates of the simulated wall-pressure disturbances with those of the LST predicted mode F and mode S at the frequency of 130 kHz along (a) the dimensional body surface coordinate and (b) the dimensionless circular frequency in Case B2.

From the observations of all three cases of different freestream Mach numbers, the receptivity modal evolution paths for all the cases observed are consistent with the one found in the earlier phase speed comparison study. However, different to Case 1, the higher freestream Mach number cases of B1 and B2 has the synchronization point appears earlier than the Branch-I neutral point. Moreover, the distance from the synchronization point to the Branch-I neutral point is longer with a higher freestream Mach number.

Additionally, the beginning locations of the mode S related second mode dominant boundary-layer disturbances growth relative to the synchronization point and the Branch-I neutral location are found to be different under different freestream Mach number. The higher freestream Mach number would cause the beginning location more upstream and closer to the synchronization point of mode F and mode S. With a lower freestream Mach number, the beginning location can be further downstream from the synchronization point, and can even pass the Branch-I neutral location. The reason behind such trend is not available in this work, since the modal decompositions of the boundary-layer disturbances at both the neutral point and synchronization point are necessary in order to conduct further receptivity mechanism investigation.

In order to confirm the previous identification of modal evolution in the induced boundary-layer disturbances during the receptivity process, we compare the mode shapes or the eigenfunctions at the sampling frequencies between the simulated boundary-layer disturbances and the mode S and the mode F calculated by LST at locations in the upstream region and the downstream region. These are shown in Figure 130 and Figure 131 for Case B1 and B2 respectively. Noticeably, the vertical axis is the dimensional wall-normal height, and the horizontal axis is the pressure perturbation amplitude that is normalized by the maximum amplitude in the current mode shape.

In Figure 130 (a), at the location of $s^* = 0.042\ \text{m}$ in the upstream region before the major multi-mode modulations shown in the phase speeds comparison in Figure 126 (a), the mode shape of the simulated boundary-layer disturbances within the boundary layer below

$H^* = 0.0012$ m is close to the one of mode F. However, the mode shape at the edge of boundary layer around $H^* = 0.002$ m and outside the boundary layer is deviated away from the mode F. This comparison shows that in such upstream location, the mode F is relatively strong in the disturbances within the boundary layer. However, there are transient forcings exist at the edge of the boundary layer and outside the boundary layer at that location.

In Figure 130 (b), at the location of $s^* = 0.345$ m further downstream from the synchronization point, the comparisons shows that the simulated mode shape compares very well to the one of mode S both inside and outside of the boundary layer. This comparison shows that the mode S is dominant in the boundary-layer disturbances at such downstream location after the synchronization of mode S and mode F, and there is no transient forcings outside the boundary layer. The current modal identifications obtained from the mode shape analyses at the upstream and downstream locations are consistent with the receptivity modal path found in the earlier phase speeds and growth rates comparisons.

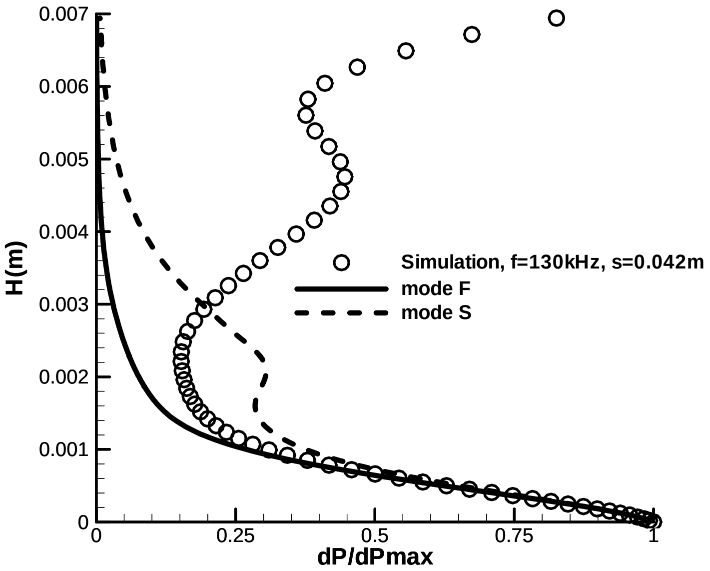

(a)

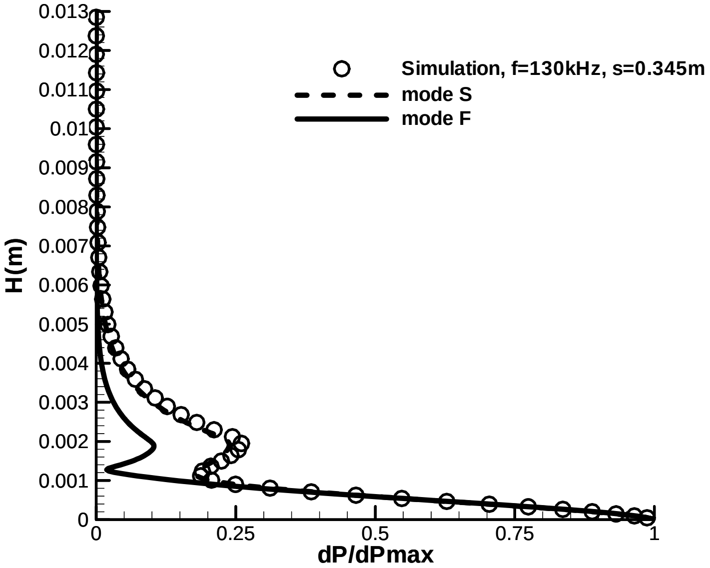

(b)

Figure 130. Comparisons of wall-normal mode shapes of pressure perturbations between the simulation and LST with the frequency of 130 kHz at (a) an upstream location, and (b) a downstream location in Case B1.

In Figure 131 (a), the location of $s^* = 0.042$ m is in the upstream region where the major modulation appears as shown in the phase speeds comparison in Figure 127 (a). The mode shape of the simulated boundary-layer disturbances within the boundary layer below $H^* = 0.0014$ m is close to the one of mode S. However, the mode shape at the edge of boundary layer around $H^* = 0.0032$ m and outside the boundary layer is deviated away from the mode S. This comparison shows that in such upstream location with the multi-mode modulation, the mode S is relatively strong in the disturbances within the boundary layer. Moreover, there are transient forcings existing as well at the edge of the boundary layer and outside the boundary layer at that location.

In Figure 131 (b), at the location of $s^* = 0.304$ m further downstream from the synchronization point, the comparisons show that the simulated mode shape compares very well to the one of mode S inside of the boundary layer. From the edge to outside the boundary layer above $H^* = 0.0016$ m , the simulated mode shape is reasonably well compared with the one of mode S. The difference between the simulated mode shape and the mode S is due to the flared cone geometry induced Mach waves downstream in the steady base flow, which are discussed in Section 4.4.1 of the steady base flow, and shown in Figure 96 and Figure 97. The overall comparison of the mode shapes in Figure 131 (b) shows that the mode S is dominant in the boundary-layer disturbances at such downstream location after the synchronization of mode S and mode F, and there is no transient forcings outside the boundary layer. The current modal identifications obtained from the mode shape analyses at the upstream and downstream locations are consistent with the receptivity modal path found in the earlier phase speeds and growth rates comparisons.

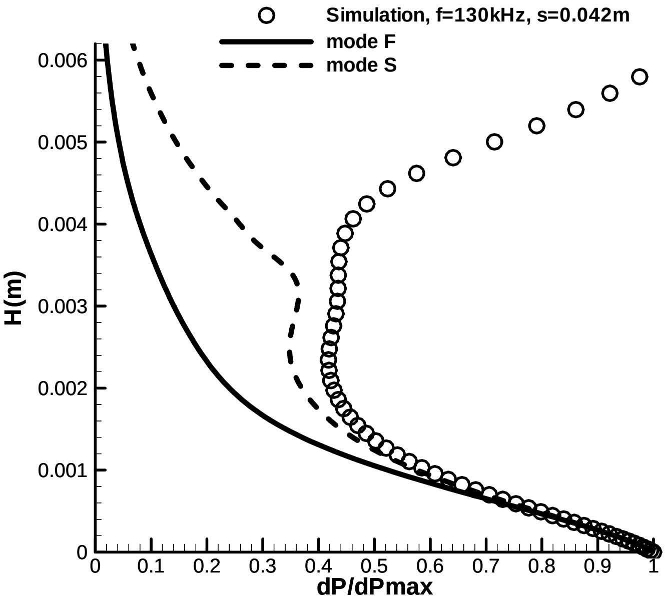

(a)

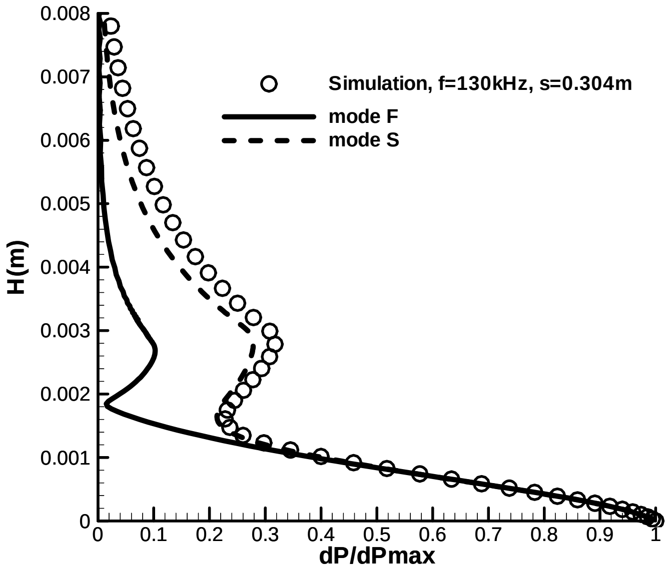

(b)

Figure 131. Comparisons of wall-normal mode shapes of pressure perturbations between the simulation and LST with the frequency of 130 kHz at (a) an upstream location, and (b) a downstream location in Case B2.

5 Conclusions

5.1 Conclusions

In the current study of the receptivity mechanisms and stability properties of hypersonic boundary layers over blunt cones, these are the new contributions to the state of the art: (1) the determination of the general mechanism of boundary-layer receptivity to freestream entropy spots over blunt cones, (2) the computations of receptivity coefficients of mode S along the Branch-I neutral stability curve, and (3) the determination of the parametric effects of nose bluntness and freestream Mach number on the boundary-layer receptivity and stability to a freestream entropy spot. The details of these new contributions are summarized as follows.

<u>Receptivity Mechanisms</u>:

The modal evolution throughout the receptivity process under nose bluntness effects and freestream Mach number effects were identified by comparing the simulated boundary-layer disturbances with the LST results. Consequently, we determined that the main mechanism of the receptivity process is a result of fast acoustic waves, which are generated from the hotspot/shock interaction in the nose region, initially entering the boundary layer and exciting mode F through the synchronization of fast acoustic waves and mode F in the upstream part of the cone. Subsequently, the synchronization of modes F and S triggers the mode-S related second mode, which eventually grows into a dominant level at the downstream part of the cone. The generalization of the receptivity mechanism was established, since similar modal evolutions were found under different parametric effects. The mechanism of boundary-layer receptivity to freestream entropy spots over blunt cones was not revealed prior to our study. Therefore, our discovery of the mechanism has advanced the understanding of boundary-layer receptivity to general freestream perturbations.

Determination of Receptivity Coefficients:

In addition to the general receptivity mechanism, wide, continuous spectra of mode-S receptivity coefficients at Branch-I neutral locations were obtained in this study. These spectra of mode-S receptivity coefficients provide the initial conditions that are crucial to future amplitude-based transition predicting methods. To our best knowledge, the receptivity coefficients of a single unstable mode over a cone have not been obtained in other published receptivity studies.

We also obtained the broad continuous spectra of boundary-layer disturbances over cones under both nose bluntness and freestream Mach number effects. These spectra were validated by the good agreements with the experimental and LST results. Furthermore, these spectra provide a comprehensive foundation for conducting future theoretical modal decomposition. Subsequently, a receptivity database, which provides all receptivity coefficients of each normal mode over the cones, can be built.

Nose Bluntness and Freestream Mach Number Effects:

The parametric effects of nose bluntness and freestream Mach number on boundary-layer receptivity were investigated through the comparative study of wide, continuous frequency spectra of receptivity coefficients. Our results showed that the nose bluntness reduces both the receptivity coefficients and ratio of mode S in overall boundary-layer disturbances at Branch-I neutral locations. These findings indicated that the nose bluntness reduces the boundary-layer receptivity to a freestream entropy spot.

On the other hand, it was found that the receptivity coefficients are higher, and that the mode S is more significant at Branch-I neutral locations, when the freestream Mach number increases. These findings indicated that the increase of freestream Mach number enhances the boundary-layer receptivity to a freestream entropy spot.

It is worth noting that the current receptivity study of nose bluntness effects was carried out based on wide, continuous frequency spectra of mode-S receptivity coefficients. In comparison, previous receptivity studies with nose bluntness effects were mostly carried out based on the receptivity coefficients of overall boundary-layer disturbances at only a few discrete frequencies. In addition, the freestream Mach number effects on boundary-layer receptivity to a freestream entropy spot over a cone have not been studied prior to this study. Moreover, the receptivity with freestream Mach number effects, in general, has been rarely studied. Therefore, the study presented in this dissertation has provided a new understanding of the freestream Mach number effects on boundary-layer receptivity to general freestream perturbations.

Besides receptivity, the effects of nose bluntness and freestream Mach number on boundary-layer stability have also been determined in the current study through a comparative study of wide, continuous frequency spectra of boundary-layer disturbances over the entire cone. We found that the nose bluntness increases the spatial growth rate of second-mode dominant disturbances but delays the growth's beginning location. Furthermore, the nose bluntness still stabilizes the perturbed boundary layer over a cone, since the nose bluntness drastically reduces the initial amplitudes of both overall disturbances and unstable second mode.

In addition, we found that the increase of freestream Mach numbers reduces the disturbances' spatial growth rate but does not change the growth's beginning location significantly. Consequently, the increase of freestream Mach numbers stabilizes the perturbed boundary layer over a cone, even though a higher freestream Mach number increases the initial amplitudes of both overall disturbances and unstable second mode.

Overall, our parametric study on stability has shown that the stability of boundary-layer disturbances is not only dependent on the spatial growth rates and the growth's beginning locations but also the initial amplitudes of both overall disturbances and unstable second mode.

5.2 Suggestions for Future Work

Recently, Michael Miselis of Professor Xiaolin Zhong's group at UCLA has developed and validated a new computer code that implements the theoretical bi-orthogonal eigenfunction decomposition method for wave-mode decomposition. The theoretical modal decomposition of the currently obtained broad, continuous spectra of boundary-layer disturbances can thus be carried out to separate mode S from mode F in the simulation results. Subsequently, a comprehensive receptivity database can be built. This receptivity database could provide wide, continuous spectra of initial amplitudes with differing nose radii and freestream Mach numbers to future amplitude-based transition predicting methods. Therefore, it is recommended that the results of receptivity be analyzed by the bi-orthogonal eigenfunction decomposition method in order to obtain precise receptivity coefficients for mode F and mode S.

In addition to the axisymmetric boundary-layer receptivity study presented in this dissertation, it is recommended that the three-dimensional receptivity mechanism over a blunt cone with an off-axis freestream hotspot be studied. Finally, more studies on receptivity mechanisms for hypersonic boundary layers involving different geometries, different kinds of freestream perturbations, and different flow conditions should be conducted in order to obtain a deeper understanding of the receptivity physics. Such studies are important for the development of more advanced amplitude-based transition predicting methods.

REFERENCES

[1] Reshotko, E., "Boundary Layer Stability and Transition," *Annual Review of Fluid Mechanics*, Vol. 8, 1976, pp. 311-349.

[2] Saric, W. S., Reshotko, E., and Arnal D., "Hypersonic Laminar-Turbulent Transition," *AGARD AR-391*, Vol. 2, 1998.

[3] Zhong, X., and Wang, X., "Direct Numerical Simulation of Receptivity, Instability, and Transition of Hypersonic Boundary Layers," *The Annual Review of Fluid Mechanics*, Vol. 44, 2012.

[4] Ma, Y., and Zhong, X., "Receptivity of a Supersonic Boundary Layer over a Flat Plate. Part 3. Effects of Different Types of Free-stream Disturbances," *Journal of Fluid Mechanics*, Vol. 532, 2005, pp. 63-109.

[5] Fong, K., "Increase of Total Skin Friction Coefficient and Heat Transfer Rate due to Boundary-Layer Transition," Private Communication with Huang, Y., 2015. Los Angeles.

[6] Duan, L., "A Higher-Order Cut-Cell Method for Numerical Simulation of Hypersonic Boundary Layer with Surface Roughness," PhD Dissertation, Department of Mechanical and Aerospace Engineering, UCLA, California, 2010.

[7] Reshotko, E., "Transition Issues for Atmospheric Entry," *Journal of Spacecraft and Rockets*, Vol. 45, No.2, 2008, pp. 161-164.

[8] Morkovin, M. V., Reshotko, E., and Herbert, T., "Transition in Open Flow Systems-A Reassessment," *Bulletin of the American Physical Society*, Vol. 39, No.1882, 1994.

[9] Reshotko, E., "Transient Growth: A Factor in Bypass Transition," *Physics of Fluids*, Vol. 13, No.5, 2001.

[10] Ma, Y., "Receptivity and Stability of Supersonic and Nonequilibrium Hypersonic Boundary Layers," PhD Dissertation, Department of Mechanical and Aerospace Engineering, UCLA, California, 2004.

[11] Herbert, T., "Secondary Instability of Boundary Layers," *Annual Review of Fluid Mechanics*, Vol. 20, 1988, pp. 487-526.

[12] Smith, A. M. O., and Gamberoni, N., "Transition, Pressure Gradient and Stability Theory," Rept. ES26388, Douglas Aircraft Co., El Segundo, California, 1956.

[13] Ingen, J. L. v., "A Suggested Semi-Empirical Method for the Calculation of the Boundary Layer Transition Region," Rept. VTH-74, Department of Aerospace Engineering, Delft University of Technology, Delft, 1956.

[14] Berridge, D. C., Chou, A., Ward, C. A. C., Steen, L. E., Gilbert, P. L., Juliano, T. J., and Schneider, S. P., "Hypersonic Boundary-Layer Transition Experiments in a Mach-6 Quiet Tunnel," AIAA paper 2010-1061, 2010.

[15] Ingen, J. L. v., *The eN Method for Transition Prediction. Historical Review of Work at TU Delft*, 2008, AIAA paper 2008-3830.

[16] Schneider, S. P., "Summary of Hypersonic Transition Research Coordinated Through NATO RTO AVT-136," AIAA paper 2010-1466, 2010.

[17] Berridge, D. C., Casper, K. M., Rufer, S. J., Alba, C. R., Lewis, D. R., Beresh, S. J., and Schneider, S. P., "Measurements and Computations of Second-Mode Instability Waves in Three Hypersonic Wind Tunnels," AIAA paper 2010-5002, 2010.

[18] Schneider, S. P., "Flight Data for Boundary-Layer Transition at Hypersonic and Supersonic Speeds," *Journal of Spacecraft and Rockets*, Vol. 36, No.1, 1999.

[19] Kimmel, R. L., "Aerothermal Design for the HIFiRE-1 Flight Vehicle," AIAA paper 2008-4034, 2008.

[20] Johnson, H. B., Alba, C. R., Bartkowicz, M. D., Drayna, T. W., and Candler, G. V., "Design Optimization of Hypersonic Vehicles for Boundary-Layer Stability," AIAA paper 2008-6221, 2008.

[21] Johnson, H. B., and Candler, G. V., "Hypersonic Boundary Layer Stability Analysis Using PSE-Chem," AIAA paper 2005-5023, 2005.

[22] Chou, A., "Mach-6 Receptivity Measurements of Laser-Generated Perturbations on a Flared Cone," PhD Dissertation, School of Aeronautics and Astronautics, Purdue Univ., W. Lafayette, IN, 2014.

[23] Wheaton, B. M., Juliano, T. J., Berridge, D. C., Chou, A., Gilbert, P. L., Casper, K. M., Steen, L. E., and Schneider, S. P., "Instability and Transition Measurements in the Mach-6 Quiet Tunnel," AIAA paper 2009-3559, 2009.

[24] Mack, L. M., "Boundary Layer Linear Stability Theory," AGARD Report 709, Jet Propul. Lab., Pasadena, CA, 1984.

[25] Saric, W. S., "Goerlter Vortices," *Annual Review of Fluid Mechanics*, Vol. 26, 1994, pp. 379-409.

[26] Reed, H. L., and Saric, W. S., "Stability of Three-Dimensional Boundary Layers," *Annual Review of Fluid Mechanics*, Vol. 21, 1989, pp. 235--84.

[27] Fedorov, V. A., "Transition and Stability of High-Speed Boundary Layers," *Annual Review of Fluid Mechanics*, Vol. 43, 2011, pp. 79-95.

[28] Zhong, X., "Receptivity of Mach 6 Flow over a Flared Cone to Freestream Disturbance," AIAA Paper 2004-253, 2004.

[29] Malik, M. R., "Prediction and Control of Transition in Supersonic and Hypersonic Boundary Layers," *AIAA Journal*, Vol. 27, No.11, 1989, pp. 1487-1493.

[30] Balakumar, P., and Kegerise, M. A., "Receptivity of Hypersonic Boundary Layers over Straight and Flared Cones," AIAA paper 2010-1065, 2010.

[31] Balakumar, P., and Kegerise, M. A., "Receptivity of Hypersonic Boundary Layers to Acoustic and Vortical Disturbances," AIAA paper 2011-371, 2011.

[32] Egorov, I. V., Novikov, A. V., and Soudakov, V. G., "Numerical Simulation of Receptivity and Stability of High-Speed Boundary Layers," NATO AVT-Specialists' Meeting on "Hypersonic Laminar-Turbulent Transition", No. 17, 2012.

[33] Egorov, I. V., Fedorov, A. V., and Soudakov, V. G., "Receptivity of a Hypersonic Boundary Layer over a Flat Plate with a Porous Coating," *Journal of Fluid Mechanics*, Vol. 601, 2008, pp. 165-187.

[34] Lei, J., "Numerical Study of Freestream Waves Receptivity and Nonlinear Breakdown in Hypersonic Boundary Layer," PhD Dissertation, Department of Mechanical and Aerospace Engineering, UCLA, California, 2013.

[35] Ma, Y., and Zhong, X., "Receptivity of a Supersonic Boundary Layer over a Flat Plate. Part 2. Receptivity to Free-Stream Sound," *Journal of Fluid Mechanics*, Vol. 488, 2003, pp. 79-121.

[36] Zhong, X., and Ma, Y., "Boundary-Layer Receptivity of Mach 7.99 Flow over a Blunt Cone to Free-Stream Acoustic Waves," *Journal of Fluid Mechanics*, Vol. 556, 2006, pp. 55-103.

[37] Sivasubramanian, J., Mayer, C. S. J., Laible, A. C., and Fasel, H. F., "Numerical Investigation of Wavepackets in a Hypersonic Cone Boundary Layer at Mach 6," AIAA paper 2009-3560, 2009.

[38] Sivasubramanian, J., and Fasel, H. F., "Numerical Investigation of Boundary-layer Transition Initiated by a Wave Packet for a Cone at Mach 6," AIAA paper 2010-900, 2010.

[39] Stetson, K. F., Thompson, E. R., Donaldson, J. C., and Siler, L. G., "Laminar Boundary Layer Stability Experiments on a Cone at Mach 8, Part 2: Blunt Cone," AIAA Paper 84-0006, 1984.

[40] Hofferth, J., Saric, W., Kuehl, J., Perez, E., Kocian, T., and Reed, H., "Boundary-Layer Instability & Transition on a Flared Cone in a Mach 6 Quiet Wind Tunnel," NATO AVT-Specialists' Meeting on "Hypersonic Laminar-Turbulent Transition", No. 10, 2012: NATO.

[41] Heitmann, D., and Radespiel, R., "Perspectives of Laser-Generated Disturbances for Stability Experiments," NATO AVT-Specialists' Meeting on "Hypersonic Laminar-Turbulent Transition", No. 19, 2012.

[42] Bountin, D. A., Sidorenko, A. A., and Shiplyuk, A. N., "Development of Natural Disturbances in a Hypersonic Boundary Layer on a Sharp Cone," *Journal of Applied Mechanics and Technical Physics*, Vol. 42, No.1, 2001, pp. 57-62.

[43] Su, C., and Zhou, H., "Stability Analysis and Transition Prediction of Hypersonic Boundary Layer over a Blunt Cone with Small Nose Bluntness at Zero Angle of Attack," *Applied Mathematics and Mechanics (English Edition)*, Vol. 28, No.5, 2007, pp. 563–572.

[44] Malik, M. R., "Numerical Method for Hypersonic Boundary Layer Stability," *Journal of Computational Physics*, Vol. 86, 1990, pp. 376-413.

[45] Malik, M. R., Spall, R. E., and Chang, C.-L., "Effect of Nose Bluntness and Boundary Layer Stability and Transition," AIAA paper 90-0112, 1990.

[46] Stetson, K. F., and Rushton, G. H., "Shock Tunnel Investigation of Boundary-Layer Transition at M=5.5," *AIAA Journal*, Vol. 5, No.5, 1967, pp. 899-906.

[47] Softley, E. J., "Transition of the Hypersonic Boundary Layer on a Cone: Part II - Experiments at Mach 10 and More on Blunt Cone Transition," GE Space Science Lab, R68SD14, 1968.

[48] Lei, J., and Zhong, X., "Linear Stability Analysis of Nose Bluntness Effects on Hypersonic Boundary Layer Transition," *Journal of Spacecraft and Rockets*, Vol. 49, No.1, 2012, pp. 24-37.

[49] Ma, Y., and Zhong, X., "Receptivity of a Supersonic Boundary Layer over a Flat Plate. Part 1. Wave Structures and Interactions," *Journal of Fluid Mechanics*, Vol. 488, 2003, pp. 31-78.

[50] Herbert, T., and Bertolotti, F. P., "Stability Analysis of Nonparallel Boundary Layers," *Bulletin of the American Physical Society*, Vol. 32, 1987, pp. 2079.

[51] Chang, C.-L., Malik, M. R., Erlebacher, G., and Hussaini, M. Y., "Linear and Nonlinear PSE for Compressible Boundary Layers," NASA Contractor Report 191537 and ICASE Report No. 93-70, 1993.

[52] Gao, B., and Park, S. O., "Compressible Parabolized Stability Equation in Curvilinear Coordinate System and Integration," *KSAS International Journal*, Vol. 7, No.2, 2006, pp. 155-174.

[53] Perez, E., Kocian, T. S., Kuehl, J. J., and Reed, H. L., "Stability of Hypersonic Compression Cones," AIAA paper 2012-2962, 2012.

[54] Huang, Y., and Zhong, X., "Numerical Study of Boundary-Layer Receptivity on Blunt Compression-Cones in Mach-6 Flow with Localized Freestream Hot-Spot

Perturbations," NATO AVT-Specialists' Meeting on "Hypersonic Laminar-Turbulent Transition", No. 20, 2012.

[55] Stetson, K. F., "On Predicting Hypersonic Boundary Layer Transition," AFWAL-TM-87-160-FIMG, 1987.

[56] Kendall, J. M., "Wind Tunnel Experiments Relating to Supersonic and Hypersonic Boundary-Layer Transition," *AIAA Journal*, Vol. 13, No.3, 1975, pp. 290-299.

[57] Stetson, K. F., "Hypersonic Boundary Layer Transition Experiments," AFWAL-TR-80-3062, 1980.

[58] Zhong, X., "Numerical Simulation of Hypersonic Boundary Layer Receptivity and Stability on Blunt Circular Cones," AIAA paper 2009-940, 2009.

[59] Rufer, S. J., and Schneider, S. P., "Hot-Wire Measurements of Instability Waves on Cones at Mach 6," AIAA paper 2006-3054, 2006.

[60] Horvath, T. J., Berry, S. A., Hollis, B. R., Chang, C.-L., and Singer, B. A., "Boundary Layer Transition on Slender Cones in Conventional and Low Disturbance Mach 6 Wind Tunnels," AIAA paper 2002-2743, 2002.

[61] Heitmann, D., Radespiel, R., and Knauss, H., "Experimental Study of Mach 6 Boundary Layer Response to Laser Generated Disturbances," AIAA paper 2011-3876, 2011.

[62] Heitmann, D., Radespiel, R., and Kahler, C. J., "Investigation of the Response of a Hypersonic 2D Boundary Layer to Controlled Acoustic Disturbances," AIAA paper 2010-536, 2010.

[63] Heitmann, D., Kahler, C. J., and Radespiel, R., "Investigation of Laser-Generated Flow Perturbations in Hypersonic Flow over a Flat Plate," AIAA paper 2008-3737, 2008.

[64] Heitmann, D., Kahler, C. J., Radespiel, R., Rodiger, T., Knauss, H., and Wagner, S., "Non-Intrusive Generation of Instability Waves in a Planar Hypersonic Boundary Layer," *Exp. Fluids*, Vol. 50, 2011, pp. 457-464.

[65] Heitmann, D., Kahler, C. J., and Radespiel, R., "Installation of a System for Laser-Generated Perturbations in Hypersonic Flow," 14th International Symposium on Application of Laser Techniques to Fluid Mechanics, 2008.

[66] Schmisseur, J. D., "Receptivity of the Boundary Layer on a Mach 4 Elliptic Cone to Laser-Generated Localized Free Stream Perturbations," Ph.D. Dissertation, School of Aeronautics and Astronautics, Purdue Univ., W. Lafayette, IN, 1997.

[67] Schmisseur, J. D., Collicott, S. H., and Schneider, S. P., "Laser-Generated Localized Freestream Perturbations in Supersonic and Hypersonic Flows," *AIAA Journal*, Vol. 38, No.4, 2000, pp. 666-671.

[68] Li, F., Choudhari, M., Chang, C.-L., Wu, M., and Greene, P. T., "Development and Breakdown of Görtler Vortices in High Speed Boundary Layers," AIAA paper 2010-705, 2010.

[69] Heitmann, D., and Radespiel, R., "Simulation of the Interaction of a Laser Generated Shock Wave with a Hypersonic Conical Boundary Layer," AIAA Paper 2011-3875, 2011.

[70] Lei, J., and Zhong, X. , "Linear Stability Study of Hypersonic Boundary Layer Transition on Blunt Circular Cones," AIAA paper 2009-939, 2009.

[71] Kara, K., Balakumar, P., and Kandil, O. A., "Effects of Nose Bluntness on Stability of Hypersonic Boundary Layers over a Blunt Cone," AIAA paper 2007-4492, 2007.

[72] Laible, A., and Fasel, H., "Numerical Investigation of Hypersonic Transition for a Flared and a Straight Cone at Mach 6," AIAA paper 2011-3565, 2011.

[73] Kara, K., Balakumar, P., and Kandil, O. A., "Effects of Nose Bluntness on Hypersonic Boundary-Layer Receptivity and Stability over Cones," *AIAA Journal*, Vol. 49, No.12, 2011, pp. 2593-2606.

[74] Rosenboom, I., Hein, S., and Dallmann, U., "Influence of Nose Bluntness on Boundary-Layer Instabilities in Hypersonic Cone Flows," AIAA paper 99-3591, 1999.

[75] Kovasznay, L. S. G., "Turbulence in Supersonic Flow," *Journal of the Aeronautical Sciences*, Vol. 20, No.10, 1953, pp. 657-682.

[76] McKenzie, J. F., and Westphal, K. O., "Interaction of Linear Waves with Oblique Shock Waves," *Physics of Fluids*, Vol. 11, No.11, 1968, pp. 2350-2362.

[77] Zhong, X., "High-Order Finite-Difference Schemes for Numerical Simulation of Hypersonic Boundary-Layer Transition," *Journal of Computational Physics*, Vol. 144, 1998, pp. 662-709.

[78] Fedorov, A., and Tumin, A., "High-Speed Boundary Layer Instability: Old Terminology and a New Framework," *AIAA Journal*, Vol. 49, No.8, 2011, pp. 1647-1657.

[79] Fedorov, V. A., "Receptivity of a High-Speed Boundary Layer to Acoustic Disturbances," *Journal of Fluid Mechanics*, Vol. 491, 2003, pp. 101-129.

[80] Fedorov, V. A., and Khokhlov, A. P., "Prehistory of Instability in a Hypersonic Boundary Layer," *Theoretical and Computational Fluid Dynamics*, Vol. 14, 2001, pp. 359-375.

[81] Maslov, A. A., Shiplyuk, A. N., Sidorenko, A. A., and Arnal, D., "Leading-Edge Receptivity of a Hypersonic Boundary Layer on a Flat Plate," *Journal of Fluid Mechanics*, Vol. 426, 2001, pp. 73-94.

[82] Ma, Y., and Zhong, X., "Numerical Simulation of Receptivity and Stability of Nonequilibrium Reacting Hypersonic Boundary Layers," AIAA paper 2001-0892, 2001.

[83] Egorov, I. V., Fedorov, A. V., and Nechaev, A. V., "Receptivity of Supersonic Boundary Layer on a Blunt Plate to Acoustic Disturbances," AIAA paper 2004-249, 2004.

[84] Tumin, A., "Multimode Decomposition of Spatially Growing Perturbations in a Two-Dimensional Boundary Layer," *Physics of Fluids*, Vol. 15, No.9, 2003, pp. 2525-2540.

[85] Tumin, A., "Three-Dimensional Spatial Normal Modes in Compressible Boundary Layers," *Journal of Fluid Mechanics*, Vol. 586, 2007, pp. 295-322.

[86] Tumin, A., Wang, X., and Zhong, X., "Direct Numerical Simulation and the Theory of Receptivity in a Hypersonic Boundary Layer," *Physics of Fluids*, Vol. 19, No.014101, 2007.

[87] Zhong, X., "Effect of Nose Bluntness on Hypersonic Boundary Layer Receptivity over a Blunt Cone," AIAA paper 2005-5022, 2005.

[88] Balakumar, P., and Kegerise, M. A., "Receptivity of Hypersonic Boundary Layers over Straight and Flared Cones," *AIAA Journal*, Vol. 53, No.8, 2015, pp. 2097-2109.

[89] Egorov, I. V., Fedorov, A. V., and Soudakov, V. G., "Numerical Simulation of a Supersonic Boundary Layer Receptivity to Acoustic, Vorticity and Entropy Disturbances," International Conference on Methods of Aerophysical Research, 2008.

[90] Egorov, I. V., Soudakov, V. G., and Fedorov, A. V., "Direct Numerical Simulation of Supersonic Boundary Layer Receptivity to Free-Stream Disturbances," European Conference for Aerospace Sciences, 2005.

[91] Egorov, I. V., Soudakov, V. G., and Fedorov, A. V., "Numerical Modeling of the Receptivity of a Supersonic Boundary Layer to Acoustic Disturbances," *Fluid Dynamics*, Vol. 41, No.1, 2006, pp. 37-48.

[92] Egorov, I. V., Soudakov, V. G., and Fedorov, A. V., "Numerical Modeling of the Stabilization of a Supersonic Flat-Plate Boundary Layer by a Porous Coating," *Fluid Dynamics*, Vol. 41, No.3, 2006, pp. 356-365.

[93] Fedorov, V. A., Ryzhov, A. A., and Soudakov, G. V., "Numerical and Theoretical Modeling of Supersonic Boundary-Layer Receptivity to Temperature Spottiness," AIAA Paper 2011-3077, 2011.

[94] Fedorov, V. A., Ryzhov, A. A., Soudakov, G. V., and Utyuzhnikov, S. V., "Receptivity of a High-Speed Boundary Layer to Temperature Spottiness," *Journal of Fluid Mechanics*, Vol. 722, 2013, pp. 533-553.

[95] Schmisseur, J. D., "Receptivity of the Boundary Layer on a Mach 4 Elliptic Cone to Laser-Generated Localized Free Stream Perturbations," Ph.D. Dissertation, School of Aeronautics and Astronautics, Purdue Univ., W. Lafayette, IN, Dec.1997.

[96] Salyer, T. R., Collicott, S. H., and Schneider, S. P., "Characterizing Laser-Generated Hot Spots for Receptivity Studies," *AIAA Journal*, Vol. 44, No.12, 2006, pp. 2871.

[97] Salyer, T. R., "Laser Differential Interferometry for Supersonic Blunt Body Receptivity Experiments," Ph.D. Dissertation, School of Aeronautics and Astronautics, Purdue Univ., W. Lafayette, IN, 2002.

[98] Chou, A., "The Effect of a Laser-Generated Perturbation on the Instabilities of a Flared Cone," Technical Report, School of Aeronautics and Astronautics, Purdue Univ., W. Lafayette, IN, 2014.

[99] Chou, A., Wheaton, B. M., Ward, C. A. C., Gilbert, P. L., Steen, L. E., and Schneider, S. P., "Instability and Transition Research in a Mach-6 Quiet Tunnel," AIAA Paper 2011-283, 2011.

[100] Huang, Y., and Zhong, X., "Parametric Study of Boundary-Layer Receptivity to Freestream Hot-Spot Perturbation over a Blunt Compression Cone," AIAA paper 2014-0774, 2014.

[101] Chou, A., "Characterization of Laser-Generated Perturbations and Instability Measurements on a Flared Cone," M.S. Thesis, School of Aeronautics and Astronautics, Purdue Univ., W. Lafayette, IN, 2010.

[102] Fu, D. X., Ma, Y. W., Li, X. L., and Wang, Q., "Direct Numerical Simulation of Compressible Turbulent Flow," *Modern Mechanics Series, China Science Publishing and Media Ltd., Beijing*, 2010.

[103] Lei, J., and Zhong, X., "Linear Stability Analysis of Nose Bluntness Effects on Hypersonic Boundary Layer Transition," AIAA Paper 2010-0898, 2010.

[104] Lees, L., and Lin, C. C., "Investigation of the Stability of the Laminar Boundary Layer in a Comrpressible Fluid," NACA TN 1115, 1946.

[105] Fong, K. D., Wang, X., Huang, Y., Zhong, X., McKiernan, G. R., Fisher, R. A., and Schneider, S. P., "Second Mode Suppression in Hypersonic Boundary Layer by Roughness: Design and Experiments," *AIAA Journal*, Vol. 53, No.10, 2015, pp. 3138-3144.

[106] Miselis, M., Huang, Y., and Zhong, X., "Analysis of Receptivity Mechanisms for a Freestream Hot-Spot Perturbation on a Blunt Compression-Cone Boundary Layer," Future AIAA paper, 2016.

[107] Lei, J., and Zhong, X., "Numerical Simulation of Freestream Waves Receptivity and Breakdown in Mach 6 Flow over Cone," AIAA Paper 2013-2741, 2013.

[108] Fedorov, V. A., and Khokhlov, A. P., "Receptivity of Hypersonic Boudnary Layer to Wall Disturbances," *Theoretical and Computational Fluid Dynamics*, Vol. 15, 2002, pp. 231-254.

[109] Fabre, D., Jacquin, L., and Sesterhenn, J., "Linear Interaction of a Cylindrical Entropy Spot with a Shock," *Physics of Fluids*, Vol. 13, No.8, 2001, pp. 2403-2422.